

Fluctuation-induced forces near continuous phase transitions in and out of equilibrium

HABILITATIONSSCHRIFT

der Fakultät für Physik
der Universität Duisburg-Essen

vorgelegt von

Alfred Hucht

aus Duisburg

Duisburg, im Juli 2012

Für Kristine, Lennart und Nils

Abstract

In this work we study two different realizations of fluctuation-induced forces near continuous phase transitions. In the first part we focus on thermodynamic Casimir forces in equilibrium systems and calculate the universal finite-size scaling functions which describe these forces near the critical point. We quantitatively calculate the temperature-dependent Casimir force for thin Helium-4 films with Dirichlet boundary conditions using Monte Carlo simulations and compare the results with experiments, finding excellent agreement without adjustable parameters. The dependency of Casimir forces and related free energies on the system shape is systematically investigated within the two- and three-dimensional Ising model, where depending on the system shape both attractive and repulsive forces are found. The analysis is completed by an exact calculation of the Casimir force scaling function for the three-dimensional $O(n)$ model with Dirichlet boundary conditions in film geometry in the large- n limit.

In the second part we investigate the properties of a simple model for fluctuation-induced friction in driven magnetic systems far from equilibrium. In this model certain subsystems of a d -dimensional Ising model are moved against each other with a given velocity v , driving the system into a steady state far from equilibrium. The energy pumped into the system is dissipated into the heat bath and induces a friction force, which is fluctuation induced as it vanishes if the magnetic states at the boundary are translationally invariant. The friction force can be of Coulomb- and of Stokes type depending on the involved time scales.

The model can be investigated in various geometries corresponding to both surface friction as well as shear stress. The driven systems show a continuous nonequilibrium phase transition at a temperature $T_c(v) > T_c(0)$, where the energy dissipation and friction force is maximal. In the limit $v \rightarrow \infty$ the system properties saturate and the model can be exactly solved by mapping it onto an appropriate equilibrium model, from which the critical temperatures and many other quantities can be computed.

For two-dimensional driven boundaries the phase transition becomes strongly anisotropic, with different critical behavior parallel and perpendicular to the driving direction. The critical exponents $\nu_{\parallel} = 3/2$ and $\nu_{\perp} = 1/2$ calculated using a simple Ginzburg-Landau-Wilson field theory are verified numerically using Monte Carlo simulations. Furthermore, the cross-over from the isotropic equilibrium case at $v = 0$ to the strongly anisotropic case at high velocities is numerically studied in detail using cross-over scaling. We find that for all finite driving velocities $v > 0$ the critical behavior becomes strongly anisotropic in the thermodynamic limit.

Finally, the analysis is extended to three-dimensional sheared systems at infinite velocity. We find the critical exponents $\nu_{\parallel} = 1$ and $\nu_{\perp} = 1/2$, with considerable corrections to scaling for the available system sizes. We suppose that also in three dimensions the phase transition becomes strongly anisotropic in the thermodynamic limit for all finite driving velocities $v > 0$, as in the two-dimensional case.

Contents

1	Introduction	1
1.1	Own prior work	2
2	Critical Casimir forces in equilibrium systems	4
2.1	The ^4He experiment of Garcia & Chan	5
2.2	Theory of the critical Casimir effect	6
2.3	Evaluation method: getting $\vartheta(x, \rho)$ in six steps	7
2.4	^4He with Dirichlet boundary conditions	9
2.5	Periodic Ising systems	12
2.5.1	Three-dimensional systems in film geometry	12
2.5.2	Three-dimensional systems with arbitrary aspect ratio	14
2.5.3	Exact results in two dimensions	15
2.6	Large- n limit with Dirichlet boundary conditions	16
2.7	Summary	17
3	Friction forces in nonequilibrium spin systems	19
3.1	Model	20
3.2	Power dissipation and friction	21
3.3	Cross-over from Coulomb to Stokes friction	22
3.4	Exact solution at high driving velocities	23
3.5	An integrable algorithm	24
3.6	1d case	26
3.6.1	1d with infinite v	26
3.6.2	Finite-size effects in 1d	28
3.6.3	1d with finite v	29
3.7	2d _b case	30
3.7.1	2d _b with infinite v	30
3.7.2	2d _b with finite v	31
3.8	Two-dimensional boundary	33
3.8.1	1+1d case	33
3.8.2	2d case	34
3.8.3	Mapping 2d onto 1+1d	34
3.8.4	Strongly anisotropic behavior	35
3.8.5	Field theory	37
3.8.6	Cross-over scaling at finite v	37
3.9	2+1d and 1+2d case	39
3.10	Some higher-dimensional geometries	42
3.11	Summary	43

4 Outlook	45
Acknowledgements	46
Bibliography	46
Publications	58
A. Hucht, J. Phys A: Math. Gen. 35, L481, Aug 2002	61
D. Grüneberg and A. Hucht, Phys. Rev. E 69, 036104, Mar 2004	69
A. Hucht, Phys. Rev. Lett. 99, 185301, Nov 2007	79
D. Kadau, A. Hucht, and D. E. Wolf, Phys. Rev. Lett. 101, 137205, Sep 2008	83
D. Comtesse, A. Hucht, and D. Grüneberg, arXiv:0904.3661v2, Apr 2009	87
A. Hucht, Phys. Rev. E 80, 061138, Dec 2009	99
A. Hucht, D. Grüneberg, and F. M. Schmidt, Phys. Rev. E 83, 051101, Mar 2011	113
M. P. Magiera, S. Angst, A. Hucht, and D. E. Wolf, Phys. Rev. B 84, 212301, Dec 2011	125
S. Angst, A. Hucht, and D. E. Wolf, Phys. Rev. E 85, 051120, May 2012	129
S. Angst, S. R. Dahmen, H. Hinrichsen, A. Hucht, and M. P. Magiera, J. Stat. Mech. 2012, L06002, Jun 2012	137
H. W. Diehl, D. Grüneberg, M. Hasenbusch, A. Hucht, S. B. Rutkevich, and F. M. Schmidt, EPL 100, 10004, Oct 2012	145
A. Hucht and S. Angst, EPL 100, 20003, Oct 2012	151
M. P. Magiera, A. Hucht, H. Hinrichsen, S. R. Dahmen, and D. E. Wolf, EPL 100, 27004, Oct 2012	157

1 Introduction

In his 1873 PhD thesis, Johannes Diderik van der Waals derived an equation of state for liquids and gases, the *van der Waals equation*, postulating an attractive force between the atoms or molecules in a real gas [vdW73]. He realized that without such an interaction a phase transition from the gaseous to the liquid phase would be impossible. Based on the work of van der Waals, his colleague Heike Kamerlingh Onnes was able to liquify Helium in 1908, leading to the discovery of superconductivity in 1911 [KO11]. Both Dutch physicists received the Nobel prize in physics for their pioneering work.

The van der Waals interaction between neutral atoms could not be explained until 1930, when Fritz London showed that correlated quantum fluctuations cause an attractive long-range force, the so called *London dispersion force* [Lon30]. In 1948, the Dutch theoretical physicists Hendrik B. G. Casimir and Dirk Polder investigated the influence of retardation, due to the finite speed of light, on the London-van der Waals forces [CP48], which finally led to the prediction of the quantum electrodynamic Casimir effect in 1948 [Cas48]: two perfectly conducting parallel plates at distance L in quantum electrodynamic vacuum attract each other with a universal force per area,

$$\frac{\mathcal{F}_C}{A} = -\frac{\pi^2 \hbar c}{240 L^4}, \quad (1.1)$$

arising from the modified energy density due to the discrete spectrum of vacuum quantum fluctuations between the plates. While this Casimir pressure is quite small at large distances L , it grows up to one atmosphere at around $L = 10$ nm and thus becomes very important in the field of nano-mechanical devices [CAK⁺01]. First experiments on the Casimir effect, with large experimental errors, were done in 1958 by M. Sparnaay [Spa58]. In recent experiments, the Casimir force was confirmed with high precision by S. K. Lamoreaux [Lam97], and by U. Mohideen and A. Roy [MR98] as shown in Fig. 1.1.

Casimir forces are prototypes of fluctuation-induced forces which are generally present if a fluctuating medium is confined in space. These fluctuation-induced forces have some special properties: they are non-additive, they depend in detail on the geometry and on the boundary conditions, and they are themselves fluctuating [BAFG02].

A similar type of Casimir force arises in thermodynamic systems in equilibrium, where correlated fluctuations of a medium give rise to effective forces [FdG78, Kre94, Gam09]. The range is limited by the correlation length of these fluctuations, which diverges at a continuous phase transition. The resulting critical Casimir forces are long-ranged in analogy to the quantum case. These thermodynamic Casimir forces can likewise be measured experimentally [GC99] and are investigated in detail in Chapter 2.

Fluctuation-induced forces far from equilibrium are less investigated up to now [Gol05, DG10], although they are believed to play an significant role in, e.g., the motion of flagella [Tay51] or in polydisperse colloids [DLL03]. In order to model such forces using Monte Carlo simulations, it would be necessary to replace the equilibrium methods described in Chapter 2

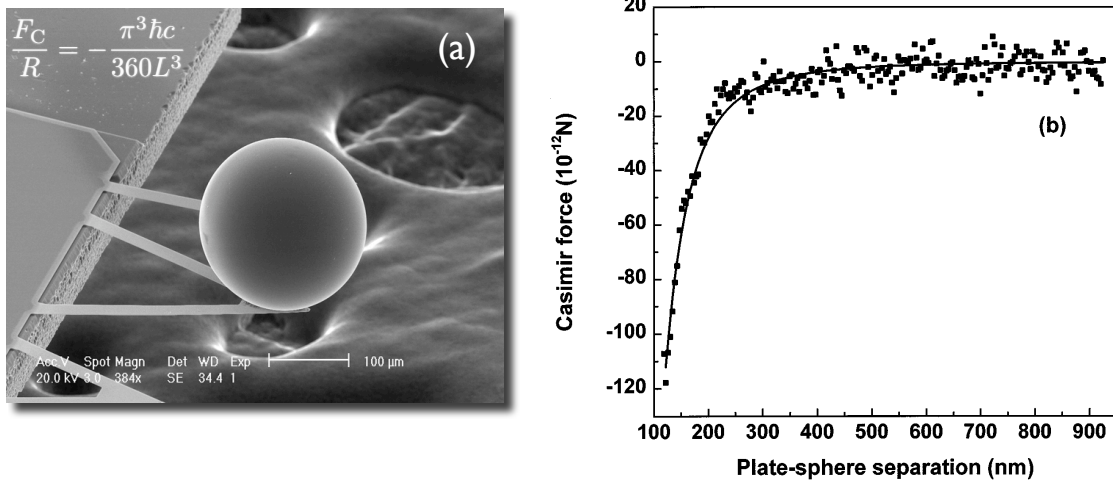


Figure 1.1: In the experiment of Mohideen and Roy [MR98] a metallized sphere with radius $R = 100 \mu\text{m}$ is mounted on a AFM cantilever (a), while the position is measured using a laser. The resulting quantum electrodynamic Casimir force is in excellent agreement with the theoretical prediction (b). (taken from Ref. [MR98])

by, e.g., the direct simulation method sketched in Chapter 4.

A different realization of fluctuation-induced forces far from equilibrium are friction forces arising from energy dissipation, if two fluctuating media are moved against each other [KHW08], if such a medium is sheared [IK85], or if a magnetic tip is moved over a magnetic surface [FWN08]. These systems provide a simple framework for the investigation of friction phenomena, which are of great technological impact [BC06]. As example, the cross-over between Coulomb friction and Stokes friction has recently been characterized within simple spin models [MAHW11], for details see Section 3.3.

These friction forces are strongest near nonequilibrium phase transitions, where fluctuations are maximal. However, in contrast to Casimir forces they are usually neither long-ranged nor universal. Nevertheless, interesting and surprising effects are found in these driven systems, which are topic of Chapter 3.

1.1 Own prior work

Both the thermodynamic Casimir effect and fluctuation-induced friction are phenomena near continuous phase transitions. In both areas it was essential to base on own preceding work, which is sketched in the following.

In Ref. [Huc02] the strongly anisotropic critical behavior of a two-dimensional Ising model with anisotropic long-range dipolar interaction was inspected using Monte Carlo simulations. A method was proposed to determine the *a priori* unknown anisotropy exponent θ by systematically varying the aspect ratio, i.e., the rectangular shape of the system at constant volume. Symmetry properties of the corresponding *universal finite-size scaling functions* (cf. [PF84]) with respect to their aspect ratio dependence were investigated and new scaling relations were predicted. Results from this work flow into the analysis performed in Section 3.8.

In Ref. [GH04] we investigated the universal finite-size scaling functions of a two-dimensional Ising model ($d = 2$) with isotropic long-range interactions of dipolar type¹. As these interactions decay algebraically as $r^{-(d+\sigma)}$ with distance r , with exponent $\sigma = 1$, the system is precisely at its upper critical dimension, $d = d_c = 2\sigma$, where the mean-field theory becomes exact. Using a special Monte Carlo algorithm for long-range systems [LB95] we were able to show that the finite-size scaling functions are identical to the exactly calculable mean-field finite-size scaling functions. As predicted by renormalization group theory [LB97], strong logarithmic corrections have to be taken into account, which, however, only modify the scaling variables and do not change the scaling functions. The mean-field finite-size scaling functions derived in [GH04] are used in Section 3.6.2 to test the mean-field character of the explored models. Furthermore, the critical Casimir force is likewise described by a universal finite-size scaling function, as will be shown in Chapter 2.

¹Ref. [GH04] is based on the diploma thesis of Daniel Grüneberg [Grü03].

2 Critical Casimir forces in equilibrium systems

Thirty years after the discovery of the Casimir-Polder force in quantum electrodynamics, M. E. Fisher and P.-G. de Gennes predicted an analogous effect in the physics of critical phenomena [FdG78, Kre94, Gam09]. This *thermodynamic Casimir effect* is caused by the spatial confinement of thermal fluctuations near the critical point of a continuous phase transition. As shown in the next sections, the resulting fluctuation-induced Casimir force is described by a universal finite-size scaling function $\vartheta(x)$ near criticality, with scaling variable x . J. Indekeu suggested to determine this scaling function experimentally by measuring the thinning of a ^4He film in the vicinity of the superfluid lambda transition [Ind86]. This experiment was finally performed in 1999 by R. Garcia and M. H. W. Chan [GC99, GSGC06], and they found a surprisingly deep minimum in the film thickness just below the critical temperature T_c .

For several years the shape of the finite-size scaling function determined experimentally by Garcia and Chan has not been understood theoretically, in particular its deep minimum right below T_c . In Ref. [DKD05] this was stressed as the main theoretical problem with respect to the explanation of the ^4He experiments. While the value of the Casimir force at criticality as well as the decay above T_c could be calculated using field theory [KD92a, Kre94, DGS06, GD08], no quantitative results were available for the scaling region $T \lesssim T_c$ except for mean-field-theoretical approaches [MGD07, ZSR⁺07], which gave unsatisfactory results. Analytic results existed only for the non-critical region below T_c , where contributions to the thermodynamic Casimir force from Goldstone modes [LK91, LK92, KG99] and from the excitation of capillary waves of the liquid-vapor ^4He interface [ZRK04] become dominant.

This unsatisfactory situation was resolved in Ref. [Huc07], where a method was proposed to calculate the thermodynamic Casimir force for $O(n)$ -symmetrical lattice models using Monte Carlo simulations without any approximations, in contrast to, e. g., the stress tensor method used by Dantchev and Krech [DK04], which furthermore was restricted to periodic systems. The Monte Carlo simulations were done for the three-dimensional XY model ($d = 3$, $n = 2$) on a simple cubic lattice with film geometry $L_{\parallel}^{d-1} \times L_{\perp}$ and open boundary conditions along the \perp direction, as this system is known to be in the same universality class as the superfluid transition in ^4He and thus displays the same asymptotic critical behavior [HD88, Die97]. The results, which are presented in Section 2.4, were found to be in excellent agreement with the experimental results of Garcia, Chan and coworkers [GC99, GSGC06], and for the first time provided a theoretical explanation for the characteristic shape of the finite-size scaling function ϑ and in particular its deep minimum below T_c . Subsequently, this method was used to determine Casimir forces in various systems and geometries [Has09b, Has10a, Has10b, HGS11, Has11, Has12b], and alternative methods for the evaluation of thermodynamic Casimir force scaling function using Monte Carlo simulations have been presented in the literature [VGMD07, MGD07, HHG⁺08, VGMD09, Has09b, Has09c].

Critical Casimir forces have also experimentally been studied in binary liquid mixtures, which belong to the Ising universality class. Fukuto *et al.* measured the thickness change of a binary wetting film [FYP05], and Hertlein *et al.* could directly measure the Casimir force on μm polystyrene particles in a binary liquid mixture of water and 2,6-lutidine [HHG⁺08,

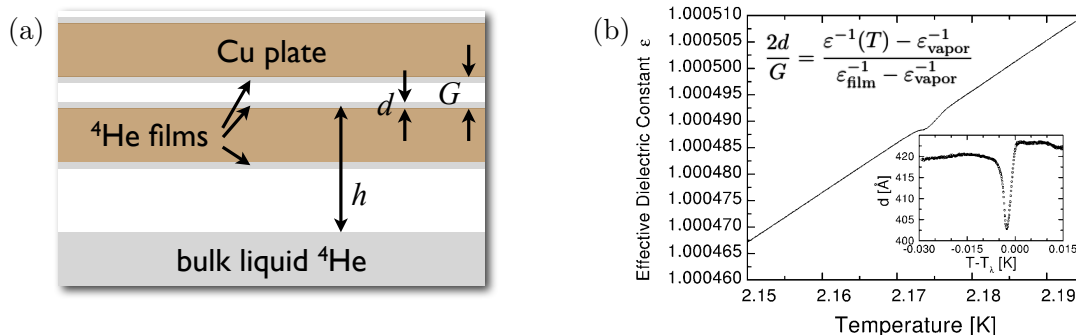


Figure 2.1: Geometry of the ^4He experiment [GC99] (a). The ^4He film with thickness d is adsorbed on Cu plates at height h above the bulk liquid ^4He reservoir. The measured effective dielectric constant ϵ and thickness d (inset) as a function of temperature T (b) (taken from Ref. [GC99]).

[GMH⁺09]. These experiments could be described using Monte Carlo simulations of three-dimensional Ising models with appropriate boundary conditions [VGMD09].

Until recently, the determination of the Casimir force scaling function $\vartheta(x)$ within exactly solvable models was limited to rather simple cases as the one- and two-dimensional Ising model [BDT00, RZSA10, HGS11] as well as the three-dimensional mean spherical model with periodic and antiperiodic boundary conditions [Kre94, Dan98, DKD03, DK04, DDG06, DG09]. Eventually, in Refs. [CHG09, DGH⁺12] we presented an exact solution of the three-dimensional $O(n)$ model with realistic Dirichlet boundary conditions in the large- n limit. The result shows all characteristic features of the ^4He Casimir force scaling function, in particular the deep minimum below T_c , and is presented in Section 2.6.

2.1 The ^4He experiment of Garcia & Chan

We start with a short description of the experiment of Garcia and Chan [GC99], which is sketched schematically in Fig. 2.1a. A ^4He film of thickness d was adsorbed on Cu plates at height h above the bulk liquid ^4He reservoir, and d was determined from the effective dielectric constant $\epsilon(T)$ measured in the Cu capacitor using the formula shown in Fig. 2.1b. The results for $\epsilon(T)$ and the thickness $d(T)$ are shown in Fig. 2.1b. In equilibrium the ^4He energy density near the superfluid transition temperature $T_\lambda = 2.1768$ K fulfills

$$mgh = \frac{\gamma_0}{d^3} \left(1 + \frac{d}{d_{1/2}}\right)^{-1} + \frac{V}{d^3} k_B T_\lambda \vartheta(x), \quad x = \left(\frac{T}{T_\lambda} - 1\right) \left(\frac{d}{\xi_+}\right)^{1/\nu}, \quad (2.1)$$

where the first two terms describe the competition between the gravitational potential energy mgh and the retardation-corrected van der Waals attraction of the Cu plate $\gamma_0/[d^3(1+d/d_{1/2})]$, with retardation length $d_{1/2} \approx 193$ Å. The last term is the contribution from the critical Casimir effect, with specific volume V and scaling function $\vartheta(x)$. Interestingly, due to the retardation both the quantum electrodynamic Casimir-Polder force as well as the critical Casimir force were relevant in this experiment. A careful analysis using capacitors at different heights h yielded the Casimir force scaling function $\vartheta(x)$ discussed in the following.

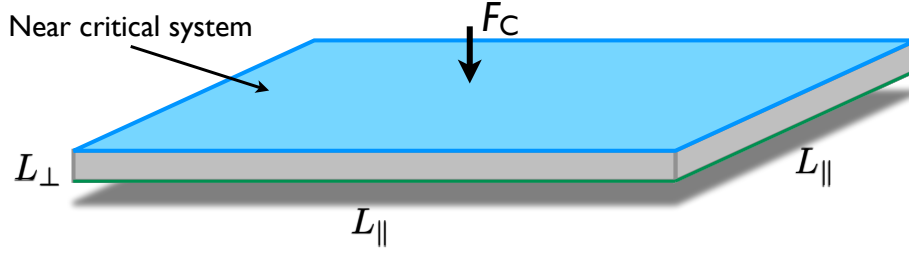


Figure 2.2: Typical system in film geometry $L_{\perp} \ll L_{\parallel}$. The Casimir force \mathcal{F}_C is acting on the perpendicular boundaries.

2.2 Theory of the critical Casimir effect

This section gives a short overview on the theory of the thermodynamic Casimir effect in cuboid systems, for details see [HGS11] and references therein. Consider a d -dimensional thermodynamic system such as a classical n -vector magnet, confined to a region with dimensions $L_{\parallel}^{d-1} \times L_{\perp}$ as shown in Fig. 2.2. We assume that the system undergoes a continuous phase transition at critical temperature T_c . The total (Helmholtz) free energy F in zero magnetic field is a function of L_{\parallel} , L_{\perp} and T , and the reduced free energy per unit area $f(T, L_{\perp}, L_{\parallel}) = L_{\parallel}^{1-d} \beta F(T, L_{\perp}, L_{\parallel})$, with the inverse temperature $\beta = 1/k_B T$, can be decomposed into a sum of the bulk free energy density $f_b(T)$, surface contributions $f_s(T)$, and a residual contribution δf as [Pri90]

$$f(T, L_{\perp}, L_{\parallel}) = L_{\perp} f_b(T) + f_s(T) + \delta f(T, L_{\perp}, L_{\parallel}). \quad (2.2)$$

As we assume periodic boundary conditions in the parallel directions, the corresponding surface terms as well as edge and corner contributions vanish in Eq. (2.2).

In terms of the *residual free energy* δf , which contains the finite-size effects important near T_c , the reduced Casimir force per surface area in \perp direction is defined as [Kre94]

$$\beta \mathcal{F}_C(T, L_{\perp}, L_{\parallel}) = -\frac{\partial}{\partial L_{\perp}} \delta f(T, L_{\perp}, L_{\parallel}) = -\frac{\partial}{\partial L_{\perp}} f(T, L_{\perp}, L_{\parallel}) + f_b(T). \quad (2.3)$$

Since the surface term f_s drop out in the L_{\perp} -derivative, we can alternatively calculate the Casimir force from the *excess free energy* per area

$$f_{\text{ex}}(T, L_{\perp}, L_{\parallel}) = f(T, L_{\perp}, L_{\parallel}) - L_{\perp} f_b(T), \quad (2.4)$$

as

$$\beta \mathcal{F}_C(T, L_{\perp}, L_{\parallel}) = -\frac{\partial}{\partial L_{\perp}} f_{\text{ex}}(T, L_{\perp}, L_{\parallel}). \quad (2.5)$$

Approaching the critical point T_c from above, the bulk correlation length ξ_b as a function

of the reduced temperature $t = T/T_c - 1$ grows and diverges as¹

$$\xi_b(t) \underset{t>0}{\simeq} \xi_+ t^{-\nu}, \quad (2.6)$$

with the correlation length exponent ν and a non-universal amplitude ξ_+ . According to the theory of finite-size scaling [Fis71] the critical Casimir force obeys the finite-size scaling form [FdG78]

$$\beta\mathcal{F}_C(T, L_\perp, L_\parallel) \simeq L_\perp^{-d} \vartheta(x, \rho), \quad (2.7)$$

where ϑ denotes a dimensionless universal finite-size scaling function, which only depends on gross properties of the system such as the bulk and surface universality classes of the phase transition, the system shape and boundary conditions, but not on its microscopic details [GH04, DDG06]. The scaling variable x and the aspect ratio ρ are defined as

$$x = t \left(\frac{L_\perp}{\xi_+} \right)^{\frac{1}{\nu}} \underset{t>0}{\simeq} \left(\frac{L_\perp}{\xi_b(t)} \right)^{\frac{1}{\nu}}, \quad (2.8a)$$

$$\rho = \frac{L_\perp}{L_\parallel}. \quad (2.8b)$$

An analogous finite-size scaling relation holds for the residual free energy per surface area,

$$\delta f(T, L_\perp, L_\parallel) \simeq L_\perp^{-(d-1)} \Theta(x, \rho), \quad (2.9)$$

with the universal scaling function Θ . The functions ϑ and Θ are related by [Doh09]

$$\vartheta(x, \rho) = \left[d - 1 - \frac{1}{\nu} \frac{x \partial}{\partial x} - \frac{\rho \partial}{\partial \rho} \right] \Theta(x, \rho). \quad (2.10)$$

At the critical point T_c the correlation length ξ_b diverges and the critical Casimir force becomes long-ranged. For sufficiently large values of the length L_\perp it decays as

$$\beta\mathcal{F}_C(T_c, L_\perp, L_\parallel) \simeq L_\perp^{-d} [(d-1)\Delta(\rho) - \rho\Delta'(\rho)], \quad (2.11)$$

where $\Delta(\rho) \equiv \Theta(0, \rho)$ is the so-called Casimir amplitude [FdG78], being, like the scaling function ϑ , a universal quantity. The film geometry is recovered by letting $\rho \rightarrow 0$, and Eq. (2.11) simplifies to

$$\beta\mathcal{F}_C(T_c, L_\perp, \infty) \simeq L_\perp^{-d} (d-1)\Delta(0). \quad (2.12)$$

2.3 Evaluation method: getting $\vartheta(x, \rho)$ in six steps

As shown in the last section, the critical Casimir force is defined as L -derivative of the excess free energy f_{ex} , see Eq. (2.5). Unfortunately, f_{ex} is hard to compute using Monte Carlo methods, because the computation requires an thermodynamic integration of, e. g., the internal

¹ Throughout this work, the symbol \simeq means “asymptotically equal” in the respective limit, $L_\parallel, L_\perp \rightarrow \infty$, $T \rightarrow T_c$, keeping the scaling variables x and ρ fixed, i. e., $f(L) \simeq g(L) \Leftrightarrow \lim_{L \rightarrow \infty} f(L)/g(L) = 1$.

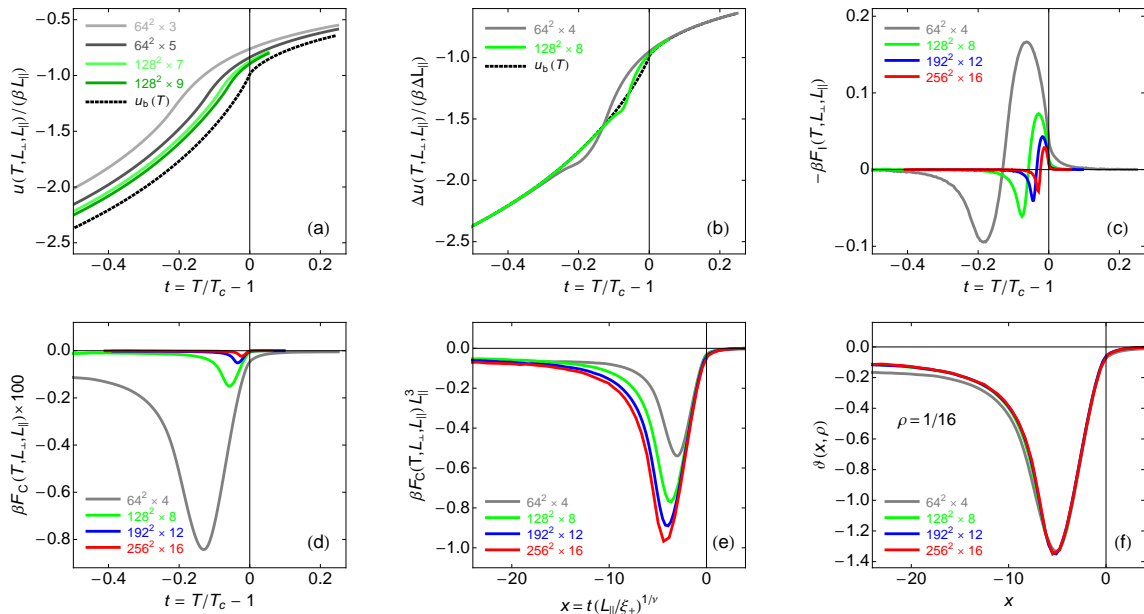


Figure 2.3: Illustration of the evaluation method. The six steps from (a) the internal energy $u(T, L_{\perp}, L_{\parallel})$ to (f) the Casimir force scaling function $\vartheta(x, \rho)$ are explained in the text.

energy over a large temperature interval. This integration introduces considerable statistical errors especially for large systems. As the critical Casimir force scales with L^{-d} for large L , only very small system sizes could be used for the determination of $\beta\mathcal{F}_C$, and dominant corrections due to the finite lattice constant made the numerical determination impossible.

To circumvent these problems, in Ref. [Huc07] a new method was developed, which is described in the following. Consider the d -dimensional isotropic nearest neighbor $O(n)$ model on a $L_{\parallel}^{d-1} \times L_{\perp}$ simple cubic lattice with Hamiltonian

$$\beta\mathcal{H} = -K \sum_{\langle ij \rangle} \mathbf{s}_i \cdot \mathbf{s}_j, \quad (2.13)$$

where $K = \beta J$ is the reduced exchange interaction, \mathbf{s}_i are n -component spin variables with $|\mathbf{s}_i| = 1$ at lattice sites i , and the sum runs over all nearest neighbor pairs $\langle ij \rangle$. Using Monte Carlo simulations we measure the reduced internal energy per surface area

$$u(T, L_{\perp}, L_{\parallel}) = L_{\parallel}^{1-d} \langle \beta\mathcal{H} \rangle \quad (2.14)$$

as a function of temperature T for several system sizes as shown in Fig. 2.3a. Instead of integrating u over T to get the free energy f as described above, we interchange integration over T and differentiation with respect to L_{\perp} : we first calculate the derivative $\partial u / \partial L_{\perp}$ using the central difference quotient,

$$\frac{\partial u(T, L_{\perp}, L_{\parallel})}{\partial L_{\perp}} \approx \frac{u(T, L_{\perp} + 1, L_{\parallel}) - u(T, L_{\perp} - 1, L_{\parallel})}{2} \quad (2.15)$$

(see Fig. 2.3b), and subtract the reduced bulk internal energy density $u_b(T)$ which can be determined with high accuracy using combinations of high- and low-temperature series expansions and Monte Carlo simulations [BCH⁺94, AF03b, FB10, Has12b]. The result is the so-called *internal Casimir force*

$$\beta\mathcal{F}_I(T, L_\perp, L_\parallel) = -\frac{\partial u(T, L_\perp, L_\parallel)}{\partial L_\perp} + u_b(T), \quad (2.16)$$

shown in Fig. 2.3c. With Eqs. (2.7, 2.19) and the hyperscaling relation $d\nu = 2 - \alpha$ with specific heat exponent α , it is straightforward to show that this quantity fulfills the finite-size scaling form

$$-\beta\mathcal{F}_I(T, L_\perp, L_\parallel) \simeq \xi_+^{-1/\nu} L_\perp^{(\alpha-1)/\nu} \vartheta'(x, \rho), \quad (2.17)$$

introducing the universal finite-size scaling function

$$\vartheta'(x, \rho) = \frac{\partial}{\partial x} \vartheta(x, \rho). \quad (2.18)$$

This quantity turns out to be extremely useful in understanding the Casimir force scaling function $\vartheta(x, \rho)$, as it contains important information from the $(d-1)$ -dimensional system [HGS11], see Sections 2.4 and 2.5.1 for details.

Finally, the thermodynamic Casimir force is obtained from Eq. (2.16) by thermodynamic integration,

$$\beta\mathcal{F}_C(T, L_\perp, L_\parallel) = -\int_T^\infty \frac{d\tau}{\tau} \beta\mathcal{F}_I(\tau, L_\perp, L_\parallel) \quad (2.19)$$

(Fig. 2.3d), where the exponential decay to zero of $\beta\mathcal{F}_I$ above T_c greatly simplifies the numerics and eliminates the problems due to statistical errors discussed in the last section.

Depending on the considered boundary conditions, the resulting approximations to the Casimir force scaling function ϑ may show non-negligible corrections to scaling as illustrated in Fig. 2.3e and discussed in the next section. Including appropriate correction terms, a convincing data collapse can be achieved for sufficiently large L (see Fig. 2.3f), resulting in an accurate determination of ϑ in the whole scaling region around the critical point. In the next sections, this method is applied to several systems and geometries.

2.4 ^4He with Dirichlet boundary conditions

In a series of papers, Garcia and Chan [GC99, GC02] and Ganshin *et al.* [GSGC06] measured the thinning of liquid ^4He films close to the λ point due to the critical Casimir effect. They found a characteristic deep minimum in the film thickness just below the superfluid transition temperature $T_\lambda = 2.1768\text{ K}$. Using finite-size scaling methods, they accurately determined the universal scaling function $\vartheta(x, 0)$ of the Casimir force in film geometry $\rho = 0$, see Sec. 2.1 for details.

As the superfluid transition is described by a complex wave function, it belongs to the XY universality class, with order parameter dimension $n = 2$. Furthermore, it is well established that the superfluid order parameter in liquid ^4He films vanishes at both surfaces of the film,

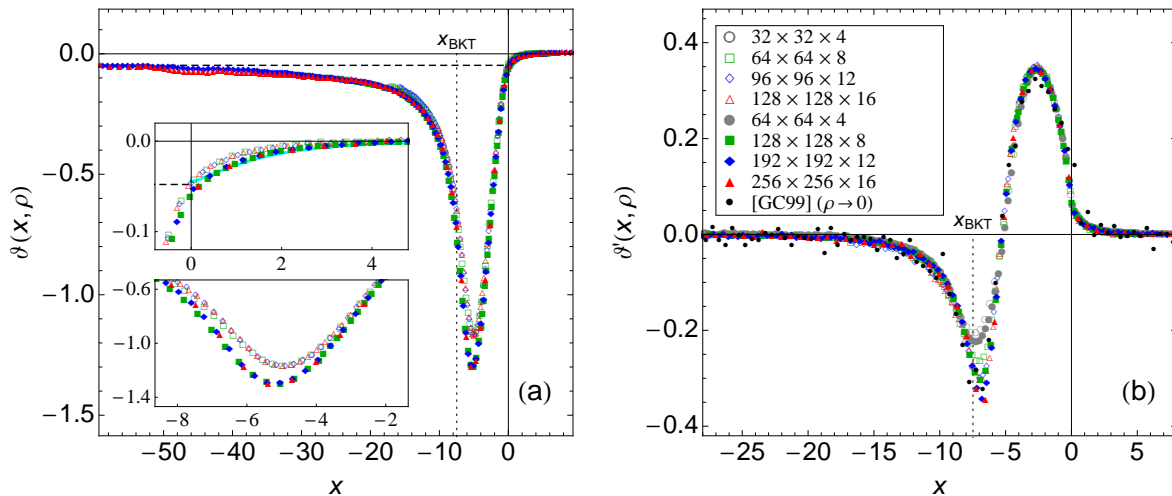


Figure 2.4: (a): Casimir force scaling function $\vartheta(x, \rho)$ from Eq. (2.21) for aspect ratios $\rho = 1/8$ (open symbols) and $\rho = 1/16$ (filled symbols). The upper and lower insets are magnifications around $x = 0$ and around the minimum, respectively. Also shown are the Goldstone amplitude $-\zeta(3)/8\pi$ [LK91] (dashed line), the field theoretical result [KD92b] (cyan curve in upper inset), and the location of the Berezinsky-Kosterlitz-Thouless transition at $x_{\text{BKT}} = -7.48(1)$. (b): Internal Casimir force scaling function $\vartheta'(x, \rho)$, Eq. (2.17). The experimental points are calculated from the data of Garcia and Chan [GC99, Cap. 1]. (adapted from [Huc07])

implying Dirichlet boundary conditions [HD88]. Here we have neglected possible contributions from surface fluctuations [ZRK04], which will be discussed later. Hence we performed Monte Carlo simulations of the classical XY model, with Hamiltonian (2.13), on a simple cubic lattice of size $L_{\parallel}^2 \times L_{\perp}$ using the Wolff cluster algorithm [Wol89]. The Dirichlet boundary conditions in perpendicular direction were implemented by open boundary conditions, which are known to be equivalent at large length scales [Die97, ZNL06], while in parallel directions we applied periodic boundary conditions. The simulations were performed for several system sizes with fixed aspect ratios $\rho = 1/8$ and $1/16$ and were finally extrapolated to $\rho = 0$ [Huc07].

While for periodic cubic systems the scaling corrections are moderate, systems with broken translational invariance and aspect ratios $\rho \ll 1$ show strong corrections to scaling. An analysis of usual thermodynamic quantities like the magnetic susceptibility χ and the Binder cumulant U [Bin81] showed that it was necessary to use a modified scaling variable x , Eq. (2.8a), with Wegner corrections [Weg72] of the form

$$x = t \left(\frac{L_{\perp}}{\xi_{+}} \right)^{1/\nu} (1 + g_{\omega} L_{\perp}^{-\omega}), \quad (2.20)$$

with $T_c/J = 2.20183(1)$, exponents $\nu = 0.672(1)$ and $\omega = 0.79(2)$, amplitude $\xi_{+} = 0.484(5)$, and unknown parameter g_{ω} . The finite-size corrections in y -direction are attributed to an effective thickness $L_{\text{eff}} = L_{\perp} + \delta L$ which corrects for the implementation of the perpendicular Dirichlet boundary conditions [Has12b]. To lowest order, this leads to a scaling correction

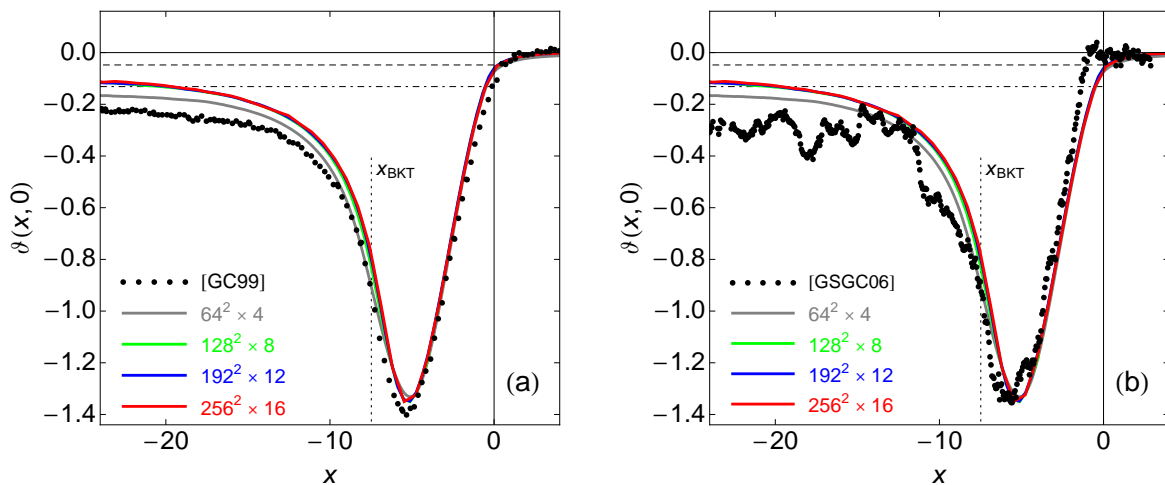


Figure 2.5: Results for the Casimir force scaling function $\vartheta(x, 0)$, compared (a) with the experimental data of Garcia and Chan [GC99, Cap. 1], as well as (b) with the results of Ganshin *et al.* [GSGC06, 238 Å]. Also shown are the Goldstone amplitude $-\zeta(3)/8\pi$ [LK91] (dashed line), the value $-11\zeta(3)/32\pi$ including surface fluctuations proposed in Ref. [ZRK04] (dotdashed line), and the location of the Berezinsky-Kosterlitz-Thouless transition at $x_{\text{BKT}} = -7.48(1)$. (adapted from [Huc07])

proportional to $(1 + g_1 L_{\perp}^{-1})$, resulting in the final scaling *ansatz*

$$\beta\mathcal{F}_{\text{C}}(T, L_{\perp}, L_{\parallel}) \simeq L_{\perp}^{-d} (1 + g_1 L_{\perp}^{-1})^{-1} \vartheta(x, \rho). \quad (2.21)$$

The results for the Casimir force are shown in Fig. 2.4a for six system sizes with $L_{\perp} \in \{8, 12, 16\}$, each with aspect ratio $\rho = 1/8$ and $\rho = 1/16$. The only fit parameters were the corrections to scaling amplitudes, $g_{\omega} = 2.0(1)$ and $g_1 = 5.5(2)$ (giving $\delta L = 1.8(1)$), without any remaining free factors in x - or y -direction. The remaining observed dependency on the aspect ratio ρ is known to scale approximately with ρ^2 [MN87], leading to additional correction factors $(1 + r_{\mu}\rho^2)$ for the x - and y -axis, with $r_x = 4(1)$ and $r_y = 10(1)$. This ρ -correction leaves the curves with $\rho = 1/16$ virtually unchanged. The resulting scaling function $\vartheta(x, 0)$ is depicted in Fig. 2.5 together with the results of Garcia and Chan [GC99] (a) as well as Ganshin *et al.* [GSGC06] (b), showing excellent agreement, within the error bars, with both measurements for $x \gtrsim -8$. The fluctuations and deviations below $x \approx -8$ can be attributed to surface fluctuations [ZRK04] as well as to the occurrences of vortices in the Berezinsky-Kosterlitz-Thouless phase [Ber71, KT73] below the BKT transition temperature at $x_{\text{BKT}} = -7.48(1)$ (c.f. Eq. (2.23)) [Has09a, Has12a]. The appearance of $(d-1)$ -dimensional critical behavior in the d -dimensional Casimir force scaling function is discussed in detail in the next section.

Finally, Fig. 2.4b shows results for the internal Casimir force scaling function $\vartheta'(x, 0)$, Eq. (2.16), together with a numerical differentiation of the experimental data of Garcia and Chan [GC99]. Again, the strong finite-size effects near the minimum around $x \approx -7$ can be attributed to the BKT transition at $x_{\text{BKT}} = -7.48(1)$ in the film limit $\rho \rightarrow 0$.

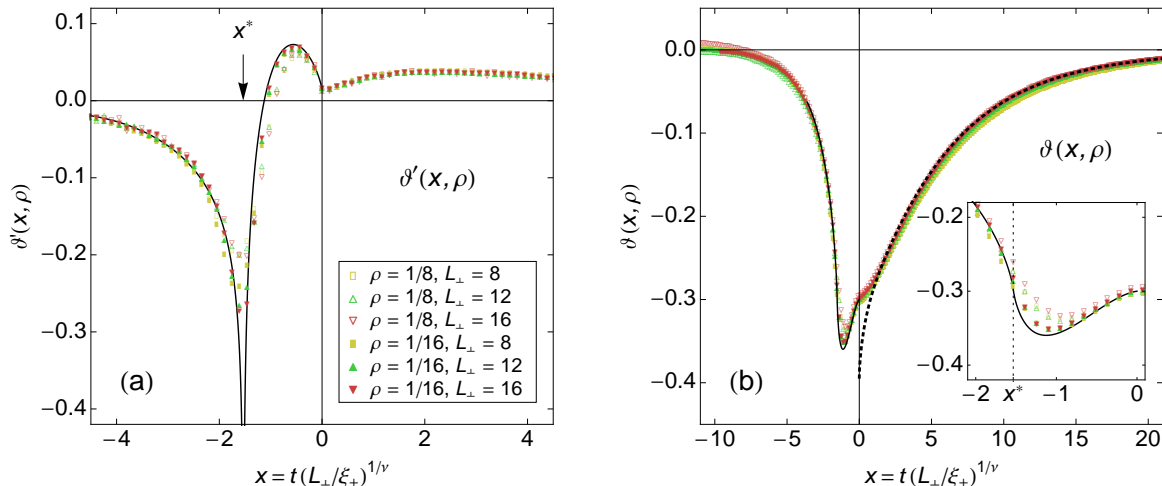


Figure 2.6: (a): Internal Casimir force scaling function $\vartheta'(x, \rho)$ for small aspect ratios $\rho = 1/16$ and $\rho = 1/8$. The black thin line is the extrapolation $\rho \rightarrow 0$, showing a logarithmic singularity at $x^* = -1.535(10)$ (see text). (b): Casimir force scaling function $\vartheta(x, \rho)$ for small aspect ratios $\rho = 1/16$ and $\rho = 1/8$. The solid line is the extrapolation $\rho \rightarrow 0$ calculated from the integrated logarithmic singularity in $\vartheta'(x, 0)$. The dotted line is the RG calculation of Grüneberg and Diehl [GD08]. (adapted from [HGS11])

2.5 Periodic Ising systems

In Ref. [HGS11] the universal finite-size scaling functions of the thermodynamic Casimir force ϑ and residual free energy Θ for the three-dimensional Ising model with cuboid geometry and periodic boundary conditions were calculated. The aspect ratio ρ was allowed to take arbitrary values from $\rho \rightarrow 0$ (film geometry) to $\rho \rightarrow \infty$ (rod geometry), while former investigations were either at $\rho = 0$ [KD92a, Kre94, DGS06, GD08, MGD07, ZSR⁺07] or limited to the case $\rho \ll 1$ [DK04, Huc07, VGMD07, Has09b, Has10a, Has09c, VGMD09, Has10b, TD10]. The results were compared to a field theory by V. Dohm [Doh09, Doh11].

Periodic systems have two main advantages over systems with broken translational invariance: first, they show much weaker corrections to scaling, and more important, the surface terms such as f_s in Eq. (2.2) vanish. As a consequence, the residual free energy δf equals the excess free energy f_{ex} , which is much easier to calculate, greatly simplifying the determination of the scaling function Θ . In the following the main results are summarized.

2.5.1 Three-dimensional systems in film geometry

We first turn to film geometry with $\rho \rightarrow 0$. In Fig. 2.6a we plot the scaling function $\vartheta'(x, \rho)$ of the internal Casimir force $\beta\mathcal{F}_I$ defined in Eqs. (2.16, 2.17), for small aspect ratios $\rho = 1/8$ (open symbols) and $\rho = 1/16$ (full symbols). In the limit $\rho \rightarrow 0$ we observe strong finite-size effects below the critical point already observed in the XY model [Huc07], which can be attributed to the influence of the phase transition in the $(d-1)$ -dimensional system. In fact it can be shown [HGS11] that in that limit $\beta\mathcal{F}_I$ is directly connected to the specific heat $c = \partial(Tu)/\partial T$ of the $(d-1)$ -dimensional system with thickness L_\perp . As a consequence,

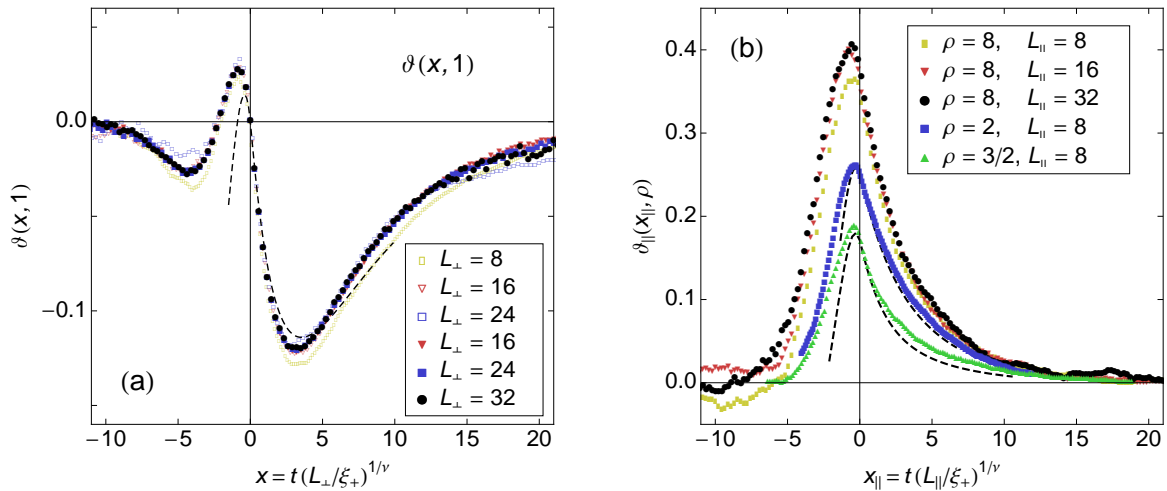


Figure 2.7: (a): Casimir force scaling function $\vartheta(x, 1)$ for the cubic system with $\rho = 1$. The filled symbols are calculated from Eq. (2.24) and have much better statistics than the other points. (b): Casimir force scaling function $\vartheta_{\parallel}(x_{\parallel}, \rho)$ for aspect ratios $\rho > 1$, now as a function of the proper scaling variable x_{\parallel} . In both figures, the dashed lines are the predictions of Dohm [Doh09]. (adapted from [HGS11])

the specific-heat singularity of the $(d-1)$ -dimensional film at critical temperature $T_c(L_{\perp})$ is directly visible in the scaling function $\vartheta'(x, 0)$ around x^* ,

$$\vartheta'(x \approx x^*, 0) \simeq B_{\pm} x |x - x^*|^{-\alpha^*} + \mathcal{O}(1), \quad (2.22)$$

where α^* denotes the specific heat exponent of the $(d-1)$ -dimensional system, B_{\pm} are non-universal amplitudes, and

$$x^* \simeq \left(\frac{T_c(L_{\perp})}{T_c} - 1 \right) \left(\frac{L_{\perp}}{\xi_{+}} \right)^{\frac{1}{\nu}} \quad (2.23)$$

marks the position of the phase transition in the $(d-1)$ -dimensional system of thickness L_{\perp} in terms of the scaling variable x . From this arguments we conclude that the scaling function $\vartheta'(x, 0)$ has a singularity at x^* dominated by the specific heat singularity of the $(d-1)$ -dimensional system, with critical exponent α^* . In our case of the $d = 3$ Ising model, $x^* = -1.535(10)$ and $\alpha^* = 0$ so that the singularity is logarithmic. This asymptotic behavior is included in Fig. 2.6 as a solid line.

In Fig. 2.6b we show the resulting scaling function of the Casimir force for $\rho = 1/8$ and $\rho = 1/16$, together with the renormalization group results of Grüneberg and Diehl [GD08] available for $x \geq 0$. The solid line is the integrated extrapolation discussed above, showing a singularity of the same type as the $(d-1)$ -dimensional internal energy at x^* . As consequence, for $\rho = 0$ and $x < x^*$ the system is long range ordered in parallel direction already at finite thickness L_{\perp} . The inset of Fig. 2.6b shows a magnification of the minimum region, where the largest finite- ρ corrections are visible slightly above x^* .

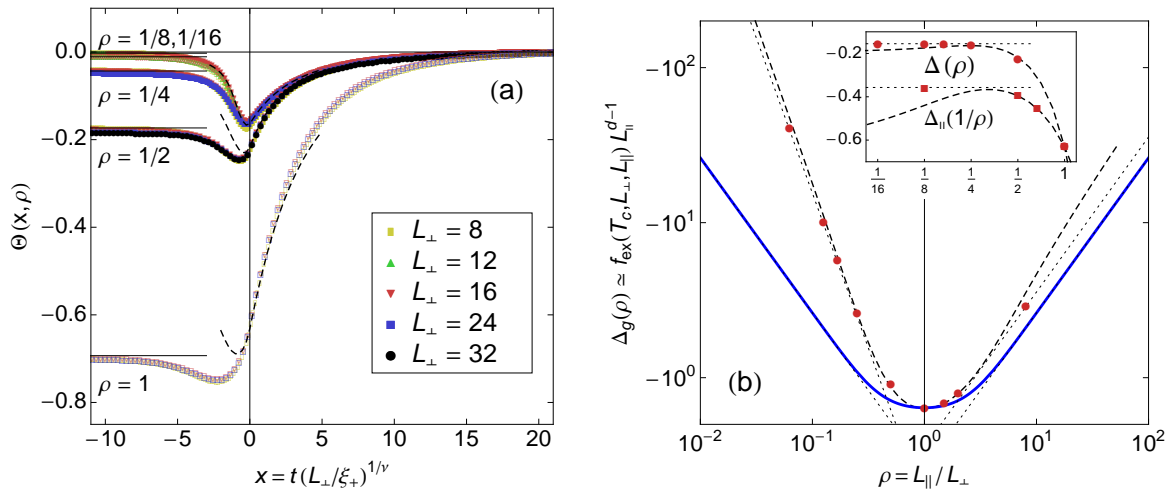


Figure 2.8: (a): Residual free energy scaling function $\Theta(x, \rho)$ for several aspect ratios ρ . The dashed lines are the predictions of Dohm [Doh09] for $\rho = \{1/4, 1/2, 1\}$, while the solid lines are the limits for $x \rightarrow -\infty$, Eq. (2.25). (b): Generalized Casimir amplitude $\Delta_g(\rho)$ [HGS11, Eq. (16)] of the Ising universality class in $d = 3$ (red circles) and in $d = 2$ (blue line). The dashed line is the prediction of Dohm [Doh09], while the dotted lines show the asymptotes. The inset depicts $\Delta(\rho)$ (circles) and $\Delta_{\parallel}(1/\rho)$ (squares). (adapted from [HGS11])

2.5.2 Three-dimensional systems with arbitrary aspect ratio

If we increase ρ to finite values, the Casimir force scaling function $\vartheta(x, \rho)$ gradually changes and reduces the depth of the minimum below T_c , for details see [HGS11, Fig. 4]. The results for the cube shaped system with $\rho = 1$ are shown in Fig. 2.7a. The case $\rho = 1$ turns out to be quite interesting, as here $\beta\mathcal{F}_C$ can be calculated from a scaling identity without integral and derivative [HGS11],

$$\beta\mathcal{F}_C(T, L, L) \simeq \frac{t}{d\nu} [u(T, L, L) - u_b(T)], \quad (2.24)$$

for the considered periodic boundary conditions. The Casimir force at $x = 0$ vanishes and even becomes positive for $\rho > 1$, although the system has symmetric, i. e., periodic boundary conditions. However, this sign change of the Casimir force at $\rho = 1$ does not contradict the prediction of Bachas that symmetric boundary conditions always imply attractive Casimir forces [Bac07], as he assumed an infinite system in parallel direction, i. e., $\rho = 0$. Fig. 2.7a shows results from both the calculation using Eqs. (2.14-2.19) (open symbols) as well as Eq. (2.24) (filled symbols), where the latter have a much better statistics, as no numerical differentiation and integration is necessary.

In Fig. 2.7b we depict the Casimir force scaling function for values of ρ larger than one. Now we are in rod geometry and use the appropriate relevant length L_{\parallel} instead of L_{\perp} , with scaling variable x_{\parallel} . Due to this rescaling, the scaling function $\vartheta_{\parallel}(x_{\parallel}, \rho)$ converges to a finite limit $\vartheta_{\parallel}(x_{\parallel}, \infty)$ which should only slightly deviate from curves for $\rho = 8$, just as in the inverse case $\rho = 1/8$ (see Fig. 2.6). In this regime the Casimir force is always positive, leading to a repulsion of the opposite surfaces.

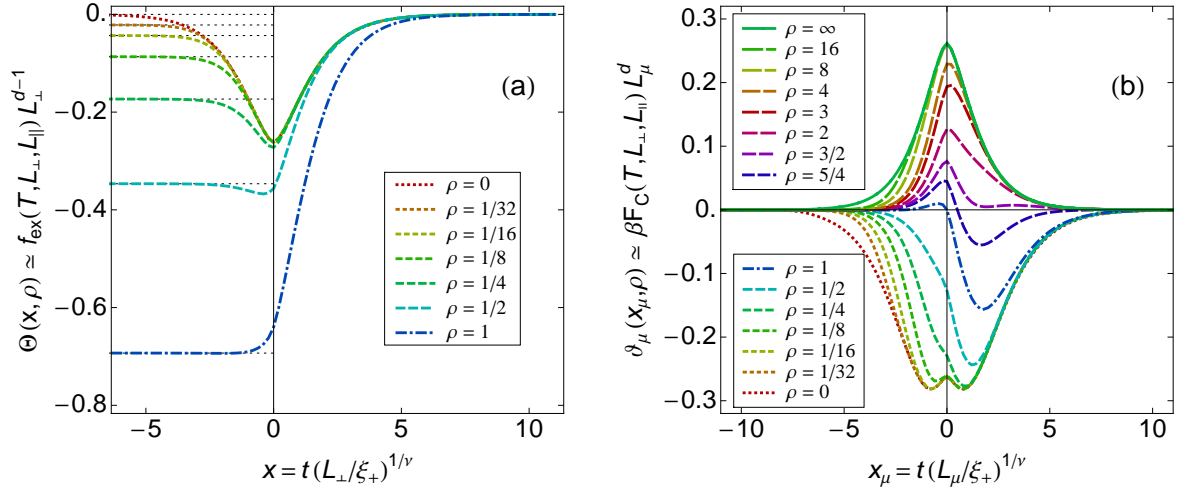


Figure 2.9: Exact results for the two-dimensional Ising model. Residual free energy scaling function (a) for several aspect ratios $\rho \leq 1$. The scaling functions for $\rho \geq 1$ can be calculated using [HGS11, Eq. (52)]. Casimir force scaling function (b) for several aspect ratios ρ . Shown is $\vartheta(x, \rho)$ for $\rho \leq 1$ and $\vartheta_{\parallel}(x_{\parallel}, \rho)$ for $\rho \geq 1$. (adapted from [HGS11])

The residual free energy is shown in Fig. 2.8a. An interesting feature of these curves is the non-vanishing limit for $x \rightarrow -\infty$,

$$\Theta(-\infty, \rho) = -\rho^{d-1} \ln 2, \quad (2.25)$$

which can be attributed to the broken symmetry in the ordered phase [PF83]. The results are compared to the field theoretical predictions of Dohm [Doh09], we find a good agreement for positive and slightly negative values of x . Furthermore, our value $\Delta(1) = -0.63(1)$ for the cube is compatible with the value $-0.657(30)$ from [Mon85]. Finally, in Fig. 2.8b we show the generalized Casimir amplitude $\Delta_{\text{g}}(\rho)$, defined in [HGS11, Eq. (16)], as determined from the MC data (red dots), together with the predictions of Dohm [Doh09]. As derived in [HGS11] the amplitude is maximal at $\rho = 1$ and goes to $-\infty$ for $\rho \rightarrow 0$ and ∞ . The inset shows the corresponding Casimir amplitudes in these limits, with the film limit value $\Delta(0) = -0.155(3)$ and the rod limit value $\Delta_{\parallel}(\infty) = -0.36(1)$, for details see [HGS11, Tab. I].

2.5.3 Exact results in two dimensions

The scaling function $\Theta(x, \rho)$ of the residual free energy in $d = 2$ was calculated exactly in [HGS11] based on the work of Ferdinand and Fisher [FF69]. Firstly, a compact closed-form expression for the bulk free energy density of the two-dimensional Ising model was derived not present in the literature before, namely

$$f_{\text{b}} = -\ln(2 \cosh 2K) + \frac{k^2}{16} {}_4F_3 \left(\begin{matrix} 1, 1, \frac{3}{2}, \frac{3}{2} \\ 2, 2, 2 \end{matrix} \middle| k^2 \right), \quad (2.26)$$

with $k = 2 \tanh 2K / \cosh 2K$ and the generalized hypergeometric function ${}_4F_3(\cdot)$ [Wol08]. After some algebra, the scaling function Θ for arbitrary x and ρ can be expressed through the

functions

$$\Theta(x, \rho) = -\rho \ln \left(\frac{P_{1/2}^+ + P_{1/2}^-}{2e^{-I_+/\rho}} + \frac{P_0^+ \pm P_0^-}{2e^{-I_-/\rho}} \right), \quad (2.27a)$$

$$P_\delta^\pm(x, \rho) = \prod_{n=-\infty}^{\infty} \left(1 \pm e^{-\sqrt{x^2 + 4\pi^2(n-\delta)^2/\rho}} \right), \quad (2.27b)$$

$$I_\pm(x) = \int_{-\infty}^{\infty} d\omega \ln \left(1 \pm e^{-\sqrt{x^2 + 4\pi^2\omega^2}} \right). \quad (2.27c)$$

The resulting residual free energy scaling function $\Theta(x, \rho)$ is depicted in Fig. 2.9a, showing a similar behavior as in the three-dimensional case. The Casimir amplitude $\Delta_g(\rho)$ is symmetric in $d = 2$ and shown as blue line in Fig. 2.8b.

Finally, the results for the Casimir force scaling function ϑ are shown in Fig. 2.9b. For $\rho \leq 1$ we show $\vartheta(x, \rho)$, while for $\rho \geq 1$ we show $\vartheta_{\parallel}(x_{\parallel}, \rho)$. Clearly the Casimir force changes sign from negative to positive values with increasing aspect ratio ρ , as in the three-dimensional case.

2.6 Large- n limit with Dirichlet boundary conditions

The $O(n)$ model with Dirichlet boundary conditions in film geometry $\rho = 0$ can be solved exactly in the limit $n \rightarrow \infty$ [Com08, CHG09, DGH⁺12], for details see [DGH⁺12, Model A]. Using a Hubbard-Stratonovich transformation and subsequent saddle point integration, the $L_{\parallel}^2 \times L_{\perp}$ -dimensional continuum system can be mapped, in the limit $L_{\parallel} \rightarrow \infty$, onto a one-dimensional Schrödinger equation with a potential $V(z)$ ($0 \leq z \leq L_{\perp}$) that has to be determined self-consistently. After discretization, the self consistent equation in its simplest form,

$$t = \langle z | \ln \mathbf{H} | z \rangle, \quad (2.28)$$

relates the reduced temperature t to the matrix logarithm diagonal of the $L_{\perp} \times L_{\perp}$ matrix $\mathbf{H} = -\mathbf{D}^2 + \mathbf{V}$, where \mathbf{D}^2 denotes the discrete second derivative and $(\mathbf{V})_{zz'} = V(z)\delta_{zz'}$. From \mathbf{H} the excess free energy can be calculated,

$$f_{\text{ex}}(t, L_{\perp}, \infty) = \frac{1}{8\pi} \text{tr}[\mathbf{H}(1 + t - \ln \mathbf{H})] - \frac{tL_{\perp}}{4\pi} - L_{\perp}f_{\text{b}}(t), \quad (2.29a)$$

where

$$f_{\text{b}}(t) = \frac{1}{4\pi} \begin{cases} \sinh t - t & t > 0 \\ 0 & t \leq 0 \end{cases} \quad (2.29b)$$

denotes the reduced bulk free energy density. The resulting Casimir force scaling function $\vartheta(x, 0)$, with $x = tL_{\text{eff}}$, is shown in Fig. 2.10a, where leading scaling corrections are accounted for by introducing an effective thickness $L_{\text{eff}} = L_{\perp} + \delta L$, with $\delta L = 0.7255032704723(3)$. It shows all characteristics of the XY case ($n = 2$) depicted in Fig. 2.5, i. e., it is attractive in the whole temperature range, it has a deep minimum below T_c , and it converges against the finite low-temperature Goldstone value. The only qualitative difference is the absence of the

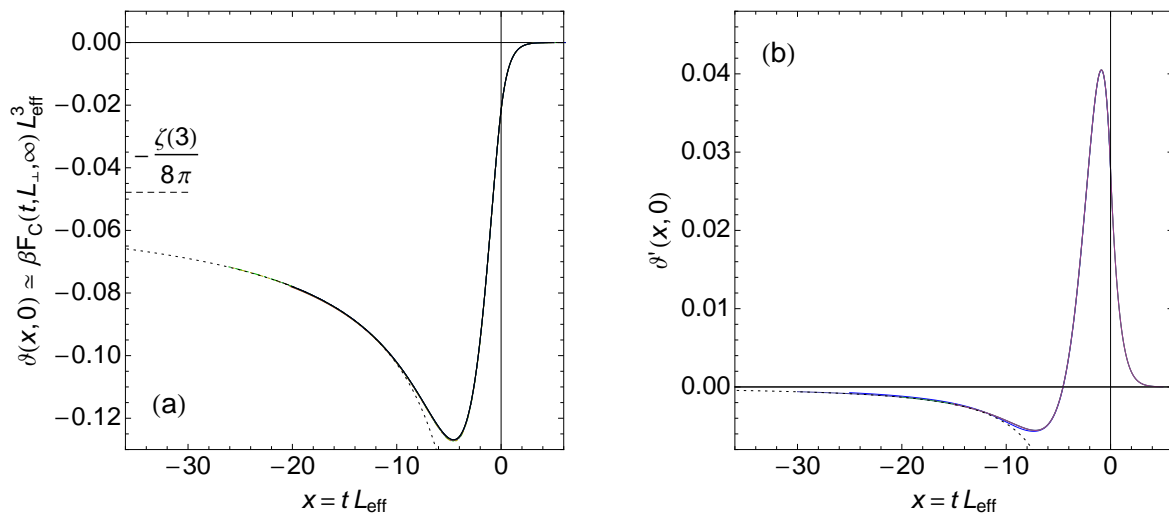


Figure 2.10: Universal Casimir force scaling functions $\vartheta(x, 0)$ and $\vartheta'(x, 0)$ of the $O(n)$ model in film geometry $\rho = 0$ with Dirichlet boundary conditions in the limit $n \rightarrow \infty$. The dashed horizontal line indicates the Goldstone value $\vartheta(-\infty, 0) = -\zeta(3)/8\pi$, and the dotted curve represents the limiting behavior $\vartheta(x, 0) \simeq \vartheta(-\infty, 0) + (c \ln |x| + d)/x$, with constants c and d . The effective thickness L_{eff} accounts for leading scaling corrections (see text). (Fig. (a) adapted from [DGH⁺12])

Berezinsky-Kosterlitz-Thouless singularity discussed in Section 2.4. At the critical point $t = 0$ the Casimir amplitude is estimated with high precision to be

$$\Delta(0) = \vartheta(0, 0)/2 = -0.01077340685024782(1). \quad (2.30)$$

For completeness we show the scaling function $\vartheta'(x, 0)$ in Fig. 2.10b, which has no singularity below zero because the two-dimensional $O(\infty)$ model has no phase transition at finite temperatures due to the presence of Goldstone modes.

The results were compared to an alternative approach using a fully discrete model in three dimensions [DGH⁺12, Model B]. The results of the two models were found to be fully consistent, demonstrating the universal character of the critical Casimir force.

2.7 Summary

In summary, in Ref. [Huc07] we proposed a method to accurately calculate thermodynamic Casimir forces and excess free energies above and below T_c using Monte Carlo simulations. The method has successfully been applied to the three-dimensional XY model ($n = 2$) with Dirichlet boundary conditions in film geometry, and the universal Casimir force finite-size scaling function was determined for the first time in the whole temperature range above and below T_c . Without any adjustable parameters, the results are in excellent agreement with experiments on ^4He by Garcia and Chan [GC99], and by Ganshin *et al.* [GSGC06], as well as with theoretical calculations for $T \geq T_c$ by Krech and Dietrich [KD91, KD92b].

Subsequently, this method was used within the Ising and XY model with different boundary

conditions [Has09b, Has10a, Has10b, HGS11, Has11, Has12b]. In Ref. [HGS11] we investigated the aspect ratio dependency of Casimir forces in the three-dimensional Ising model ($n = 1$). In the film limit we identified signatures of the $(d-1)$ -dimensional phase transition in the Casimir force scaling function. Furthermore, we showed that the Casimir force, which is commonly attractive especially for symmetric boundary conditions, can become repulsive within cube-shaped systems. The results were confirmed within an exact solution of the two-dimensional Ising model [HGS11].

Finally, the three-dimensional $O(n)$ model with Dirichlet boundary conditions was investigated in the spherical limit $n \rightarrow \infty$. In this case the system can be solved exactly by a mapping onto the one-dimensional Schrödinger equation [DGH⁺12]. The resulting universal Casimir force scaling function shows all characteristics of the XY case, i. e., it is attractive in the whole temperature range, it has a deep minimum below T_c , and it converges against the finite low-temperature Goldstone value.

3 Friction forces in nonequilibrium spin systems

Friction forces are present almost everywhere in our daily life. Without friction, we would not be able to walk or to drive a car. Dry friction between solids is usually of Coulomb type, with a non-vanishing friction force at zero velocity v . On the other hand, the drag friction force of a solid through a liquid is linear in v for small v and vanishes for $v \rightarrow 0$ as shown by Stokes in the 19th century. Both types of friction forces can be described within the atomistic Prandtl-Tomlinson model [Pra28, Tom29], where a point particle is dragged over a one-dimensional sinusoidal potential [Müs11].

Beyond electronic and phononic friction mechanisms, magnetic contributions to friction due to spin correlations have attracted increasing interest in recent years. One interesting aspect is the energy dissipation due to spin waves in magnetic force microscopy, where magnetic structures are investigated by moving a magnetic tip over a surface [Mag08, FWN08, MBWN09, MWBN09, MHH⁺12]. We could show recently that these friction forces can also be of Stokes or Coulomb type [MAHW11], for details see Section 3.3.

On the other hand, magnetic friction is present in bulk magnetic systems which are moved in close proximity. In this context, Kadau *et al.* [KHW08, Kad98] proposed a simple model for magnetic friction mediated solely by spin degrees of freedom. In this model an Ising spin system is moved over a second spin system along a boundary, with constant velocity v . This permanent perturbation drives the system to a steady state far from equilibrium, leading to a permanent energy flow from the boundary to the heat bath.

This problem can be analyzed for several different geometries in one, two and three dimensions, depicted in Fig. 3.1: besides the original problem of two half-infinite two-dimensional systems moving along the one-dimensional boundary, denoted $2d_b$ in the following, we will consider the homogeneous cases 1d and 2d where all spins are at the friction boundary, as well as the experimentally relevant three-dimensional case $3d_b$. Additionally, we will extend the analysis to sheared systems in two [CL90, CGL98, CGS05] and three [IK85] dimensions, denoted 1+1d and 2+1d. These systems are experimentally accessible within the framework of shear flow in binary liquid mixtures (for a review, see [Onu97]), though with conserved order parameter, while we deal with a non-conserved order parameter.

The models exhibit a nonequilibrium phase transition, which has been investigated in several different geometries [Huc09] by means of analytical treatment as well as Monte Carlo (MC) simulations. The critical temperatures T_c of the considered models depend on the velocity v and has been calculated exactly for various geometries in the limit $v \rightarrow \infty$. In this limit the class of models show mean-field-like critical behavior. We find many similarities to the *driven lattice gas* (DLG) proposed by Katz *et al.* [KLS83] (see [SZ95] for a review), where a Ising system is driven out of equilibrium by an applied field which favors the motion of particles in one direction. We will discuss these similarities throughout this work.

Subsequent investigations have been done in a variety of contexts, in particular for driven Potts models [IPT11] and for rotating Ising chains of finite length [Hil11] which can be mapped to a two-lane traffic model [ARHS10]. In the following we first turn to the definition of the model and a description of the dissipation mechanism.

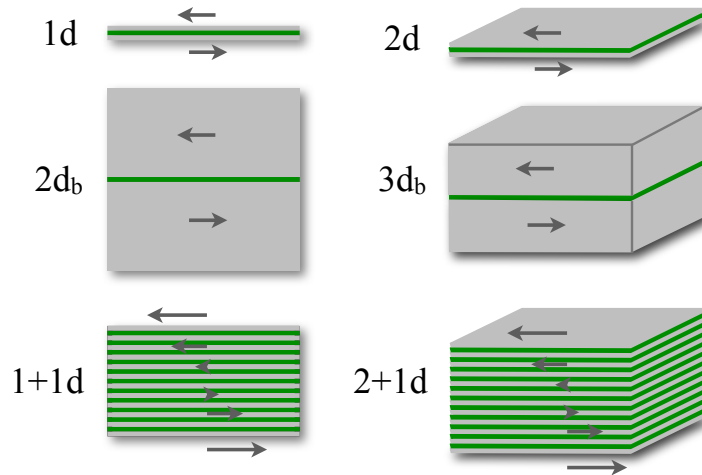


Figure 3.1: Overview of the geometries considered in this work. The grey regions are the magnetic systems, while the green regions are the moving boundaries. The arrows indicate the motion of the subsystems. (adapted from [Huc09])

3.1 Model

In general the considered systems are build from Ising spin variables $\sigma_i = \pm 1$ at lattice sites i on a d -dimensional cubic lattice. The lattice is divided into subsystems which are moved stepwise against each other, with velocity v , in a direction denoted parallel in the following. As the time is measured in units of Monte Carlo sweeps (MCS) and distances are given in units of the lattice constant, v is given in lattice constants per MCS such that $v = 1$ corresponds to approximately 1 cm/s [KHW08].

To simplify the implementation of the motion, instead of moving the parts of the lattice with respect to each other we reorder the couplings at the boundaries with time. This procedure is analogous to the Lees–Edwards or *moving boundary condition* in molecular dynamics simulations of fluids [AT87] and leads to a system as shown exemplary for geometry 2d_b in Fig. 3.2. The general time-dependent Hamiltonian can be written as

$$\beta\mathcal{H}(t) = -K \sum_{\langle ij \rangle_s} \sigma_i \sigma_j - K_b \sum_{\langle ij \rangle_b(t)} \sigma_i \sigma_j, \quad (3.1)$$

with reduced coupling $K = \beta J$ for the static nearest neighbor bonds $\langle ij \rangle_s$ (black lines) and reduced boundary coupling $K_b = \beta J_b$ for the time-dependent boundary bonds $\langle ij \rangle_b(t)$ with parallel offset $\Delta(t) = vt$ (green lines), moving at the boundaries with velocity v . We use the inverse temperature $\beta = 1/k_B T$ and set $k_B = 1$.

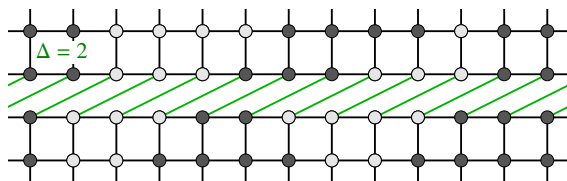


Figure 3.2: Typical configuration of geometry 2d_b for $\Delta = 2$. Black/white circles are up/down spins, green lines are boundary bonds.

3.2 Power dissipation and friction

The energy dissipation and friction force associated with Hamiltonian (3.1) were investigated in [KHW08] for geometry 2d_b shown in Fig. 3.2. If the two subsystems are moved against each other, energy is pumped into the system at the boundary with length L_{\parallel} : in each shift step this energy is given by $\Delta E_b = E_b^{(f)} - E_b^{(i)}$, where $E_b^{(i)}$ and $E_b^{(f)}$ denotes the boundary energy before and after a move. This energy goes into the spin system and eventually dissipates into the heat bath coupled homogeneously to all spins. The dissipation power under the motion is thus given by

$$P(T, v) = \frac{\langle \Delta E_b \rangle}{\Delta t}, \quad (3.2)$$

where the brackets denote the time average taken within the nonequilibrium steady state, and Δt denotes the time between two shift steps. From the dissipation power we can determine the friction force as

$$F(T, v) = \frac{P(T, v)}{v} = \frac{\langle \Delta E_b \rangle}{\Delta s}, \quad (3.3)$$

where the displacement under one step Δs is always one lattice constant.

For low velocities $v \rightarrow 0$ the friction force F can be calculated exactly [KHW08]: in this regime the system relaxes to equilibrium after each shift step. Thus the energies E_b before and after a shift can be calculated from the equilibrium correlation functions $\langle \sigma_i \sigma_j \rangle_0$ across the shift boundary, leading to

$$\begin{aligned} F(T, v \rightarrow 0) &= \frac{\langle \Delta E_b \rangle_0}{\Delta s} = -L_{\parallel} J_b \left(\langle \begin{array}{ccc} \circ & \circ & \circ \\ \circ & \circ & \circ \end{array} \rangle_0 - \langle \begin{array}{ccc} \circ & \circ & \circ \\ \circ & \circ & \circ \end{array} \rangle_0 \right) \\ &= -L_{\parallel} J_b (\langle \sigma_{0,0} \sigma_{1,1} \rangle_0 - \langle \sigma_{0,0} \sigma_{1,0} \rangle_0). \end{aligned} \quad (3.4)$$

The correlation functions are given by [MW73, Eqs. (VIII.4.5) and (VIII.4.9)]

$$\langle \sigma_{0,0} \sigma_{1,0} \rangle_0 = \frac{1}{2} \sqrt{1 + k_{<}} + \frac{1}{\pi} \sqrt{1 + k_{>}} (1 - k_{<}) \sqrt{k} \mathbf{K}(k), \quad (3.5a)$$

$$\langle \sigma_{0,0} \sigma_{1,1} \rangle_0 = \frac{2}{\pi \sqrt{k k_{>}}} [\mathbf{E}(k) + (k k_{>} - 1) \mathbf{K}(k)], \quad (3.5b)$$

where $k = k_{>}$ above and $k = k_{<}$ below T_c , with $k_{>} = \sinh^2 2K = k_{<}^{-1}$, and \mathbf{K} and \mathbf{E} are the complete elliptic integrals¹.

The resulting friction force $F(T, v)$ over T is depicted in Fig. 3.3a for $J = J_b = 1$ and $v = 1$ (blue and red lines). The force is exponentially small at low temperatures and grows strongly near the critical temperature T_c . After a maximum above T_c the friction force vanishes $\propto 1/T$. The exact solution for small v , Eq. (3.4), is shown as black line, together with Monte Carlo results for $v = 1/10$. Note that the friction force becomes independent of v for $v \rightarrow 0$ similar to Coulomb friction in solid friction. The explanation for this behavior is given in the next section.

In Fig. 3.3b we show the dissipation power P over velocity v for $J = J_b = 1$ and $T = 2.5$

¹We use the usual definition of elliptic integrals, e.g., $\mathbf{K}(k) = \int_0^{\pi/2} (1 - k^2 \sin^2 \theta)^{-1/2} d\theta$.

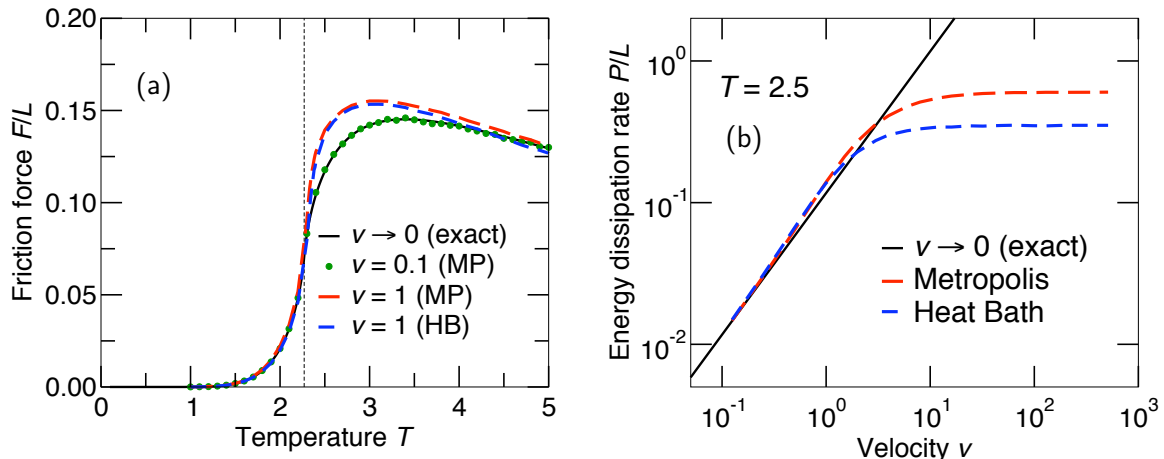


Figure 3.3: (a): Friction force per boundary length over temperature T for different velocities v . (b): Reduced dissipation power P/L_{\parallel} over velocity v for two different MC rates. The black line is the exact solution for small v , Eq. (3.4). (adapted from [KHW08])

slightly above T_c . For small v the red and blue curves follow the exact solution (black line) and saturate for high v . The saturation limits depend on the used Monte Carlo rate, see Section 3.5 for details. This saturation to a constant led to the idea that these driven systems can be solved exactly in the limit $v \rightarrow \infty$, as shown in Section 3.4.

Finally, we estimate the force and dissipation power in realistic systems. For the experimentally relevant geometry $3d_b$ shown in Fig. 3.1 we find a shear stress of

$$\sigma(T_c, v) = \frac{F(T_c, v)}{L_{\parallel} L_{\perp}} \approx 10 \text{ MPa} \quad (3.6)$$

for small v and a power dissipation per area of

$$p(T_c, v \gg 1) \approx 100 \text{ Wcm}^{-2} \quad (3.7)$$

near T_c for a typical ferromagnet. These values are surprisingly high, indicating that an experimental determination of these fluctuation-induced friction forces might be feasible.

3.3 Cross-over from Coulomb to Stokes friction

In the last section we saw that fluctuation-induced friction is of Coulomb type for the considered driven Ising model, as $F(T, v \rightarrow 0)$ is finite [KHW08]. However, driven Heisenberg models with Landau-Lifshitz-Gilbert (LLG) dynamics, where a magnetic dipolar tip is moved continuously over a magnetic surface, showed friction of Stokes type, linear in v for small v [FWN08, MBWN09]. The situation became even more complicated after Démercy and Dean published a work where they claimed to have observed Stokes friction in an Ising model with discrete dynamics [DD10].

The central question is: which property is crucial for the friction behavior at small velocities

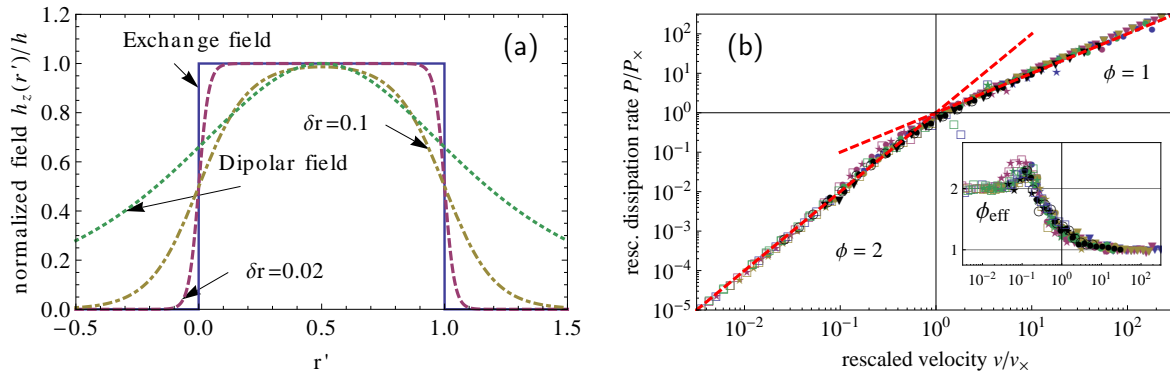


Figure 3.4: Tip field characteristics (a) for different cases, as explained in the text. Cross-over scaling function (b) of the dissipation rate P from Stokes ($P \propto v^2$) to Coulomb ($P \propto v$) friction with increasing velocity v . (adapted from [MAHW11])

and thus responsible for the different findings? Is it (a) the different spin dynamics (MC vs. LLG), (b) the different driving dynamics (discrete vs. continuous motion), (c) the different boundary interaction range (exchange vs. dipolar), or (d) the different spin models (Ising vs. Heisenberg)?

These questions were answered in [MAHW11]: considering the simplest case of a one-dimensional spin system we defined a tip magnetic field $h_z(r')$ with tunable dependency on the relative distance r' , see Fig. 3.4a. Varying the rise width δr , we could change the field characteristics from step-like ($\delta r = 0$) to slowly varying as in the dipolar case ($\delta r = 0.1$). Note that the case $\delta r = 0$ is equivalent to a step-like motion of the tip.

As the tip is moved continuously with velocity v , the tip field acting on one spin changes in a time interval $\tau_{\text{switch}} = \delta r/v$. It turned out that the crucial factor is the ratio of τ_{switch} to the spin relaxation time τ_{rel} of the considered spin dynamics. If $\tau_{\text{switch}} > \tau_{\text{rel}}$, we found Stokes-like friction, while in the opposite case Coulomb-like friction is observed. Performing extensive simulations both in the Heisenberg model with LLG dynamics and in the Ising model with the Monte Carlo method, we found in both systems a similar cross-over from Stokes- to Coulomb-like friction with increasing driving velocity v . Dividing v by a suitably defined cross-over velocity v_\times , a convincing data collapse could be achieved for both models with different model parameters [MAHW11]. The resulting cross-over scaling plot is shown in Fig. 3.4b, together with the effective exponent of the dissipation rate ϕ_{eff} changing non-monotonically from $\phi = 2$ (Stokes) to $\phi = 1$ (Coulomb).

3.4 Exact solution at high driving velocities

The exact solution of Eq. (3.1) in the limit $v \rightarrow \infty$ is sketched in the following, for details see Ref. [Huc09]. Consider the second term in Eq. (3.1) at high velocities v . In every time step t the bond rearrangement (green lines in Fig. 3.5) couples uncorrelated spins σ_j to spin σ_i , which thus can be replaced by a fluctuating degrees of freedom μ_i (blue circles in Fig. 3.5) with average² $\langle \mu_i \rangle = m_b$. The degrees of freedom μ_i can be trace out exactly, leading to a

²The boundary magnetization m_b is assumed to be equal for all boundaries without loss of generality.

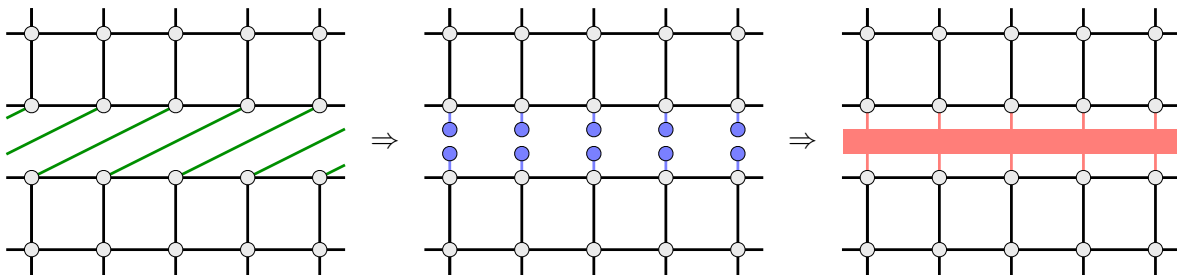


Figure 3.5: Exact solution for $v \rightarrow \infty$ in two steps: the driven system for $\Delta = 2$ with boundary couplings (green) is first mapped onto disconnected systems with fluctuating surface fields (blue). These fields are then traced out to give an equilibrium system with static boundary fields (red).

homogeneous and static boundary field h_b (shown red in Fig. 3.5) fulfilling

$$\tanh h_b = m_b \tanh K_b \quad (3.8)$$

for the case of $f = 1$ boundary bond³ per boundary spin σ_i . We end with the self-consistency condition

$$m_{b,\text{eq}}[K, h_b(m_b)] = m_b \quad (3.9)$$

for the nonequilibrium order parameter m_b . Here $m_{b,\text{eq}}(K, h_b)$ denotes the boundary magnetization of the corresponding equilibrium system with couplings K and boundary fields h_b , a quantity known exactly for many of the considered geometries.

The critical temperature T_c of the driven system can be calculated from the reduced zero-field boundary susceptibility of the equilibrium model,

$$\chi_{b,\text{eq}}^{(0)}(K) = \left. \frac{\partial m_{b,\text{eq}}(K, h_b)}{\partial h_b} \right|_{h_b=0}, \quad (3.10)$$

via the identity

$$\chi_{b,\text{eq}}^{(0)}(K_c) f \tanh K_{b,c} = 1. \quad (3.11)$$

In the following we will apply these results to the different geometries shown in Fig. 3.1. However, we first have to deal with a subtle problem connected to the Monte Carlo algorithm.

3.5 An integrable algorithm

While equilibrium properties are most efficiently investigated in Monte Carlo simulations using cluster algorithms, nonequilibrium systems have to be treated with random sequential single spin flip dynamics like the non-conserved Glauber dynamics [Gla63] or the conserved Kawasaki dynamics [Kaw66]. The driven system is permanently under an external perturbation which

³For systems with $f > 1$ see Section 3.9 and [Huc09].

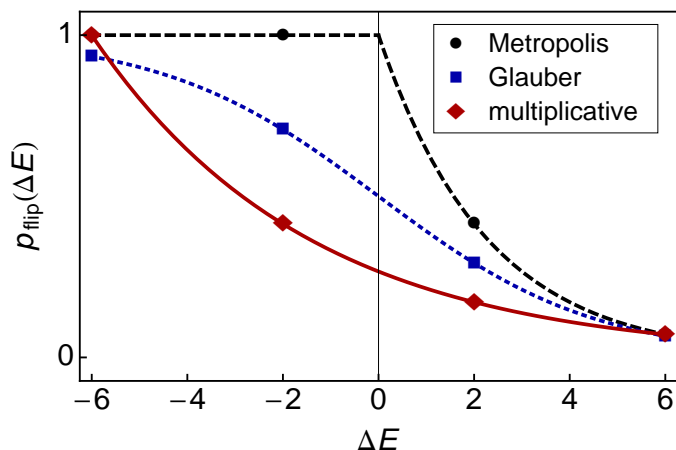


Figure 3.6: Spin flip probabilities of the Metropolis and Glauber rates, Eqs. (3.13), together with the multiplicative rate, Eq. (3.14), for the 1d system at criticality ($J = J_b = 1$). (adapted from [Huc09])

drives it out of equilibrium, while the internal degrees of freedom are coupled to a heat bath in thermal equilibrium. From this coupling the probability $p_{\text{flip}}(\Delta E)$ of a single spin flip with energy change ΔE fulfills the detailed balance condition

$$\frac{p_{\text{flip}}(\Delta E)}{p_{\text{flip}}(-\Delta E)} = e^{-\beta \Delta E} \quad (3.12)$$

just like in the equilibrium case. The most common rates fulfilling Eq. (3.12) are the Metropolis rate [MRR⁺53] and the Glauber rate [Gla63],

$$p_{\text{flip}}^{\text{M}}(\Delta E) = \min(1, e^{-\beta \Delta E}), \quad (3.13a)$$

$$p_{\text{flip}}^{\text{G}}(\Delta E) = \frac{1}{1 + e^{\beta \Delta E}}. \quad (3.13b)$$

Using these rates in simulations of, e. g., the 1d driven system, Eq. (3.15), it turns out that for all $v > 0$ the critical temperature $T_c(v)$ depends on the used rate (see also Fig. 3.12): We find, for $v \rightarrow \infty$ and $J_b = J = 1$, the values $T_c^{\text{M}} = 1.910(2)$ and $T_c^{\text{G}} = 2.031(2)$ for the Metropolis and Glauber rate, respectively, while the exact solution Eq. (3.18) of the model presented in Section 3.4 gives $T_c = 2.269\dots$. Note that a similar dependency was recently found in the DLG by Kwak *et al.* [KLS04].

In Ref. [Huc09] these deviations were attributed to correlations induced by the commonly used rates Eq. (3.13), and a *multiplicative rate*

$$p_{\text{flip}}^*(\Delta E) = e^{-\frac{\beta}{2}(\Delta E - \Delta E_{\text{min}})} \quad (3.14)$$

fulfilling $p_{\text{flip}}^*(\Delta E_1 + \Delta E_2) = p_{\text{flip}}^*(\Delta E_1)p_{\text{flip}}^*(\Delta E_2)$ was proposed that completely eliminated them⁴. The constant ΔE_{min} is the minimum possible value of ΔE at given geometry; this assures that $p_{\text{flip}}^*(\Delta E)$ is maximal but never larger than one. This rate reproduces the calculated critical temperatures in all considered geometries, e.g. $T_c^* = 2.269(1)$ for the 1d case at $v \rightarrow \infty$.

The resulting spin flip rates for the 1d case at criticality are shown in Fig. 3.6. Clearly, the

⁴Eq. (3.14) is mentioned in the literature [vBS84, NB99] without stressing the multiplicative property.

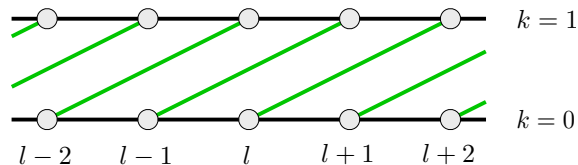


Figure 3.7: Sketch of geometry 1d after $\Delta = 2$ moves. Spin $\sigma_{0,l}$ interacts with spin $\sigma_{1,l+2}$ with coupling J_b (green lines), while all other couplings are J (black lines). (adapted from [Huc09])

multiplicative algorithm Eq. (3.14) has a smaller overall acceptance rate than Eqs. (3.13) and is thus slightly less efficient: a finite-size scaling analysis of the acceptance rate $A = \langle p_{\text{flip}} \rangle$ at criticality in the 1d case yields $A_c^M = 0.476(2)$, $A_c^G = 0.366(2)$ and $A_c^* = 0.242(2)$ for the three algorithms, rendering this method roughly two times slower than the Metropolis algorithm for these parameters. In fact, $A_c = 3\sqrt{2} - 4 = 0.24264\dots$ can be calculated exactly from Eq. (3.22). However, we assume that this deficit can be eliminated by combining rate Eq. (3.14) with kinetic Monte Carlo methods [YE66].

3.6 1d case

For periodic boundary conditions $\sigma_{k,l} \equiv \sigma_{k,l \bmod L_{\parallel}}$ in parallel direction the time-dependent Hamiltonian of geometry 1d shown in Fig. 3.7 reads

$$\beta\mathcal{H}(t) = -K \sum_{k=0}^1 \sum_{l=1}^{L_{\parallel}} \sigma_{k,l} \sigma_{k,l+1} - K_b \sum_{l=1}^{L_{\parallel}} \sigma_{0,l} \sigma_{1,l+\Delta(t)} \quad (3.15)$$

with time-dependent displacement $\Delta(t) = vt$. We first discuss the limit $v \rightarrow \infty$.

3.6.1 1d with infinite v

Applying the self-consistency condition Eq. (3.9) to the well known expression for the equilibrium magnetization of the one-dimensional Ising model [cf. Bax82],

$$m_{\text{eq}}(K, h) = \frac{\sinh h}{\sqrt{e^{-4K} + \sinh^2 h}}, \quad (3.16)$$

we obtain the zero-field magnetization of the 1d driven system in the ordered phase for velocity $v \rightarrow \infty$,

$$m(K, K_b) = \sqrt{\frac{\cosh 2K_b - \coth 2K}{\cosh 2K_b - 1}}, \quad (3.17)$$

with critical temperature fulfilling

$$e^{2K_c} \tanh K_{b,c} = 1, \quad (3.18)$$

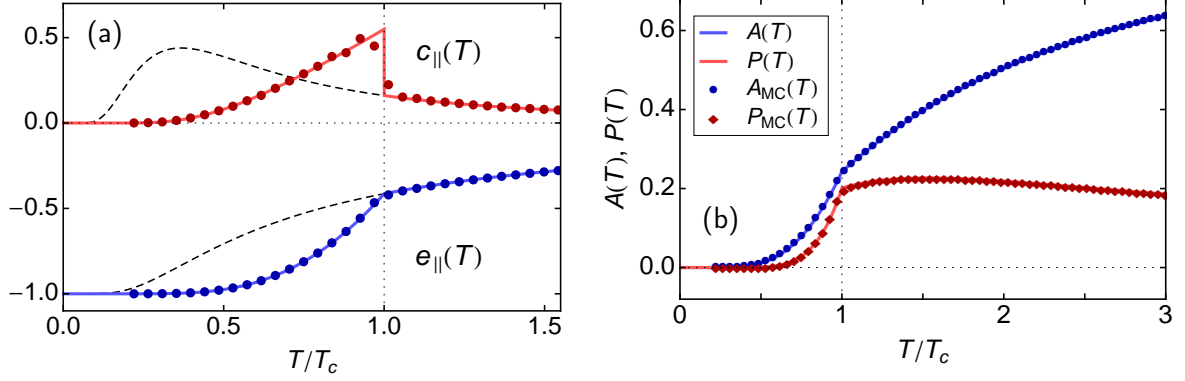


Figure 3.8: (a): Internal energy $e_{\parallel}(T)$, Eq. (3.20), and specific heat $c_{\parallel}(T)$, Eq. (3.21), of the 1d driven system at $v \rightarrow \infty$. The points are MC results for $L_{\parallel} = 2^{11}$, and the dashed lines are results for the one-dimensional Ising model in equilibrium. (b): Spin flip acceptance rate $A(T)$, Eq. (3.22), and energy dissipation rate $P(T)$, Eq. (3.23), versus T/T_c for the 1d system at $v \rightarrow \infty$, together with MC data for $L_{\parallel} = 2^{11}$. (adapted from [Huc09])

as $\chi_{\text{eq}}^{(0)}(K) = e^{2K}$ in this case. As noted in [Huc09], Eq. (3.17) is equal to the spontaneous surface magnetization of the two-dimensional equilibrium Ising model [MW73, Chapter VI, Eq. 5.20], if we identify K and K_b with the couplings \parallel and \perp to the surface, and consequently has the identical critical temperature T_c . For the special case $K = K_b$ this gives the well known Ising value [KW41, Ons44]

$$T_c^{1d} = \frac{2}{\log(1 + \sqrt{2})} = 2.2691853 \dots \quad (3.19)$$

However, we regard this equality as coincidence without deeper meaning, as Eq. (3.17) is the solution of a simple quadratic equation with small integer coefficients when written in the natural variables.

Several other quantities were derived exactly in [Huc09] using a transfer matrix formulation, including static properties like the internal energy $e_{\parallel} = -J\langle\sigma_{k,l}\sigma_{k,l+1}\rangle$ and the specific heat $c_{\parallel} = \partial e_{\parallel}/\partial T$ in parallel direction,

$$e_{\parallel,<} = \frac{J e^{-2K-K_b}}{\sinh 2K \sinh K_b} - 1, \quad e_{\parallel,>} = -J \tanh K, \quad (3.20)$$

$$c_{\parallel,<} = \frac{2K^2}{\sinh^2 K} (\coth K_b - 1), \quad c_{\parallel,>} = \frac{K^2}{\cosh^2 K}, \quad (3.21)$$

as well as dynamical properties like the spin flip acceptance rate A and the energy dissipation rate P per spin,

$$A_{<} = \frac{\cosh(K + K_b) - \sinh(K - K_b)}{4e^{2(K+K_b)} \sinh K \cosh^2 K \sinh K_b}, \quad A_{>} = e^{-K_b} \cosh K_b (1 - \tanh K)^2, \quad (3.22)$$

$$\frac{P_{<}}{A_{<}} = \frac{2J_b e^{-4K}}{\tanh K_b}, \quad \frac{P_{>}}{A_{>}} = 2J_b \tanh K_b, \quad (3.23)$$

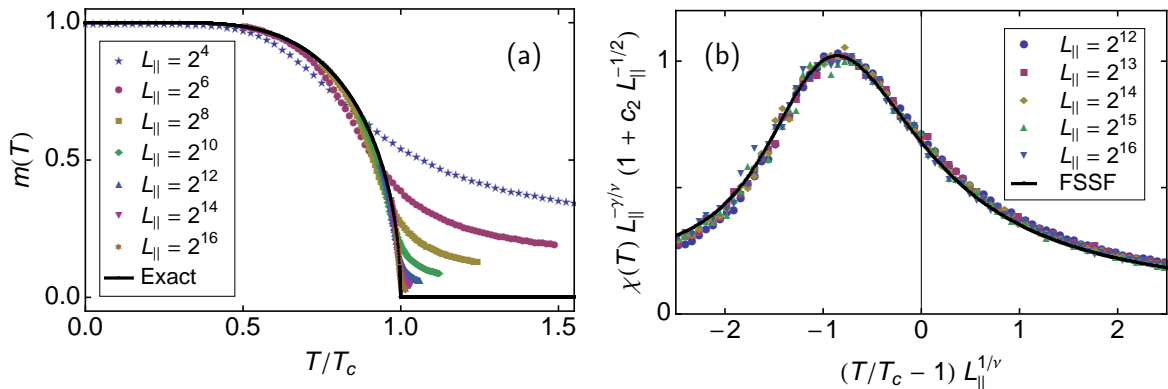


Figure 3.9: (a): Magnetization $m_{\text{abs}}(T)$ of the 1d system at $v = \infty$ for several system sizes $L_{||}$ from Monte Carlo simulations, together with the exact solution Eq. (3.17). (b): Finite-size scaling plot of the reduced susceptibility $\chi_{\text{abs}}(T)$ of the 1d system for $v = \infty$ and system sizes $L_{||} = 2^{12}, \dots, 2^{16}$, together with the exact MF finite-size scaling function (black line) from Ref. [GH04]. The correction factor is set to $c_2 = 2.7(1)$. (adapted from [Huc09])

where $<$ and $>$ denotes solutions below and above T_c , respectively. These results are shown in Fig. 3.8, together with data from MC simulations. Note that the dynamical results are only valid for the multiplicative rate p_{flip}^* from Eq. (3.14). Finally we list the critical exponents for the 1d driven system at $v \rightarrow \infty$ to be

$$\beta = \frac{1}{2}, \quad \gamma = 1, \quad \alpha = 0, \quad (3.24)$$

verifying the mean-field (MF) behavior of this limit.

3.6.2 Finite-size effects in 1d

The exact solution sketched in Section 3.4 was derived in the thermodynamic limit $L_{||} \rightarrow \infty$, as we assumed a constant and non-fluctuating order parameter m_b in the self-consistency condition Eq. (3.9). However, in a finite system the assumption $m_b = \text{const}$ is not fulfilled and finite-size effects occur, leading to a non-trivial dependency of the physical quantities on system size. These finite-size corrections have recently been investigated for the 1d case by Hilhorst [Hil11].

The fluctuating order parameter gives rise to additional correlations between spins at large distances not included in the exact solution. As the driven system shows mean-field behavior, we can use the standard finite-size scaling theory for mean-field systems: near criticality the correlation length parallel to the boundary fulfills $\xi_{||}(\tau) \propto |\tau|^{-\nu_{||}}$ with critical exponent $\nu_{||} = 2/d_b$, where d_b denotes the boundary dimension. We have $d_b = 1$ in both the 1d and the $2d_b$ case, leading to $\nu_{||} = 2$ in these cases.

To illustrate these finite-size effects in the 1d case, in Fig. 3.9a we show Monte Carlo results for the magnetization $m_{\text{abs}}(T)$, Eq. (63a) in [Huc09], for $v = \infty$ and several system sizes $L_{||}$. The exact solution, Eq. (3.17), is only approached in the limit $L_{||} \rightarrow \infty$.

The finite-size scaling behavior is demonstrated exemplarily for the susceptibility $\chi_{\text{abs}}(T)$,

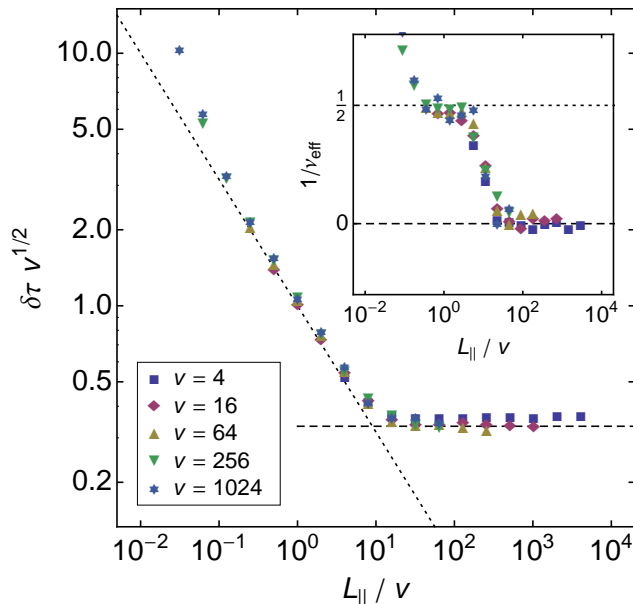


Figure 3.10: Velocity-dependent cross-over behavior in the 1d case. Shown is the rescaled width of the critical region $\delta\tau v^{1/2}$ as a function of the cross-over scaling variable L_{\parallel}/v for several velocities v and several system sizes $L_{\parallel} = 2^4, \dots, 2^{16}$ (see text). The inset shows the corresponding cross-over of the effective correlation length exponent ν_{eff}^{-1} from $\nu_{\text{eff}}^{-1} = 1/2$ (MF, dotted line) to $\nu_{\text{eff}}^{-1} = 0$ (Ising non-critical, dashed line). (adapted from [Huc09])

Eq. (63b) in [Huc09], which is shown in a finite-size scaling plot in Fig. 3.9b: after rescaling the MC data in the usual way we indeed find the expected mean-field exponents $\gamma = 1$ and $\nu_{\parallel} = 2$, furthermore the data collapse onto the universal finite-size scaling function calculated in Ref. [GH04]. The same analysis was performed for the magnetization $m_{\text{abs}}(T)$ and specific heat $c(T)$, Eq. (63e) in [Huc09], verifying the exponents $\beta = 1/2$ and $\alpha = 0$.

3.6.3 1d with finite v

We now turn to finite velocities v , where the 1d system always shows a cross-over from MF to non-critical Ising behavior with increasing system size L_{\parallel} [Huc09]. Only in the limit $v \rightarrow \infty$ the system undergoes a phase transition at finite temperatures. To investigate this velocity-dependent cross-over, we measured the width $\delta\tau$ of the critical region by analyzing the Binder cumulant, see Ref. [Huc09] for details. For several velocities v and system sizes L_{\parallel} we determined $\delta\tau$ and plotted the results in a cross-over scaling plot shown in Fig. 3.10. We found that the cross-over scaling variable is L_{\parallel}/v in this case. At finite v the width $\delta\tau$ stops shrinking at the cross-over system size $L_{\parallel}^{\times}(v) \approx 9v$, and only goes to zero for $v \rightarrow \infty$, indicating a sharp phase transition only in this limit. The inset shows the effective exponent ν_{eff} obtained from the logarithmic derivative

$$\nu_{\text{eff}}^{-1} = -\frac{\partial \log \delta\tau}{\partial \log L_{\parallel}}, \quad (3.25)$$

whose value changes from $\nu_{\text{eff}}^{-1} = 1/2$ (MF) to $\nu_{\text{eff}}^{-1} = 0$ (Ising) with growing system size. In the next section we will see that this behavior changes substantially in the $2d_b$ case.

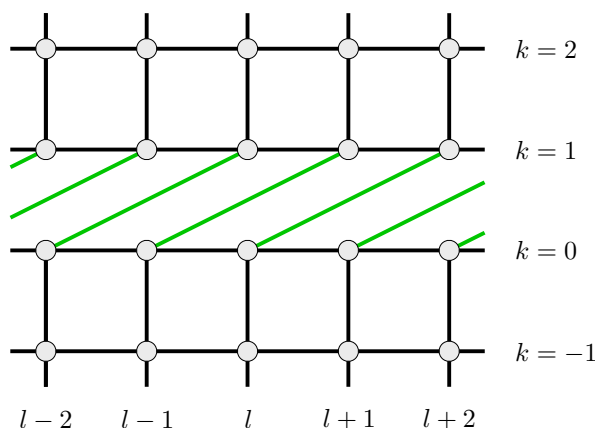


Figure 3.11: Sketch of geometry $2d_b$ after $\Delta = 2$ moves. Spin $\sigma_{0,l}$ interacts with spin $\sigma_{1,l+2}$ with coupling J_b (green lines), while all other couplings are J (black lines). (adapted from [Huc09])

3.7 $2d_b$ case

Now we consider the $2d_b$ case shown in Fig. 3.11, introduced by Kadau *et al.* [KHW08]. It consists of a square lattice with $L_{\parallel} \times L_{\perp}$ sites and periodic boundary conditions in both directions. The Hamiltonian of this system becomes

$$\beta\mathcal{H}(t) = - \sum_{k=1}^{L_{\perp}} \sum_{l=1}^{L_{\parallel}} (K\sigma_{k,l}\sigma_{k,l+1} + K_{\perp,k}\sigma_{k,l}\sigma_{k+1,l+\Delta_k(t)}), \quad (3.26)$$

with $\Delta_k(t) \equiv 0$ and $K_{\perp,k} = K$ for all rows except row $k = 1$, where the couplings to row $k = 1$ are shifted with constant velocity $\Delta_0(t) \equiv \Delta(t) = vt$. The coupling $K_{\perp,0} \equiv K_b$ across the boundary is allowed to be different from K . For $v = 0$ and $J_b = J = 1$ this system simplifies to the $2d$ Ising model in equilibrium, which was solved exactly by Onsager [Ons44] and shows a continuous phase transition at [KW41]

$$T_{c,\text{eq}} = \frac{2}{\log(1 + \sqrt{2})} = 2.2691853\dots \quad (3.27)$$

3.7.1 $2d_b$ with infinite v

The $2d_b$ case can be solved exactly at $v \rightarrow \infty$ using the expression for the equilibrium surface magnetization $m_{b,\text{eq}}$ of the two-dimensional Ising model in a static surface field h_b obtained by McCoy and Wu [MW73, Eq. (VI.5.1)]. The integral representation given in their work was further evaluated and written in closed form in Ref. [Huc09, Eq. (A2)]. The critical temperature T_c of the driven system can be evaluated from Eq. (3.11) using the reduced zero-field boundary susceptibility

$$\chi_{b,\text{eq}}^{(0)}(z) = \left(\frac{1}{z^2} - 1 \right) \left[(1 + 2w - 8w^2) \frac{\mathbf{K}(4w)}{4\pi w} - \frac{\mathbf{E}(4w)}{4\pi w} - \frac{1}{4} \right] \quad (3.28)$$

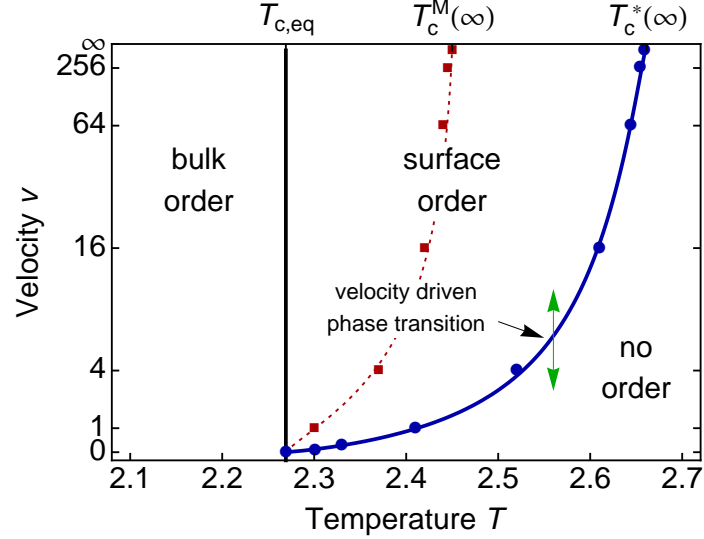


Figure 3.12: Phase diagram of the $2d_b$ case. Below $T_{c,\text{eq}}$ the two-dimensional bulk is ordered, while surface order is observed even above $T_{c,\text{eq}}$ up to the velocity-dependent phase boundary $T_c(v)$. The position of this boundary depends on the algorithm, the blue line holds for the multiplicative rate, Eq. (3.14), while the thin red dotted line holds for the Metropolis rate, Eq. (3.13a). At fixed temperatures between $T_{c,\text{eq}}$ and $T_c(v)$ a velocity driven phase transition is possible. The points are results from MC simulations. (adapted from [Huc09])

also derived in [Huc09], with $z = \tanh K$, $w = z(1 - z^2)/(1 + z^2)^2$, and the complete elliptic integrals⁵ of first and second kind \mathbf{K} and \mathbf{E} , to give

$$T_c^{2d_b} = 2.6614725655752\dots \quad (3.29)$$

for the case $J_b = J = 1$. As this critical temperature is larger than the equilibrium critical temperature, Eq. (3.27), the driven boundary induces a surface phase transition where only the driven surface has long-range order above $T_{c,\text{eq}}$. The velocity dependence of this transition and the resulting phase diagram is discussed in more detail in the next section.

3.7.2 $2d_b$ with finite v

In the $2d_b$ case the moving boundary is coupled to a bulk two-dimensional Ising model, which undergoes a phase transition at $T_{c,\text{eq}}$, Eq. (3.27), independent of the velocity v . In addition, the moving boundary shows a boundary phase transition at temperature $T_c(v)$, which grows with increasing v and eventually approaches the value given in Eq. (3.29) for $v \rightarrow \infty$. As $T_c(v) > T_{c,\text{eq}}$ for all $v > 0$ we expect a boundary phase transition with paramagnetic bulk. Then the correlation length ξ_{\perp} perpendicular to the boundary is finite at criticality, $T_c(v)$, and adopts the Ising value $\xi_{\perp,c}(v) = \xi_{\text{eq}}[T_c(v)]$, with [MW73]

$$\xi_{\text{eq}}^{-1}(T > T_{c,\text{eq}}) = \log \coth K - 2K. \quad (3.30)$$

⁵We use the usual definition of elliptic integrals, e.g., $\mathbf{K}(k) = \int_0^{\pi/2} (1 - k^2 \sin^2 \theta)^{-1/2} d\theta$.

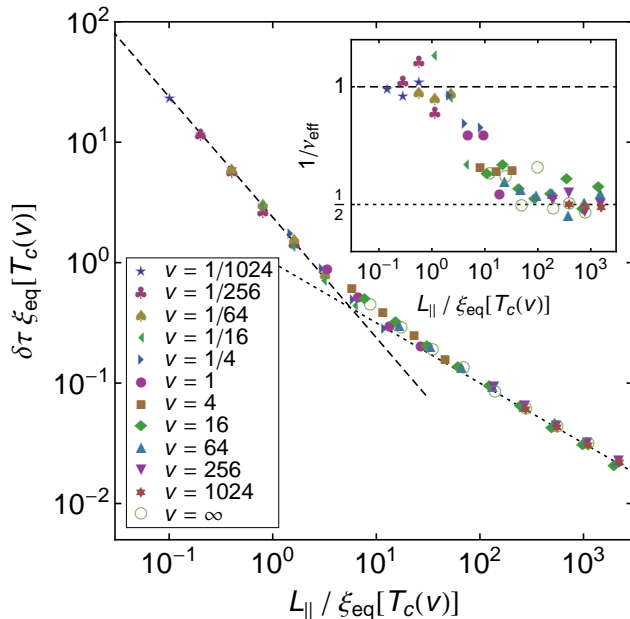


Figure 3.13: Velocity-dependent cross-over behavior in the $2d_b$ case. Shown is the rescaled width of the critical region $\delta\tau \xi_{\text{eq}}[T_c(v)]$ as a function of the cross-over scaling variable $L_{\parallel}/\xi_{\text{eq}}[T_c(v)]$ for several velocities v and different system sizes $L_{\parallel} = 2^4, \dots, 2^{10}$ (see text). The inset shows the corresponding cross-over of the effective correlation length exponent ν_{eff} from $\nu_{\text{eff}} = 1$ (Ising, dashed line) to $\nu_{\text{eff}} = 2$ (MF, dotted line). (adapted from [Huc09])

We performed MC simulations and determined the critical temperatures for different velocities v by performing a finite-size scaling analysis of the boundary susceptibility $\chi_{\text{abs,b}}(T)$ and the boundary cumulant $U_b(T)$ as described in Section 3.6.2. The results are compiled into the phase diagram shown in Fig. 3.12. An important aspect of this phase diagram is the possibility of a velocity driven nonequilibrium phase transition at fixed temperature (double arrow): while the system is paramagnetic at $v = 0$ and up to $v_c(T)$ (thick blue line), the boundary shows long-range order above that velocity. It would be interesting to see this transition in experiments, which could be performed in the corresponding geometry $3d_b$ (see Fig. 3.1), e.g., using two close rotating magnets slightly above the Curie temperature. The magnets should be isolators to avoid eddy currents [KHW08].

In the $2d_b$ case the cross-over scaling variable can be determined from the $T_c(v)$ dependency discussed above. The correlation length ξ_{eq} at the critical point of the driven system, $T_c(v)$, plays a key role: The system is Ising-like as long as correlations span the whole system in both directions \parallel and \perp , i.e., as long as the system size L_{\parallel} is of the order of the bulk correlation length ξ_{eq} at the critical point $T_c(v)$ of the driven system. This leads to the cross-over scaling variable $L_{\parallel}/\xi_{\text{eq}}[T_c(v)]$, and the resulting cross-over scaling plot is shown in Fig. 3.13. For all finite $v > 0$ the critical behavior changes from Ising to mean-field at the cross-over system size $L_{\parallel}^{\times} \approx 6\xi_{\text{eq}}[T_c(v)]$: below this value $\delta\tau$ shrinks according to $\delta\tau \propto L_{\parallel}^{-1}$ with $\nu_{\text{eff}} = 1$ (Ising, dashed line), while above this value $\delta\tau \propto L_{\parallel}^{-1/2}$ with $\nu_{\text{eff}} = 2$ holds (MF, dotted line).

In summary, the 1d and the $2d_b$ systems with boundary dimension $d_b = 1$ have the standard mean-field exponents $\alpha = 0$, $\beta = 1/2$, and $\gamma = 1$, as well as the correlation length exponent $\nu_{\parallel} = 2$, and fulfill the scaling relations

$$2 - \alpha = 2\beta + \gamma = d_b\nu_{\parallel}. \quad (3.31)$$



Figure 3.14: Geometries 1+1d and 2d considered in this section. The grey regions are the magnetic systems, while the green regions are the moving boundaries. The arrows indicate the motion of the subsystems.

3.8 Two-dimensional boundary

The previously studies cases 1d and 2d_b had boundary dimension $d_b = 1$, leading to mean-field behavior with correlation length exponent $\nu_{\parallel} = 2$. In the following, we consider the homogeneous systems 1+1d and 2d with boundary dimension $d_b = d = 2$ as shown in Fig. 3.14. As the motion is still along the parallel direction only, the two directions \parallel and \perp behave differently now. The motion greatly enhances the parallel correlations, leading to parallel stripe domains in the ordered phase [AHW12, Fig. 3]. This domain formation can be understood as a consequence of a strongly anisotropic phase transition in the driven system, for details see Section 3.8.4.

In this section the main results from Ref. [AHW12] are presented. At infinite velocity v the critical temperature is known exactly [Huc09], which greatly simplifies the numerical analysis. Using Monte Carlo simulations as well as a field theoretical *ansatz* we compute the anisotropy exponent θ . In addition, the case of finite velocities v is studied by means of a cross-over scaling, where a broad range of velocities and system sizes are analyzed. We show that for all $v > 0$ the considered models end up in the mean-field universality class with strongly anisotropic correlations, as soon as the system size exceeds a velocity-dependent cross-over length $L_{\times}(v)$.

While cross-over behavior from Ising to mean-field class occurs in various thermodynamic systems such as ionic fluid [Fis94, GAS01] and spin systems with long-range interactions [LBB97], to our knowledge a cross-over scaling with change from isotropic to strongly anisotropic behavior has not been investigated before.

3.8.1 1+1d case

The 1+1d system consists of a sheared two-dimensional Ising model, where all rows are moved relative to each other. The displacement $\Delta(t) = vt$ as well as the coupling K_{\perp} is equal for all adjacent rows, leading to the Hamiltonian

$$\beta\mathcal{H}(t) = -K_{\parallel} \sum_{k=1}^{L_{\perp}} \sum_{l=1}^{L_{\parallel}} \sigma_{k,l} \sigma_{k,l+1} - K_{\perp} \sum_{k=1}^{L_{\perp}} \sum_{l=1}^{L_{\parallel}} \sigma_{k,l} \sigma_{k+1,l+\Delta(t)}. \quad (3.32)$$

Within the scope of the 1+1d model the velocity v corresponds to a shear rate, which is often denoted as $\dot{\gamma}$ in the literature [SG09, WVHB10]. However, we continue to use the term velocity for the driving mechanisms. This system is translationally invariant in both directions, as discontinuities in \perp direction are avoided through the homogeneous displacement $\Delta(t)$

[Huc09]. This setup drastically simplifies the analysis of the critical behavior, in contrast to the open boundary conditions used in [SG09].

At high velocities $v \rightarrow \infty$ the system decouples into parallel chains. Due to $f = 2$ fluctuating fields at each spin σ the condition Eq. (3.8) changes to

$$\tanh h = \frac{2m \sinh 2K_{\perp}}{1 - m^2 + (1 + m^2) \cosh 2K_{\perp}}. \quad (3.33)$$

Inserting this into Eq. (3.16) we get the order parameter of the sheared 1+1d system

$$m(K_{\parallel}, K_{\perp}) = \frac{\sqrt{1 - 2e^{4K_{\parallel}} + 2e^{2K_{\parallel}} \sqrt{e^{4K_{\parallel}} - 1 + \tanh^2 K_{\perp}}}}{\tanh K_{\perp}}, \quad (3.34)$$

with critical temperature

$$T_c^{1+1d} = 1/\log\left(\frac{1}{2}\sqrt{3 + \sqrt{17}}\right) = 3.4659074\dots \quad (3.35)$$

for $J_{\parallel} = J_{\perp} = 1$ from Eq. (3.11).

3.8.2 2d case

The 2d system is a two-dimensional two-layer Ising model with $2 \times L_{\parallel} \times L_{\perp}$ lattice sites, where the two layers are moved relative to each other along the parallel direction. The Hamiltonian reads

$$\beta\mathcal{H}(t) = -K \sum_{j=0}^1 \sum_{k=1}^{L_{\perp}} \sum_{l=1}^{L_{\parallel}} \sigma_{j,k,l} (\sigma_{j,k,l+1} + \sigma_{j,k+1,l}) - K_b \sum_{k=1}^{L_{\perp}} \sum_{l=1}^{L_{\parallel}} \sigma_{0,k,l} \sigma_{1,k+\Delta(t),l}. \quad (3.36)$$

With Eq. (3.11) we can express T_c using the high temperature series expansion for the reduced zero-field susceptibility $\chi_{\text{eq}}^{(0)}(K)$ of the two-dimensional Ising model, which was calculated to higher than 2000th order recently using an efficient polynomial time algorithm [BGH⁺08]. Using this extremely accurate result we find, for $J = J_b = 1$, the critical temperature

$$T_c^{2d} = 4.058782423137980000987775040680\dots \quad (3.37)$$

for geometry 2d. Due to the high accuracy of the series this value can be calculated to approximately 500 digits.

3.8.3 Mapping 2d onto 1+1d

In the following, we argue that both systems 1+1d and 2d show the same underlying critical behavior. In order to emphasize the similarity, Fig. 3.15 illustrates slight variations of both models. First of all we start with the 1+1d model (a) and change every second bond perpendicular to the motion into a stationary bond. Additionally, we perform a transformation that changes the homogeneous shear $\Delta(t)$ into an alternating shift $\pm\Delta(t)$ of the double chains and reverses ($l \rightarrow -l$) every second double chain, leading to the configuration in Fig. 3.15b.

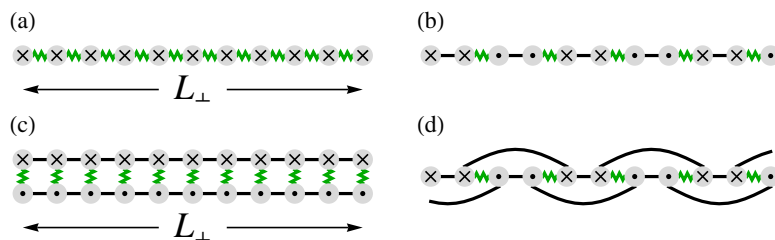


Figure 3.15: Cross sections of the 1+1d (a) and the 2d model (c), and slight modifications of both models, (b) and (d). The grey circles represent spin chains and the connecting lines symbolize the couplings, where green wiggled lines stand for moving and black lines for stationary bonds. Black crosses and dots indicate a motion into and out of the plane, respectively. (adapted from [AHW12])

These modifications do not change the critical behavior of the 1+1d system, since still one-dimensional chains (now consisting of two rows) are moved relative to each other. On the other hand, the cross section of the 2d model can be visualized in a slightly different way (see Fig. 3.15d) without altering the corresponding Hamiltonian, Eq. (3.36). As the next nearest double chains in (b) are not moving relative to each other, the only difference between (b) and (d) are the third nearest neighbor bonds in (d), which are irrelevant at the critical point where long-range correlations dominate. Hence we conclude that both systems belong to the same universality class.

3.8.4 Strongly anisotropic behavior

A strongly anisotropic phase transition is characterized by correlation lengths ξ_μ diverging with direction-dependent critical exponents ν_μ (and amplitudes $\hat{\xi}_\mu$) at the critical point,

$$\xi_\mu(t) \stackrel{t \rightarrow 0}{\sim} \hat{\xi}_\mu t^{-\nu_\mu}. \quad (3.38)$$

Here $\mu = \{\perp, \parallel\}$ denotes the direction and $t = T/T_c - 1$ the reduced critical temperature. Defining the *anisotropy exponent* [Bin90, Hen99]

$$\theta = \frac{\nu_\parallel}{\nu_\perp}, \quad (3.39)$$

isotropic scaling takes place for $\theta = 1$, while strongly anisotropic scaling is implied by $\theta \neq 1$. Several models with strongly anisotropic behavior were studied in the past, some examples are Lifshitz points [HLS75] as present in the anisotropic next nearest neighbor Ising (ANNNI) model [Sel88, PH01, BDS10], the nonequilibrium phase transition in the DLG [SZ95], the two-dimensional dipolar in-plane Ising-model [Huc02], and wetting transitions [AB12]. Furthermore, strongly anisotropic behavior usually occurs in dynamical systems, where the parallel direction can be identified with time and the perpendicular direction(s) with space [Hen99, Hin00]. In the latter case the anisotropy exponent θ corresponds to the dynamical exponent z .

The knowledge of the anisotropy exponent θ is essential and necessary for appropriate simulations of strongly anisotropic systems. To avoid complicated shape effects it is required

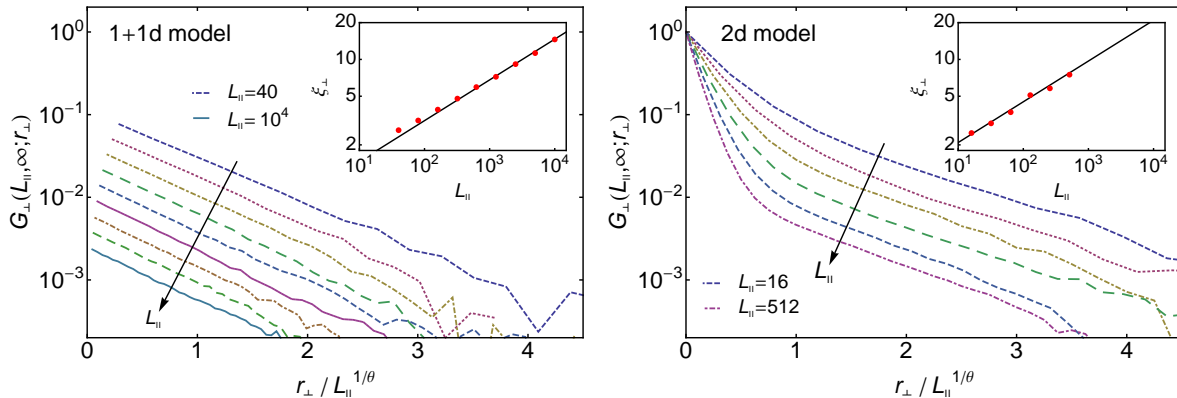


Figure 3.16: Rescaled correlation function $G_{\perp}(L_{\parallel}, \infty; r_{\perp})$, Eq. (3.41), at criticality for $v \rightarrow \infty$ and different system size L_{\parallel} . The insets show $\xi_{\perp}(L_{\parallel})$, Eq. (3.42), together with the field-theoretically predicted slope $\theta^{-1} = 1/3$ (solid lines). (adapted from [AHW12])

to keep the generalized aspect ratio [Bin90, Hen99, Huc02]

$$\rho = \frac{L_{\parallel}/\hat{\xi}_{\parallel}}{(L_{\perp}/\hat{\xi}_{\perp})^{\theta}} \quad (3.40)$$

fixed, which usually requires the *a priori* knowledge of θ , or to perform systematic aspect ratio variations [Huc02]. However, in the limit $\rho \rightarrow 0$ the exponent θ can be determined independently [AHW12]: measuring the perpendicular correlation function $G_{\perp}(L_{\parallel}, \infty; r_{\perp}) = \langle \sigma_{i,j} \sigma_{i,j+r_{\perp}} \rangle$ at criticality $t = 0$ we gain the correlation length $\xi_{\perp}(L_{\parallel})$ through

$$G_{\perp}(L_{\parallel}, \infty; r_{\perp}) \simeq \hat{G}_{\perp}(L_{\parallel}) e^{-r_{\perp}/\xi_{\perp}(L_{\parallel})}. \quad (3.41)$$

The so-determined critical perpendicular correlation length ξ_{\perp} is known to fulfill

$$\xi_{\perp}(L_{\parallel}) \simeq A_{\perp} L_{\parallel}^{1/\theta}, \quad (3.42)$$

with nonuniversal amplitude A_{\perp} [HS01, Huc02]. Measuring the correlation length ξ_{\perp} in dependency of the parallel extension L_{\parallel} allows us to determine the anisotropy exponent θ , where the limit $L_{\perp} \rightarrow \infty$ implied by $\rho \rightarrow 0$ is implemented by the condition $L_{\perp}/\xi_{\perp} \gtrsim 10$ in the Monte Carlo simulations [AHW12].

Fig. 3.16 displays the correlation functions for both models in the limit $v \rightarrow \infty$. For the 1+1d case these correlations are purely exponential even at short distances, since the coupling in perpendicular direction is mediated through fluctuating fields [Huc09], leading to dimensional reduction to an effectively one-dimensional system. The resulting correlation length ξ_{\perp} is shown in the inset of Fig. 3.16. The growth of $\xi_{\perp}(L_{\parallel})$ follows a power law with exponent $\theta^{-1} = 1/3$ and with prefactor

$$A_{\perp}^{1+1d} = \lim_{L_{\parallel} \rightarrow \infty} L_{\parallel}^{-1/\theta} \xi_{\perp}^{1+1d}(L_{\parallel}) = 0.68(2), \quad (3.43)$$

indicated as a black line. We find corrections to scaling for $L_{\parallel} \lesssim 100$, which are not crucial in two dimensions as we can simulate system sizes up to $L_{\parallel} = 10^4$, but become relevant in higher dimensions as shown in Section 3.9.

In the case of the 2d model we find two regions with different characteristics. The short-distance correlations are affected by the perpendicular nearest-neighbor interactions within the planes which are not present in the 1+1d model. These correlations decay with a correlation length of the order $\xi_{\perp}^{\text{eq}}(T_c^{2\text{d}}) \approx 1$, with $T_c^{2\text{d}}$ from Eq. (3.37). For large distances the correlations become strongly anisotropic as in the 1+1d case, with amplitude

$$A_{\perp}^{2\text{d}} = \lim_{L_{\parallel} \rightarrow \infty} L_{\parallel}^{-1/\theta} \xi_{\perp}^{2\text{d}}(L_{\parallel}) = 0.94(3). \quad (3.44)$$

From the anisotropy exponent $\theta = 3$ we can derive the correlation length exponents $\nu_{\parallel} = 3/2$ and $\nu_{\perp} = 1/2$ using the generalized hyperscaling relation [HLS75, BW89]

$$2 - \alpha = 2\beta + \gamma = \nu_{\parallel} + (d_b - 1)\nu_{\perp}, \quad (3.45)$$

with $d_b = 2$ and mean-field exponents $\alpha = 0$, $\beta = 1/2$, and $\gamma = 1$, whose validity has been demonstrated in [Huc09] by a mapping onto a mean-field equilibrium model.

3.8.5 Field theory

The calculation of the anisotropy exponent θ in the limit $v \rightarrow \infty$ is done within a one-dimensional Ginzburg-Landau-Wilson (GLW) field theory [BZJ85]. For $v \rightarrow \infty$ it was shown in Ref. [Huc09] that the 1+1d model can be mapped onto an *equilibrium* system consisting of one-dimensional chains that only couple via fluctuating magnetic fields. Due to the stripe geometry with short length L_{\parallel} and the periodic boundary conditions in parallel direction the magnetization is homogeneous in this direction, and parallel correlations are irrelevant. Hence we can use the zero-mode approximation in this direction. However, it is necessary to include a gradient term representing the interaction between adjacent spin chains. Therefore the minimal GLW field theory describing this strongly anisotropic mean-field system is given by

$$\beta\mathcal{H} = L_{\parallel} \int_0^{L_{\perp}} dx \left(\frac{t}{2} m(x)^2 + \frac{1}{2} m'(x)^2 + \frac{u}{4!} m(x)^4 \right), \quad (3.46)$$

with phenomenological parameters t and u , whereas $m(x)$ represents the magnetization of the spin chain at perpendicular coordinate x . The partition function of Eq. (3.46) can be mapped onto a one-dimensional Schrödinger equation in a quartic anharmonic oscillator potential using an appropriate rescaling [AHW12], which yields the critical exponents

$$\theta = 3, \quad \nu_{\parallel} = \frac{3}{2}, \quad \nu_{\perp} = \frac{1}{2}. \quad (3.47)$$

3.8.6 Cross-over scaling at finite v

The critical behavior at finite velocities v was analyzed in detail in [AHW12]. We expect a cross-over from an isotropic Ising model with $\theta = 1$ to a strongly anisotropic system with $\theta = 3$,

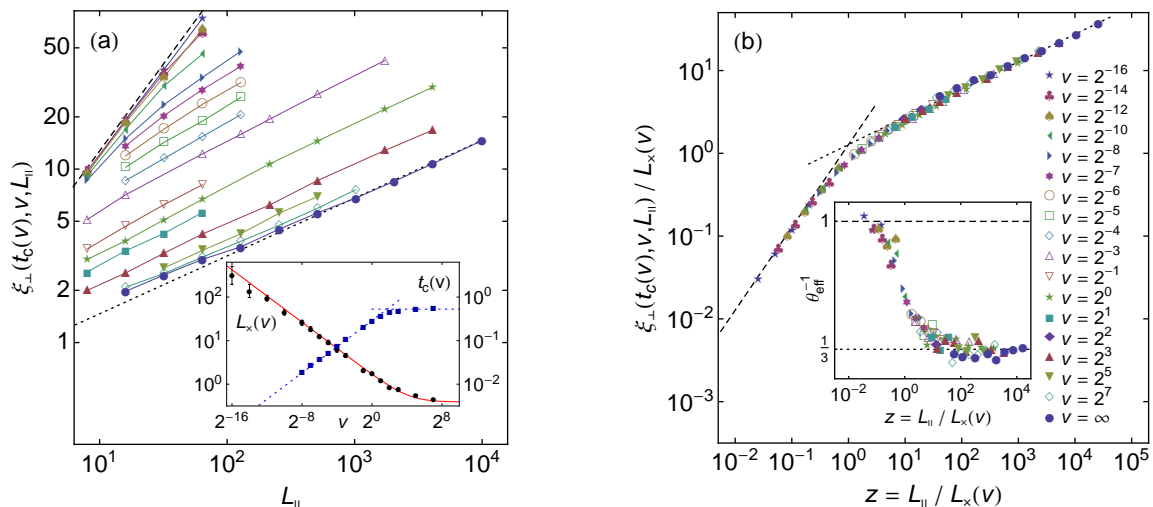


Figure 3.17: Cross-over behavior in the 1+1d case. Both graphs show log-log plots of the correlation length $\xi_{\perp}(t_c(v), v, L_{\parallel})$ as a function of the system size L_{\parallel} at reduced critical temperature $t_c(v)$ for different velocities v . The dashed line is the analytically known Ising limit $\xi_{\perp}(0, 0, L_{\parallel})/L_{\parallel} \simeq 4/\pi$ valid for $v \rightarrow 0$ [Car84], while the dotted line has slope $\theta^{-1} = 1/3$. Figure (a) shows the unscaled data, and the inset displays the cross-over length $L_{\times}(v)$ as well as the reduced critical temperature $t_c(v)$. Figure (b) displays the same data, rescaled with the cross-over length $L_{\times}(v)$, leading to an excellent data collapse. The inset in (b) shows the cross-over of the effective anisotropy exponent θ_{eff} from $\theta_{\text{eff}} = 1$ (Ising, dashed line) to $\theta_{\text{eff}} = 3$ (MF, dotted line). (adapted from [AHW12])

hence we cannot use a fixed finite generalized aspect ratio ρ , Eq. (2.8b), in the simulations, as the effective exponent θ_{eff} is not constant. The only possible choice is $\rho \rightarrow 0$ (or $\rho \rightarrow \infty$), where the θ -dependency drops out. Extensive MC simulations were performed in this limit in order to understand the cross-over behavior, resulting in, to our knowledge, the first cross-over scaling analysis of a cross-over from an isotropic to a strongly anisotropic system.

We focused on the 1+1d system and considered the correlation length $\xi_{\perp}(t_c(v), v, L_{\parallel})$ at velocity-dependent reduced critical temperature

$$t_c(v) = \frac{T_c(v)}{T_c(0)} - 1, \quad (3.48)$$

where $T_c(0) = 2/\log(\sqrt{2} + 1)$ from Eq. (3.27). $t_c(v)$ was determined from a finite-size scaling analysis of ξ_{\perp} for the different velocities v and is depicted in the inset of Fig. 3.17a.

Fig. 3.17a shows the unscaled data, demonstrating that the correlation length ξ_{\perp} of systems moved at high velocities v is well described by the expected exponent $\theta = 3$ (dotted line), whereas for low velocities $v \lesssim 2^{-12}$ effectively the Ising exponent $\theta = 1$ (dashed line) holds for the simulated system sizes L_{\parallel} . The curvature of the data of intermediate velocities suggest the cross-over. After rescaling of both axes with the measured *cross-over length* $L_{\times}(v)$ (see inset of Fig. 3.17a) we find an excellent data collapse as shown in Fig. 3.17b. We conclude that for all finite velocities $v > 0$ the critical behavior changes from Ising type to mean-field type if

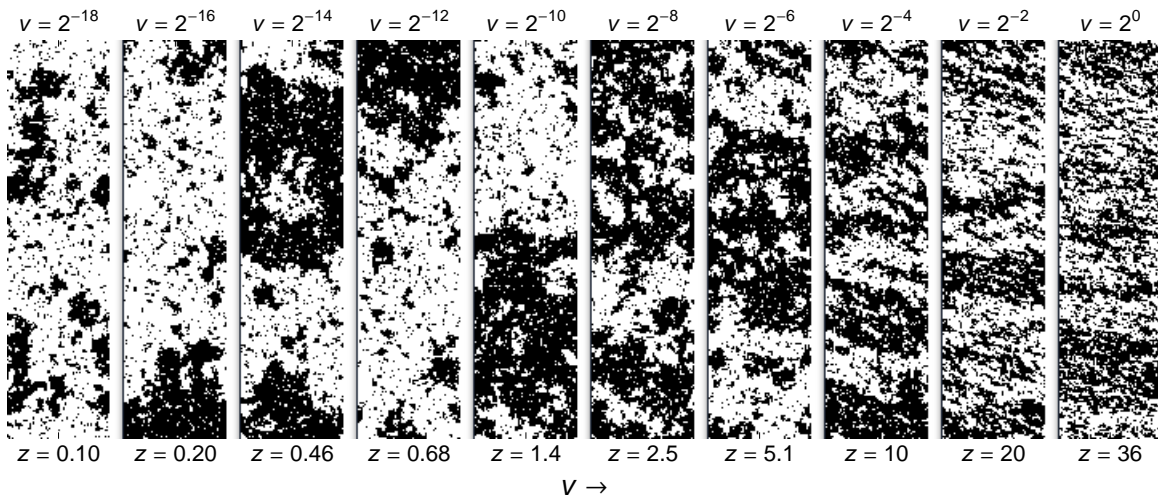


Figure 3.18: Typical spin configurations of the critical 1+1d system for $L_{\parallel} = 64$ and different velocities $v = 2^{-18}, \dots, 1$, or, cross-over scaling variable $z = L_{\parallel}/L_{\times}(v)$. The critical domains are isotropic and Ising-like for $z \ll 1$ and become anisotropic for $z \gtrsim 1$. (adapted from [AHW12])

the parallel length L_{\parallel} exceeds the velocity-dependent cross-over length $L_{\times}(v)$, approximately given by

$$L_{\times}(v) \approx \left(\frac{A_{\perp}^{1+1d}}{A^{\text{eq}}} \right)^{3/2} \sqrt{1 + \frac{v_{\times}}{v}} \quad (3.49)$$

and shown as red curve in the inset of Fig. 3.17a, with $v_{\times} = 18(2)$.

The inset in Fig. 3.17b shows the effective exponent θ_{eff} , obtained from the logarithmic derivative

$$\theta_{\text{eff}}^{-1} = \frac{\partial \log \xi_{\perp}}{\partial \log L_{\parallel}}, \quad (3.50)$$

whose value changes monotonically from $\theta_{\text{eff}} = 1$ (Ising, isotropic) to $\theta_{\text{eff}} = 3$ (MF, strongly anisotropic). In order to illustrate the change of the critical behavior, Fig. 3.18 shows typical critical spin configurations for different values of the cross-over scaling variable $z = L_{\parallel}/L_{\times}(v)$. As long as $z < 1$ the critical domains look isotropic, while for $z > 1$ a clear anisotropy becomes visible.

3.9 2+1d and 1+2d case

These two cases describe experimentally relevant three-dimensional sheared systems, which were investigated in the limit $v \rightarrow \infty$ [HA12]. In both cases the boundary dimension is $d_b = d = 3$. In the 2+1d case shown in Fig. 3.19 we must distinguish all three directions and denote the direction perpendicular to the planes with \perp_1 and the inplane direction perpendicular to



Figure 3.19: Geometries 2+1d and 1+2d considered in this section. The grey regions are the magnetic systems, while the green regions are the moving boundaries. The arrows indicate the motion of the subsystems. Note that we have rotated the 1+2d system by 45° around the shear direction such that the shear normal is pointing upwards in both cases. (adapted from [HA12])

the parallel shear direction with \perp_2 , leading to the Hamiltonian

$$\beta\mathcal{H}(t) = - \sum_{k=1}^{L_{\perp_1}} \sum_{l=1}^{L_{\perp_2}} \sum_{m=1}^{L_{\parallel}} \sigma_{klm} (K_{\parallel}\sigma_{k,l,m+1} + K_{\perp_2}\sigma_{k,l+1,m} + K_{\perp_1}\sigma_{k+1,l,m+\Delta(t)}), \quad (3.51)$$

with critical temperature ($J_{\parallel} = J_{\perp_1} = J_{\perp_2} = 1$)

$$T_c^{2+1d} = 5.264750414514743550598017203424\dots \quad (3.52)$$

from the same high temperature series [BGH⁺08] as in the 2d case, but now with $f = 2$. This value can be calculated to approximately 700 digits. Using the notation ($\perp_1 \perp_2 \parallel$) for directions, the shear is in (001)-direction and the shear normal is in (100)-direction in this case.

The geometry 1+2d is similar to the previous case, but now the shear normal is in the (110)- instead of the (100)-direction. As a consequence, all four perpendicular coupling partners of a spin σ are in other shear planes than σ . The Hamiltonian of this case reads

$$\beta\mathcal{H}(t) = - \sum_{k=1}^{L_{\perp}} \sum_{l=1}^{L_{\perp}} \sum_{m=1}^{L_{\parallel}} \sigma_{klm} [K_{\parallel}\sigma_{k,l,m+1} + K_{\perp}(\sigma_{k,l+1,m+\Delta(t)} + \sigma_{k+1,l,m+\Delta(t)})]. \quad (3.53)$$

For $v \rightarrow \infty$ the system decouples into an array of one-dimensional parallel chains with four nearest neighbors. Hence we can use Eq. (3.11) with $f = 4$ to get the critical temperature

$$T_c^{1+2d} = \frac{2}{\ln[\frac{1}{8}(5 + \sqrt{41})]} = 5.642611138\dots \quad (3.54)$$

for $J_{\parallel} = J_{\perp} = 1$.

For the considered systems with $d_b > 2$ we cannot map the corresponding Hamiltonian onto a Schrödinger equation as done in Sec. 3.8.5, as the $(d_b - 1)$ -dimensional integral over the perpendicular directions cannot be interpreted as a time integral. Instead we use a simple dimensional analysis in order to predict the critical exponents [HA12]

$$\theta = 5 - d_b, \quad \nu_{\parallel} = \frac{5 - d_b}{2}, \quad \nu_{\perp} = \frac{1}{2}, \quad (3.55)$$

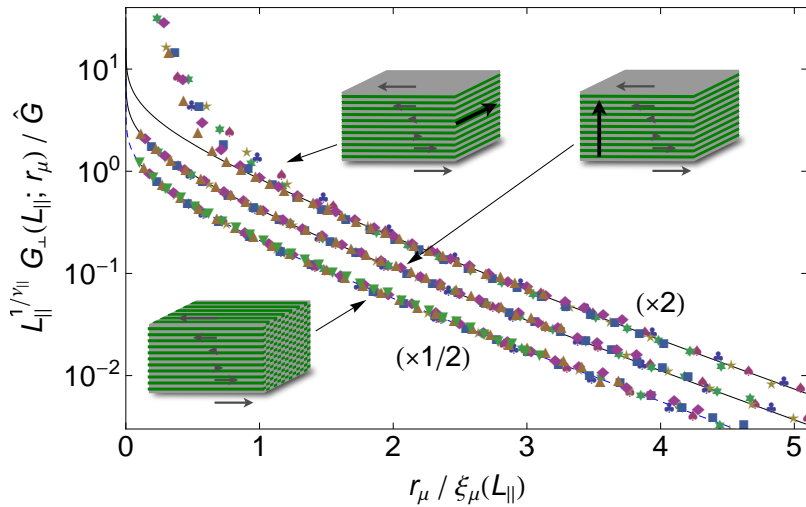


Figure 3.20: Rescaled correlation function $G_{\perp}(L_{\parallel}; r_{\mu})$ with $\mu = \{\perp, \perp_1, \perp_2\}$ for both models at criticality, with $L_{\parallel} = \{8, 16, 32, 64, 128, 256, 512, 1024\}$. As $\xi_{\mu}(L_{\parallel}) \simeq A_{\mu} L_{\parallel}^{1/\theta}$ we get the anisotropy exponent $\theta = 2$ as predicted by the dimensional analysis. A rescaling of the y -axis with L_{\parallel} results in an excellent data collapse, verifying $\nu_{\parallel} = 1$. In the case of the 2+1d model we have to distinguish two perpendicular directions as indicated by the sketches: one within a layer, the other perpendicular to the layers. The solid lines represent the exactly known correlation function from Eq. (3.58). Note that we multiplied the collapsed data with different factors as indicated in order to show them in one plot. (adapted from [HA12])

reproducing the results for $d_b = 1$ [Huc09] and $d_b = 2$ [AHW12] and fulfilling the generalized hyperscaling relation Eq. (3.45). For our case $d_b = 3$ we find

$$\theta = 2, \quad \nu_{\parallel} = 1, \quad \nu_{\perp} = \frac{1}{2}, \quad (3.56)$$

while for $d_b \geq 4$ we predict usual isotropic or weakly anisotropic behavior with $\theta = 1$ and $\nu_{\parallel} = \nu_{\perp} = 1/2$, as then the upper critical dimension $d_c = 4$ is reached and the shear becomes an irrelevant perturbation.

To test these predictions we measured the critical perpendicular correlation function

$$G_{\perp}(L_{\parallel}; \mathbf{r}_{\perp}) = \langle \sigma_{000} \sigma_{r_{\perp_1}, r_{\perp_2}, 0} \rangle \quad (3.57)$$

for film geometry $L_{\perp} \rightarrow \infty$ in analogy to Section 3.8.4. The resulting data collapse is shown in Fig. 3.20 and nicely fits to the analytically known correlation function of the Gaussian theory

$$G_{\perp}(L_{\parallel}; r_{\mu}) \simeq \hat{G} L_{\parallel}^{-1/\nu_{\parallel}} K_0[r_{\mu}/\xi_{\mu}(L_{\parallel})], \quad (3.58)$$

with modified Bessel function of the second kind K_0 and $\mu = \{\perp, \perp_1, \perp_2\}$. However, corrections to scaling had to be taken into account in $\xi_{\mu}(L_{\parallel})$, as the maximal system sizes were limited to $L_{\parallel} \lesssim 1024$ by the available computational power [HA12].

3.10 Some higher-dimensional geometries

Just for reference we finally give the critical indices at $v \rightarrow \infty$ for several higher-dimensional cases and a tabular overview of the results.

3d_b case The experimentally accessible 3d_b case is shown in Fig. 3.1. We find $T_c^{3d_b} = 4.8(1)$ using the 8th order high temperature series from Ref. [BH74, Tab. IV], unfortunately no longer series expansions are available in the literature. As the boundary dimension is $d_b = 2$, we predict strongly anisotropic behavior with $\theta = 3$ and correlation length exponents $\nu_{\parallel} = 3/2$ and $\nu_{\perp} = 1/2$. The correlation length perpendicular to the boundary should be finite and equal to the equilibrium correlation length of the three-dimensional Ising model at $T_c^{3d_b}$ just as in the case 2d_b discussed in Section 3.7.

3d case The quite theoretical 3d case describes two three-dimensional systems in direct contact along the fourth dimension. Now we obtain $T_c^{3d} = 5.983835(1)$ using the 32th order high temperature series from [AF03a]. In this case $d_b = 3$, and we predict a strongly anisotropic phase transition with $\theta = 2$, $\nu_{\parallel} = 1$ and $\nu_{\perp} = 1/2$, comparable to the 2+1d and 1+2d cases.

1+3d case This four-dimensional sheared system was investigated numerically for linear dimensions $L_{\mu} \lesssim 32$ in [HA12]. The exact critical temperature for $v \rightarrow \infty$ and $J_{\mu} = 1$ is determined from Eq. (3.11) with $f = 6$ and reads $T_c^{1+3d} = 2/\ln[\frac{1}{12}(7 + \sqrt{73})] = 7.728921\dots$. The simulation results showed strong, possibly logarithmic scaling corrections, which made a determination of the predicted exponents impossible. From the scaling behavior of the available data we estimated that system sizes of at least $L_{\mu} \gtrsim 1000$ would be required to find the correct scaling behavior [HA12].

General case In the general case of a d_b -dimensional hyper-cubic lattice with d_{\parallel} driven dimensions and d_{\perp} perpendicular dimensions we again must distinguish between the $d_{\perp 1}$ dimensions normal to the shear and $d_{\perp 2}$ “inplane” dimensions without shear motion, with $d_{\perp} = d_{\perp 1} + d_{\perp 2}$. The critical temperature T_c at infinite shear velocity v is again given by Eq. (3.11). It can be calculated from the zero-field boundary susceptibility $\chi_{b,eq}^{(0)}$ of a d_{eq} -dimensional equilibrium system which has f fluctuating fields at each lattice point, where $d_{eq} = d_{\parallel} + d_{\perp 2}$. The number f is $f = 1$ for the moved systems and $f = 2d_{\perp 1}$ for the sheared systems, see Table 3.1. From a simple generalization of Eq. (3.55) we find the correlation length exponents

$$\theta = \frac{4 - d_{\perp}}{d_{\parallel}}, \quad \nu_{\parallel} = \frac{4 - d_{\perp}}{2d_{\parallel}}, \quad \nu_{\perp} = \frac{1}{2}, \quad (3.59)$$

fulfilling the generalized hyperscaling relation $d_{\parallel}\nu_{\parallel} + d_{\perp}\nu_{\perp} = 2$.

In Table 3.1 we conclude with an overview of the determined exponents and critical temperatures T_c at infinite driving velocity v , including two cases denoted “mix” where we assumed a suitable two-dimensional motion of the interacting planes. These systems have $d_{\parallel} = 2$, but notwithstanding the same T_c as the corresponding systems with unidirectional motion at infinite v . For the layered case 2+1d_m we predict the exponents $\theta = 3/2$ and $\nu_{\parallel} = 3/4$. A test of these predictions is left for future work.

	model	d_b	d_{\parallel}	d_{\perp}	d_{\perp_1}	d_{\perp_2}	θ	ν_{\parallel}	f	d_{eq}	T_c/J at $v \rightarrow \infty$
moved	1d	1	1	–	–	–	–	2	1	1	2.2691853... Eq. (3.19)
	2d	2	1	1	0	1	3	3/2	1	2	4.0587824... Eq. (3.37)
	3d	3	1	2	0	2	2	1	1	3	5.983835(1) Sec. 3.10
	2d _b	1	1	–	–	–	–	2	1	2	2.6614725... Eq. (3.29)
	3d _b	2	1	1	0	1	3	3/2	1	3	4.8(1) Sec. 3.10
sheared	1+1d	2	1	1	1	0	3	3/2	2	1	3.4659074... Eq. (3.35)
	2+1d	3	1	2	1	1	2	1	2	2	5.2647504... Eq. (3.52)
	1+2d	3	1	2	2	0	2	1	4	1	5.6426111... Eq. (3.54)
	1+3d	4	1	3	3	0	1	1/2	6	1	7.728921... Sec. 3.10
mix	2d _m	2	2	–	–	–	–	1	1	1	4.0587824... Eq. (3.37)
	2+1d _m	3	2	1	1	0	3/2	3/4	2	2	5.2647504... Eq. (3.52)

Table 3.1: Relevant dimensions, exponents and parameters of the models considered in this work as shown in Fig. 3.1. The various dimensions are described in the text, and the critical temperatures are given for the isotropic case $J_{\mu} = J$.

3.11 Summary

In this chapter we investigated driven Ising models with friction due to magnetic correlations in various geometries. This friction is governed by energy dissipation from the driven boundary to the heat bath and can be of Coulomb and of Stokes type [MAHW11]. It may yield to a considerably high power dissipation of up to 100 W/cm² when the systems are in close vicinity.

The nonequilibrium phase transitions present in these systems were investigated in detail using analytical methods and Monte Carlo simulations. In the far from equilibrium limit of high driving velocities $v \rightarrow \infty$ the models were solved exactly by integrating out the nonequilibrium boundary degrees of freedom. The resulting exact self-consistency equation was analyzed for various geometries, leading, in most cases, to precise values of the critical temperature T_c of the nonequilibrium phase transition. In the limit $v \rightarrow \infty$ the systems always show mean-field behavior due to dimensional reduction, independent of geometry. In the simplest one-dimensional case denoted 1d a complete analysis of both equilibrium as well as nonequilibrium quantities was presented [Huc09].

The analytic results were reproduced using an introduced multiplicative Monte Carlo rate, which eliminates correlations due to many-particle dynamics as introduced by the common Metropolis and Glauber rates. First considering the geometries 1d and 2d_b with boundary dimension $d_b = 1$, we analyzed the critical behavior at finite velocities v and studied the cross-over behavior from low to high velocities. While the phase transition in the one-dimensional system 1d only survives for $v = \infty$ in the thermodynamic limit, for the two-dimensional case 2d_b we found that the velocity v is a relevant perturbation, always driving the system to a nonequilibrium state with mean-field character.

For geometries 1+1d and 2d with boundary dimension $d_b = 2$ we found strongly anisotropic critical behavior and calculated the anisotropy exponent θ in the limit of high driving velocity $v \rightarrow \infty$. Determining the correlation length perpendicular to the driving direction, Eq. (3.42),

we got $\theta = 3$ as well as the correlation length exponents $\nu_{\parallel} = 3/2$ and $\nu_{\perp} = 1/2$. The analytic deviation of these exponents within the framework of a Ginzburg-Landau-Wilson Hamiltonian led to the same values. Comparing the results to the driven lattice gas [KLS83, SZ95] we note that it also shows a strongly anisotropic phase transition at a critical temperature which grows with the velocity. Remarkably this phase transition is characterized by the same critical exponents at large drive.

Using extensive MC simulations, the critical behavior at finite velocities v was investigated in order to calculate the cross-over scaling function describing the cross-over from the Ising universality class at $v = 0$ to the nonequilibrium critical behavior at $v \rightarrow \infty$. It turned out that for all finite velocities $v > 0$ both models undergo a cross-over, at a cross-over length $L_{\times}(v)$, from a quasi-equilibrium isotropic Ising-like phase transition to a nonequilibrium mean-field behavior with strongly anisotropic correlations.

Finally, the analysis was extended to the three-dimensional sheared systems 2+1d and 1+2d with boundary dimension $d_b = 3$, where we only focused on the limit $v \rightarrow \infty$. Although these two systems only differ in the direction of the shear normal, we found different critical temperatures at high velocities. The correlation length exponents ν_{μ} were numerically verified to obey the field theoretical predictions $\nu_{\parallel} = 1$ and $\nu_{\perp} = 1/2$, with anisotropy exponent $\theta = 2$. However, considerable corrections to scaling hampered the analysis of the simulation data.

The corrections to scaling became even stronger in the four-dimensional sheared case 1+3d, for which the dimensional analysis predicts isotropic behavior with $\theta = 1$, as the upper critical dimension $d_c = 4$ is reached. These corrections made a verification of the predicted exponents impossible.

4 Outlook

The main topic of this work were fluctuation-induced forces near continuous phase transitions. On the one hand we focused on critical Casimir forces in equilibrium systems and calculated the universal finite-size scaling functions which describe these forces near the critical point. On the other hand we investigated the properties of a simple model for fluctuation-induced friction in driven Ising systems far from equilibrium.

A recent development not shown in this overview is the combination of both effects, i.e., to investigate both Casimir forces and friction forces simultaneously in a nonequilibrium system. These considerations require a modified definition of thermodynamic Casimir forces independent of a free energy, as this quantity is not well defined far from equilibrium. This can indeed be achieved within a Monte Carlo simulation, if we introduce Monte Carlo steps that change the geometry of the given system at constant volume, e.g., by moving a boundary: imagine a d -dimensional Ising model with $L_{\parallel}^{d-1} \times L_{\perp}$ sites, periodic boundary conditions in the parallel directions and arbitrary boundary conditions in perpendicular direction. At row z_b we introduce an additional boundary of fixed spins with, say, up direction, $\sigma_{x,y,z_b} = 1$, which divides the system into two halves. Beside the usual Monte Carlo dynamics for the spin degrees of freedom, we also move the boundary according to $z_b \rightarrow z_b \pm 1$ with the correct detailed balance rate, respecting a possible additional linear external potential $V_{\text{ext}}(z) = -\mathcal{F}_{\text{ext}}z$. Measuring the average boundary position $\langle z_b \rangle$, we conclude that the Casimir force fulfills $\mathcal{F}_C(\langle z_b \rangle) + \mathcal{F}_{\text{ext}} = 0$. The fluctuating boundary position can alternatively be measured in a histogram, from which the Casimir energy and force can be determined for a broad range of z -values even without an external potential.

This direct measurement of Casimir forces can also be implemented with other geometrical objects like spheres with fixed boundary conditions and is then in complete analogy to experiments by Hertlein et al. [HHG⁺08]. This method is topic of the actual Bachelor thesis by Hendrik Hobrecht [Hob12].

It is also planned to generalize this method to an ensemble of spherical particles interacting through fluctuation-induced Casimir forces. First test simulations show interesting phenomena, as the resulting many-body interaction between the particles can be tuned via temperature changes in complete analogy to recent experiments on colloidal suspensions [SZH⁺08, BOS⁺09, GD10, BWS10].

The simulation method described above can easily be generalized to nonequilibrium systems, where, e.g., a sphere is moved through a critical system parallel to a surface. The sphere will experience longitudinal friction forces as well as transversal Casimir forces, which independently can be measured using the introduced methods. In the case of strongly anisotropic nonequilibrium transitions as found in [AHW12] we expect strongly anisotropic Casimir forces [BDS10]. These nonequilibrium systems will be a topic of future work.

Another yet hypothetic idea is to investigate fluctuation-induced forces and phase transitions in systems described by a recently proposed nonequilibrium spin dynamics [ADH⁺12] based on explosive percolation [ADS09]. While the explosive percolation transition is in fact a continuous phase transition with very small critical exponent β [dCDGM10], the addition of spin degrees of freedom adds a memory to the system, leading to a strong first order phase transition with hysteresis [ADH⁺12]. Casimir as well as friction forces could be determined in this system, possibly leading to new and interesting physics.

Acknowledgements

I have to thank many people and coworkers for very fruitful discussions, criticism and comments: first of all I would like to thank K. D. Usadel, P. Entel, and especially J. König for giving me the opportunity to independently work in their groups.

D. Grüneberg pointed out to me the missing theoretical explanation of the critical Casimir effect in Helium-4 films. This triggered a very fruitful cooperation with the group of H. W. Diehl, especially with F. M. Schmidt, D. Grüneberg, M. Burgsmüller, and S. Rutkevich. The resulting constructive cooperation with M. Hasenbusch from the Humboldt-Universität zu Berlin is highly appreciated.

The field of fluctuation-induced friction forces was introduced to me by D. Kadau from the group of D. E. Wolf, now at the Eidgenössische Technische Hochschule Zürich. I enjoyed many interesting discussions with S. Angst, M. P. Magiera, and L. Brendel. This led to intense cooperations with H. Hinrichsen from the Universität Würzburg and S. R. Dahmen from the Universidade Federal do Rio Grande do Sul in Porto Alegre, Brasil.

Special thanks go to S. Lübeck and D. Comtesse for critical and refreshing comments.

Parts of this work were supported by CAPES–DAAD through the PROBRAL program, by the Center for Nanointegration Duisburg-Essen (CENIDE), as well as by the German Research Society (DFG) through SFB 616 “Energy Dissipation at Surfaces”.

Bibliography

- [AB12] Ezequiel V. Albano and Kurt Binder. Wetting transition in the two-dimensional Blume-Capel model: A Monte Carlo study. *Phys. Rev. E* **85**, 061601, Jun 2012. → p. [35](#)
- [ADH⁺12] Sebastian Angst, Silvio R. Dahmen, Haye Hinrichsen, Alfred Hucht, and Martin P. Magiera. Explosive Ising. *J. Stat. Mech.* **2012**, L06002, Jun 2012. arXiv:1204.5196. → p. [45](#)
- [ADS09] Dimitris Achlioptas, Raissa M. D'Souza, and Joel Spencer. Explosive percolation in random networks. *Science* **323**, 1453-1455, 2009. → p. [45](#)
- [AF03a] H. Arisue and T. Fujiwara. New algorithm of the high-temperature expansion for the Ising model in three dimensions. *Nucl. Phys. B Proc. Suppl.* **119**, 855, 2003. arXiv:hep-lat/0209019. → p. [42](#)
- [AF03b] Hiroaki Arisue and Toshiaki Fujiwara. Algorithm of the finite-lattice method for high-temperature expansion of the Ising model in three dimensions. *Phys. Rev. E* **67**, 066109, Jun 2003. There is a typo in the 42th order term, the correct value appears in arXiv:hep-lat/0209002. → p. [9](#)
- [AHW12] Sebastian Angst, Alfred Hucht, and Dietrich E. Wolf. Strongly anisotropic nonequilibrium phase transition in Ising models with friction. *Phys. Rev. E* **85**, 051120, May 2012. arXiv:1201.1998. → p. [33](#), [35](#), [36](#), [37](#), [38](#), [39](#), [41](#), [45](#)
- [ARHS10] C. Appert-Rolland, H. J. Hilhorst, and G. Schehr. Spontaneous symmetry breaking in a two-lane model for bidirectional overtaking traffic. *J. Stat. Mech.* **2010**, P08024, 2010. → p. [19](#)
- [AT87] M. P. Allen and D. J. Tildesley. *Computer Simulation of Liquids*. Clarendon Press, Oxford, 1987. → p. [20](#)
- [Bac07] C. P. Bachas. Comment on the sign of the Casimir force. *J. Phys A: Math. Theor.* **40**, 9089, 2007. → p. [14](#)
- [BAFG02] Denis Bartolo, Armand Ajdari, Jean-Baptiste Fournier, and Ramin Golestanian. Fluctuations of fluctuation-induced Casimir-like forces. *Phys. Rev. Lett.* **89**, 230601, Nov 2002. → p. [1](#)
- [Bax82] R. J. Baxter. *Exactly Solved Models in Statistical Mechanics*. Academic Press, London, 1982. → p. [26](#)
- [BC06] Tristan Baumberger and Christiane Caroli. Solid friction from stick-slip down to pinning and aging. *Advances in Physics* **55**, 279-348, 2006. → p. [2](#)

- [BCH⁺94] Gyan Bhanot, Michael Creutz, Ivan Horvath, Jan Lacki, and John Weckel. Series expansions without diagrams. *Phys. Rev. E* **49**, 2445–2453, Mar 1994. → *p. 9*
- [BDS10] Matthias Burgsmüller, H. W. Diehl, and M. A. Shpot. Fluctuation-induced forces in strongly anisotropic critical systems. *J. Stat. Mech.* **2010**, P11020, 2010. → *p. 35, 45*
- [BDT00] J. G. Brankov, D. M. Dantchev, and N. S. Tonchev. *Theory of Critical Phenomena in Finite-Size Systems – Scaling and Quantum Effects*. World Scientific, Singapore, 2000. → *p. 5*
- [Ber71] V. L. Berezinsky. Destruction of long range order in one-dimensional and two-dimensional systems having a continuous symmetry group. 1. Classical systems. *Sov. Phys.-JETP* **32**, 493, 1971. → *p. 11*
- [BGH⁺08] S. Boukraa, A. J. Guttmann, S. Hassani, I. Jensen, J.-M. Maillard, B. Nickel, and N. Zenine. Experimental mathematics on the magnetic susceptibility of the square lattice Ising model. *J. Phys A: Math. Theor.* **41**, 455202 (51pp), 2008. → *p. 34, 40*
- [BH74] K. Binder and P. C. Hohenberg. Surface effects on magnetic phase transitions. *Phys. Rev. B* **9**, 2194, 1974. → *p. 42*
- [Bin81] K. Binder. Finite size scaling analysis of Ising model block distribution functions. *Z. Phys. B* **43**, 119, 1981. → *p. 10*
- [Bin90] K. Binder. Some recent progress in the phenomenological theory of finite size scaling and applications to Monte Carlo studies of critical phenomena. In V. Privman, editor, *Finite Size Scaling and Numerical Simulation of Statistical Systems*, chapter 4. World Scientific, Singapore, 1990. → *p. 35, 36*
- [BOS⁺09] Daniel Bonn, Jakub Otwinowski, Stefano Sacanna, Hua Guo, Gerard Wegdam, and Peter Schall. Direct observation of colloidal aggregation by critical Casimir forces. *Phys. Rev. Lett.* **103**, 156101, Oct 2009. → *p. 45*
- [BW89] K. Binder and J.-S. Wang. Finite-size effects at critical points with anisotropic correlations: Phenomenological scaling theory and Monte Carlo simulations. *J. Stat. Phys.* **55**, 87, 1989. → *p. 37*
- [BWS10] Daniel Bonn, Gerard Wegdam, and Peter Schall. Bonn, Wegdam, and Schall Reply. *Phys. Rev. Lett.* **105**, 059602, Jul 2010. → *p. 45*
- [BZJ85] E. Brézin and J. Zinn-Justin. Finite size effects in phase transitions. *Nucl. Phys. B* **257**, 687, 1985. → *p. 37*
- [CAK⁺01] H. B. Chan, V. A. Aksyuk, R. N. Kleiman, D. J. Bishop, and Federico Capasso. Quantum mechanical actuation of microelectromechanical systems by the Casimir force. *Science* **291**, 1941-1944, 2001. → *p. 1*
- [Car84] J. Cardy. Conformal invariance and universality in finite-size scaling. *J. Phys A: Math. Gen.* **17**, L385, 1984. → *p. 38*

-
- [Cas48] H. B. G. Casimir. On the attraction between two perfectly conducting plates. Proc. K. Ned. Akad. Wet. **51**, 793, 1948. → *p. 1*
- [CGL98] F. Corberi, G. Gonnella, and A. Lamura. Spinodal decomposition of binary mixtures in uniform shear flow. Phys. Rev. Lett. **81**, 3852–3855, Nov 1998. → *p. 19*
- [CGS05] E. N. M. Cirillo, G. Gonnella, and G. P. Saracco. Monte Carlo results for the Ising model with shear. Phys. Rev. E **72**, 026139, 2005. → *p. 19*
- [CHG09] Denis Comtesse, Alfred Hucht, and Daniel Grüneberg. Thermodynamic Casimir effect in the large- n limit. Apr 2009. arXiv:0904.3661v2. → *p. 5, 16*
- [CL90] C. K. Chan and L. Lin. Effects of shear on the phase transition of binary mixtures. EPL **11**, 13-18, 1990. → *p. 19*
- [Com08] Denis Comtesse. Thermodynamischer Casimireffekt in ϕ^4 -Theorien im Limes $n \rightarrow \infty$. Diplomarbeit, Universität Duisburg-Essen, 2008. → *p. 16*
- [CP48] H. B. G. Casimir and D. Polder. The influence of retardation on the London-van der Waals forces. Phys. Rev. **73**, 360–372, Feb 1948. → *p. 1*
- [Dan98] Daniel M. Danchev. Exact three-dimensional Casimir force amplitude, c function, and Binder’s cumulant ratio: Spherical model results. Phys. Rev. E **58**, 1455–1462, Aug 1998. → *p. 5*
- [dCDGM10] R. A. da Costa, S. N. Dorogovtsev, A. V. Goltsev, and J. F. F. Mendes. Explosive percolation transition is actually continuous. Phys. Rev. Lett. **105**, 255701, Dec 2010. → *p. 45*
- [DD10] Vincent Démery and David S. Dean. Drag forces in classical fields. Phys. Rev. Lett. **104**, 080601, Feb 2010. → *p. 22*
- [DDG06] Daniel Dantchev, H. W. Diehl, and Daniel Grüneberg. Excess free energy and Casimir forces in systems with long-range interactions of van der Waals type: General considerations and exact spherical-model results. Phys. Rev. E **73**, 016131, 2006. → *p. 5, 7*
- [DG09] Daniel Dantchev and Daniel Grüneberg. Casimir force in $O(n)$ systems with a diffuse interface. Phys. Rev. E **79**, 041103, Apr 2009. → *p. 5*
- [DG10] David S. Dean and Ajay Gopinathan. Out-of-equilibrium behavior of Casimir-type fluctuation-induced forces for free classical fields. Phys. Rev. E **81**, 041126, Apr 2010. → *p. 1*
- [DGH⁺12] H. W. Diehl, Daniel Grüneberg, Martin Hasenbusch, Alfred Hucht, Sergei B. Rutkevich, and Felix M. Schmidt. Exact thermodynamic Casimir forces for an interacting three-dimensional model system in film geometry with free surfaces. EPL **100**, 10004, Oct 2012. arXiv:1205.6613. → *p. 5, 16, 17, 18*

- [DGS06] H. W. Diehl, D. Grüneberg, and M. A. Shpot. Fluctuation-induced forces in periodic slabs: Breakdown of ϵ expansion at the bulk critical point and revised field theory. *EPL* **75**, 241, 2006. \rightarrow p. 4, 12
- [Die97] H. W. Diehl. The theory of boundary critical phenomena. *Int. J. Mod. Phys. B* **11**, 3503–3523, 1997. \rightarrow p. 4, 10
- [DK04] Daniel Dantchev and Michael Krech. The critical Casimir force and its fluctuations in lattice spin models: exact and Monte Carlo results. *Phys. Rev. E* **69**, 046119-1–20, 2004. \rightarrow p. 4, 5, 12
- [DKD03] D. Dantchev, M. Krech, and S. Dietrich. Universality of the thermodynamic Casimir effect. *Phys. Rev. E* **67**, 066120, 2003. \rightarrow p. 5
- [DKD05] D. Dantchev, M. Krech, and S. Dietrich. Thermodynamic Casimir force in models of ^4He films. *Phys. Rev. Lett.* **95**, 259701, 2005. \rightarrow p. 4
- [DLL03] J. Dzubiella, H. Löwen, and C. N. Likos. Depletion forces in nonequilibrium. *Phys. Rev. Lett.* **91**, 248301, Dec 2003. \rightarrow p. 1
- [Doh09] V. Dohm. Critical Casimir force in slab geometry with finite aspect ratio: Analytic calculation above and below T_c . *EPL* **86**, 20001, 2009. \rightarrow p. 7, 12, 13, 14, 15
- [Doh11] Volker Dohm. Critical free energy and Casimir forces in rectangular geometries. *Phys. Rev. E* **84**, 021108, Aug 2011. \rightarrow p. 12
- [FB10] Xiaomei Feng and Henk W. J. Blöte. Specific heat of the simple-cubic Ising model. *Phys. Rev. E* **81**, 031103, Mar 2010. \rightarrow p. 9
- [FdG78] M. E. Fisher and P.-G. de Gennes. Phénomènes aux parois dans un mélange binaire critique. *C. R. Acad. Sci. Paris, Ser. B* **287**, 207, 1978. \rightarrow p. 1, 4, 7
- [FF69] A. E. Ferdinand and M. E. Fisher. Bounded and inhomogeneous Ising models. I. Specific-heat anomaly of a finite lattice. *Phys. Rev.* **185**, 832, 1969. There is a typo in Eq. (3.36), the term $\xi S_1(n)\tau^2/2$ is missing. \rightarrow p. 15
- [Fis71] M. E. Fisher. The theory of critical point singularities. In M. S. Green, editor, *Critical Phenomena, Proceedings of the 51st Enrico Fermi Summer School, Varenna, Italy*, pages 73–98. Academic Press, New York, 1971. \rightarrow p. 7
- [Fis94] M. E. Fisher. The story of Coulomb criticality. *J. Stat. Phys.* **75**, 1-36, 1994. \rightarrow p. 33
- [FWN08] C. Fusco, D. E. Wolf, and U. Nowak. Magnetic friction of a nanometer-sized tip scanning a magnetic surface: Dynamics of a classical spin system with direct exchange and dipolar interactions between the spins. *Phys. Rev. B* **77**, 174426, 2008. \rightarrow p. 2, 19, 22
- [FYP05] M. Fukuto, Y. F. Yano, and P. S. Pershan. Critical Casimir effect in three-dimensional Ising systems: Measurements on binary wetting films. *Phys. Rev. Lett.* **94**, 135702, 2005. \rightarrow p. 4

-
- [Gam09] Andrea Gambassi. The Casimir effect: From quantum to critical fluctuations. *Journal of Physics: Conference Series* **161**, 012037, 2009. → *p. 1, 4*
- [GAS01] K. Gutkowski, M. A. Anisimov, and J. V. Sengers. Crossover criticality in ionic solutions. *J. Chem. Phys.* **114**, 3133-3148, 2001. → *p. 33*
- [GC99] R. Garcia and M. H. W. Chan. Critical fluctuation-induced thinning of ^4He films near the superfluid transition. *Phys. Rev. Lett.* **83**, 1187, 1999. → *p. 1, 4, 5, 9, 10, 11, 17*
- [GC02] R. Garcia and M. H. W. Chan. Critical Casimir effect near the ^3He - ^4He tricritical point. *Phys. Rev. Lett.* **88**, 086101, 2002. → *p. 9*
- [GD08] Daniel Grüneberg and H. W. Diehl. Thermodynamic Casimir effects involving interacting field theories with zero modes. *Phys. Rev. B* **77**, 115409, 2008. → *p. 4, 12, 13*
- [GD10] Andrea Gambassi and S. Dietrich. Colloidal aggregation and critical Casimir forces. *Phys. Rev. Lett.* **105**, 059601, Jul 2010. → *p. 45*
- [GH04] Daniel Grüneberg and Alfred Hucht. Universal finite-size scaling analysis of Ising models with long-range interactions at the upper critical dimensionality: Isotropic case. *Phys. Rev. E* **69**, 036104, Mar 2004. → *p. 3, 7, 28, 29*
- [Gla63] R. J. Glauber. Time-dependent statistics of the Ising model. *J. Math. Phys.* **4**, 294, 1963. → *p. 24, 25*
- [GMH⁺09] A. Gambassi, A. Maciołek, C. Hertlein, U. Nellen, L. Helden, C. Bechinger, and S. Dietrich. Critical Casimir effect in classical binary liquid mixtures. *Phys. Rev. E* **80**, 061143, Dec 2009. → *p. 5*
- [Gol05] Ramin Golestanian. Fluctuation-induced forces in and out of equilibrium. *Pramana - Journal of physics* **64**, 1029, 2005. → *p. 1*
- [Grü03] Daniel Grüneberg. Untersuchung der kritischen Eigenschaften zweidimensionaler Isingmodelle mit langreichweitigen Wechselwirkungen: Theorie und Simulation. Diplomarbeit, Universität Duisburg-Essen, Campus Duisburg, 2003. → *p. 3*
- [GSGC06] A. Ganshin, S. Scheidemantel, R. Garcia, and M. H. W. Chan. Critical Casimir force in ^4He films: Confirmation of finite-size scaling. *Phys. Rev. Lett.* **97**, 075301, 2006. → *p. 4, 9, 11, 17*
- [HA12] Alfred Hucht and Sebastian Angst. Sheared Ising models in three dimensions. *EPL* **100**, 20003, Oct 2012. arXiv:1207.3970. → *p. 39, 40, 41, 42*
- [Has09a] Martin Hasenbusch. The Kosterlitz-Thouless transition in thin films: a Monte Carlo study of three-dimensional lattice models. *J. Stat. Mech.* **2009**, P02005, 2009. → *p. 11*

- [Has09b] Martin Hasenbusch. The thermodynamic Casimir effect in the neighbourhood of the lambda-transition: A Monte Carlo study of an improved three-dimensional lattice model. *J. Stat. Mech.* **2009**, P07031, 2009. arXiv:0905.2096. → p. 4, 12, 18
- [Has09c] Martin Hasenbusch. Yet another method to compute the thermodynamic Casimir force in lattice models. *Phys. Rev. E* **80**, 061120, 2009. arXiv:0908.3582. → p. 4, 12
- [Has10a] Martin Hasenbusch. Specific heat, internal energy, and the thermodynamic Casimir force in the neighbourhood of the lambda transition. *Phys. Rev. B* **81**, 165412, 2010. arXiv:0907.2847. → p. 4, 12, 18
- [Has10b] Martin Hasenbusch. Thermodynamic Casimir effect for films in the three-dimensional Ising universality class: Symmetry-breaking boundary conditions. *Phys. Rev. B* **82**, 104425, Sep 2010. arXiv:1005.4749. → p. 4, 12, 18
- [Has11] Martin Hasenbusch. Thermodynamic Casimir force: A Monte Carlo study of the crossover between the ordinary and the normal surface universality class. *Phys. Rev. B* **83**, 134425, Apr 2011. → p. 4, 18
- [Has12a] Martin Hasenbusch. private communication, 2012. → p. 11
- [Has12b] Martin Hasenbusch. Thermodynamic Casimir effect: Universality and corrections to scaling. *Phys. Rev. B* **85**, 174421, May 2012. → p. 4, 9, 10, 18
- [HD88] W. Huhn and V. Dohm. Possible resolution of the finite-size scaling problem in ^4He . *Phys. Rev. Lett.* **61**, 1368–1371, Sep 1988. → p. 4, 10
- [Hen99] M. Henkel. *Conformal Invariance and Critical Phenomena*. Texts and Monographs in Physics. Springer-Verlag, Berlin Heidelberg, 1999. → p. 35, 36
- [HGS11] Alfred Hucht, Daniel Grüneberg, and Felix M. Schmidt. Aspect-ratio dependence of thermodynamic Casimir forces. *Phys. Rev. E* **83**, 051101, Mar 2011. arXiv:1012.4399. → p. 4, 5, 6, 9, 12, 13, 14, 15, 18
- [HHG⁺08] C. Hertlein, L. Helden, A. Gambassi, S. Dietrich, and C. Bechinger. Direct measurement of critical Casimir forces. *Nature* **451**, 172, 2008. → p. 4, 45
- [Hil11] H. J. Hilhorst. Two interacting Ising chains in relative motion. *J. Stat. Mech.* **2011**, P04009, 2011. → p. 19, 28
- [Hin00] Haye Hinrichsen. Nonequilibrium critical phenomena and phase transitions into absorbing states. *Advances in Physics* **49**, 815, 2000. → p. 35
- [HLS75] R. M. Hornreich, M. Luban, and S. Shtrikman. Critical behavior at the onset of \mathbf{k} -space instability on the λ line. *Phys. Rev. Lett.* **35**, 1678, 1975. → p. 35, 37
- [Hob12] Hendrik Hobrecht. Monte-Carlo-Simulation von fluktuationsinduzierten Kräften. Bachelorarbeit, Universität Duisburg-Essen, 2012. → p. 45

-
- [HS01] M. Henkel and U. Schollwöck. Universal finite-size scaling amplitudes in anisotropic scaling. *J. Phys A: Math. Gen.* **34**, 3333, 2001. → *p.* 36
- [Huc02] Alfred Hucht. On the symmetry of universal finite-size scaling functions in anisotropic systems. *J. Phys A: Math. Gen.* **35**, L481, Aug 2002. → *p.* 2, 35, 36
- [Huc07] Alfred Hucht. Thermodynamic Casimir effect in ^4He films near T_λ : Monte Carlo results. *Phys. Rev. Lett.* **99**, 185301, Nov 2007. → *p.* 4, 8, 10, 11, 12, 17
- [Huc09] Alfred Hucht. Nonequilibrium phase transition in an exactly solvable driven Ising model with friction. *Phys. Rev. E* **80**, 061138, Dec 2009. → *p.* 19, 20, 23, 24, 25, 26, 27, 28, 29, 30, 31, 32, 33, 34, 36, 37, 41, 43
- [IK85] Tatsuhiro Imaeda and Kyozi Kawasaki. Dimensional reduction in phase-separating critical fluids under shear flow. *Prog. Theor. Phys.* **73**, 559, 1985. → *p.* 2, 19
- [Ind86] J. O. Indekeu. General discussion remark on the thickness of wetting layers at critical endpoints in Helium. *J. Chem. Soc. Faraday Trans. II* **82**, 1835–1838, 1986. → *p.* 4
- [IPT11] F. Igloi, M. Pleimling, and L. Turban. Nonequilibrium phase transition in a driven Potts model with friction. *Phys. Rev. E* **83**, 041110, 2011. → *p.* 19
- [Kad98] Dirk Kadau. Magnetische Beiträge zur Reibung. Diplomarbeit, Gerhard-Mercator-Universität – Gesamthochschule Duisburg, 1998. → *p.* 19
- [Kaw66] K. Kawasaki. Diffusion constants near the critical point for time-dependent Ising models. I. *Phys. Rev.* **145**, 224, 1966. → *p.* 24
- [KD91] M. Krech and S. Dietrich. Finite-size scaling for critical films. *Phys. Rev. Lett.* **66**, 345, 1991. [Erratum: **67**, 1055 (1991)]. → *p.* 17
- [KD92a] M. Krech and S. Dietrich. Free energy and specific heat of critical films and surfaces. *Phys. Rev. A* **46**, 1886, 1992. → *p.* 4, 12
- [KD92b] M. Krech and S. Dietrich. Specific heat of critical films, the Casimir force, and wetting films near critical end points. *Phys. Rev. A* **46**, 1922, 1992. → *p.* 10, 17
- [KG99] Mehran Kardar and Ramin Golestanian. The “friction” of vacuum, and other fluctuation-induced forces. *Rev. Mod. Phys.* **71**, 1233, 1999. → *p.* 4
- [KHW08] Dirk Kadau, Alfred Hucht, and Dietrich E. Wolf. Magnetic friction in Ising spin systems. *Phys. Rev. Lett.* **101**, 137205, Sep 2008. → *p.* 2, 19, 20, 21, 22, 30, 32
- [KLS83] Sheldon Katz, Joel L. Lebowitz, and H. Spohn. Phase transitions in stationary nonequilibrium states of model lattice systems. *Phys. Rev. B* **28**, 1655, 1983. → *p.* 19, 44

- [KLS04] Wooseop Kwak, D. P. Landau, and B. Schmittmann. Driven diffusive systems: How steady states depend on dynamics. *Phys. Rev. E* **69**, 066134, Jun 2004. → *p. 25*
- [KO11] Heike Kamerlingh Onnes. Further experiments with liquid Helium. C. On the change of electric resistance of pure metals at very low temperatures etc. IV. The resistance of pure Mercury at Helium temperatures. *Proc. K. Ned. Akad. Wet.* **13**, 1274, 1911. → *p. 1*
- [Kre94] M. Krech. *Casimir Effect in Critical Systems*. World Scientific, Singapore, 1994. → *p. 1, 4, 5, 6, 12*
- [KT73] J. M. Kosterlitz and D. J. Thouless. Ordering, metastability and phase transitions in two-dimensional systems. *J. Phys. C* **6**, 1181, 1973. → *p. 11*
- [KW41] H. A. Kramers and G. H. Wannier. Statistics of the two-dimensional ferromagnet. Part I. *Phys. Rev.* **60**, 252, 1941. → *p. 27, 30*
- [Lam97] S. K. Lamoreaux. Demonstration of the Casimir force in the 0.6 to $6\mu m$ range. *Phys. Rev. Lett.* **78**, 5–8, Jan 1997. *Phys. Rev. Lett.*, **81**, 5475 (1998) (Erratum), arXiv:1007.4276. → *p. 1*
- [LB95] E. Luijten and H. W. J. Blöte. Monte Carlo method for spin models with long-range interactions. *Int. J. Mod. Phys. C* **6**, 359, 1995. → *p. 3*
- [LB97] E. Luijten and H. W. J. Blöte. Classical critical behavior of spin models with long-range interactions. *Phys. Rev. B* **56**, 8945, 1997. → *p. 3*
- [LBB97] E. Luijten, H. W. J. Blöte, and K. Binder. Crossover scaling in two dimensions. *Phys. Rev. E* **56**, 6540, 1997. → *p. 33*
- [LK91] Hao Li and Mehran Kardar. Fluctuation-induced forces between rough surfaces. *Phys. Rev. Lett.* **67**, 3275, 1991. → *p. 4, 10, 11*
- [LK92] Hao Li and Mehran Kardar. Fluctuation-induced forces between manifolds immersed in correlated fluids. *Phys. Rev. A* **46**, 6490, 1992. → *p. 4*
- [Lon30] Fritz London. Zur Theorie und Systematik der Molekularkräfte. *Zeitschrift für Physik A Hadrons and Nuclei* **63**, 245-279, 1930. → *p. 1*
- [Mag08] Martin Magiera. Simulationen zur magnetischen Reibung. Diplomarbeit, Universität Duisburg-Essen, Campus Duisburg, 2008. → *p. 19*
- [MAHW11] Martin P. Magiera, Sebastian Angst, Alfred Hucht, and Dietrich E. Wolf. Magnetic friction: From Stokes to Coulomb behavior. *Phys. Rev. B* **84**, 212301, Dec 2011. → *p. 2, 19, 23, 43*
- [MBWN09] M. P. Magiera, L. Brendel, D. E. Wolf, and U. Nowak. Spin excitations in a monolayer scanned by a magnetic tip. *EPL* **87**, 26002 (6pp), 2009. → *p. 19, 22*
- [MGD07] A. Maciolek, A. Gambassi, and S. Dietrich. Critical Casimir effect in superfluid wetting films. *Phys. Rev. E* **76**, 031124, 2007. → *p. 4, 12*

-
- [MHH⁺12] Martin P. Magiera, Alfred Hucht, Haye Hinrichsen, Silvio R. Dahmen, and Dietrich E. Wolf. Magnetic vortices induced by a moving tip. *EPL* **100**, 27004, Oct 2012. arXiv:1207.3225. → p. 19
- [MN87] K. K. Mon and M. P. Nightingale. Critical surface free energies and universal finite-size scaling amplitudes of three-dimensional XY models by direct Monte Carlo sampling. *Phys. Rev. B* **35**, 3560–3562, Mar 1987. → p. 11
- [Mon85] K. K. Mon. Direct calculation of absolute free energy for lattice systems by Monte Carlo sampling of finite-size dependence. *Phys. Rev. Lett.* **54**, 2671–2673, Jun 1985. → p. 15
- [MR98] U. Mohideen and A. Roy. Precision measurement of the Casimir force from 0.1 to 0.9 μm . *Phys. Rev. Lett.* **81**, 4549–4552, Nov 1998. → p. 1, 2
- [MRR⁺53] N. Metropolis, A. W. Rosenbluth, M. N. Rosenbluth, A. H. Teller, and E. Teller. Equations of state calculations by fast computing machines. *J. Chem. Phys.* **21**, 1087, 1953. → p. 25
- [Müs11] Martin H. Müser. Velocity dependence of kinetic friction in the Prandtl-Tomlinson model. *Phys. Rev. B* **84**, 125419, Sep 2011. → p. 19
- [MW73] B. M. McCoy and T. T. Wu. *The Two-Dimensional Ising Model*. Harvard University Press, Cambridge, 1973. → p. 21, 27, 30, 31
- [MWBN09] M. P. Magiera, D. E. Wolf, L. Brendel, and U. Nowak. Magnetic friction and the role of temperature. *IEEE Trans. Magn.* **45**, 3938, 2009. → p. 19
- [NB99] M. E. J. Newman and G. T. Barkema. *Monte Carlo Methods in Statistical Mechanics*. Clarendon Press, Oxford, 1999. → p. 25
- [Ons44] L. Onsager. Crystal statistics. I. A two-dimensional model with an order-disorder transition. *Phys. Rev.* **65**, 117, 1944. → p. 27, 30
- [Onu97] Akira Onuki. Phase transitions of fluids in shear flow. *J. Phys: Condens. Matter* **9**, 6119–6157, 1997. → p. 19
- [PF83] V. Privman and M. E. Fisher. Finite-size effects at first-order transitions. *J. Stat. Phys.* **33**, 385, 1983. → p. 15
- [PF84] V. Privman and M. E. Fisher. Universal critical amplitudes in finite-size scaling. *Phys. Rev. B* **30**, 322, 1984. → p. 2
- [PH01] Michel Pleimling and Malte Henkel. Anisotropic scaling and generalized conformal invariance at Lifshitz points. *Phys. Rev. Lett.* **87**, 125702, 2001. → p. 35
- [Pra28] L. Prandtl. Ein Gedankenmodell zur kinetischen Theorie der festen Körper. *Zeitschrift für Angewandte Mathematik und Mechanik* **8**, 85–106, 1928. → p. 19

- [Pri90] V. Privman. Finite-size scaling theory. In V. Privman, editor, *Finite Size Scaling and Numerical Simulation of Statistical Systems*, chapter 1. World Scientific, Singapore, 1990. → p. 6
- [RZSA10] Joseph Rudnick, Roya Zandi, Aviva Shackell, and Douglas Abraham. Boundary conditions and the critical Casimir force on an Ising model film: Exact results in one and two dimensions. *Phys. Rev. E* **82**, 041118, Oct 2010. → p. 5
- [Sel88] Walter Selke. The ANNNI model — Theoretical analysis and experimental application. *Physics Reports* **170**, 213-264, 1988. → p. 35
- [SG09] G. P. Saracco and G. Gonnella. Monte Carlo study of the phase transition in the critical behavior of the Ising model with shear. *Phys. Rev. E* **80**, 051126, 2009. → p. 33, 34
- [Spa58] M. J. Sparnaay. Measurements of attractive forces between flat plates. *Physica* **24**, 751 - 764, 1958. → p. 1
- [SZ95] B. Schmittmann and R. K. P. Zia. Statistical mechanics of driven diffusive systems. In C. Domb and J. L. Lebowitz, editors, *Phase Transitions and Critical Phenomena*, volume 17. Academic Press, London, 1995. → p. 19, 35, 44
- [SZH⁺08] Florian Soyka, Olga Zvyagolskaya, Christopher Hertlein, Laurent Helden, and Clemens Bechinger. Critical Casimir forces in colloidal suspensions on chemically patterned surfaces. *Phys. Rev. Lett.* **101**, 208301, Nov 2008. → p. 45
- [Tay51] Geoffrey Taylor. Analysis of the swimming of microscopic organisms. *Proc. Roy. Soc. London A* **209**, 447, 1951. → p. 1
- [TD10] Francesco Parisen Toldin and S. Dietrich. Critical Casimir forces and adsorption profiles in the presence of a chemically structured substrate. *J. Stat. Mech.* **2010**, P11003, 2010. → p. 12
- [Tom29] G. A. Tomlinson. A molecular theory of friction. *Phil. Mag.* **7**, 905, 1929. → p. 19
- [vBS84] Henk van Beijeren and Lawrence S. Schulman. Phase transitions in lattice-gas models far from equilibrium. *Phys. Rev. Lett.* **53**, 806–809, Aug 1984. → p. 25
- [vdW73] J. D. van der Waals. *Over de continueit van de gas- en vloeistofoestand (On the continuity of the gaseous and liquid states)*. doctoral thesis, Leiden, 1873. → p. 1
- [VGMD07] O. Vasilyev, A. Gambassi, A. Maciołek, and S. Dietrich. Monte Carlo simulation results for critical Casimir forces. *EPL* **80**, 60009, 2007. → p. 4, 12
- [VGMD09] O. Vasilyev, A. Gambassi, A. Maciołek, and S. Dietrich. Universal scaling functions of critical Casimir forces obtained by Monte Carlo simulations. *Phys. Rev. E* **79**, 041142, 2009. → p. 4, 5, 12
- [Weg72] F. Wegner. Corrections to scaling laws. *Phys. Rev. B* **5**, 4529, 1972. → p. 10

-
- [Wol89] U. Wolff. Collective Monte Carlo updating for spin systems. *Phys. Rev. Lett.* **62**, 361, 1989. → *p.* [10](#)
- [Wol08] Wolfram Research, Inc. *Mathematica V7.0*. Champaign, Illinois, 2008. → *p.* [15](#)
- [WVHB10] D. Winter, P. Virnau, J. Horbach, and K. Binder. Finite-size scaling analysis of the anisotropic critical behavior of the two-dimensional Ising model under shear. *EPL* **91**, 60002, 2010. → *p.* [33](#)
- [YE66] W. M. Young and E. W. Elcock. Monte Carlo studies of vacancy migration in binary ordered alloys - I. *Proc. Phys. Soc. (London)* **89**, 735, 1966. → *p.* [26](#)
- [ZNL06] Chongshan Zhang, Kwangsik Nho, and D. P. Landau. Finite-size effects on the thermal resistivity of ^4He in the quasi-two-dimensional geometry. *Phys. Rev. B* **73**, 174508, 2006. → *p.* [10](#)
- [ZRK04] Roya Zandi, Joseph Rudnick, and Mehran Kardar. Casimir forces, surface fluctuations, and thinning of superfluid films. *Phys. Rev. Lett.* **93**, 155302, 2004. → *p.* [4](#), [10](#), [11](#)
- [ZSR⁺07] Roya Zandi, Aviva Shackell, Joseph Rudnick, Mehran Kardar, and Lincoln P. Chayes. Thinning of superfluid films below the critical point. *Phys. Rev. E* **76**, 030601, 2007. → *p.* [4](#), [12](#)

Publications

- [Huc02] Alfred Hucht. On the symmetry of universal finite-size scaling functions in anisotropic systems. *J. Phys A: Math. Gen.* **35**, L481, Aug 2002 (doi: [10.1088/0305-4470/35/31/103](https://doi.org/10.1088/0305-4470/35/31/103)) → Sec. 1.1
- [GH04] Daniel Grüneberg and Alfred Hucht. Universal finite-size scaling analysis of Ising models with long-range interactions at the upper critical dimensionality: Isotropic case. *Phys. Rev. E* **69**, 036104, Mar 2004 (doi: [10.1103/PhysRevE.69.036104](https://doi.org/10.1103/PhysRevE.69.036104)) → Sec. 1.1
[model, software, data analysis (with DG)]
- [Huc07] Alfred Hucht. Thermodynamic Casimir effect in ^4He films near T_λ : Monte Carlo results. *Phys. Rev. Lett.* **99**, 185301, Nov 2007 (doi: [10.1103/PhysRevLett.99.185301](https://doi.org/10.1103/PhysRevLett.99.185301)) → Sec. 2.4
- [KHW08] Dirk Kadau, Alfred Hucht, and Dietrich E. Wolf. Magnetic friction in Ising spin systems. *Phys. Rev. Lett.* **101**, 137205, Sep 2008 (doi: [10.1103/PhysRevLett.101.137205](https://doi.org/10.1103/PhysRevLett.101.137205)) → Sec. 3.2
[velocity dependence for large v , exact solution for small v]
- [CHG09] Denis Comtesse, Alfred Hucht, and Daniel Grüneberg. Thermodynamic Casimir effect in the large- n limit. Apr 2009. arXiv:0904.3661v2 → Sec. 2.6
[method, data analysis]
- [Huc09] Alfred Hucht. Nonequilibrium phase transition in an exactly solvable driven Ising model with friction. *Phys. Rev. E* **80**, 061138, Dec 2009 (doi: [10.1103/PhysRevE.80.061138](https://doi.org/10.1103/PhysRevE.80.061138)) → Sec. 3.4–3.7
- [HGS11] Alfred Hucht, Daniel Grüneberg, and Felix M. Schmidt. Aspect-ratio dependence of thermodynamic Casimir forces. *Phys. Rev. E* **83**, 051101, Mar 2011. arXiv:1012.4399 (doi: [10.1103/PhysRevE.83.051101](https://doi.org/10.1103/PhysRevE.83.051101)) → Sec. 2.5
[software, data analysis, two-dimensional solution, appendix A]
- [MAHW11] Martin P. Magiera, Sebastian Angst, Alfred Hucht, and Dietrich E. Wolf. Magnetic friction: From Stokes to Coulomb behavior. *Phys. Rev. B* **84**, 212301, Dec 2011 (doi: [10.1103/PhysRevB.84.212301](https://doi.org/10.1103/PhysRevB.84.212301)) → Sec. 3.3
[cross-over mechanism]
- [AHW12] Sebastian Angst, Alfred Hucht, and Dietrich E. Wolf. Strongly anisotropic nonequilibrium phase transition in Ising models with friction. *Phys. Rev. E* **85**, 051120, May 2012. arXiv:1201.1998 (doi: [10.1103/PhysRevE.85.051120](https://doi.org/10.1103/PhysRevE.85.051120)) → Sec. 3.8
[model, data analysis (with SA), cross-over scaling (with SA), field theory]

-
- [ADH⁺12] Sebastian Angst, Silvio R. Dahmen, Haye Hinrichsen, Alfred Hucht, and Martin P. Magiera. Explosive Ising. *J. Stat. Mech.* **2012**, L06002, Jun 2012. arXiv:1204.5196 (doi: [10.1088/1742-5468/2012/06/L06002](https://doi.org/10.1088/1742-5468/2012/06/L06002)) → Sec. 4
[cluster algorithm, hysteresis mechanism, conjecture]
- [DGH⁺12] H. W. Diehl, Daniel Grüneberg, Martin Hasenbusch, Alfred Hucht, Sergei B. Rutkevich, and Felix M. Schmidt. Exact thermodynamic Casimir forces for an interacting three-dimensional model system in film geometry with free surfaces. *EPL* **100**, 10004, Oct 2012. arXiv:1205.6613 (doi: [10.1209/0295-5075/100/10004](https://doi.org/10.1209/0295-5075/100/10004)) → Sec. 2.6
[model A: method, numerics, analysis, large- g limit (all with FMS and DG)]
- [HA12] Alfred Hucht and Sebastian Angst. Sheared Ising models in three dimensions. *EPL* **100**, 20003, Oct 2012. arXiv:1207.3970 (doi: [10.1209/0295-5075/100/20003](https://doi.org/10.1209/0295-5075/100/20003)) → Sec. 3.9
[model, data analysis (with SA)]
- [MHH⁺12] Martin P. Magiera, Alfred Hucht, Haye Hinrichsen, Silvio R. Dahmen, and Dietrich E. Wolf. Magnetic vortices induced by a moving tip. *EPL* **100**, 27004, Oct 2012. arXiv:1207.3225 (doi: [10.1209/0295-5075/100/27004](https://doi.org/10.1209/0295-5075/100/27004)) → Sec. 3
[model (with MPM)]

LETTER TO THE EDITOR

On the symmetry of universal finite-size scaling functions in anisotropic systems

Alfred Hucht

Theoretische Physik, Gerhard-Mercator-Universität, D-47048 Duisburg, Germany

E-mail: fred@thp.Uni-Duisburg.de

Received 20 May 2002

Published 26 July 2002

Online at stacks.iop.org/JPhysA/35/L481

Abstract

We postulate a symmetry of universal finite-size scaling functions under a certain anisotropic scale transformation, which connects the properties of a finite two-dimensional (2D) system at criticality with generalized aspect ratio $\rho > 1$ to a system with $\rho < 1$. The symmetry is formulated within a finite-size scaling theory and expressions for several universal amplitude ratios are derived. The predictions are confirmed within the exactly solvable weakly anisotropic 2D Ising model and are checked within the strongly anisotropic 2D dipolar in-plane Ising model using Monte Carlo simulations.

PACS numbers: 05.70.Fh, 75.40.Cx, 05.50.+q

The theory of universal finite-size scaling (UFSS) functions is a key concept in the modern understanding of continuous phase transitions [1–3]. In particular, it is known that the UFSS functions of a rectangular two-dimensional (2D) system of size $L_{\parallel} \times L_{\perp}$ depend on the aspect ratio L_{\parallel}/L_{\perp} [4]. For instance, in *isotropic* systems, the scaling function at criticality \bar{U}_c of the Binder cumulant $U = 1 - \frac{1}{3} \langle m^4 \rangle / \langle m^2 \rangle^2$ [5], where $\langle m^n \rangle$ is the n th moment of the order parameter, is known to be a universal function $\bar{U}_c(L_{\parallel}/L_{\perp})$ for a given boundary condition. This quantity has been investigated by several authors in the isotropic 2D Ising model with periodic boundary conditions [6, 7], while the influence of other boundary conditions on $\bar{U}_c(L_{\parallel}/L_{\perp})$ has recently been studied in [8, 9].

In *weakly anisotropic* systems, where the couplings are anisotropic ($J_{\parallel} \neq J_{\perp}$ in the 2D Ising case), the correlation length of the infinite system in direction $\mu = \parallel, \perp$ becomes anisotropic and scales like $\xi_{\mu}^{(\infty)}(t) \sim \hat{\xi}_{\mu} t^{-\nu}$ near criticality. ($t = (T - T_c)/T_c$ is the reduced temperature and we assume $t > 0$, without loss of generality.) This leads to a correlation length amplitude ratio $\hat{\xi}_{\parallel}/\hat{\xi}_{\perp}$ different from unity. The UFSS functions then depend on this ratio, i.e. $\bar{U}_c = \bar{U}_c(L_{\parallel}/L_{\perp}, \hat{\xi}_{\parallel}/\hat{\xi}_{\perp})$. However, isotropy can be restored asymptotically by an anisotropic scale transformation, where all lengths are rescaled with the corresponding correlation length amplitudes $\hat{\xi}_{\mu}$ [10–12]. Thus, the UFSS functions depend on L_{\parallel}/L_{\perp} and $\hat{\xi}_{\parallel}/\hat{\xi}_{\perp}$ only through the *reduced* aspect ratio $(L_{\parallel}/\hat{\xi}_{\parallel})/(L_{\perp}/\hat{\xi}_{\perp})$.

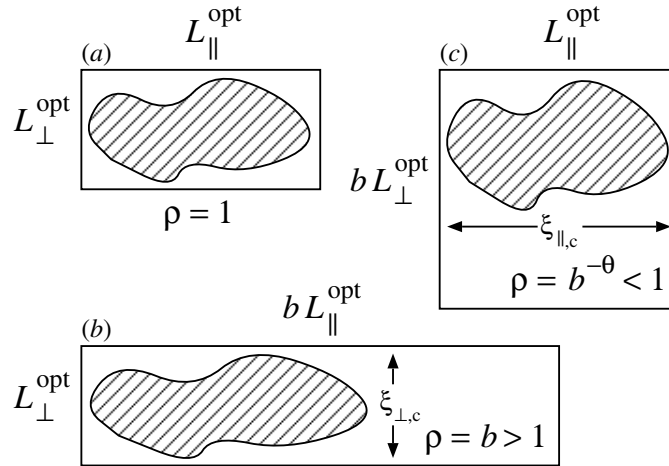


Figure 1. Three systems with different aspect ratio ρ (equation (2)) at criticality. In (a), the critical correlation volume $\xi_{\parallel,c}\xi_{\perp,c}$ (shaded area) spans the whole system, while in (b) and (c), correlations are limited by symmetric finite-size effects.

In *strongly anisotropic* systems, both the amplitudes $\hat{\xi}_{\mu}$ as well as the correlation length exponents ν_{μ} are different and the correlation length in direction μ scales like

$$\xi_{\mu}^{(\infty)}(t) \sim \hat{\xi}_{\mu} t^{-\nu_{\mu}}. \quad (1)$$

Examples for strongly anisotropic phase transitions are Lifshitz points [13] as present in the anisotropic next nearest neighbour Ising (ANNNI) model [14–16], or the non-equilibrium phase transition in the driven lattice gas model [17, 18]. Furthermore, in dynamical systems one can identify the \parallel -direction with time and the \perp -direction(s) with space [19], which in most cases give strongly anisotropic behaviour.

Using the same arguments as above, we conclude that UFSS functions of strongly anisotropic systems depend on the *generalized* reduced aspect ratio (cf [6])

$$\rho = L_{\parallel} L_{\perp}^{-\theta} / r_{\xi} \quad \text{with} \quad r_{\xi} = \hat{\xi}_{\parallel} \hat{\xi}_{\perp}^{-\theta} \quad (2)$$

being the *generalized* correlation length amplitude ratio, and with the anisotropy exponent $\theta = \nu_{\parallel} / \nu_{\perp}$ [19]. Up to now, no attempts have been made to describe the dependence of UFSS functions such as $\bar{U}_c(\rho)$ on the shape ρ of strongly anisotropic systems. In particular, it is not known if the anisotropy exponent θ can be determined from $\bar{U}_c(\rho)$. This problem is addressed in this work.

Consider a 2D strongly anisotropic finite system with periodic boundary conditions. When the critical point of the infinite system is approached from temperatures $t > 0$, the correlation lengths ξ_{μ} in the different directions μ are limited by the direction in which $\xi_{\mu}^{(\infty)}$ from equation (1) reaches the system boundary first [4]. For a given volume $N = L_{\parallel} L_{\perp}$, we define an ‘optimal’ shape $L_{\parallel}^{\text{opt}} \times L_{\perp}^{\text{opt}}$ at which both correlation lengths $\xi_{\mu}^{(\infty)}$ reach the system boundary simultaneously, i.e.

$$L_{\mu}^{\text{opt}} := \xi_{\mu}^{(\infty)}(t) \quad (3)$$

for some temperature $t > 0$ (figure 1(a)). We immediately find, using equations (1) and (2), that the optimal shape obeys $\rho_{\text{opt}} \equiv 1$ for all N , giving $L_{\parallel}^{\text{opt}} = r_{\xi} (L_{\perp}^{\text{opt}})^{\theta}$. A system of optimal shape should show the strongest critical fluctuations for a given volume N as the critical correlation volume $\xi_{\parallel,c} \xi_{\perp,c}$ spans the whole system.

At the optimal aspect ratio $\rho = 1$, the correlations are limited by both directions \parallel and \perp (figure 1(a)). If the system is enlarged by a factor $b > 1$ in the \parallel -direction (figure 1(b)), the correlation volume may relax into this direction but does not fill the whole system due to the limitation in the \perp -direction. A similar situation with exchanged roles occurs if the system is enlarged by a factor $b > 1$ in the \perp -direction (figure 1(c)). We now *assume* that systems (b) and (c) are similar in the scaling region $L_\mu^{\text{opt}} \rightarrow \infty$, i.e. their correlation volumes are asymptotically equal.

Hence, we can formulate a *symmetry hypothesis*: Consider a system with periodic boundary conditions and optimal aspect ratio $\rho = 1$ at the critical point. If this system is enlarged by a factor $b > 1$ in the \parallel -direction, it behaves asymptotically the same as if enlarged by *the same factor* b in the \perp -direction.

To formulate this hypothesis within a finite-size scaling theory, we consider a 2D strongly anisotropic system of size $L_\parallel \times L_\perp$ which fulfils the generalized hyperscaling relation $2 - \alpha = \nu_\parallel + \nu_\perp$ [6]. For our purpose, it is sufficient to focus on the critical point. The universal finite-size scaling *ansatz* [1–4, 6] for the singular part of the free energy density $f_c = F_{s,c}/(Nk_B T_c)$ reads [20]

$$f_c(L_\parallel, L_\perp) \sim \frac{b_\parallel b_\perp}{N} Y_c(b_\parallel, b_\perp) \quad (4)$$

with the scaling variables $b_\mu = \lambda^{\nu_\mu} L_\mu / \hat{\xi}_\mu$, where λ is a free-scaling parameter. The scaling function Y_c is universal for a given boundary condition, and all non-universal properties are contained in the metric factors $\hat{\xi}_\mu$. These metric factors occur due to the usual requirement that the relevant lengths are $L_\mu / \xi_\mu^{(\infty)}(t)$ near criticality and cannot be absorbed into λ in contrast to isotropic systems. For the three systems in figure 1, we set $\lambda = (L_\mu^{\text{opt}} / \hat{\xi}_\mu)^{-1/\nu_\mu}$ to get

$$f_c(L_\parallel^{\text{opt}}, L_\perp^{\text{opt}}) \sim \frac{1}{N} Y_c(1, 1) \quad (5a)$$

$$f_c(bL_\parallel^{\text{opt}}, L_\perp^{\text{opt}}) \sim \frac{b}{N} Y_c(b, 1) \quad (5b)$$

$$f_c(L_\parallel^{\text{opt}}, bL_\perp^{\text{opt}}) \sim \frac{b}{N} Y_c(1, b). \quad (5c)$$

The proposed symmetry hypothesis states that for $b > 1$, equations (5b) and (5c) are asymptotically equal in the scaling region where L_μ^{opt} is large,

$$f_c(bL_\parallel^{\text{opt}}, L_\perp^{\text{opt}}) \stackrel{b>1}{\sim} f_c(L_\parallel^{\text{opt}}, bL_\perp^{\text{opt}}). \quad (6)$$

Hence, the scaling function Y_c has the simple symmetry

$$Y_c(b, 1) \stackrel{b>1}{=} Y_c(1, b). \quad (7)$$

To rewrite Y_c as a function of the generalized aspect ratio ρ (equation (2)), instead of the quantities b_μ , we set $b_\perp = 1$ in system (c) and get, as then $\lambda = (bL_\perp^{\text{opt}} / \hat{\xi}_\perp)^{-1/\nu_\perp}$,

$$f_c(L_\parallel^{\text{opt}}, bL_\perp^{\text{opt}}) \sim \frac{b^{-\theta}}{N} Y_c(b^{-\theta}, 1). \quad (8)$$

Equations (5c) and (8) are identical and we conclude that $bY_c(1, b) = b^{-\theta}Y_c(b^{-\theta}, 1)$. At this point, it is convenient to define the scaling function $\bar{Y}_c(b) = bY_c(b, 1)$ which fulfils

$$f_c(L_\parallel, L_\perp) \sim \frac{1}{N} \bar{Y}_c(\rho). \quad (9)$$

For this scaling function, the symmetry reads

$$\bar{Y}_c(\rho) \stackrel{\rho \geq 1}{=} \bar{Y}_c(\rho^{-\theta}). \quad (10)$$

We see from equation (9) that the critical free energy density f_c is a universal function of the reduced aspect ratio $\rho = L_{\parallel} L_{\perp}^{-\theta} / r_{\xi}$ without any non-universal prefactor, and that at criticality, *all* system specific properties are contained in the non-universal ratio r_{ξ} from equation (2).

Ansatz equation (4) can also be made for the inverse spin–spin correlation length at criticality [20]

$$\xi_{\mu,c}^{-1}(L_{\parallel}, L_{\perp}) \sim \frac{b_{\mu}}{L_{\mu}} X_{\mu,c}(b_{\parallel}, b_{\perp}). \quad (11)$$

The proposed symmetry gives $X_{\mu,c}(b, 1) \stackrel{b \geq 1}{=} X_{\bar{\mu},c}(1, b)$, where $\bar{\mu}$ denotes the direction perpendicular to μ . Hence, the correlation volumes $\xi_{\parallel,c} \xi_{\perp,c}$ of systems (b) and (c) in figure 1 are indeed equal as assumed above and become $\xi_{\parallel,c} \xi_{\perp,c} \sim \frac{N}{b} X_{\parallel,c}^{-1}(b, 1) X_{\perp,c}^{-1}(b, 1)$.

The correlation length amplitudes A_{ξ}^{μ} in cylindrical geometry ($b_{\mu} \rightarrow \infty, b_{\bar{\mu}} = 1$), which can be calculated exactly for many isotropic two-dimensional models within the theory of conformal invariance [21], generalize to the strongly anisotropic form [3]

$$A_{\xi}^{\mu} = \lim_{L_{\bar{\mu}} \rightarrow \infty} L_{\bar{\mu}}^{-\nu_{\mu}/\nu_{\bar{\mu}}} \lim_{L_{\mu} \rightarrow \infty} \xi_{\mu,c}(L_{\parallel}, L_{\perp}). \quad (12)$$

Inserting equation (11), they become

$$A_{\xi}^{\parallel} = r_{\xi} X_{\parallel,c}^{-1}(\infty, 1) \quad A_{\xi}^{\perp} = r_{\xi}^{-1/\theta} X_{\perp,c}^{-1}(1, \infty) \quad (13)$$

which shows that in general A_{ξ}^{μ} is not universal. The symmetry hypothesis states that both limits of the scaling function $X_{\mu,c}$ are equal. Denoting this universal limit by $A_{\xi} := X_{\parallel,c}^{-1}(\infty, 1) = X_{\perp,c}^{-1}(1, \infty)$, we obtain $A_{\xi}^{\parallel} = r_{\xi} A_{\xi}$ and $A_{\xi}^{\perp} = r_{\xi}^{-1/\theta} A_{\xi}$ as well as the amplitude relations

$$A_{\xi}^{1+\theta} = A_{\xi}^{\parallel} (A_{\xi}^{\perp})^{\theta} \quad \frac{A_{\xi}^{\parallel}}{A_{\xi}^{\perp}} = r_{\xi}^{1+1/\theta}. \quad (14)$$

These predictions can be checked within the exactly solved weakly anisotropic 2D Ising model with different couplings J_{\parallel} and J_{\perp} , where the paramagnetic correlation length reads $\xi_{\mu}^{(\infty)}(t) = (\log \coth(\beta J_{\mu}) - 2\beta J_{\bar{\mu}})^{-1}$ with $\beta = 1/k_B T$ [22]. The amplitude ratio r_{ξ} at the critical point $\sinh(2\beta_c J_{\parallel}) \sinh(2\beta_c J_{\perp}) = 1$ [22] becomes $r_{\xi} = \sinh(2\beta_c J_{\parallel})$ [23]. On the other hand, the inverse correlation length amplitudes in cylinder geometry, equation (12), have been calculated [24] to give $A_{\xi}^{\mu} = \frac{4}{\pi} \sinh(2\beta_c J_{\mu})$, which immediately yields equations (13) if we insert the well-known universal value $A_{\xi} = 4/\pi$ [21, 25]. The left relation of equations (14) has already been derived for several weakly anisotropic models, where it simplifies to $A_{\xi}^2 = A_{\xi}^{\parallel} A_{\xi}^{\perp}$ [24, equation (7)].

To check the symmetry numerically in strongly anisotropic systems, we now focus on the Binder cumulant U . The scaling *ansatz* at criticality equation (4) becomes

$$U_c(L_{\parallel}, L_{\perp}) \sim \frac{1}{b_{\parallel} b_{\perp}} \tilde{U}_c(b_{\parallel}, b_{\perp}) = \bar{U}_c(\rho) \quad (15)$$

with the scaling function $\bar{U}_c(b) = \tilde{U}_c(b, 1)/b$, and the calculation is completely analogous to the free-energy case. The symmetry hypothesis for the cumulant scaling functions \tilde{U}_c and \bar{U}_c thus reads (cf equations (7) and (10))

$$\tilde{U}_c(b, 1) \stackrel{b \geq 1}{=} \tilde{U}_c(1, b) \quad \bar{U}_c(\rho) \stackrel{\rho \geq 1}{=} \bar{U}_c(\rho^{-\theta}). \quad (16)$$

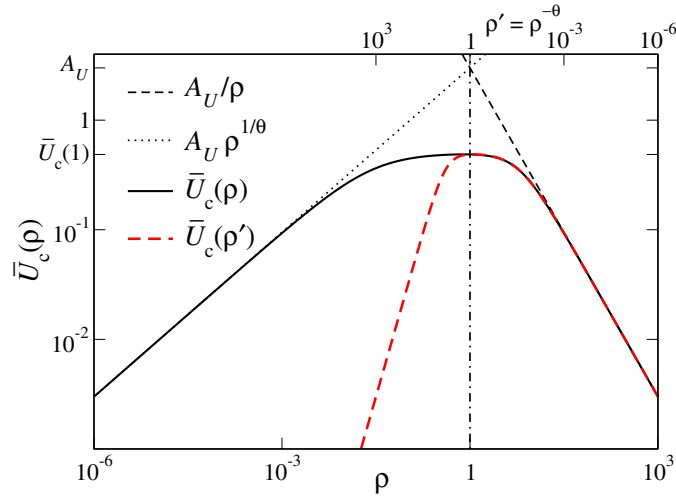


Figure 2. Sketch of critical cumulant scaling functions $\bar{U}_c(\rho)$ and $\bar{U}_c(\rho')$ with $\rho' = \rho^{-\theta}$ for assumed anisotropy exponent $\theta = 2$. We have $\bar{U}_c(\rho \gg 1) \sim A_U/\rho$ and $\bar{U}_c(\rho \ll 1) \sim A_U\rho^{1/\theta}$. For $\rho > 1$ $\bar{U}_c(\rho)$ fulfils $\bar{U}_c(\rho) = \bar{U}_c(\rho')$.

The generalization of the cumulant amplitude A_U^μ [5, 26] to strongly anisotropic systems is similar to equation (12) and gives

$$A_U^\mu = \lim_{L_\mu \rightarrow \infty} L_\mu^{-\nu_\mu/\nu_\rho} \lim_{L_\perp \rightarrow \infty} L_\mu U_c(L_\parallel, L_\perp). \tag{17}$$

Inserting the scaling *ansatz* equation (15) we now find

$$A_U^\parallel = r_\xi \tilde{U}_c(\infty, 1) \quad A_U^\perp = r_\xi^{-1/\theta} \tilde{U}_c(1, \infty) \tag{18}$$

which again are, in general, not universal. Using the symmetry hypothesis, we can define $A_U := \tilde{U}_c(\infty, 1) = \tilde{U}_c(1, \infty)$ and get $A_U^\parallel = r_\xi A_U$, $A_U^\perp = r_\xi^{-1/\theta} A_U$ as well as the identities (cf equations (14))

$$A_U^{1+\theta} = A_U^\parallel (A_U^\perp)^\theta \quad \frac{A_U^\parallel}{A_U^\perp} = r_\xi^{1+1/\theta}. \tag{19}$$

The cumulant scaling function $\bar{U}_c(\rho)$ must be extremal at $\rho = 1$ due to symmetry. Furthermore, as a deviation from the optimal aspect ratio $\rho = 1$ reduces the cumulant, it has a maximum at this point [6]. A sketch of $\bar{U}_c(\rho)$ for an assumed anisotropy exponent $\theta = 2$ is depicted in figure 2. For $\rho > 1$, both $\bar{U}_c(\rho)$ and $\bar{U}_c(\rho' = \rho^{-\theta})$ collapse onto a single curve, reflecting the proposed symmetry. It is obvious from figure 2 that $\bar{U}_c(\rho)$ (and thus, also $\bar{Y}_c(\rho)$ from equation (10)) cannot be analytic at $\rho = 1$ in strongly anisotropic systems, as the two branches $\bar{U}_c(\rho)$ and $\bar{U}_c(\rho')$ identical for $\rho > 1$ fork at $\rho = 1$ [20]. On the other hand, $\bar{Y}_c(\rho)$ and $\bar{U}_c(\rho)$ can be analytic at $\rho = 1$ if the anisotropy exponent $\theta = 1$, as in the case of the isotropic 2D Ising model [27, equation (3.37)].

To check the symmetry hypothesis in a strongly anisotropic system, I performed Monte Carlo simulations of the two-dimensional dipolar in-plane Ising model [20]

$$\mathcal{H} = -\frac{J}{2} \sum_{\langle ij \rangle} \sigma_i \sigma_j + \frac{\omega}{2} \sum_{i \neq j} \frac{(r_{ij}^\perp)^2 - 2(r_{ij}^\parallel)^2}{|\vec{r}_{ij}|^5} \sigma_i \sigma_j \tag{20}$$

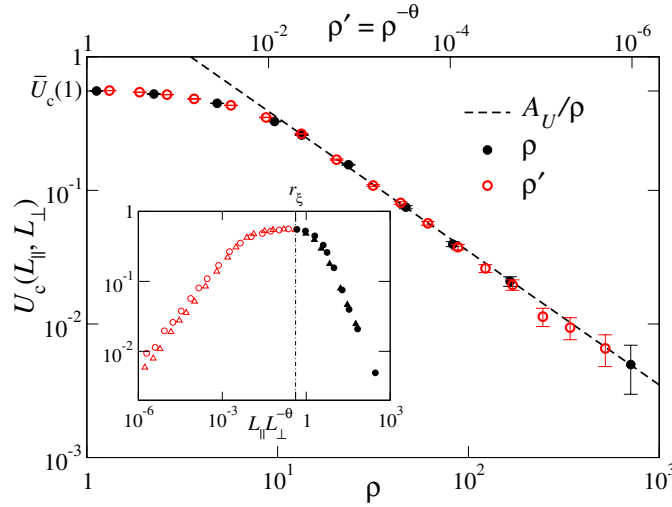


Figure 3. Cumulant $U_c(L_{\parallel}, L_{\perp})$ of the dipolar in-plane Ising model (equation (20)) for dipole strength $\omega/J = 0.1$ and system size $N = 43\,200$ at the critical point $k_B T_c/J = 2.764(1)$. The data points collapse for $\rho > 1$ if we set $\theta = 2.1(3)$ and $r_{\xi} = 0.415(40)$, giving the universal amplitudes $\bar{U}_c(1) = 0.555(5)$ and $A_U = 3.5(2)$. The inset shows U_c as a function of the non-reduced generalized aspect ratio $L_{\parallel} L_{\perp}^{-\theta}$ for system size $N = 43\,200$ (circles) and $N = 4320$ (triangles).

with spin variables $\sigma = \pm 1$, ferromagnetic nearest neighbour exchange interaction $J > 0$ and dipole interaction $\omega > 0$. The distance $\vec{r}_{ij} = (r_{ij}^{\parallel}, r_{ij}^{\perp})$ between spins σ_i and σ_j is decomposed into contributions parallel and perpendicular to the spin axis. In the simulations, the Wolff cluster algorithm [28] for long-range systems proposed by Luijten and Blöte [29] was used, modified to anisotropic interactions. In contrast to earlier work [30, 31] using renormalization group techniques, it is found that this model shows a strongly anisotropic phase transition. The details of the simulations will be published elsewhere [20].

After T_c was determined, systems with constant volume $N = L_{\parallel} L_{\perp}$ were simulated, which was chosen to have a large number of divisors in order to get many different aspect ratios (e.g., $N = 2^6 3^3 5^2 = 43\,200$ has 84 divisors). The resulting critical cumulant $U_c(L_{\parallel} L_{\perp}^{-\theta})$ for two different volumes $N = 4320, 43\,200$ is depicted in the inset of figure 3. As expected, both curves have the same maximum value $\bar{U}_c(1) = 0.555(5)$ at criticality. With variation of θ , the curves are shifted horizontally and collapse for $\theta = 2.1(3)$, with maximum at $r_{\xi} = 0.415(40)$. To check the proposed symmetry, we fold the left branch with $\rho < 1$ (open symbols) to the right and rescale the ρ -axis with θ . The resulting data collapse for $\rho > 1$ is shown in figure 3. This collapse and the additional condition that both curves must go to zero as A_U/ρ allows a precise determination of θ and r_{ξ} as well as of the universal amplitude $A_U = 3.5(2)$.

In conclusion, I postulate a symmetry of universal finite-size scaling functions under a certain anisotropic scale transformation and generalize the Privman–Fisher equations [1] to strongly anisotropic phase transitions on rectangular lattices at criticality. It turns out that for a given boundary condition, the only relevant variable is the generalized reduced aspect ratio $\rho = L_{\parallel} L_{\perp}^{\theta}/r_{\xi}$ and that, e.g., the free energy scaling function equation (9) obeys the symmetry $\bar{Y}_c(\rho) \stackrel{\rho > 1}{=} \bar{Y}_c(\rho^{-\theta})$. At criticality, the free energy density f_c , the inverse correlation lengths $\xi_{\mu,c}$ and the Binder cumulant U_c are universal functions of ρ , without a non-universal prefactor. All system specific properties are contained in the non-universal correlation length amplitude ratio r_{ξ} (equation (2)).

The generalization to higher dimensions is straightforward [20], an interesting application would be the precise determination of the exponent θ at the Lifshitz point of the three-dimensional ANNNI model [15, 16]. An open question is the validity of the proposed symmetry in non-equilibrium systems with appropriate boundary conditions, which have recently been shown to exhibit Privman–Fisher universality [3].

Acknowledgments

I thank Sven Lübeck and Erik Luijten for valuable discussions and Malte Henkel for a critical reading of the manuscript. This work was supported by the Deutsche Forschungsgemeinschaft through SFB 491.

References

- [1] Privman V and Fisher M E 1994 *Phys. Rev. B* **30** 322
- [2] Privman V 1990 *Finite Size Scaling and Numerical Simulation of Statistical Systems* ed V Privman (Singapore: World Scientific) ch 1
- [3] Henkel M and Schollwöck U 2001 *J. Phys. A: Math. Gen.* **34** 3333
- [4] Binder K 1990 *Finite Size Scaling and Numerical Simulation of Statistical Systems* ed V Privman (Singapore: World Scientific) ch 4
- [5] Binder K 1981 *Z. Phys. B* **43** 119
- [6] Binder K and Wang J-S 1989 *J. Stat. Phys.* **55** 87
- [7] Kamieniarz G and Blöte H W J 1993 *J. Phys. A: Math. Gen.* **26** 201
- [8] Okabe Y, Kaneda K, Kikuchi M and Hu C-K 1999 *Phys. Rev. E* **59** 1585
- [9] Kaneda K and Okabe Y 2001 *Phys. Rev. Lett.* **86** 2134
- [10] Landau D P and Swendsen R H 1984 *Phys. Rev. B* **30** 2787
- [11] Indekeu J O, Nightingale M P and Wang W V 1986 *Phys. Rev. B* **34** 330
- [12] Yurishchev M A 1997 *Phys. Rev. E* **55** 3915
- [13] Hornreich R M, Luban M and Shtrikman S 1975 *Phys. Rev. Lett.* **35** 1678
- [14] Selke W 1992 *Phase Transitions and Critical Phenomena* vol 15, ed C Domb and M S Green (London: Academic)
- [15] Diehl H W and Shpot M 2000 *Phys. Rev. B* **62** 12338
- [16] Pleimling M and Henkel M 2001 *Phys. Rev. Lett.* **87** 125702
- [17] Katz S, Lebowitz J L and Spohn H 1983 *Phys. Rev. B* **28** 1655
- [18] Schmittmann B and Zia R K P 1995 *Phase Transitions and Critical Phenomena* vol 17, ed C Domb and J L Lebowitz (London: Academic)
- [19] Henkel M 1999 *Conformal Invariance and Critical Phenomena (Texts and Monographs in Physics)* (Berlin: Springer)
- [20] Hucht A 2002 in preparation
- [21] Cardy J 1984 *J. Phys. A: Math. Gen.* **17** L385
- [22] Onsager L 1944 *Phys. Rev.* **65** 117
- [23] Zia R K P and Avron J E 1982 *Phys. Rev. B* **25** 2042
- [24] Nightingale P and Blöte H 1983 *J. Phys. A: Math. Gen.* **16** L657
- [25] Luck J M 1982 *J. Phys. A: Math. Gen.* **15** L169
- [26] Burkhardt T W and Derrida B 1985 *Phys. Rev. B* **32** 7273
- [27] Ferdinand A E and Fisher M E 1969 *Phys. Rev.* **185** 832
- [28] Wolff U 1989 *Phys. Rev. Lett.* **62** 361
- [29] Luijten E and Blöte H W J 1995 *Int. J. Mod. Phys. C* **6** 359
- [30] De’Bell K and Geldart D J W 1989 *Phys. Rev. B* **39** 743
- [31] Bulenda M, Täuber U C and Schwabl F 2000 *J. Phys. A: Math. Gen.* **33** 1

Universal finite-size scaling analysis of Ising models with long-range interactions at the upper critical dimensionality: Isotropic case

Daniel Grüneberg* and Alfred Hucht†

Fakultät für Naturwissenschaften, Theoretische Physik, Universität Duisburg-Essen, D-47048 Duisburg, Germany

(Received 10 October 2003; published 9 March 2004)

We investigate a two-dimensional Ising model with long-range interactions that emerge from a generalization of the magnetic dipolar interaction in spin systems with in-plane spin orientation. This interaction is, in general, anisotropic whereby in the present work we focus on the isotropic case for which the model is found to be at its upper critical dimensionality. To investigate the critical behavior the temperature and field dependence of several quantities are studied by means of Monte Carlo simulations. On the basis of the Privman-Fisher hypothesis and results of the renormalization group the numerical data are analyzed in the framework of a finite-size scaling analysis and compared to finite-size scaling functions derived from a Ginzburg-Landau-Wilson model in zero mode (mean-field) approximation. The obtained excellent agreement suggests that at least in the present case the concept of universal finite-size scaling functions can be extended to the upper critical dimensionality.

DOI: 10.1103/PhysRevE.69.036104

PACS number(s): 05.50.+q, 05.70.Fh, 75.10.Hk, 89.75.Da

I. INTRODUCTION

In the last decade, spin models with long-range interactions were the subject of several extensive Monte Carlo studies. Utilizing an efficient cluster algorithm [1] these studies were addressed to the verification of some unproved predictions on the critical behavior of spin models with algebraically decaying long-range interactions [2]. Furthermore, the crossover from Ising-like to classical critical behavior was investigated [3,4] and first numerical results on the critical behavior of the dipolar in-plane Ising (DIPI) model were obtained [5]. This two-dimensional model displays a strongly anisotropic phase transition, i.e., the correlation lengths in direction parallel and perpendicular to spin orientation diverge in the infinite system (let $t > 0$) as [5]

$$\xi_{\parallel}^{(\infty)}(t) \sim \hat{\xi}_{\parallel} t^{-\nu_{\parallel}}, \quad \xi_{\perp}^{(\infty)}(t) \sim \hat{\xi}_{\perp} t^{-\nu_{\perp}} \quad (1)$$

at the critical point, where both $\hat{\xi}_{\parallel} \neq \hat{\xi}_{\perp}$ and $\nu_{\parallel} \neq \nu_{\perp}$, and $t \equiv (T - T_c)/T_c$ denotes the reduced temperature. Except the anisotropy exponent $\theta = \nu_{\parallel}/\nu_{\perp}$ neither any numerical estimates of the critical exponents exist for the DIPI model, nor is it clear whether the model exhibits Lifshitz type critical behavior [6] as it is observed, e.g., in the anisotropic next nearest neighbor Ising model [7–9].

To address such questions in a broader context we present a two-dimensional long-range spin model that arises from generalizing the DIPI model by introducing an additional parameter. Assuming $L_{\parallel} \times L_{\perp}$ geometry and periodic boundary conditions this model is described by the Hamiltonian

$$\mathcal{H} = -\frac{1}{2} \sum_{i \neq j} s_i J(\mathbf{r}_{ij}) s_j - B \sum_i s_i \quad (2a)$$

with magnetic Ising spin variables $s_i = \pm 1$, the spin-spin distance vector \mathbf{r}_{ij} , and an external field B . The pair coupling $J(\mathbf{r})$ is given by

$$J(\mathbf{r}) = J \delta_{|\mathbf{r}|,1} + \frac{\omega_{\parallel} r_{\parallel}^2 + \omega_{\perp} r_{\perp}^2}{|\mathbf{r}|^5} \quad (2b)$$

and consists of both a ferromagnetic short-range nearest neighbor exchange coupling with the coupling constant $J \geq 0$ and a long-range contribution, where r_{\parallel} and r_{\perp} are the components of the vector \mathbf{r} parallel and perpendicular to spin orientation. Using this general form of the pair coupling $J(\mathbf{r})$, several well known spin systems can be mapped onto this model by making an explicit choice of the parameters ω_{\parallel} , ω_{\perp} , and J . With $\omega_{\parallel} = -2\omega_{\perp} > 0$, and for symmetry reasons $-2\omega_{\parallel} = \omega_{\perp} > 0$, and $J > 0$ the DIPI model is recovered, and if $\omega_{\parallel} = \omega_{\perp} > 0$ and $J = 0$ Eq. (2a) corresponds to an Ising model with an isotropic ferromagnetic long-range interaction algebraically decaying as $J(\mathbf{r}) \propto |\mathbf{r}|^{-3}$. Another special case is the dipolar Ising model with perpendicular spin orientation [10,11] that can be obtained for $\omega_{\parallel} = \omega_{\perp} < 0$ and $J > 0$.

Figure 1 shows the ground state phase diagram of the model whereby we took into account four different ground state spin configurations: the *ferromagnetic state* where all spins point to the same direction (fm), the *totally antiferromagnetic state* that is referred to as checkerboard state (check), and *commensurate stripe domain states* with a domain wall orientation parallel (mod \parallel) and perpendicular (mod \perp) to spin orientation and the periods $N_{\parallel, \perp}$. Dependent on the values of the quotients ω_{\parallel}/J and ω_{\perp}/J all considered spin configurations were found as stable ground states. Due to symmetry reasons the arrangement of the corresponding phases in Fig. 1 is symmetric with respect to the line $\omega_{\parallel} = \omega_{\perp}$. The periods $N_{\parallel, \perp}$ of the stripe domain states diverge when approaching the dashed lines in Fig. 1.

The region in parameter space where the model displays a ferromagnetic ground state is of particular interest to us. In that region the observed phase transitions are isotropic (an-

*Electronic address: daniel@thp.Uni-Duisburg.de

†Electronic address: fred@thp.Uni-Duisburg.de

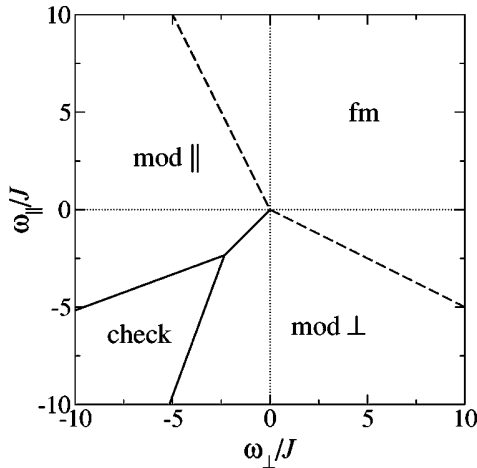


FIG. 1. The model [Eqs. (2)] exhibits a ferromagnetic ground state in the region denoted by “fm.” The dashed lines $\omega_{\parallel} = -2\omega_{\perp} > 0$ and $-2\omega_{\parallel} = \omega_{\perp} > 0$, respectively, and the origin $\omega_{\parallel} = \omega_{\perp} = 0$ also represent ferromagnetic ground states. All other regions correspond to modulated spin configurations (see text).

isotropic) when $\omega_{\parallel} = \omega_{\perp}$ ($\omega_{\parallel} \neq \omega_{\perp}$) whereby in the present work we draw our attention to the isotropic ferromagnetic long-range case

$$\omega_{\parallel} = \omega_{\perp} > 0, \quad J = 0 \quad (3)$$

before we turn to the case of an anisotropic pair coupling [12]. It is known that the upper critical dimension of long-range spin models with ferromagnetic interactions decaying as $J(\mathbf{r}) \propto |\mathbf{r}|^{-(d+\sigma)}$ is given by $d_u = 2\sigma$ [13]. Comparison with the pair coupling $J(\mathbf{r})$ defined in Eq. (2b) yields in the isotropic case, Eq. (3), $\sigma = 1$ for a two-dimensional system and consequently $d = d_u = 2$.

So in this paper we investigate the critical behavior of the model at its borderline dimensionality d_u by means of Monte Carlo (MC) simulations and finite-size scaling methods. For that purpose in the following Sec. II the finite-size scaling form of the free energy density is discussed and the finite-size scaling relations of the considered quantities are derived as they are used for the finite-size scaling analysis. These relations define finite-size scaling functions for which in Sec. III we evaluate analytical expressions in the framework of the so-called zero mode theory that is based on the Ginzburg-Landau-Wilson (GLW) model. In the last Sec. IV the zero mode results are compared to numerical data within a finite-size scaling analysis.

II. FINITE-SIZE SCALING RELATIONS

To study the critical properties of the model in the isotropic long-range case we have carried out a finite-size scaling analysis of MC data. This analysis requires the finite-size scaling relations of the quantities that were considered in the simulations.

Via a renormalization group approach, Luijten and Blöte [2] derived the scaling form of the free energy density of $O(n)$ spin models with ferromagnetic long-range interac-

tions decaying as $J(\mathbf{r}) \propto |\mathbf{r}|^{-(d+\sigma)}$. At the upper critical dimension, that is given by $d_u = 2$ for $\sigma = 1$ (see Sec. I), the singular part of the reduced free energy density was found to scale as ($n = 1$)

$$f_s(t, h; L) \sim L^{-2} \tilde{f} \left(u^{-1/3} L \ln^{1/6} \left(\frac{L}{L'_0} \right) \right) \times \left[t - v' L^{-1} \ln^{-2/3} \left(\frac{L}{L'_0} \right) \right], L^{3/2} \ln^{1/4} \left(\frac{L}{L'_0} \right) h \quad (4)$$

with the reduced temperature t , the reduced external field $h \equiv \beta B$ where $\beta \equiv 1/(k_B T)$ denotes the inverse temperature (we set $k_B = 1$ throughout this paper), and the so-called dangerous irrelevant variable u [14,15]. Note that we rewrote the formula given in Ref. [2] in terms of the parameters v' and L'_0 , where L'_0 can be regarded as a reference length that fixes the length scale in the logarithms (see also Ref. [16]), and we absorbed constant factors into \tilde{f} . The symbol \sim means “asymptotically equal” and, unless stated otherwise, refers to the limit $(t, h, L) \rightarrow (0, 0, \infty)$ with $tL \ln^{1/6}(L)$ and $hL^{3/2} \ln^{1/4}(L)$ fixed [cf. Eq. (7)].

Proceeding from Eq. (4) we adapt the Privman-Fisher hypothesis [17] and propose the finite-size scaling form of the singular part of the reduced free energy density

$$f_s(t, h; L) \sim L^{-2} Y(x_{\text{rg}}, y_{\text{rg}}) \quad (5)$$

with the universal finite-size scaling (UFSS) function $Y(x, y)$. The arguments of this function correspond to the temperature scaling variable

$$x_{\text{rg}} = C_1 \hat{t} L \ln^{1/6} \left(\frac{L}{L'_0} \right) \quad (6a)$$

with the shifted reduced temperature

$$\hat{t} = t - v L^{-1} \ln^{-2/3} \left(\frac{L}{L'_0} \right), \quad (6b)$$

and the field scaling variable

$$y_{\text{rg}} = C_2 h L^{3/2} \ln^{1/4} \left(\frac{L}{L'_0} \right), \quad (6c)$$

whereby C_1 and C_2 are nonuniversal metric factors. Let us note that we have replaced the constants v' and L'_0 which arise from the renormalization group by the constants v and L_0 that will be used as fit parameters in the finite-size scaling analysis.

It is also important to point out that the terms that result from v and L_0 in the temperature scaling variable x_{rg} and the field scaling variable y_{rg} are merely corrections since they do not contribute to the leading orders in the expansions

$$\hat{t}L \ln^{1/6} \left(\frac{L}{L_0} \right)^{L \rightarrow \infty} = tL \ln^{1/6}(L) + vO(\ln^{-1/2}(L)) \\ + tL \ln(L_0)O(\ln^{-5/6}(L)), \quad (7a)$$

$$hL^{3/2} \ln^{1/4} \left(\frac{L}{L_0} \right)^{L \rightarrow \infty} = hL^{3/2} \ln^{1/4}(L) + hL^{3/2} \ln(L_0)O(\ln^{-3/4}(L)). \quad (7b)$$

However, due to the slow convergence of the logarithms appearing at the upper critical dimension these corrections are substantial for the quality of the data collapse in the finite-size scaling analysis, as will be discussed in Sec. IV [see also Sec. IV(B) in Ref. [2], and Ref. [16]].

In the following we derive the finite-size scaling forms of the quantities that were considered in the simulations. Let

$$\bar{s} = \frac{1}{L^d} \sum_{j=1}^{L^d} s_j \quad (8)$$

denote the average of the spin variables s_j , these quantities are the magnetization $m(t, h; L) = \langle \bar{s} \rangle$ and the susceptibility $\chi(t, h; L) = \beta L^d (\langle \bar{s}^2 \rangle - \langle \bar{s} \rangle^2)$, whose finite-size scaling forms can be obtained by taking derivatives of the singular part of the reduced free energy density, Eq. (5), according to

$$m(t, h; L) = - \frac{\partial}{\partial h} f_s(t, h; L) \sim C_2 L^{-1/2} \ln^{1/4} \left(\frac{L}{L_0} \right) Y_m(x_{\text{rg}}, y_{\text{rg}}), \quad (9a)$$

$$\beta^{-1} \chi(t, h; L) = - \frac{\partial^2}{\partial h^2} f_s(t, h; L) \\ \sim C_2^2 L \ln^{1/2} \left(\frac{L}{L_0} \right) Y_\chi(x_{\text{rg}}, y_{\text{rg}}). \quad (9b)$$

We also consider the dimensionless Binder cumulant [18] $U(t; L) = 1 - \langle \bar{s}^4 \rangle / (3 \langle \bar{s}^2 \rangle^2)$ that can be evaluated from the susceptibility $\chi(t, h; L)$ and the nonlinear susceptibility $\chi^{(\text{nl})}(t, h; L)$ using the identity [19]

$$U(t; L) = - \frac{\chi^{(\text{nl})}(t, 0; L)}{3\beta L^2 \chi^2(t, 0; L)}, \quad (10)$$

where $\chi^{(\text{nl})}(t, h; L)$ is given by

$$\beta^{-3} \chi^{(\text{nl})}(t, h; L) = - \frac{\partial^4}{\partial h^4} f_s(t, h; L) \\ \sim C_2^4 L^4 \ln \left(\frac{L}{L_0} \right) Y_{\chi^{(\text{nl})}}(x_{\text{rg}}, y_{\text{rg}}). \quad (11)$$

Hence, the Binder cumulant scales as

$$U(t; L) \sim Y_U(x_{\text{rg}}), \quad (12)$$

where $Y_U(x) \equiv -Y_{\chi^{(\text{nl})}}(x, 0) / [3Y_\chi^2(x, 0)]$. Since the ensemble averages $\langle \bar{s}^{2m+1} \rangle$ with $m \in \mathbb{N}_0$ vanish in the absence of an external field, we, in addition, analyze the magnetization $m_{\text{abs}}(t, h; L) = \langle |\bar{s}| \rangle$ and the susceptibility $\chi_{\text{abs}}(t, h; L) = \beta L^d (\langle \bar{s}^2 \rangle - \langle |\bar{s}| \rangle^2)$. It is understood that these quantities also fulfill the finite-size scaling forms of $m(t, h; L)$ and $\chi(t, h; L)$, Eqs. (9), respectively with the corresponding UFSS functions $Y_{m_{\text{abs}}}(x, y)$ and $Y_{\chi_{\text{abs}}}(x, y)$.

III. MEAN-FIELD THEORY

An appropriate description of spin systems of dimensions $L \times L \times \dots \times L = L^d$ with mean-field-like (classical) critical behavior can be achieved by the mean-field theory employed by Brézin and Zinn-Justin [20] and Rudnick *et al.* [21]. This theory, also known as zero mode approximation, yields in contrast to conventional mean-field theories a rounded transition for finite systems. In the thermodynamic limit $L \rightarrow \infty$ the usual power laws with the expected mean-field values of the critical exponents can be recovered.

In the following, this theory is reviewed and used to evaluate analytical expressions for the finite-size scaling functions defined in the preceding section in order to compare them to the numerical data, as it is demonstrated in Sec. IV. The basis of this evaluation is the reduced GLW Hamiltonian in momentum space that corresponds to the underlying spin system with a long-range interaction $J(\mathbf{r}) \propto |\mathbf{r}|^{-(d+\sigma)}$. It is given by (see, e.g., Ref. [22])

$$\mathcal{H} = L^d \left(\frac{1}{2} \sum_{\mathbf{k}} (r + A_\sigma |\mathbf{k}|^\sigma) \varphi_{\mathbf{k}} \varphi_{-\mathbf{k}} - h \varphi_0 \right. \\ \left. + \frac{u}{4!} \sum_{\mathbf{k}_1} \sum_{\mathbf{k}_2} \sum_{\mathbf{k}_3} \varphi_{\mathbf{k}_1} \varphi_{\mathbf{k}_2} \varphi_{\mathbf{k}_3} \varphi_{-\mathbf{k}_1 - \mathbf{k}_2 - \mathbf{k}_3} \right) \quad (13)$$

with the temperaturelike parameter $r \propto T - T_c^{\text{mf}}$ that measures the deviation of the temperature from the mean-field critical temperature T_c^{mf} , the reduced external field h , and the dangerous irrelevant variable $u > 0$. Each sum in Eq. (13) runs for each component k_j of \mathbf{k} over integer multiples of $2\pi/L$ up to a momentum space cutoff $k_\Lambda = \pi/a$ ($|k_j| \leq k_\Lambda$) with the lattice constant a .

The essential step of the zero mode approximation is the neglect of all modes except the zero mode $\varphi \equiv \varphi_0$ in Eq. (13). This leads to the reduced zero mode Hamiltonian (see, e.g., Ref. [21])

$$\bar{\mathcal{H}}_0(\varphi) = L^d \left(\frac{r}{2} \varphi^2 + \frac{u}{4!} \varphi^4 - h \varphi \right) \quad (14)$$

with the corresponding partition function

$$\mathcal{Z}_0 = \int_{-\infty}^{\infty} d\varphi e^{-\bar{\mathcal{H}}_0(\varphi)}. \quad (15)$$

So the normalized probability distribution of the zero mode is given by

$$\mathcal{P}_0(\varphi) = \frac{1}{\mathcal{Z}_0} e^{-\bar{\mathcal{H}}_0(\varphi)} \quad (16)$$

and it can be used to evaluate averages of the form

$$\langle g(\varphi) \rangle_0 = \int_{-\infty}^{\infty} d\varphi g(\varphi) \mathcal{P}_0(\varphi). \quad (17)$$

A further central quantity is the reduced free energy density that is given by $f_0 = -L^{-d} \ln(\mathcal{Z}_0)$ within the zero mode approximation [19,20]. Using this expression and the zero mode partition function defined in Eq. (15), the rescaling (see, e.g., Ref. [20])

$$\varphi \rightarrow (uL^d)^{-1/4} \varphi \quad (18)$$

immediately yields the zero mode finite-size scaling form of f_0 . It reads

$$f_0(r, h; L) = L^{-d} \tilde{f}_0(x_{\text{mf}}, y_{\text{mf}}) + c(L) \quad (19)$$

with the mean-field temperature and field scaling variables

$$x_{\text{mf}} = ru^{-1/2} L^{d/2}, \quad y_{\text{mf}} = hu^{-1/4} L^{3d/4}, \quad (20)$$

and an additive term $c(L)$ that is without significance in the following since it is absent after taking derivatives of $f_0(r, h; L)$ with respect to r or h . Instead we focus on the finite-size scaling function

$$\tilde{f}_0(x, y) = -\ln \left(\int_{-\infty}^{\infty} d\varphi e^{-[(x/2)\varphi^2 + (1/24)\varphi^4 - y\varphi]} \right) \quad (21)$$

from which, as seen in the preceding section, the finite-size scaling functions of other quantities like the magnetization m and the susceptibility χ follow.

The asymptotics of this function are given by

$$\tilde{f}_0(x, 0) \underset{x \rightarrow -\infty}{\sim} -\frac{3}{2}x^2 + \frac{1}{2} \ln \left(\frac{|x|}{4\pi} \right), \quad (22a)$$

$$\tilde{f}_0(x, 0) \underset{x \rightarrow +\infty}{\sim} \frac{1}{2} \ln \left(\frac{x}{2\pi} \right), \quad (22b)$$

$$\tilde{f}_0(0, y) \underset{y \rightarrow \pm\infty}{\sim} -\left(\frac{81}{32} \right)^{1/3} |y|^{4/3}. \quad (22c)$$

Following the convention suggested in Ref. [23], the normalized finite-size scaling function $Y^{\text{mf}}(x, y)$ of the reduced free energy density should be defined such that their asymptotics read

$$Y^{\text{mf}}(x, 0) \underset{x \rightarrow -\infty}{\sim} -x^2, \quad (23a)$$

$$Y^{\text{mf}}(0, y) \underset{y \rightarrow \pm\infty}{\sim} -|y|^{4/3} \quad (23b)$$

instead of the leading orders in Eqs. (22). This requirement fixes some arbitrariness of the reduced free energy density finite-size scaling function and can be fulfilled by a rescaling of the parameters r and u , which are the only phenomenological quantities entering the reduced zero mode Hamil-

tonian, Eq. (14). Replacing x and y in Eqs. (22) explicitly with the mean-field scaling variables x_{mf} and y_{mf} from Eqs. (20), the rescaling

$$r \rightarrow \frac{3\sqrt{3}}{4}r, \quad u \rightarrow \frac{81}{32}u \quad (24)$$

leads to a cancellation of the corresponding coefficients of $-x_{\text{mf}}^2$ and $-|y_{\text{mf}}|^{4/3}$ and one obtains the desired asymptotics. It is important to note that we do not alter the definitions of x_{mf} and y_{mf} due to this rescaling, but the scaling function itself. Starting from the zero mode partition function, Eq. (15), with the rescaled parameters r and u , we, after the procedure discussed above, finally end up with

$$Y^{\text{mf}}(x, y) = -\ln(\Xi_0(x, y) + \Xi_0(x, -y)), \quad (25)$$

where

$$\Xi_m(x, y) = \int_0^{\infty} d\varphi \varphi^m e^{-[(3\sqrt{3}/8)x\varphi^2 + (27/256)\varphi^4 - y\varphi]}, \quad (26)$$

instead of $\tilde{f}_0(x, y)$ given in Eq. (21).

Having defined the reduced free energy density finite-size scaling function, in the following the finite-size scaling forms and the corresponding zero mode finite-size scaling functions of the quantities considered in the preceding section will be derived. Since the quantities $m_{\text{abs}}(t, h; L)$ and $\chi_{\text{abs}}(t, h; L)$ cannot be evaluated by taking derivatives of the reduced free energy density, we instead make use of the average defined in Eq. (17). Setting here $g(\varphi) = \varphi^m$ and $g(\varphi) = |\varphi|^m$, respectively, the rescaling of the parameters r and u [Eq. (24)] and the rescaling of the zero mode [Eq. (18)] immediately yields the finite-size scaling forms of these averages. They read

$$\langle \varphi^m \rangle_0 = (uL^d)^{-m/4} Y^{(m), \text{mf}}(x_{\text{mf}}, y_{\text{mf}}), \quad (27a)$$

$$\langle |\varphi|^m \rangle_0 = (uL^d)^{-m/4} Y_{\text{abs}}^{(m), \text{mf}}(x_{\text{mf}}, y_{\text{mf}}), \quad (27b)$$

with the finite-size scaling functions

$$Y^{(m), \text{mf}}(x, y) = \frac{\Xi_m(x, y) + (-1)^m \Xi_m(x, -y)}{\Xi_0(x, y) + \Xi_0(x, -y)}, \quad (28a)$$

$$Y_{\text{abs}}^{(m), \text{mf}}(x, y) = \frac{\Xi_m(x, y) + \Xi_m(x, -y)}{\Xi_0(x, y) + \Xi_0(x, -y)}. \quad (28b)$$

Since, as discussed in Ref. [20], the zero mode φ is related to the order parameter field $\phi(\mathbf{r})$ in real space via

$$\varphi = \frac{1}{L^d} \sum_{j=1}^{L^d} \phi(\mathbf{r}_j) \quad (29)$$

and consequently corresponds to the average order parameter per volume, one immediately obtains the finite-size scaling forms of the quantities defined in Sec. II, using Eqs. (27). Due to this correspondence, the magnetization $m(r, h; L)$ and the susceptibility $\chi(r, h; L)$ are given by

$$m(r, h; L) = \langle \varphi \rangle_0, \quad (30a)$$

$$\beta^{-1} \chi(r, h; L) = L^d (\langle \varphi^2 \rangle_0 - \langle \varphi \rangle_0^2) \quad (30b)$$

and therefore, according to Eq. (27a), scale as

$$m(r, h; L) = u^{-1/4} L^{-d/4} Y_m^{\text{mf}}(x_{\text{mf}}, y_{\text{mf}}), \quad (31a)$$

$$\beta^{-1} \chi(r, h; L) = u^{-1/2} L^{d/2} Y_\chi^{\text{mf}}(x_{\text{mf}}, y_{\text{mf}}) \quad (31b)$$

with the zero mode finite-size scaling functions $Y_m^{\text{mf}}(x, y)$ and $Y_\chi^{\text{mf}}(x, y)$. The finite-size scaling forms of the quantities

$$m_{\text{abs}}(r, h; L) = \langle |\varphi| \rangle_0, \quad (32a)$$

$$\beta^{-1} \chi_{\text{abs}}(r, h; L) = L^d (\langle \varphi^2 \rangle_0 - \langle |\varphi| \rangle_0^2) \quad (32b)$$

are identical to Eqs. (31), respectively, with the corresponding finite-size scaling functions $Y_{m_{\text{abs}}}^{\text{mf}}(x, y)$ and $Y_{\chi_{\text{abs}}}^{\text{mf}}(x, y)$. A further quantity of interest is the dimensionless Binder cumulant

$$U(r; L) = 1 - \frac{\langle \varphi^4 \rangle_0}{3 \langle \varphi^2 \rangle_0^2} \Big|_{h=0} \quad (33)$$

for which within the zero mode approximation one obtains the scaling form

$$U(r; L) = Y_U^{\text{mf}}(x_{\text{mf}}) \quad (34)$$

with the finite-size scaling function $Y_U^{\text{mf}}(x)$.

All zero mode finite-size scaling functions $Y_i^{\text{mf}}(x, y)$ can be expressed as combinations of the functions $\Xi_m(x, y)$ defined in Eq. (26) with $m = \{0, 1, 2, 4\}$. Since to analyze the critical behavior, as it is done in the MC simulations, either the temperature scaling variable or the field scaling variable is kept at its critical point value, it is sufficient to evaluate $\Xi_m(x, 0)$ and $\Xi_m(0, y)$ for the pertinent values of m . Analytical expressions for the needed functions can be found in the Appendix.

IV. MONTE CARLO RESULTS

In this section we present the results of MC simulations that were carried out for the model Eq. (2) with $(\omega_{\parallel}, \omega_{\perp}, J) = (1, 1, 0)$. We have used the Wolff cluster algorithm [24] for long-range spin models proposed by Luijten and Blöte [1]. To study the properties of the model in the presence of an external magnetic field, a histogram reweighting technique [25] was used.

In the simulations quadratic spin systems with $L := L_{\parallel} = L_{\perp} = \{32, 64, 128, 256, 512, 1024\}$ were considered and we started with recording the magnetization m_{abs} , the susceptibilities χ and χ_{abs} , and the Binder cumulant U at zero field for various temperatures close to the corresponding mean-field critical temperature T_c^{mf} . This temperature is given by $T_c^{\text{mf}} = \tilde{J}(\mathbf{0})$ (see, e.g., Ref. [26]) where $\tilde{J}(\mathbf{k})$ denotes the Fourier transform of the pair coupling Eq. (2b). Setting the coupling constant to $J=0$ the evaluation of this expression yields, the divergent term at $\mathbf{r}=\mathbf{0}$ is excluded,

$$T_c^{\text{mf}} = \sum_{\mathbf{r} \in \mathbb{Z}^2} \frac{\omega_{\parallel} r_{\parallel}^2 + \omega_{\perp} r_{\perp}^2}{|\mathbf{r}|^5} = \frac{1}{2} (\omega_{\parallel} + \omega_{\perp}) \Theta \left(\frac{3}{2} \right) \quad (35)$$

with the two-dimensional lattice sum [27]

$$\Theta(s) = 4^{1-s} \zeta(s) \left[\zeta \left(s, \frac{1}{4} \right) - \zeta \left(s, \frac{3}{4} \right) \right], \quad (36)$$

where $\zeta(s, a)$ denotes the generalized Riemann Zeta function. Setting $\omega_{\parallel} = \omega_{\perp} = 1$, the mean-field critical temperature takes the value

$$T_c^{\text{mf}} = \Theta \left(\frac{3}{2} \right) \approx 9.0336. \quad (37)$$

According to the finite-size scaling relations listed in Sec. II the UFSS functions were evaluated from the MC data and plotted against the temperature scaling variable x_{rg} (see Fig. 2). The data collapse was achieved by adjusting the critical temperature $T_c \equiv T_c(\infty)$ and the parameters ν and L_0 in the following way. First we determined L_0 from the requirement that the maximum of the scaled susceptibility $T \chi_{\text{abs}}(t, 0; L) L^{-1} \ln^{-1/2}(L/L_0)$ collapses for different L [Fig. 2(b)], as this peak height is independent of T_c and ν . After that we adjusted T_c and ν until the scaled cumulant $U(t; L)$ vs x_{rg} [Eqs. (12) and (6a)] collapses [Fig. 2(d)] and fits the well known critical value [2,20]

$$Y_U(0) = 1 - \frac{\Gamma \left(\frac{1}{4} \right)^4}{24\pi^2} = 0.27052 \dots \quad (38)$$

at $x_{\text{rg}}=0$. Finally, in order to compare the numerical data to the zero mode finite-size scaling functions listed in Sec. III, these functions were fitted to the numerical data by tuning the nonuniversal metric factors C_1 and C_2 . The values of all parameters as they were determined from this analysis are listed in Table I. The whole data analysis was done using FSSCALE [28].

In addition to the temperature dependence we also studied the dependence of the quantities m , m_{abs} , χ , and χ_{abs} on an external field at the temperature

$$T_c(L) = T_c(\infty) \left[1 + \nu L^{-1} \ln^{-2/3} \left(\frac{L}{L_0} \right) \right] \quad (39)$$

that can be regarded as an effective critical temperature of the finite system (see, e.g., Ref. [19]). Note that $t_c(L) = T_c(L)/T_c(\infty) - 1$ corresponds to the value of t for which the shifted reduced temperature \hat{t} as defined in Eq. (6b) and consequently the temperature scaling variable x_{rg} [Eq. (6a)] vanishes, as $\hat{t} = t - t_c(L)$. Due to this choice the numerical data obtained at this temperature and nonzero fields might then be compared to the corresponding zero mode finite-size scaling functions $Y_i^{\text{mf}}(0, y)$ within a finite-size scaling plot. Therefore we stored for each of the system lengths $L = \{16, 32, 64, 128, 256\}$ a magnetization histogram at the corresponding temperature $T_c(L)$ and zero external field, i.e., at

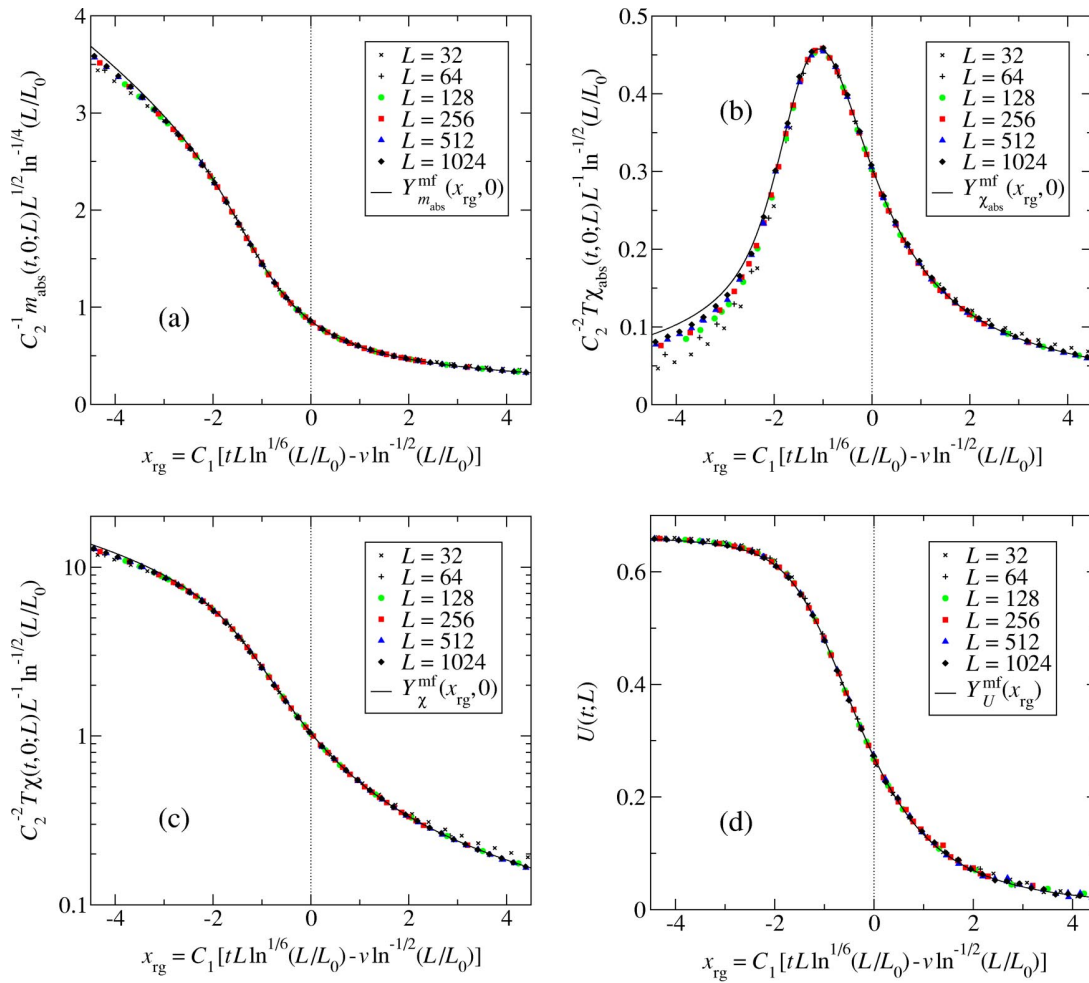


FIG. 2. (Color online) Finite-size scaling plot of the magnetization $m_{\text{abs}}(t,0;L)$ (a), the susceptibility $\chi_{\text{abs}}(t,0;L)$ (b), the susceptibility $\chi(t,0;L)$ (c), and the Binder cumulant $U(t;L)$ (d), vs scaling argument x_{rg} . The corresponding zero mode finite-size scaling functions $Y_i^{\text{mf}}(x,0)$ are displayed as solid lines. Each data point was obtained by averaging over 10^5 MCS.

$x_{\text{rg}} = y_{\text{rg}} = 0$. Using these histograms, the considered quantities were extrapolated to nonzero fields [25] and plotted as implied by their finite-size scaling forms (see Fig. 3). The values of the fit parameters required for these plots are taken consistently as they were determined from the temperature runs (cf. Table I). Since the reweighting technique allows the extrapolation of the quantities to arbitrary values of the external field, the data are displayed as continuous lines.

Within the intervals of the scaling variables x_{rg} and y_{rg} that were considered in the simulations we find excellent agreement of the MC data with the zero mode theory. In Figs. 2(a,b) merely for negative values of the temperature scaling variable x_{rg} remarkable deviations occur and the MC data with increasing system size L converge to the corre-

sponding zero mode finite-size scaling function. This effect indicates the presence of further corrections that are expected to vanish in the limit $L \rightarrow \infty$ (see also Ref. [29] that refers to the five-dimensional short-range nearest neighbor Ising model).

The deviations visible in Fig. 3 for large values of the field scaling variable y_{rg} are due to the finite size of the histograms that were used to obtain the curves shown there by means of the reweighting technique. They originate from the fact that a magnetization histogram of size K that is based on K values of the average spin \bar{s} [Eq. (8)] sampled in a MC simulation, in the mean does not contain values of \bar{s} occurring in a simulation with a lower probability than $1/K$. As will be demonstrated in the following, these deviations can also be reproduced within the zero mode theory by truncating the zero mode probability distribution $\mathcal{P}_0(\varphi)$, Eq. (16), from which we start and perform the rescaling, Eq. (24). After that we set $x_{\text{mf}} = 0$ and $y_{\text{mf}} = 0$ since the magnetization histograms we used to obtain the curves shown in Fig. 3 were recorded in the simulations also for vanishing x_{rg} and y_{rg} . The corresponding normalized zero mode probability distribution denoted as $\mathcal{P}_{0,c}(\varphi)$ then reads

TABLE I. Values of the fit parameters used throughout this work.

$T_c(\infty)$	L_0	v	C_1	C_2
8.0302(3)	3.0(2)	1.16(2)	0.735(10)	0.92(1)

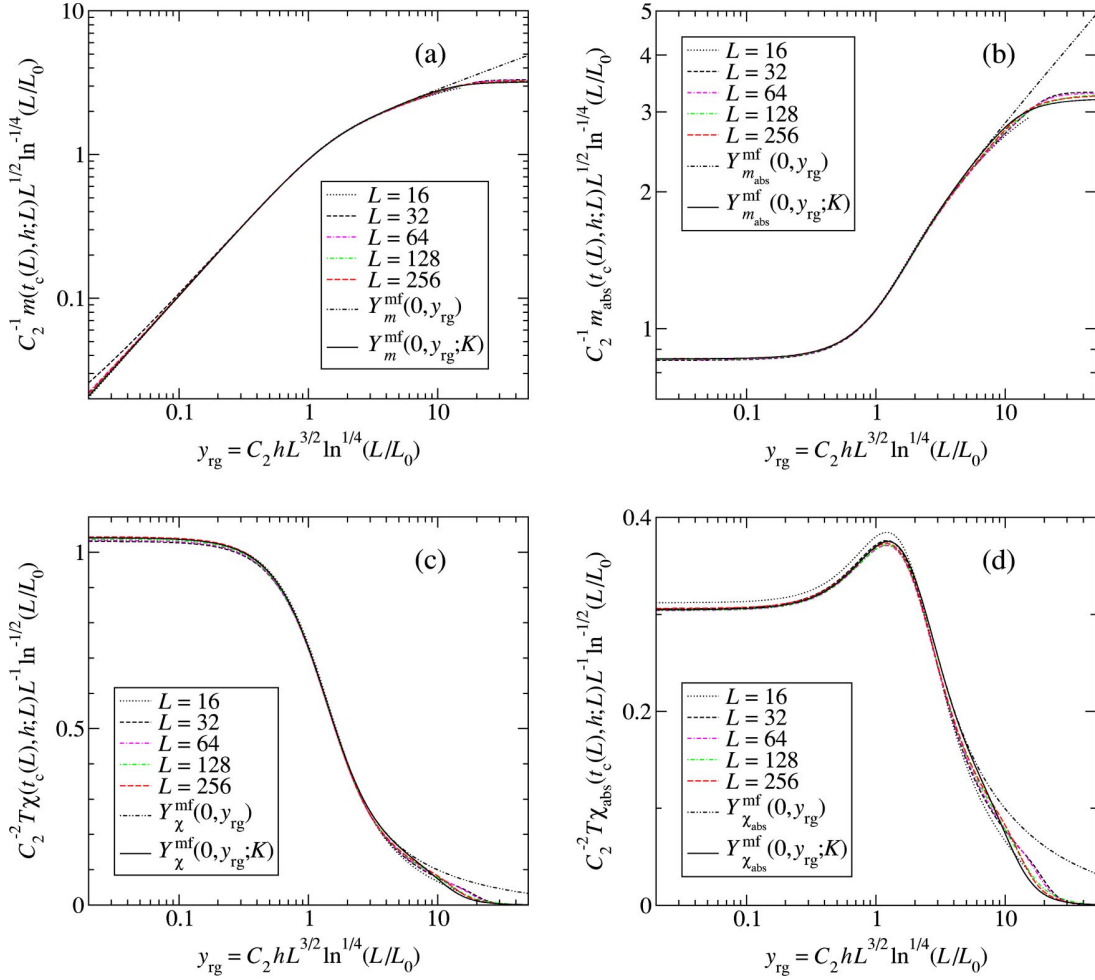


FIG. 3. (Color online) Finite-size scaling plot of the magnetization $m(t_c(L), h; L)$ (a) and $m_{\text{abs}}(t_c(L), h; L)$ (b), and the susceptibility $\chi(t_c(L), h; L)$ (c) and $\chi_{\text{abs}}(t_c(L), h; L)$ (d), vs scaling argument y_{rg} . The size of the histograms that were used to obtain the curves amounts $K = 2 \times 10^6$ MCS for each system length L . The zero mode finite-size scaling functions $Y_i^{\text{mf}}(x, y; K)$ are plotted as solid lines where the cutoff parameter takes the value $q_\Lambda(2 \times 10^6) \approx 3.2201$ (see text).

$$\mathcal{P}_{0,c}(\varphi) = (uL^d)^{1/4} Y_{\mathcal{P}_{0,c}}^{\text{mf}}((uL^d)^{1/4} \varphi) \quad (40a)$$

with the zero mode finite-size scaling function

$$Y_{\mathcal{P}_{0,c}}^{\text{mf}}(q) = \frac{3^{3/4}}{2\Gamma\left(\frac{1}{4}\right)} e^{-(27/256)q^4} \quad (40b)$$

and hence decreases monotonically for increasing $|\varphi|$. So to reproduce the effect that is due to the finite size of the histograms we chop the tails of this distribution by limiting the integration range in Eq. (17) and the zero mode partition function, Eq. (15), to a finite interval $[-\varphi_\Lambda, \varphi_\Lambda]$. To make an appropriate definition of the cutoff parameter $\varphi_\Lambda \equiv \varphi_\Lambda(K) > 0$ we use an estimation that is known from extreme value statistics [30]. We assume that in the mean only one out of K measured values of the average order parameter φ lies outside the interval $]-\varphi_\Lambda, \varphi_\Lambda[$, i.e., it fulfills $|\varphi| \geq \varphi_\Lambda$. This implies

$$P(|\varphi| \geq \varphi_\Lambda) = 2 \int_{\varphi_\Lambda}^{\infty} d\varphi \mathcal{P}_{0,c}(\varphi) = \frac{1}{K} \quad (41)$$

from which the cutoff φ_Λ is implicitly defined. Replacing $\mathcal{P}_{0,c}(\varphi)$ according to Eqs. (40) the evaluation of the resulting integral yields

$$2 \int_{q_\Lambda}^{\infty} dq Y_{\mathcal{P}_{0,c}}^{\text{mf}}(q) = \frac{\Gamma\left(\frac{1}{4}, \frac{27}{256} q_\Lambda^4\right)}{\Gamma\left(\frac{1}{4}\right)} = \frac{1}{K}, \quad (42)$$

where $q_\Lambda = (uL^d)^{1/4} \varphi_\Lambda$ and $\Gamma(a, b)$ denotes the incomplete Gamma function. Expanding this expression and separating $q_\Lambda \equiv q_\Lambda(K)$ yields to leading order a logarithmic dependence on the histogram size K of the form

$$q_\Lambda(K) \stackrel{K \rightarrow \infty}{\sim} \sqrt{\frac{8}{3}} \left[\frac{4}{3} \ln\left(\frac{K}{K_0}\right) - \ln\left(\frac{4}{3} \ln\left(\frac{K}{K_0}\right)\right) \right]^{1/4} \quad (43)$$

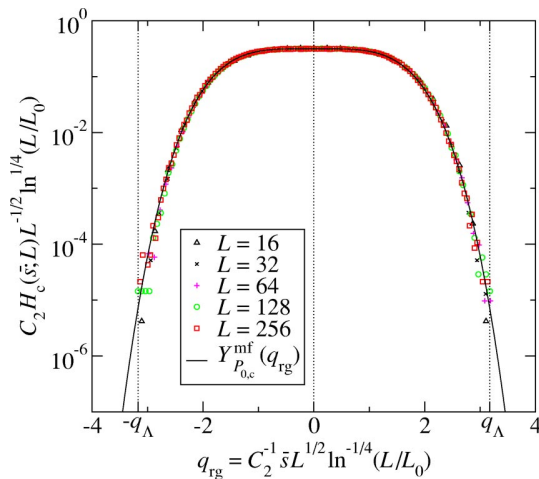


FIG. 4. (Color online) Finite-size scaling plot of the critical histogram $H_c(\bar{s};L)$. The size of the histogram depicted here amounts $K=10^6$ MCS for each system length L . According to Eq. (42) this corresponds to a cutoff value of $q_\Lambda(10^6)\approx 3.1728$. The value of the fit parameter L_0 and the nonuniversal metric factor C_2 are taken as they are listed in Table I.

with the constant $K_0=(3/4)^{3/4}\Gamma(\frac{1}{4})$.

To demonstrate the validity of the definition of the cutoff φ_Λ , respectively, q_Λ , Fig. 4 shows a finite-size scaling plot of the critical magnetization histogram H_c that was recorded for $x_{rg}=y_{rg}=0$. Starting from the finite-size scaling form of the magnetization, Eq. (9a), it is straightforward to show that this histogram scales as

$$H_c(\bar{s};L)\sim C_2^{-1}L^{1/2}\ln^{-1/4}\left(\frac{L}{L_0}\right)Y_{H_c}(q_{rg}) \quad (44)$$

with the finite-size scaling function $Y_{H_c}(q)$ and the scaling variable $q_{rg}=C_2^{-1}\bar{s}L^{1/2}\ln^{-1/4}(L/L_0)$. As is expected also in Fig. 4, the MC data are found to be in very good agreement with the zero mode expression $Y_{p_{0,c}}^{mf}(q)$ [Eq. (40b)] of the

finite-size scaling function $Y_{H_c}(q)$. It furthermore turns out that all data points lie accurately within the interval $[-q_\Lambda(K),q_\Lambda(K)]$ that corresponds to the size of the displayed histogram. The zero mode finite-size scaling functions $Y_i^{mf}(x,y;K)$ that were evaluated using the truncated zero mode probability distribution with the cutoff $q_\Lambda(K)$ are also shown in Fig. 3, and nicely agree with the extrapolated data.

Before finishing this section we also want to discuss the importance of the corrections to the leading orders in the expansions in Eqs. (7) that are determined by the parameters L_0 and ν . For that purpose Figs. 5(a, b) show the finite-size scaling plot of the susceptibility $\chi_{\text{abs}}(t,0;L)$ versus scaling variable x_{rg} [Fig. 2(b)] where we set $\nu=0$ in Fig. 5(a) and $L_0=1$ in Fig. 5(b). The values of the other parameters entering the plots are taken from Table I. As is expected, neglecting one of the corrections causes a significant displacement between the MC data and the zero mode finite-size scaling function $Y_{\chi_{\text{abs}}}^{mf}(x_{rg},0)$. This effect could partially be compensated by readjusting the remaining fit parameters, but this procedure would in the case of Fig. 5(a) lead to a wrong determination of the critical temperature $T_c(\infty)$ (see also discussions in Ref. [31] that refer to spin models above the upper critical dimensionality).

V. CONCLUSIONS

We have introduced a two-dimensional long-range spin model that displays both isotropic and anisotropic phase transitions and, in particular, strongly anisotropic phase transitions. As a first stage the critical behavior of the model in the isotropic case for which it is found to be at its upper critical dimensionality was investigated. For that purpose we have carried out Monte Carlo simulations and studied the temperature and field dependence of several quantities. Using results of the renormalization group, the numerical data obtained for different system sizes were analyzed by means of a finite-size scaling analysis. It turns out that beside a size-dependent shift that has already been discussed in the literature a characteristic length L_0 that was inserted into the

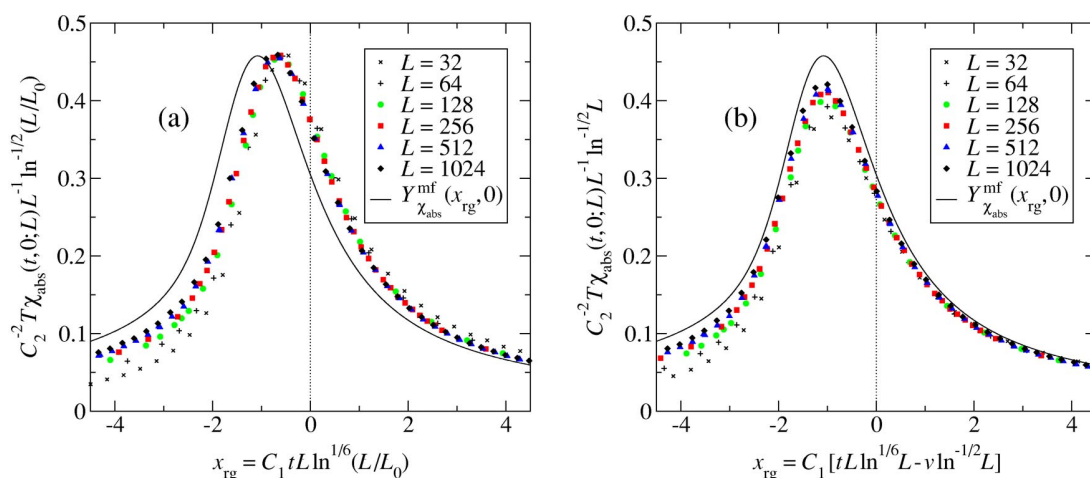


FIG. 5. (Color online) Finite-size scaling plot of the susceptibility $\chi_{\text{abs}}(t,0;L)$ without the shift correction ($\nu=0$) (a) and with $L_0=1$ (b).

logarithms is an important correction that must not be neglected.

Furthermore, the collapsed data were compared to the zero mode (mean-field) theory and found to be in excellent agreement. It turns out that the logarithmic corrections typically occurring at the upper critical dimensionality do only enter the finite-size scaling functions through their arguments, whereby these functions were derived from zero mode theory. This shows that at least in the present case the concept of universal finite-size scaling functions can be extended to the upper critical dimensionality.

Finally we note that the numerical results strongly indicate the validity of the zero mode theory at the upper critical dimensionality and might shed new light on recent controversial discussions about its correctness for $d \geq d_u$ [32,29].

As it will be subject of a future work it is desirable to extend the analysis shown above to the anisotropic case $\omega_{\parallel} \neq \omega_{\perp}$. In particular, the critical behavior of the model should be investigated when approaching the strongly anisotropic cases $\omega_{\parallel} = -2\omega_{\perp}$ and $-2\omega_{\parallel} = \omega_{\perp}$, respectively.

ACKNOWLEDGMENTS

The authors would like to thank S. Lübeck, Professor K. D. Usadel, and Professor H. W. Diehl for valuable discussions.

APPENDIX: THE FUNCTIONS $\Xi_m(x,0)$ AND $\Xi_m(0,y)$

The evaluation of the function $\Xi_m(x,0)$ with MATHEMATICA [33] yields

$$\begin{aligned} \Xi_m(x,0) = & 3^{-3(m+1)/4} 4^m \left[\Gamma\left(\frac{m+1}{4}\right) {}_1F_1\left(\frac{m+1}{4}; \frac{1}{2}; x^2\right) \right. \\ & \left. - 2x \Gamma\left(\frac{m+3}{4}\right) {}_1F_1\left(\frac{m+3}{4}; \frac{3}{2}; x^2\right) \right] \quad (\text{A1}) \end{aligned}$$

with the confluent hypergeometric function ${}_1F_1(a;b;x)$. This expression is valid for $x \in \mathbb{R}$ and $m \in \mathbb{R}^{>-1}$ and can be simplified further for a given integer value of the parameter m . For $m = \{0,1,2,4\}$ one obtains

$$\Xi_0(x,0) = 3^{-3/4} e^{x^2/2} Y_{1/4}(x), \quad (\text{A2a})$$

$$\Xi_1(x,0) = \frac{4}{3} \sqrt{\frac{\pi}{3}} e^{x^2} \text{erfc}(x), \quad (\text{A2b})$$

$$\Xi_2(x,0) = \frac{8}{9} 3^{-1/4} e^{x^2/2} [Y_{3/4}(x) - x Y_{1/4}(x)], \quad (\text{A2c})$$

$$\Xi_4(x,0) = \frac{64}{81} 3^{1/4} e^{x^2/2} [2x^2 Y_{1/4}(x) - 3x Y_{3/4}(x) - Y_{5/4}(x)], \quad (\text{A2d})$$

where the function

$$Y_a(x) = \pi(x^2)^a \left[I_{-a}\left(\frac{1}{2}x^2\right) - \text{sgn}(x) I_a\left(\frac{1}{2}x^2\right) \right] \quad (\text{A3})$$

with the modified Bessel function of the first kind $I_a(x)$ has been introduced, and $\text{erfc}(x)$ denotes the complementary error function. The function $Y_a(x)$ is well behaved through zero argument for the pertinent noninteger positive values of a . Assuming $x > 0$, Eq. (A3) simplifies to

$$Y_a(x) = 2x^{2a} K_a\left(\frac{1}{2}x^2\right) \sin(\pi a) \quad (\text{A4})$$

with the modified Bessel function of the second kind $K_a(x)$.

An analogous treatment of the function $\Xi_m(0,y)$ results in

$$\begin{aligned} \Xi_m(0,y) = & \frac{1}{4} \sum_{k=1}^4 \left(\frac{256}{27} \right)^{(m+k)/4} \frac{y^{k-1}}{\Gamma(k)} \Gamma\left(\frac{m+k}{4}\right) \\ & \times {}_2F_4\left(\frac{m+k}{4}; 1; \frac{k}{4}, \frac{k+1}{4}, \frac{k+2}{4}, \frac{k+3}{4}; \frac{y^4}{27}\right), \quad (\text{A5}) \end{aligned}$$

where ${}_pF_q(a_1, \dots, a_p; b_1, \dots, b_q; x)$ denotes the generalized hypergeometric function. This expression is also valid for $y \in \mathbb{R}$ and $m \in \mathbb{R}^{>-1}$ and cannot be simplified further for a given value of m involving less general functions. Finally let us note that the function $\Xi_m(x,y)$ fulfills the recursion relations

$$\Xi_{m+2}(x,y) = -\frac{8}{3\sqrt{3}} \frac{\partial}{\partial x} \Xi_m(x,y), \quad (\text{A6a})$$

$$\Xi_{m+1}(x,y) = \frac{\partial}{\partial y} \Xi_m(x,y) \quad (\text{A6b})$$

as follows from Eq. (26).

-
- [1] E. Luijten and H.W.J. Blöte, *Int. J. Mod. Phys. C* **6**, 359 (1995).
 [2] E. Luijten and H.W.J. Blöte, *Phys. Rev. B* **56**, 8945 (1997).
 [3] E. Luijten, H.W.J. Blöte, and K. Binder, *Phys. Rev. E* **54**, 4626 (1996).
 [4] E. Luijten, H.W.J. Blöte, and K. Binder, *Phys. Rev. E* **56**, 6540 (1997).
 [5] A. Hucht, *J. Phys. A* **35**, L481 (2002).

- [6] R.M. Hornreich, M. Luban, and S. Shtrikman, *Phys. Rev. Lett.* **35**, 1678 (1975).
 [7] W. Selke, in *Phase Transitions and Critical Phenomena*, edited by C. Domb and J. L. Lebowitz (Academic Press, London, 1992), Vol. 15.
 [8] H.W. Diehl and M. Shpot, *Phys. Rev. B* **62**, 12 338 (2000).
 [9] M. Pleimling and M. Henkel, *Phys. Rev. Lett.* **87**, 125702 (2001).

- [10] M.B. Taylor and B.L. Györfy, *J. Phys.: Condens. Matter* **5**, 4527 (1993).
- [11] A.B. MacIsaac, J.P. Whitehead, M.C. Robinson, and K. De'Bell, *Phys. Rev. B* **51**, 16 033 (1995).
- [12] A. Hucht and D. Grüneberg (unpublished).
- [13] M.E. Fisher, S.k. Ma, and B.G. Nickel, *Phys. Rev. Lett.* **29**, 917 (1972).
- [14] M.E. Fisher, in *Proceedings of the School on Critical Phenomena, Stellenbosch, South Africa, 1982*, edited by F.J.W. Hahne (Springer-Verlag, Berlin, 1983), Vol. 186, Chap. 1.
- [15] V. Privman and M.E. Fisher, *J. Stat. Phys.* **33**, 385 (1983).
- [16] S. Lübeck and P.C. Heger, *Phys. Rev. E* **68**, 056102 (2003).
- [17] V. Privman and M.E. Fisher, *Phys. Rev. B* **30**, 322 (1984).
- [18] K. Binder, *Z. Phys. B: Condens. Matter* **43**, 119 (1981).
- [19] K. Binder, M. Nauenberg, V. Privman, and A.P. Young, *Phys. Rev. B* **31**, 1498 (1985).
- [20] E. Brézin and J. Zinn-Justin, *Nucl. Phys. B* **257**, 687 (1985).
- [21] J. Rudnick, H. Guo, and D. Jasnow, *J. Stat. Phys.* **41**, 353 (1985).
- [22] A. Aharony, in *Phase Transitions and Critical Phenomena*, edited by C. Domb and M.S. Green (Academic Press, London, 1976), Vol. 6, Chap. 6.
- [23] M.L. Glasser, V. Privman, and L.S. Schulman, *Phys. Rev. B* **35**, 1841 (1987).
- [24] U. Wolff, *Phys. Rev. Lett.* **62**, 361 (1989).
- [25] A.M. Ferrenberg and R.H. Swendsen, *Phys. Rev. Lett.* **61**, 2635 (1988).
- [26] A. Aharony, in *Proceedings of the School on Critical Phenomena, Stellenbosch, South Africa, 1982*, edited by F.J.W. Hahne (Springer-Verlag, Berlin, 1983), Vol. 186, Chap. 3.
- [27] A. Hucht, A. Moschel, and K.D. Usadel, *J. Magn. Magn. Mater.* **148**, 32 (1995).
- [28] F. Hucht, *Fsscale: A program for doing Finite-Size Scaling (1998-2003)*, URL:<http://www.thp.Uni-Duisburg.de/fsscale/>
- [29] E. Luijten, K. Binder, and H.W.J. Blöte, *Eur. Phys. J. B* **9**, 289 (1999).
- [30] S. Kotz and S. Nadarajah, *Extreme Value Distributions* (Imperial College Press, London, 2000).
- [31] E. Luijten and H.W.J. Blöte, *Phys. Rev. Lett.* **76**, 1557 (1996).
- [32] X.S. Chen and V. Dohm, *Int. J. Mod. Phys. C* **9**, 1007 (1998).
- [33] S. Wolfram, *The Mathematica Book*, 4th ed. (Wolfram Media, Cambridge University Press, 1999).

Thermodynamic Casimir Effect in ^4He Films near T_λ : Monte Carlo Results

Alfred Hucht

*Theoretical Physics, University of Duisburg-Essen, 47048 Duisburg, Germany**

(Received 23 June 2007; revised manuscript received 13 August 2007; published 2 November 2007)

The universal finite-size scaling function of the critical Casimir force for the three dimensional XY universality class with Dirichlet boundary conditions is determined using Monte Carlo simulations. The results are in excellent agreement with recent experiments on ^4He Films at the superfluid transition and with available theoretical predictions.

DOI: [10.1103/PhysRevLett.99.185301](https://doi.org/10.1103/PhysRevLett.99.185301)

PACS numbers: 67.40.Kh, 05.10.Ln, 64.60.Fr, 67.70.+n

Casimir forces are always present in nature when a medium with long-range fluctuations is confined to restricted geometries. The quantum mechanical Casimir effect was proposed theoretically 60 years ago by H. B. G. Casimir [1] and describes an attractive force between two conducting plates in vacuum, induced by the vacuum fluctuations of the electromagnetic field. Furthermore, Goldstone modes [2] and surface fluctuations [3] can give rise to Casimir forces. Near continuous phase transitions, long-range fluctuations of the order parameter lead to the analogous *thermodynamic* Casimir effect [4], which can change the thickness of critical liquid films [5]. In a series of papers, Garcia and Chan [6,7] and Ganshin *et al.* [8] were able to measure the thinning of liquid ^4He films close to the λ point due to the thermodynamic Casimir effect. They found a characteristic deep minimum (dip) in the film thickness just below the superfluid transition temperature T_λ . Using finite-size scaling methods, they accurately determined the scaling function $\vartheta(x)$ of the Casimir force, which is universal for given universality class and boundary conditions. For liquid ^4He films it is believed that the superfluid order parameter vanishes at both surfaces of the film, implying Dirichlet boundary conditions [9].

Unfortunately, a theoretical explanation of the strong dip and a determination of the scaling function $\vartheta(x)$ is still lacking. In Ref. [10], this is stressed as the main theoretical problem with respect to the explanation of the ^4He experiments. While field theoretical results [11–13] are restricted to temperatures $T \geq T_c$, Monte Carlo simulations have been only available for periodic boundary conditions until now [14], as only in this case the used stress tensor representation of the Casimir force is applicable. Recent attempts [15,16] to explain the strong dip within mean field theories only find qualitative agreement with the experiments, neglecting the noncritical contributions of Goldstone modes.

In this Letter, I present a direct calculation of the Casimir force using Monte Carlo simulations of the classical XY model. This method requires the computation of the free energy of the system with high accuracy, which is a major challenge within Monte Carlo simulations. Fortunately, it turns out that the determination is greatly simplified by the fact that only the difference of two free

energies is needed, which goes to zero exponentially fast above T_c . The resulting finite-size scaling function is in excellent agreement with the experimental results [6–8] as well as with available theoretical predictions [2,11,17].

The Casimir force per unit area of a system with size $L_\parallel^{d-1} \times L_\perp$ ($L_\parallel \rightarrow \infty$) is defined as [18,19]

$$\beta F_{\text{Cas}}(T, L_\perp) = -\frac{\partial f_{\text{ex}}(T, L_\perp)}{\partial L_\perp}, \quad (1)$$

where $f_{\text{ex}}(T, L_\perp)$ denotes the excess free energy

$$f_{\text{ex}}(T, L_\perp) = f(T, L_\perp) - L_\perp f_\infty(T) \quad (2)$$

of the system. Here $f(T, L_\perp)$ is the free energy per unit area of a film of thickness L_\perp , measured in units of $k_B T$, and $f_\infty(T)$ is the bulk free energy density. For large L_\perp and near T_c the Casimir force fulfills the scaling *ansatz* [20]

$$\beta F_{\text{Cas}}(T, L_\perp) \sim L_\perp^{-d} \vartheta(x) \quad (3)$$

with the universal finite-size scaling function $\vartheta(x)$ and the scaling variable

$$x = t \left(\frac{L_\perp}{\xi_0^+} \right)^{1/\nu} \underset{t>0}{\sim} \left(\frac{L_\perp}{\xi_\infty^+(t)} \right)^{1/\nu}. \quad (4)$$

Here I introduce the reduced temperature $t = T/T_c - 1$ and the bulk correlation length

$$\xi_\infty^+(t) \sim \xi_0^+ t^{-\nu}, \quad (t > 0). \quad (5)$$

Note that the universal finite-size scaling function $\vartheta(x)$ depends on the boundary conditions in the L_\perp direction.

We can directly calculate the Casimir force (1) by integration of the internal energy as follows: Let us define the ‘‘internal Casimir force’’

$$\beta F_{\text{int}}(T, L_\perp) = -\left(\frac{\partial u(T, L_\perp)}{\partial L_\perp} - u_\infty(T) \right) \quad (6)$$

with the internal energy per unit area in units of $k_B T$

$$u(T, L_\perp) = -T \frac{\partial f(T, L_\perp)}{\partial T} \quad (7)$$

and the corresponding bulk density $u_\infty(T)$. The quantity $\partial u(T, L_\perp)/\partial L_\perp$ is directly accessible in Monte Carlo simulations using $u = \langle \beta \mathcal{H} \rangle / L_\parallel^{d-1}$, and the central difference quotient

$$\frac{\partial u(T, L_\perp)}{\partial L_\perp} \approx \frac{u(T, L_\perp + 1) - u(T, L_\perp - 1)}{2}. \quad (8)$$

The Casimir force is then obtained by integration

$$\beta F_{\text{Cas}}(T, L_\perp) = - \int_T^\infty \frac{d\tau}{\tau} \beta F_{\text{int}}(\tau, L_\perp). \quad (9)$$

By Eqs. (3) and (9), the internal Casimir force fulfills the scaling form

$$- \beta F_{\text{int}}(T, L_\perp) \sim (\xi_0^+)^{-1/\nu} L_\perp^{(\alpha-1)/\nu} \vartheta'(x) \quad (10)$$

with the universal finite-size scaling function $\vartheta'(x)$. Note that within the scaling regime, Eq. (10), the relative error of Eq. (8) is $\mathcal{O}(L^{1/\nu-2-d})$.

We now consider the isotropic XY model on a simple cubic lattice of size $L_\parallel \times L_\parallel \times L_\perp$ in three dimensions with periodic boundary conditions in the parallel directions. The Dirichlet boundary conditions in the perpendicular direction are implemented by open boundary conditions, which are known to be equivalent at large length scales [21,22], although alternative implementations are possible [23]. The Hamiltonian reads

$$\mathcal{H} = - \frac{J}{2} \sum_{\langle ij \rangle} \vec{s}_i \cdot \vec{s}_j, \quad (11)$$

where $J > 0$ is the ferromagnetic exchange interaction, \vec{s}_i are 2-component unit vectors at site i , and the sum is restricted to nearest neighbors on the lattice. The simulations were performed for several system sizes with fixed aspect ratios $\rho = L_\perp/L_\parallel = 1:8$ and $1:16$ using the standard Wolff cluster algorithm [24]. To calculate Eq. (8), systems with thicknesses $L'_\perp = L_\perp \pm 1$ at constant L_\parallel were simulated for every combination of L_\parallel and L_\perp . At least 10^5 Monte Carlo sweeps per data point were performed.

To calculate the Casimir forces, Eqs. (1) and (6), it is necessary to have an expression for the bulk internal energy density $u_\infty(T)$. This is achieved using a combination of direct simulations of a large cubic system ($L = 96$) with periodic boundary conditions and the results of Cucchieri *et al.* [25]. They determined the scaling behavior of the internal energy and specific heat of the XY model (11) in the region $|t| < 0.015$, where finite-size effects arise, using the scaling *ansatz*

$$k_B T u_\infty(T) = \epsilon_{\text{ns}} + T_c t \left[C_{\text{ns}} + \frac{A^+}{\alpha} |t|^{-\alpha} \left(\frac{1}{1-\alpha} + \frac{c_1^\pm}{1-\alpha+\nu\omega} |t|^{\nu\omega} + \frac{c_2^\pm}{2-\alpha} t \right) \right]. \quad (12)$$

The critical indices of the considered XY model are fixed to the values $\nu = 0.672(1)$, $\alpha = -0.017(3)$, $\omega = 0.79(2)$, $T_c/J = 2.20183(1)$, and $\xi_0^+ = 0.484(5)$ in this Letter, leading to the parameters $\epsilon_{\text{ns}} = -0.98841(3)$, $C_{\text{ns}} = 22.03(8)$, $A^+ = 0.3790(8)$, $A^- = 0.3533(8)$, $c_1^+ = 0.015(1)$, $c_1^- = 0.109(2)$, $c_2^+ = -0.041(3)$, and $c_2^- =$

$0.211(4)$ [25]. For $|t| > 0.015$ finite-size effects are negligible; note that at $t = 0.015$ the correlation length, Eq. (5), has the value $\xi_\infty^+(0.015) \approx 8.1$, which is sufficiently small with respect to $L = 96$. While for periodic cubic systems the scaling corrections are moderate, systems with broken translational invariance and aspect ratios $\rho \ll 1$ show strong corrections to scaling. An analysis of usual thermodynamic quantities like the magnetic susceptibility $\chi(T, L_\perp)$ and the Binder cumulant $U(T, L_\perp)$ shows that it is necessary to use a modified scaling variable x [Eq. (4)] with Wegner corrections [26] of the form

$$x = t \left(\frac{L_\perp}{\xi_0^+} \right)^{1/\nu} (1 + g_\omega L_\perp^{-\omega}), \quad (13)$$

while the y direction has rather small corrections for systems with constant ρ . However, for the numerical derivative with respect to L_\perp in (6) it is necessary to combine data of systems with $L'_\perp = L_\perp \pm 1$, leading to systems with different aspect ratio $\rho' \neq \rho$. This and the expected uncertainty of the numerical derivative itself introduces a scaling correction of the order $(1 + g_1 L_\perp^{-1})$ in the y direction, leading to the final scaling *ansatz*

$$\beta F_{\text{Cas}}(T, L_\perp) \sim L_\perp^{-d} (1 + g_1 L_\perp^{-1})^{-1} \vartheta(x) \quad (14)$$

with x from Eq. (13).

The results for the Casimir force are shown in Fig. 1 for six system sizes with $L_\perp \in \{8, 12, 16\}$, each with aspect ratio $\rho = 1:8$ and $\rho = 1:16$. It should be emphasized that the only fit parameters are the corrections to scaling amplitudes, $g_\omega = 2.0(1)$ and $g_1 = 5.5(2)$, which are adjusted

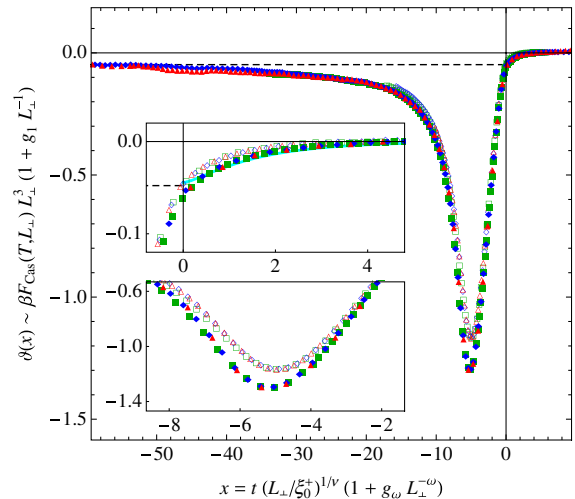


FIG. 1 (color online). Results for the Casimir force using Eq. (14), for systems with $L_\perp = 8$ (green squares), $L_\perp = 12$ (blue diamonds), and $L_\perp = 16$ (red triangles), with aspect ratios $\rho = 1:8$ (open) and $\rho = 1:16$ (filled). The statistical error is of the order of the symbol size. The upper and lower insets are magnifications around $x = 0$ and around the minimum, respectively. Also shown are the Goldstone amplitude $-\zeta(3)/8\pi$ [2] (dashed line) and the field theoretical result [12] [gray (cyan online) curve in upper inset].

[27] until the numerical data collapse onto a single curve, and that there is no free factor in either the x or y direction. We can identify a slight dependence on the aspect ratio ρ in both directions. As the corrections due to the finite ρ are known to scale approximately with ρ^2 [28], a full data collapse can be achieved by adding a factor $(1 + r_1\rho^2)$ to the x axis and a factor $(1 + r_2\rho^2)$ to the y axis, with $r_1 = 4(1)$ and $r_2 = 10(1)$. Note that these corrections mainly shift the curves for $\rho = 1:8$, while the $\rho = 1:16$ curves are virtually unchanged within the error bars. The resulting scaling function is depicted in Fig. 2, together with the results of Garcia and Chan [6] (left) as well as Ganshin *et al.* [8] (right). In the first case, only data for the thickest film with $d = 423 \text{ \AA}$ are shown, which are regarded to have the highest quality [29], while the thinner films showed deviations in y direction, presumably due to surface roughness [6,8]. In order to compare the experimental data quantitatively with the present results, they are made dimensionless in x direction using the measured correlation length amplitude $\xi_0^+ = 1.432 \text{ \AA}$ of ^4He at T_λ [30], leading to a factor $(\xi_0^+)^{-1/\nu} = 0.586 \text{ \AA}^{-1/\nu}$.

We find an excellent agreement within the error bars with both measurements for $x \geq -8$. The universal amplitude of $\vartheta(x)$ at the minimum is $\vartheta(x_{\min}) = -1.35(3)$ at $x_{\min} = -5.3(1)$. These values agree with the values $x_{\min} = -5.4(1)$ of Garcia and Chan [6] and $\vartheta(x_{\min}) = -1.30(3)$ at $x_{\min} = -5.7(5)$ of Ganshin *et al.* [8]. It turns out that the overall agreement with Ref. [6] is even better than with Ref. [8], which might be attributed to the smaller fluctuations in y direction in the data of Ref. [6], mainly visible below $x \approx -10$, and to the 5 times smaller error estimate in x direction, clearly visible in the insets and at $x = 0$. For $x \lesssim -8$ we see an enhancement of the measured Casimir

force not present in the calculated scaling function. This onset is weaker in the left figure. A possible explanation is the occurrence of surface fluctuations below this temperature, as proposed in Ref. [3]. At the critical point ($x = 0$) we find $\vartheta(0) = -0.047(2)[-0.059(2)]$ for $\rho = 1:8[1:16]$, which gives $\vartheta(0) = -0.062(5)$ for $\rho \rightarrow 0$. The resulting Casimir amplitude $\Delta = -0.031(3)$ agrees well with the estimate $\Delta = -0.03$ from Refs. [5,28]. For $x \geq 1$ the results lie nicely on the scaling function calculated by Krech and Dietrich [12] using renormalization group theory. Here $r_1 = 30$ was used, which again mainly shifts the data for $\rho = 1:8$; see upper inset in Fig. 2 (left). The quality of the method used, especially of the numerical integration, is demonstrated by the convergence of the calculated scaling function to the low temperature Goldstone value $\vartheta_{\text{Goldstone}} = -\zeta(3)/8\pi$ [2] for $x \rightarrow -\infty$ (dashed line in Figs. 1 and 2).

Figure 3 shows the results for the scaling function $\vartheta'(x)$ of the internal Casimir force, Eq. (6). The scaling plot contains data from eight system sizes with $L_\perp \in \{4, 8, 12, 16\}$, each with aspect ratio $\rho = 1:8$ and $\rho = 1:16$. While the aspect ratio correction in the y direction becomes $r_3 = r_2 - r_1$, the scaling correction g_2 cannot be expressed through g_ω and g_1 , as the corresponding L_\perp exponents are different. The effective calculated value at $L_\perp \approx 10$ is $g_2 = 1.7$, which is modified to $g_2 = 2.0(2)$ to get the best data collapse. The results are compared to a numerical differentiation of the experimental data of Garcia and Chan ([6], Cap. 1). The results of Ganshin *et al.* [8] are not shown due to large fluctuations of the numerical derivative. The data collapse and the agreement with the experimental data is very convincing, also showing the small influence of statistical errors in the simula-

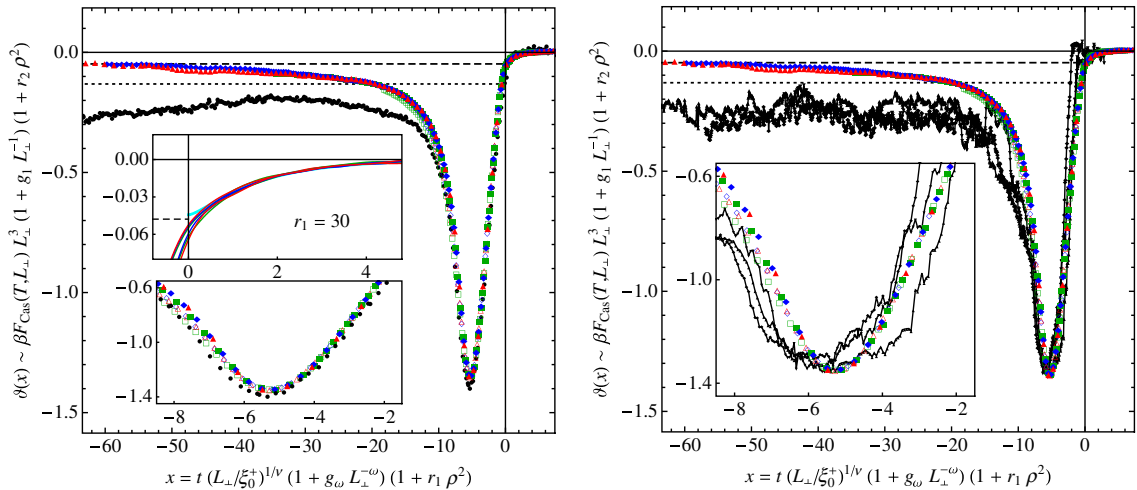


FIG. 2 (color online). Universal finite-size scaling function $\vartheta(x)$ of the Casimir force for systems with $L_\perp = 8$ (green squares), $L_\perp = 12$ (blue diamonds), and $L_\perp = 16$ (red triangles), with aspect ratios $\rho = 1:8$ (open) and $\rho = 1:16$ (filled). The insets are magnifications of the respective regions. The results are compared (left) to the experimental data of Garcia and Chan ([6], Cap. 1) (\bullet), as well as with the results (right) of Ganshin *et al.* [8] (\blacktriangle : 340 \AA , \blacklozenge : 285 \AA , \blacktriangledown : 238 \AA ; solid lines are guides to the eye). Also shown are the Goldstone amplitude $-\zeta(3)/8\pi$ [2] (dashed line), the value $-11\zeta(3)/32\pi$ including surface fluctuations proposed in Ref. [3] (dotted line), and the field theoretical result [12] [gray (cyan online) curve in left upper inset].

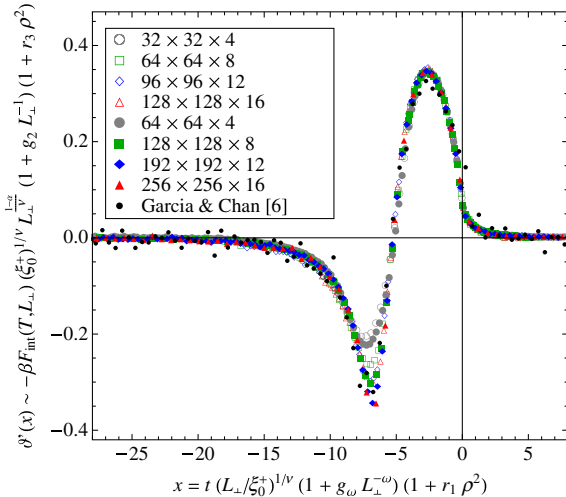


FIG. 3 (color online). Universal finite-size scaling function $\vartheta'(x)$ of the internal Casimir force, Eq. (6), determined from eight different system sizes with aspect ratios $\rho = 1:8$ and $1:16$. The experimental results are obtained by binning (with $\Delta x = 0.5$) and numerical differentiation of the data from Garcia and Chan ([6] Cap. 1).

tions. Only in the interval $-9 \lesssim x \lesssim -5$ we see higher order corrections to scaling, which are believed to stem from uncertainties in the numerical derivative, Eq. (8). However, these corrections only have a small influence on the integrated Casimir force. Further work is necessary to clarify this behavior. Note that $\partial u(T, L_{\perp})/\partial L_{\perp} \sim u_{\infty}(T)$ at the minimum of $F_{\text{Cas}}(T, L_{\perp})$, which implies that the shift of the minimum to negative x is a direct consequence of the strong shift in $T_c(L_{\perp})$ in systems with Dirichlet boundary conditions.

In summary, I have determined the universal finite-size scaling function $\vartheta(x)$ of the Casimir force within the XY universality class with Dirichlet boundary conditions using Monte Carlo simulations. For sufficiently small aspect ratio $\rho = 1:16$ the results are in excellent agreement with the experimental results on ${}^4\text{He}$ by Garcia and Chan [6], and by Ganshin *et al.* [8], as well as with theoretical calculations for $T \geq T_c$ by Krech and Dietrich [11,12]. The universal function $\vartheta(x)$ has a deep minimum at $x_{\min} = -5.3(1)$, with $\vartheta(x_{\min}) = -1.35(3)$. The results are in conformity with the assumption that the order parameter in ${}^4\text{He}$ asymptotically obeys Dirichlet boundary conditions. The method proposed in this Letter has also been applied to systems with periodic boundary conditions [31], where a similar good agreement with available results [13,14] is obtained. The application to other boundary conditions as well as to Ising and Heisenberg models is straightforward.

I would like to thank Daniel Grüneberg, Hans Werner Diehl, Ralf Meyer, Daniel Dantchev, and Rafael Garcia for useful discussions and comments.

Note added.—Recently Vasilyev *et al.* presented an alternative method to calculate $\vartheta(x)$ using Monte Carlo simulations [32].

*fred@thp.Uni-DuE.de

- [1] H. B. G. Casimir, Proc. K. Ned. Akad. Wet., B Phys. Sci. **51**, 793 (1948).
- [2] H. Li and M. Kardar, Phys. Rev. Lett. **67**, 3275 (1991).
- [3] R. Zandi, J. Rudnick, and M. Kardar, Phys. Rev. Lett. **93**, 155302 (2004). Note that due to an imprecision in this article ($\Delta d \approx -1.85 \text{ \AA}$ instead of $\Delta d \approx -2.2 \text{ \AA}$ for the considered film) the deviation from experiment ($\Delta d_{\min} \approx -2.65 \text{ \AA}$) is nearly twice as large as reported; see Fig. 2 (left).
- [4] M. E. Fisher and P.-G. de Gennes, C.R. Seances Acad. Sci. Ser. B **287**, 207 (1978).
- [5] J. O. Indekeu, J. Chem. Soc., Faraday Trans. 2 **82**, 1835 (1986).
- [6] R. Garcia and M. H. W. Chan, Phys. Rev. Lett. **83**, 1187 (1999); <http://users.wpi.edu/~garcia/casimirdata/>.
- [7] R. Garcia and M. H. W. Chan, Phys. Rev. Lett. **88**, 086101 (2002).
- [8] A. Ganshin, S. Scheidemantel, R. Garcia, and M. H. W. Chan, Phys. Rev. Lett. **97**, 075301 (2006).
- [9] W. Huhn and V. Dohm, Phys. Rev. Lett. **61**, 1368 (1988).
- [10] D. Dantchev, M. Krech, and S. Dietrich, Phys. Rev. Lett. **95**, 259701 (2005).
- [11] M. Krech and S. Dietrich, Phys. Rev. Lett. **66**, 345 (1991); **67**, 1055(E) (1991).
- [12] M. Krech and S. Dietrich, Phys. Rev. A **46**, 1922 (1992).
- [13] H. W. Diehl, D. Grüneberg, and M. A. Shpot, Europhys. Lett. **75**, 241 (2006).
- [14] D. Dantchev and M. Krech, Phys. Rev. E **69**, 046119 (2004).
- [15] R. Zandi, A. Shackell, J. Rudnick, M. Kardar, and L. P. Chayes, Phys. Rev. E **76**, 030601 (2007).
- [16] A. Maciołek, A. Gambassi, and S. Dietrich, Phys. Rev. E **76**, 031124 (2007).
- [17] J. O. Indekeu, M. P. Nightingale, and W. V. Wang, Phys. Rev. B **34**, 330 (1986).
- [18] J. G. Brankov, D. M. Dantchev, and N. S. Tonchev, *Theory of Critical Phenomena in Finite-Size Systems—Scaling and Quantum Effects* (World Scientific, Singapore, 2000).
- [19] M. Krech, *Casimir Effect in Critical Systems* (World Scientific, Singapore, 1994).
- [20] \sim means “asymptotically equal” in the respective limit, $L_{\perp} \rightarrow \infty$, $T \rightarrow T_c$, or both, keeping the scaling variable x fixed, e.g., $f(L) \sim g(L) \Leftrightarrow \lim_{L \rightarrow \infty} f(L)/g(L) = 1$.
- [21] H. W. Diehl, Int. J. Mod. Phys. B **11**, 3503 (1997).
- [22] C. Zhang, K. Nho, and D. P. Landau, Phys. Rev. B **73**, 174508 (2006).
- [23] N. Schultka and E. Manousakis, Phys. Rev. Lett. **75**, 2710 (1995).
- [24] U. Wolff, Phys. Rev. Lett. **62**, 361 (1989).
- [25] A. Cucchieri, J. Engels, S. Holtmann, T. Mendes, and T. Schulze, J. Phys. A **35**, 6517 (2002).
- [26] F. Wegner, Phys. Rev. B **5**, 4529 (1972).
- [27] F. Hucht, Fsscale: A Program for Doing Finite-Size Scaling, <http://www.thp.Uni-DuE.de/fsscale/>.
- [28] K. K. Mon and M. P. Nightingale, Phys. Rev. B **35**, 3560 (1987).
- [29] R. Garcia (private communication).
- [30] W. Y. Tam and G. Ahlers, Phys. Rev. B **32**, 5932 (1985).
- [31] A. Hucht and D. Grüneberg (to be published).
- [32] O. Vasilyev, A. Gambassi, A. Maciołek, and S. Dietrich, arXiv:0708.2902v1.

Magnetic Friction in Ising Spin Systems

Dirk Kadau,^{1,2} Alfred Hucht,¹ and Dietrich E. Wolf¹

¹*Department of Physics and CeNIDE, University of Duisburg-Essen, D-47048 Duisburg, Germany*

²*Institute for Building Materials, ETH Zurich, 8092 Zurich, Switzerland*

(Received 19 March 2007; revised manuscript received 21 May 2008; published 26 September 2008)

A new contribution to friction is predicted to occur in systems with magnetic correlations: Tangential relative motion of two Ising spin systems pumps energy into the magnetic degrees of freedom. This leads to a friction force proportional to the area of contact. The velocity and temperature dependence of this force are investigated. Magnetic friction is strongest near the critical temperature, below which the spin systems order spontaneously. Antiferromagnetic coupling leads to stronger friction than ferromagnetic coupling with the same exchange constant. The basic dissipation mechanism is explained. A surprising effect is observed in the ferromagnetically ordered phase: The relative motion can act like a heat pump cooling the spins in the vicinity of the friction surface.

DOI: [10.1103/PhysRevLett.101.137205](https://doi.org/10.1103/PhysRevLett.101.137205)

PACS numbers: 75.30.Sg, 05.50.+q, 05.70.Ln, 68.35.Af

As friction is an intriguingly complex phenomenon of enormous practical importance, the progress in experimental techniques on the micro- and nanoscale [1,2] as well as the improved computational power for atomic simulations [3–5] has led to a renaissance of this old research field in recent years. Currently a large variety of microscopic models compete with one another [1,6,7]. Major complications are wear, plastic deformation at the contact, impurities, and lubricants. It is unlikely that in the general case only a single dissipation mechanism will be active. Defect motion, phononic and electronic excitations may be involved in a very complex blend. To reduce these complications and to focus on the elementary dissipation processes, increasing attention has been paid to noncontact friction: It can be measured as damping of an atomic force microscope tip which oscillates in front of a surface without touching it [8,9]. For this setup, too, phononic [10,11] as well as electronic dissipation mechanisms [12,13] have been discussed. Recently, a Heisenberg model with magnetic dipole-dipole interactions was studied at zero temperature as a model for magnetic force microscopy. In this case the moving tip excites spin waves, which dissipate part of the energy [14].

In this Letter a different mechanism is considered, by which the spin degrees of freedom of an Ising model contribute to friction. We imagine two magnetic materials with planar surfaces sliding on each other. Of course, if one of the materials is metallic, their relative motion will induce eddy currents [15]. The corresponding Joule heat is commonly associated with the term “magnetic friction,” although the energy is not dissipated into the spin degrees of freedom, which can even be considered as frozen. By contrast, here we are interested in the case that both materials are nonmetallic (e.g., magnetite Fe_3O_4). To highlight the role of the spin degrees of freedom we do not take phononic and electronic excitations into account explicitly, but regard them as a heat bath of fixed temperature T to

which all spins are coupled. Energy dissipation in Ising spin systems was studied previously [16,17], but there it was due to an oscillating magnetic field rather than the tangential relative motion of two lattices. The competition between the time scales for driving the system out of equilibrium and for its relaxation gave rise to hysteretic, and hence dissipative behavior. These time scales play also a role for magnetic friction, as we will show.

Specifically, we present Monte Carlo (MC) simulation results for a two-dimensional Ising square lattice with periodic boundary conditions. Each of the N lattice sites carries a classical spin variable S_i which can take the values ± 1 . The Hamiltonian is $H = -J \sum_{\langle i,j \rangle} S_i S_j$, where $\langle i,j \rangle$ denotes nearest neighbors, and J is chosen as energy unit. Coupling to a heat bath of constant temperature T lets the spin configuration C relax towards thermal equilibrium. The relaxation kinetics are determined by the transition rate $w(C \rightarrow C')$ to a new configuration C' , in which one randomly chosen spin is flipped. We consider fast relaxation with Metropolis rate [18]

$$w_M(C \rightarrow C') = t_0^{-1} \min(1, e^{-\beta \Delta E}) \quad (1)$$

and slow relaxation with Glauber rate [18]

$$w_G(C \rightarrow C') = w_M(C \rightarrow C') / (1 + e^{-\beta |\Delta E|}), \quad (2)$$

where $\beta = (k_B T)^{-1}$. The energy difference $\Delta E = E(C') - E(C)$ is received from ($\Delta E > 0$), respectively, transferred to ($\Delta E < 0$) the heat bath, when the spin is flipped. $t_0 \approx 10^{-8}$ s [19] is the typical time for relaxation of a spin into the direction of the local Weiss-field.

The system is constantly driven out of equilibrium in the following way: The lattice is cut parallel to an axis into an upper and a lower half. The former is displaced by one lattice constant $a \approx 10^{-10}$ m in regular time intervals a/v , where v is the sliding velocity (in the following given in natural units a/t_0). This means that N/v random sequential spin updates (i.e., $1/v$ Monte Carlo steps) are followed

by a rigid translation of the upper half by one lattice constant parallel to the cut. $v = 1$ corresponds to 10^{-2} m/s. (Note that due to the periodic boundary conditions there is a second slip plane separating the upper half of the simulation cell from the periodic image of the lower half.) The exchange interaction J is the same, no matter whether the interacting spins are on the same or on different sides of the cut. This has the advantage that the relative velocity v and the temperature T (in natural units $|J|/k_B$) are the only parameters in the model. In the following we evaluate the accumulated energy (divided by two, because of the two equivalent slip planes) that has been exchanged with the heat bath during the time interval t , $\Delta E_{\text{bath}}(t)$, for different sliding velocities v and temperatures T . We first present our results for ferromagnetic coupling, $J > 0$. In the end we also discuss what is different for antiferromagnetic coupling, $J < 0$.

Is there any energy dissipation within this simple model at all? To answer this question we first simulated a system consisting of 80×80 spins thermalized for 200 MC steps per spin at a temperature $T = 2.5$ above the critical temperature $T_c = 2/\ln(\sqrt{2} + 1)$ [20] (initial configuration). Figure 1 shows the energy exchange per spin with the heat bath for two cases: Without relative motion ($v = 0$) of the half-spaces ΔE_{bath} fluctuates around 0; i.e., no energy is dissipated. Switching on the relative motion with a velocity $v = 1$ leads to a linear increase of $\Delta E_{\text{bath}}(t)$. The total system energy E per spin stays constant at about the same value in both cases. This means that the sliding system quickly develops a steady state, where energy is transferred continuously to the heat bath. The slope in Fig. 1 is the constant dissipation rate $P = \Delta E_{\text{bath}}/\Delta t$. It is directly connected to the friction force F

by $P = Fv$. We conclude that the Ising model gives rise to a truly magnetic friction force: The relative motion pumps energy into the spin degrees of freedom, which in the steady state is then transferred further into the heat bath.

The magnetic friction force turns out to be proportional to the length L of the periodic cell along the direction of the cut through the two-dimensional lattice. On the other hand, varying the system size perpendicular to the slip plane does not change the above results, as long as it remained larger than about 20 lattice constants. This shows that whatever energy the relative motion pumps locally into the spin degrees of freedom near the slip plane, gets transferred completely to the heat bath before it can drive more distant parts of the system out of equilibrium.

Figure 2 shows that the dissipation rate for small velocities starts out linearly, with a slight upward curvature, and saturates for large velocities. The saturation is expected when the velocity times the relaxation time τ becomes larger than the correlation length ξ [21], i.e., when $v > \xi/\tau$. Then the lower half-space is essentially confronted with uncorrelated configurations of the upper half-space, and a further increase of v does not change anything. For Glauber dynamics the relaxation time is larger by a factor of about 1.5 than for Metropolis dynamics. This explains the difference between the curves in Fig. 2: If one rescales time by this factor, i.e., multiplies velocity and dissipation rate by 1.5, the curve for Glauber dynamics is shifted such that it essentially coincides with the one for Metropolis dynamics. For small velocities the linear v dependence in Fig. 2 implies that the magnetic friction force approaches a constant, F_0 . For $T = 2.5$ the velocity independent part of the magnetic frictional shear stress has the value $F_0/L = 0.114 \pm 0.004$. It is the same for Metropolis and Glauber dynamics.

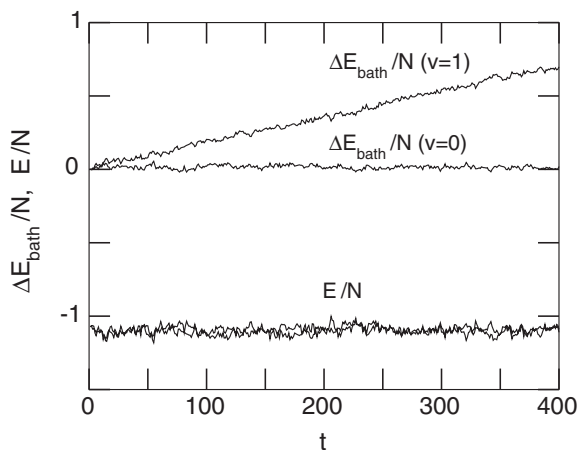


FIG. 1. Accumulated energy ΔE_{bath} per spin which is transferred to the heat bath during a time interval t , without motion ($v = 0$) and with motion ($v = 1$) of the two half-spaces. Simulation with Metropolis rates. The total energy per spin fluctuates around the exact value $E/N \approx -1.10608$ [20] in both cases.

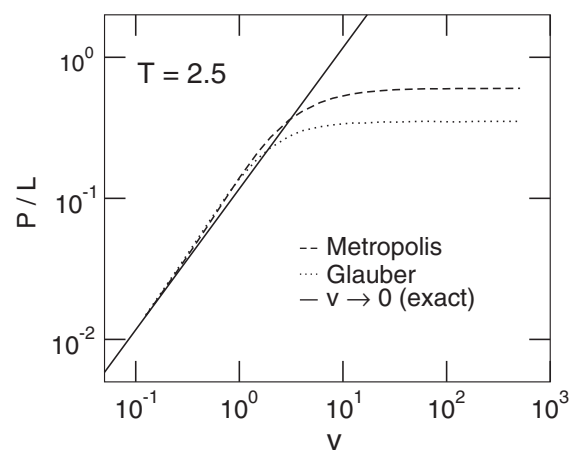


FIG. 2. Energy dissipation rate P per unit length as a function of the relative velocity v of the two half-spaces (averaged over 100 runs). Dashed line: Metropolis rates. Dotted line: Glauber rates. Solid line: Exact solution for the limit $v \rightarrow 0$.

F_0/L can be calculated analytically in the quasistatic limit, $v \rightarrow 0$, where the spin system has time enough to relax back into equilibrium after each displacement of the upper half. The energy of the spin configuration immediately after a displacement minus the equilibrium energy must be transferred to the heat bath during the time interval a/v . The rigid shift of all spins in the equilibrated upper half by one lattice constant places former next nearest neighbors in nearest neighbor positions on opposite sides of the slip plane. Thus the dissipated energy per unit length a (i.e., the friction force) can simply be expressed as JL times the nearest neighbor spin correlation function minus the next nearest neighbor spin correlation function. Both are known analytically; see, e.g., Eqs. (4.5) and (4.9) of [20]. At $T = 2.5$ this gives the value $F_0/L \approx 0.117$ in good agreement with the numerical result. For general temperature one obtains the solid curve in Fig. 3.

According to the picture of Bowden and Tabor [22] also Coulomb friction is independent of v and proportional to the real contact area, which due to surface roughness is smaller than the sliding surface macroscopically appears to be, and grows proportional to the normal load. Therefore, the velocity independent part of the magnetic friction force behaves like Coulomb friction. How does it compare to typical values for solid friction? The above results show that the magnetic shear stress $\sigma_t = F_0/L$ is of the order of 0.1 for the two-dimensional Ising model. The unit is J/a^2 , the exchange constant divided by the lattice constant squared. If we regard the two-dimensional Ising model as a slice of thickness a of a three-dimensional system, then we may assume that the magnetic shear stress for a three-

dimensional Ising model is of the order of $\sigma_{t,3d} \approx 0.1J/a^3$. Inserting typical values ($J \approx 0.6 \times 10^{-20}$ Joule, $a \approx 3 \times 10^{-10}$ m) one gets the estimate $\sigma_{t,3d} \approx 20$ MPa. This is a surprisingly large value. Ordinary solid friction shear stresses are given by $\sigma_{t,\text{Coulomb}} = \mu\sigma_c$ according to the Bowden-Tabor-theory, where a typical value for the friction coefficient is $\mu = 0.2$, and the yield stress σ_c at high temperatures is a few hundred to thousand MPa. We conclude that magnetic friction is probably not too weak compared with ordinary solid friction to be observable.

There is one caveat, however: The exchange interaction is extremely short range, but in the simulation results presented here no reduced value was inserted for the interaction of spins on opposite sides of the slip plane. The above estimate should therefore only be applied if the surfaces are in close contact. As expected, simulations with a reduced magnetic exchange interaction across the slip plane lead to a smaller friction force.

Magnetic friction has characteristic features near the critical temperature, which should be useful to separate this contribution to solid friction from other ones. It is nearly zero at low temperatures, where the ferromagnetic ordering implies almost perfect translational invariance along the surface. As thermal fluctuations destroy the translational invariance, magnetic friction raises sharply to a maximum slightly above the critical temperature (Fig. 3). In the paramagnetic region the exact quasistatic limit shows that the friction force has the same $1/T$ asymptotics as JL times the nearest neighbor correlation function, because the next nearest neighbor correlation ($\propto 1/T^2$) becomes negligible.

What is the basic mechanism leading to magnetic friction in the Ising model? Obviously, shearing reduces the correlation length locally by disturbing the equilibrium correlations between spins on opposite sides of the slip plane. Above T_c this corresponds to an effective temperature increase, which explains the energy flow into the cooler heat bath. Since more neighbor pairs with antiparallel spin are present, the energy density is locally increased in the steady state, compared with its value in thermal equilibrium. As the correlation length vanishes for $T \rightarrow \infty$, this picture explains why magnetic friction vanishes in this limit.

Below T_c the correlation length can be associated with the diameter of thermally activated minority clusters of spins pointing into the direction opposite to the spontaneous magnetization. The relative motion distorts minority clusters, which extend across the slip plane, and possibly cuts them into two pieces. Again this reduces the effective correlation length. In thermal equilibrium a smaller correlation length indicates a better ordered magnetic state. Indeed we find an increased magnetization locally at the slip plane (Fig. 4). This effect is less pronounced for the Metropolis algorithm, where the spin configurations relax more quickly into thermal equilibrium.

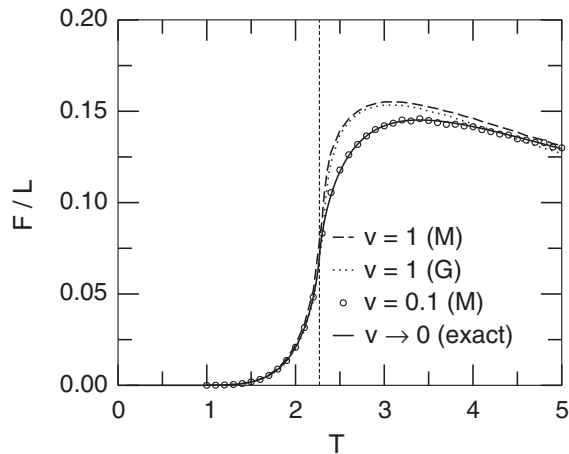


FIG. 3. Temperature dependence of the friction force per unit length, F/L . Solid line: Exact quasistatic limit $v \rightarrow 0$. Simulation results with Metropolis rates (circles) for $v = 0.1$ agree with the quasistatic limit. For $v = 1$ the friction forces for Metropolis rates (dashed line), respectively, Glauber rates (dotted line) are larger corresponding to the upward curvature in Fig. 2. All data are averaged over 100 runs. The critical temperature is indicated by the dashed vertical line.

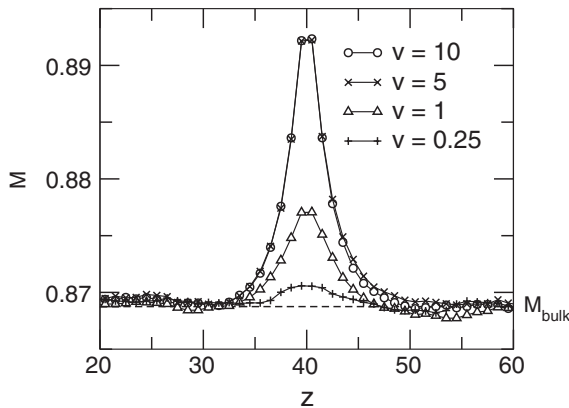


FIG. 4. Magnetization profile along the z axis perpendicular to the slip plane (at $z = 40$ in units of the lattice constant a) at $T = 2.1 < T_c$ for Glauber rates at different velocities. The local magnetization near the slip plane is enhanced. This effect becomes stronger for increasing velocity and saturates for the same reason as in Fig. 2. When using Metropolis rates this effect is less pronounced (not shown).

The local spin temperature in the vicinity of the slip plane drops due to the influence of shearing. The driven system acts like a “heat pump” cooling the spin degrees of freedom below the temperature of the heat bath. The shearing creates additional domain walls by deforming or fragmenting minority clusters. The system continuously tries to reduce these excess domain walls, thereby transferring domain wall energy to the heat bath. This is the dissipation mechanism.

Why does this “heat pump” work better for higher velocities, as shown by Fig. 4? Let us discuss first the case of sufficiently high velocities, where the magnetization near the slip plane saturates at a maximal value. Then correlations between the two half-spaces can be neglected. Instead, the spins in the lower half see an effective surface field corresponding to the average surface magnetization of the upper half. Hence minority spins near the slip plane flip more easily into the majority direction than in the bulk. For smaller velocities, however, minority clusters can be stabilized more and more because of correlations across the slip plane. Hence the surface magnetization decreases.

Analogous investigations for antiferromagnetic coupling ($J < 0$) were done, too. The dissipation rate turns out to be much higher than in the ferromagnetic case (with the same $|J|$). The friction maximum is more than 3 times larger for the Ising antiferromagnet than for the ferromagnet. The reason is that the local antiferromagnetic order across the slip plane is destroyed whenever the upper lattice is displaced by one lattice constant. This is a stronger perturbation than in the ferromagnetic case, where only the correlations of thermal disorder could be de-

stroyed by the relative motion. In particular, magnetic friction does not vanish for $T \rightarrow 0$ in the antiferromagnetic case.

We acknowledge funding by the DFG through SFB 616 (“Energy dissipation at surfaces”) and support by Federal Mogul Technology GmbH.

-
- [1] T. Baumberger and C. Caroli, *Adv. Phys.* **55**, 279 (2006).
 - [2] K. B. Jinesh and J. W. M. Frenken, *Phys. Rev. Lett.* **96**, 166103 (2006).
 - [3] U. Landmann, W. D. Luedtke, and E. M. Ringer, *Wear* **153**, 3 (1992).
 - [4] M. R. Sorensen, K. W. Jacobsen, and P. Stoltze, *Phys. Rev. B* **53**, 2101 (1996).
 - [5] J. E. Hammerberg, B. L. Holian, T. C. Germann, and R. Ravelo, *Metall. Mater. Trans. A* **35**, 2741 (2004).
 - [6] M. H. Müser, M. Urbakh, and M. O. Robbins, *Adv. Chem. Phys.* **126**, 187 (2003).
 - [7] B. N. J. Persson, *Sliding Friction* (Springer, Berlin, 1998).
 - [8] O. Pfeiffer, R. Bennewitz, A. Baratoff, E. Meyer, and P. Grütter, *Phys. Rev. B* **65**, 161403(R) (2002).
 - [9] T. Kunstmann, A. Schlarb, M. Fendrich, D. Paulowski, T. Wagner, and R. Möller, *Appl. Phys. Lett.* **88**, 153112 (2006).
 - [10] L. N. Kantorovich, *J. Phys. Condens. Matter* **13**, 945 (2001).
 - [11] T. Trevelyan and L. Kantorovich, *Nanotechnology* **16**, S79 (2005).
 - [12] J. B. Pendry, *J. Phys. Condens. Matter* **9**, 10301 (1997).
 - [13] A. I. Volokitin and B. N. J. Persson, *Phys. Rev. B* **65**, 115419 (2002).
 - [14] C. Fusco, D. E. Wolf, and U. Nowak, *Phys. Rev. B* **77**, 174426 (2008).
 - [15] B. Hoffmann, R. Houbertz, and U. Hartmann, *Appl. Phys.* **66**, S409 (1998).
 - [16] M. Acharyya and B. K. Chakrabarti, *Phys. Rev. B* **52**, 6550 (1995).
 - [17] J. Ortin and J. Goicoechea, *Phys. Rev. B* **58**, 5628 (1998).
 - [18] D. P. Landau and K. Binder, *A Guide to Monte Carlo Simulations in Statistical Physics* (Cambridge University Press, Cambridge, 2000) Chap. 4.2.1.
 - [19] M. B. Stearns, in *Magnetic Properties of Metals*, edited by H. P. J. Wijn and Landolt-Börnstein, New Series, Group III, Vol. 19, Pt. a (Springer, Berlin, 1986).
 - [20] B. M. McCoy and T. T. Wu, *The Two-Dimensional Ising Model* (Harvard University Press, Cambridge, Massachusetts, 1973).
 - [21] The equilibrium bulk correlation length ξ is defined by the exponential cutoff of the spin-spin correlation function, $\langle S_i S_j \rangle - \langle S \rangle^2 \sim |i - j|^{-1/2} \exp(-|i - j|a/\xi)$ for large $|i - j|$ and $T \neq T_c$ [Ornstein-Zernike-form, [18], Eq. (2.22)].
 - [22] F. P. Bowden and D. Tabor, *Friction and Lubrication* (Methuen, London, 1967).

Thermodynamic Casimir Effect in the large- n limit

Denis Comtesse, Alfred Hucht, and Daniel Grüneberg
Fachbereich Physik, Universität Duisburg-Essen, D-47048 Duisburg, Germany

We consider systems with slab geometry of finite thickness L that undergo second order phase transitions in the bulk limit and belong to the universality class of $O(n)$ -symmetric systems with short-range interactions. In these systems the critical fluctuations at the bulk critical temperature $T_{c,\infty}$ induce a long-range effective force called the “thermodynamic Casimir force”. We describe the systems in the framework of the $O(n)$ -symmetric ϕ^4 -model, restricting us to the large- n limit $n \rightarrow \infty$. In this limit the physically relevant case of three space dimensions $d = 3$ can be treated analytically in systems with translational symmetry as, e.g., in the bulk or slabs with periodic or antiperiodic boundary conditions. We consider Dirichlet and open boundary conditions at the surfaces that break the translational invariance along the axis perpendicular to the slab. From the broken translational invariance we conclude the necessity to solve the systems numerically. We evaluate the Casimir amplitudes for Dirichlet and open boundary conditions on both surfaces and for Dirichlet on one and open on the other surface. Belonging to the same surface universality class we find the expected asymptotic equivalence of Dirichlet and open boundary conditions. To test the quality of our method we confirm the analytical results for periodic and antiperiodic boundary conditions.

PACS numbers: 05.70.Jk, 68.35.Rh, 11.10.Hi, 68.15.+e, 75.40.-s

Keywords: Casimir effect, fluctuation-induced forces, scaling functions, large n -limit, spherical model

I. INTRODUCTION

In a fluctuating medium confined between two surfaces long-range forces may arise. This effect was first predicted by H. B. G. Casimir [1] who considered a confinement of the electromagnetic vacuum fluctuations between two perfectly conducting metal plates. The boundary conditions imposed by the two plates modify these fluctuations in such a way that the energy of the system becomes dependent on the separation of the plates. From this energy gradient in the separation a long-range force, the so called Casimir force arises. This force was experimentally measured for the first time in 1998 by Mohideen and Roy [2]. After this breakthrough more measurements followed [3, 4], confirming Casimir’s prediction with high accuracy.

An analogous effect is the so called *thermodynamic* Casimir effect which was first proposed by Fisher and de Gennes [5]. It is caused by critical fluctuations of a medium near its bulk critical point $T_{c,\infty}$, where these fluctuations are correlated over an infinite range. The spatial confinement of such fluctuations also gives rise to a long-range Casimir force.

The thermodynamic Casimir effect was experimentally proven for the first time by Garcia and Chan in thin films of liquid ^4He at its transition temperature to superfluidity [6]. They measured a characteristic dip of the film thickness at the critical temperature, that can be attributed to the thermodynamic Casimir force. The experimental data are excellently reproduced by Monte Carlo simulations of the XY model with open boundary conditions [7] which is in the same universality class as the superfluid transition in ^4He .

Due to the presence of strong fluctuations in critical systems there are only a few exact results for the thermodynamic Casimir effect yet. These are usually restricted to the case of periodic boundary conditions along the slab. Though there are perturbation theory results up to second order for experimentally relevant boundary conditions as, e.g., Dirichlet boundary conditions [8], exact results for these are still lacking.

The remainder of this paper is organized as follows. In the next section we carry the elementary features of the thermodynamic Casimir effect together, and introduce the large- n limit. In Section II the model considered in the present work will be defined and its excess free energy will be derived in Section III. This calculation leads to a self-consistent eigenvalue problem, which is solved numerically, providing the possibility for numerical estimation of the Casimir amplitudes. The paper is closed with a discussion of the achieved results.

A. Casimir effect

As predicted by finite-size scaling theory a statistical system confined between two parallel surfaces exhibits a dependence of the free energy on the separation L of the surfaces [9]. This L -dependence leads to an effective force between the surfaces which is a typical example of a finite-size effect. This thermodynamic Casimir force is defined

as [5, 10–12]

$$\mathcal{F}_C(T, L) = -k_B T \frac{\partial f_{\text{ex}}(T, L)}{\partial L}, \quad (1.1)$$

where f_{ex} denotes the reduced excess free energy per unit area, which is given by $f_{\text{ex}} = f_L - Lf_b$ with the total free energy per unit area f_L and the reduced bulk free energy density f_b . The limit $A \rightarrow \infty$ of the cross sectional area has been taken.

For temperatures away from the bulk critical point the bulk correlation length $\xi_\infty(T)$ is much smaller than the macroscopic separation L . In this regime the Casimir force decays exponentially for large L .

As it is generally known, $\xi_\infty(T)$ diverges as $|T - T_{c,\infty}|^{-\nu}$ at the bulk critical temperature $T_{c,\infty}$, with critical exponent ν , so in the vicinity of $T_{c,\infty}$ the bulk correlation length is of the same order as L . This implies that the Casimir force $\mathcal{F}_C(T, L)$ extends to distances much larger than the microscopic scale a (\simeq lattice constant). In this regime the Casimir force decays algebraically for large L [5].

Examining the excess free energy more precisely one finds that it can be decomposed into two contributions

$$f_{\text{ex}}(T, L) = f_s(T) + f_{\text{res}}(T, L). \quad (1.2)$$

The first one is the L -independent nonlocal surface excess free energy $f_s(T) \equiv f_{\text{ex}}(T, \infty)$ [13]. The second one is the residual finite-size contribution $f_{\text{res}}(T, L)$ which contains the whole information about the L -dependence of the free energy.

At the bulk critical point $T_{c,\infty}$ the finite-size contribution has the characteristic algebraic behavior [31]

$$f_{\text{res}}(T_{c,\infty}, L) \underset{L \rightarrow \infty}{\sim} \Delta_C L^{-(d-1)}, \quad (1.3)$$

leading to a long-range effective Casimir force

$$\frac{\mathcal{F}_C(T_{c,\infty}, L)}{k_B T_{c,\infty}} \underset{L \rightarrow \infty}{\sim} (d-1) \Delta_C L^{-d}. \quad (1.4)$$

The quantity Δ_C is an universal finite-size quantity, called the Casimir amplitude [5]. Universal means that it depends only on the bulk universality class of the phase transition and the surface universality class of the boundary planes [13]. It is in particular independent of microscopic details of the system, such as, e.g., the lattice structure.

Near the bulk critical point the residual free energy density and the Casimir force obey the scaling forms

$$f_{\text{res}}(T, L) \sim L^{-(d-1)} \Theta(L/\xi_\infty(T)) \quad (1.5)$$

and

$$\frac{\mathcal{F}_C(T, L)}{k_B T} \sim L^{-d} \vartheta(L/\xi_\infty(T)), \quad (1.6)$$

where $\Theta(x)$ and $\vartheta(x)$ are universal functions with the scaling argument $x = L/\xi_\infty$. At $T_{c,\infty}$, where $L/\xi_\infty = 0$, they take the values $\Theta(0) = \Delta_C$ and $\vartheta(0) = (d-1)\Delta_C$.

There is no complete analytic theory for the thermodynamic Casimir effect joining the regimes above and below $T_{c,\infty}$. In the framework of the ϕ^4 -theory perturbative calculations up to second order for different boundary conditions at and above $T_{c,\infty}$ [8, 14–16] were performed. There are also exact results for the spherical model with periodic [12] and antiperiodic [17] boundary conditions. However, for slab systems with non-periodic boundary conditions no exact results are available. This is the aim of the present work.

B. The large- n limit and the spherical model

To investigate the thermodynamic Casimir effect one needs a model that shows the characteristic critical properties of a second order phase transition. There are various classes of models that exhibit critical behavior but here we restrict ourselves to the class of classical $O(n)$ -invariant n -vector lattice models. Those can be represented by the Hamiltonian

$$\mathcal{H}_n = -\frac{J}{2} \sum_{\langle i,j \rangle} \mathbf{S}_i \cdot \mathbf{S}_j, \quad (1.7)$$

where the $\mathbf{S} = (s_1, \dots, s_n)$ are n -component vector spin variables, restricted to the local constraint $|\mathbf{S}|^2 = 1$. The exchange coupling J is assumed to have a positive nonzero value and the sum runs over all nearest neighbors.

In the limit $n \rightarrow \infty$, which is called the large- n limit this model can be solved analytically for the bulk or for systems of finite size [18]. This case is connected to the so called the spherical model, which was first introduced and solved by Berlin and Kac [19] and is defined by the Hamiltonian

$$\mathcal{H}_{\text{SM}} = -\frac{J'}{2} \sum_{\langle i,j \rangle} s_i s_j. \quad (1.8)$$

Here the s_i are scalar spin variables fulfilling a global constraint $\sum_i s_i^2 = N$ called ‘‘spherical constraint’’, where N is the number of lattice sites.

This model is even more easy to handle if one uses the constraint $\langle \sum_i s_i^2 \rangle = N$ where one takes the statistical mean over the sum. It is then called the ‘‘mean spherical model’’ but the both formulations are equivalent in translationally invariant systems.

It was found by Stanley [20] that these spherical models are equivalent to the large- n limit for translationally invariant systems as, e.g., the bulk case or systems with periodic boundary conditions.

To hold this equivalence in non-translationally invariant systems the spherical constraint has to be modified [21]. In the case of a slab where the boundary conditions are non periodic one needs a spherical constraint for each layer parallel to the surfaces. These multiple constraints make the analytical treatment impossible so that numerical calculations are needed. This is the challenge we are going to face here.

The large- n limit can also be understand as the zeroth order of a systematical expansion in $1/n$ [22]. This connects our theory to the physical relevant case of, e.g., three order parameter components known as the Heisenberg model. But this expansion is more useful for formal studies than to comparison to experimental observations.

II. DEFINITION OF THE MODEL

In the last chapter we have discussed $O(n)$ -symmetrical lattice models but now we turn to the description of the universal critical behavior in the framework of an $O(n)$ -symmetrical ϕ^4 -model. The connection between both is that the n -vector lattice model can be mapped on the n -vector ϕ^4 -model by means of coarse graining [23].

We consider a d -dimensional slab of finite thickness L , which occupies the volume $\mathfrak{V} = \mathbb{R}^{d-1} \times [0, L]$. Let the x_j with $j = 1 \dots, d$, be cartesian coordinates and we write $x_d \equiv z$ to denote the coordinate of the finite direction called the perpendicular direction. The full position vector is given by $\mathbf{x} = (\mathbf{y}, z)$, where $\mathbf{y} = (x_1, \dots, x_{d-1})$ denotes the coordinates of the directions along the slab called parallel directions.

As discussed in detail in [13] the general Hamiltonian of ϕ^4 -models with surfaces is given by

$$\mathcal{H}[\phi(\mathbf{x})] = \int_{\mathfrak{V}} \mathcal{L}_{\mathfrak{V}}[\phi(\mathbf{x})] dV + \int_{\partial\mathfrak{V}} \mathcal{L}_{\partial\mathfrak{V}}[\phi(\mathbf{x})] dA. \quad (2.1)$$

The densities $\mathcal{L}_{\mathfrak{V}}(\mathbf{x})$ and $\mathcal{L}_{\partial\mathfrak{V}}(\mathbf{x})$ depend on the n -component order parameter field $\phi(\mathbf{x})$ and its derivatives. This order parameter field is a classical n -component vector field that, using the language of magnetism, can be interpreted as the local spin density. The first part is the bulk Hamiltonian and the second is the additional surface Hamiltonian. The latter is taken in account because the coupling at the surface might deviate from that in the bulk.

The bulk density $\mathcal{L}_{\mathfrak{V}}(\mathbf{x})$ is given by

$$\mathcal{L}_{\mathfrak{V}}[\phi(\mathbf{x})] = \frac{1}{2} \sum_{\alpha=1}^n (\nabla\phi_{\alpha}(\mathbf{x}))^2 + \frac{\hat{\tau}}{2} \phi^2(\mathbf{x}) + \frac{\hat{u}}{4!n} (\phi^2(\mathbf{x}))^2, \quad (2.2)$$

where $\hat{\tau}$ is the temperature variable often called mass and \hat{u} is the coupling constant.

Note that in contrast to ϕ^4 -theories with a finite number of order parameter field components there is an additional $1/n$ in front of the ϕ^4 -term, which is needed to make the limit $n \rightarrow \infty$ well defined [24].

The general boundary density $\mathcal{L}_{\partial\mathfrak{V}}(\mathbf{x})$ reads

$$\mathcal{L}_{\partial\mathfrak{V}}[\phi(\mathbf{x})] = \frac{\hat{c}(\mathbf{x})}{2} \phi^2(\mathbf{x}). \quad (2.3)$$

The $\hat{c}(\mathbf{x})$ is the surface enhancement that controls the additional couplings at the surface. It may have different values on the two boundaries $\partial\mathfrak{B}_1$ and $\partial\mathfrak{B}_2$, i.e.,

$$\hat{c}(\mathbf{x}) = \begin{cases} \hat{c}_1 & \text{for } \mathbf{x} \in \partial\mathfrak{B}_1, \\ \hat{c}_2 & \text{for } \mathbf{x} \in \partial\mathfrak{B}_2. \end{cases} \quad (2.4)$$

In our framework these boundary terms need not to be taken into account any longer because they give no contribution to the finite size energy that we are interested in and one can take account for the boundary conditions on the surface without those additional terms. The boundary conditions will be taken into account in the calculation of the eigensystem of the system. How this is done will be described in the next section.

III. THE FREE ENERGY

We now want to derive the exact expression for the free energy of the system. In the large- n limit such an expression can be obtained in different ways. One can use, e.g., variational techniques as well as the saddle-point approximation [25]. Both become exact in the limit $n \rightarrow \infty$. In the following we resort on the saddle-point approximation method.

We start the calculation by computing the canonical partition function \mathcal{Z} of the system. It is given by the functional integral over all possible configurations of the order parameter field $\phi(\mathbf{x})$. We write

$$\mathcal{Z} = \int \mathcal{D}[\phi] e^{-\mathcal{H}[\phi]} = \int \mathcal{D}[\phi] \exp \left\{ - \int d^d \mathbf{x} \left[\frac{1}{2} \sum_{\alpha=1}^n (\nabla \phi_\alpha)^2 + \frac{\dot{\tau}}{2} \phi^2 + \frac{\dot{u}}{4!n} (\phi^2)^2 \right] \right\}. \quad (3.1)$$

To determine the partition function with the saddle-point approximation we transform the last expression by applying the Hubbard-Stratonovich decoupling technique [26] and introducing an additional parameter ψ . This leads to

$$\mathcal{Z} = C \int \mathcal{D}[\phi] \int \mathcal{D}[i\psi] \exp \left\{ - \frac{1}{2} \int d^d \mathbf{x} \left[\phi(\mathbf{x}) (-\nabla^2 + \dot{\tau} - \psi(z)) \phi(\mathbf{x}) - \frac{3n}{\dot{u}} \psi^2(z) \right] \right\}. \quad (3.2)$$

The constant pre-factor C is irrelevant since it does not contribute to the excess free energy. The introduced variational parameter ψ is chosen to depend on z because the boundary conditions break the translational invariance along that axis.

The integration over $\phi(\mathbf{x})$ is now Gaussian and can be carried out (see e.g. [27]). This leads us to the expression

$$\mathcal{Z} = \bar{C} \int \mathcal{D}[i\psi] \exp \left[- \frac{n}{2} \text{Tr} \log(-\nabla^2 + \dot{\tau} - \psi(z)) + \frac{3n}{2\dot{u}} \int_0^L dz \psi^2(z) \right]. \quad (3.3)$$

The remaining functional integral can be evaluated by the saddle-point approximation. This means that we take the value of the integrand at its saddle point as solution of the integral. The number of order parameter components n serves as large parameter in the exponential function that makes the saddle-point a sharp peak as required for this approximation. With growing n the peak becomes sharper so that the approximation gets better and will become exact in the limit $n \rightarrow \infty$. So we conclude that the partition function is given by

$$\mathcal{Z} = \bar{C} \exp \left[- \frac{n}{2} \text{Tr} \log(-\nabla^2 + \dot{\tau} - \psi_0(z)) + \frac{3n}{2\dot{u}} \int_0^L dz \psi_0^2(z) \right]. \quad (3.4)$$

From the partition function we obtain the reduced free energy using its definition $F(L) = \mathcal{F}/k_B T = -\log \mathcal{Z}$. It is useful to consider the reduced free energy density per cross sectional area and order parameter component, $f_L = F/An$ with $A \rightarrow \infty$, that comes out as

$$f_L = f_0 + \frac{1}{2} \int_{\mathbf{p}}^{(d-1)} \int_0^L dz \langle z | \log(-\partial_z^2 + \mathbf{p}^2 + \dot{\tau} - \psi_0(z)) | z \rangle - \frac{3}{2\dot{u}} \int_0^L dz \psi_0^2(z), \quad (3.5)$$

where we used the Dirac notation $\text{Tr}(\circ) = \int_0^L dz \langle z | \circ | z \rangle$ and defined

$$\int_{\mathbf{p}}^{(d-1)} \equiv \prod_{i=1}^{d-1} \int_{-\infty}^{\infty} \frac{dp_i}{2\pi}. \quad (3.6)$$

Note that we have set $\psi = \psi_0$ in equations (3.4) and (3.5) where ψ_0 is the saddle-point value. It is defined by requiring that at the saddle-point the integrand must be extremal in ψ , and obeys the self-consistent equation

$$\psi_0(z) = - \frac{\dot{u}}{6} \int_{\mathbf{p}}^{(d-1)} \langle z | \frac{1}{-\partial_z^2 + \mathbf{p}^2 + \dot{\tau} - \psi_0(z)} | z \rangle. \quad (3.7)$$

We now examine this self-consistent equation and determine the saddle-point value and the eigensystem along the z axis. But first we want to remark the following: The problem can also be approached with the help of diagrammatic perturbation theory. From this theory one obtains the Dyson equation

$$\left[\tilde{G}(\mathbf{k})\right]^{-1} = \mathbf{k}^2 + \hat{\tau} - \tilde{\Sigma}(\mathbf{k}) \quad (3.8)$$

for the two point correlation function of the system often named propagator $\tilde{G}(\mathbf{k})$. The contributions from all orders of perturbation theory are summed in the mass-operator $\Sigma(\mathbf{k})$. Usually this cannot be done without approximation but, in the large- n limit the contributions to the mass operator can be summed up exactly (see [24, 28]). That mass-operator has the same self-consistent structure as $\psi_0(z)$ in equation (3.7). So in comparison we can identify $\psi_0(z) = \Sigma(z)$ and we will use $\Sigma(z)$ instead of $\psi_0(z)$ the following. For simplicity we write the mass-operator $\Sigma(z)$ in the mixed \mathbf{p} - z -representation

$$\Sigma(z) = -\frac{\dot{u}}{6} \int_{\mathbf{p}} \int^{\nu} \frac{\hat{\varphi}_{\nu}(z) \hat{\varphi}_{\nu}^*(z)}{\hat{\epsilon}_{\nu} + \mathbf{p}^2 + \hat{\tau}}. \quad (3.9)$$

The $\hat{\varphi}_{\nu}(z)$ and the $\hat{\epsilon}_{\nu}$ are the eigenfunctions and the eigenvalues used to expand the z -dependence and are given by the equation

$$[-\partial_z^2 - \Sigma(z)] \hat{\varphi}_{\nu}(z) = \hat{\epsilon}_{\nu} \hat{\varphi}_{\nu}(z). \quad (3.10)$$

Obviously the quantity $\Sigma(z)$ is not well defined because the \mathbf{p} -integration is UV-divergent. Usually one would have to deal with the procedures of regularization and renormalization to give the divergent expression a physical meaning. But our case is much simpler because we are not interested in the mass-operator itself. Thus we define another quantity which is UV-convergent by taking the difference of $\Sigma(z)$ and a quantity which is UV-divergent to the same order.

For this purpose we decompose the mass $\hat{\tau}$ into $\hat{\tau} = \hat{\tau}_c + \delta\hat{\tau}$. The $\hat{\tau}_c$ gives the value of $\hat{\tau}$ at which the corresponding bulk system reaches criticality and $\delta\hat{\tau}$ gives the deviation from this critical value. The $\hat{\tau}_c$ is given by the expression [24]

$$\hat{\tau}_c = -\frac{\dot{u}}{6} \int_{\mathbf{p}} \int_{-\infty}^{\infty} \frac{dq}{2\pi} \frac{1}{\mathbf{p}^2 + q^2}. \quad (3.11)$$

It is UV-divergent to the same order as $\Sigma(z)$. From the sum of both we now obtain a UV-convergent expression. We define the new quantity

$$U(z) = -\Sigma(z) + \hat{\tau}_c = \frac{\dot{u}}{6} \int_{\mathbf{p}} \int^{\nu} \left(\frac{\varphi_{\nu}(z) \varphi_{\nu}^*(z)}{\epsilon_{\nu} + \mathbf{p}^2 + \delta\hat{\tau}} - \int_{-\infty}^{\infty} \frac{dq}{2\pi} \frac{1}{\mathbf{p}^2 + q^2} \right). \quad (3.12)$$

Introducing this quantity the eigensystem is given by

$$[-\partial_z^2 + U(z)] \varphi_{\nu}(z) = \epsilon_{\nu} \varphi_{\nu}(z). \quad (3.13)$$

To simplify the further discussion we will interpret the two terms on the right hand side of equation (3.12) analogously to Ref. [28]. The first term on the right hand side is the propagator of the slab system for temperature deviations from the critical point defined by $\delta\hat{\tau}$. The second term is the propagator of the corresponding bulk system at criticality where $\delta\hat{\tau} = 0$. With this definitions one may write equation (3.12) in the following form

$$U(z) = \frac{\dot{u}}{6} \int_{\mathbf{p}} \int^{\nu} \left(\tilde{G}(\mathbf{p}; z, z) - \int_{-\infty}^{\infty} \frac{dq}{2\pi} \tilde{G}_{\text{bulk}}(\mathbf{p}; q) \right). \quad (3.14)$$

Equations (3.12) and (3.13) form a self-consistent eigenvalue problem similar to the one dimensional Schrödinger equation of a particle in a potential $U(z)$. The numerical solution of this problem is the content of the following subsection.

A. Discretization of the problem

Using a numerical method we now calculate the potential $U(z)$ and the corresponding eigensystem self-consistently. Therefore the model needs to be discrete along the z -axis. We introduce a discretization of the z -direction with L points and set the lattice constant $a = 1$ without loss of generality, such that $z \rightarrow z_i$ with $z_i \in \{1, 2, 3, \dots, L\}$.

This discretization leads to some more changes. At first the number of eigenvalues ϵ_ν and functions φ_ν is restricted to the number of discrete points L . At second there is also a change of the dispersion relation in the corresponding bulk model. The q^2 in the second term of the right hand side of equation (3.12) has to be replaced by the dispersion relation

$$\epsilon(q) = 4 \sin^2\left(\frac{q}{2}\right) \quad (3.15)$$

of a lattice theory. Due to the periodicity of (3.15) the integration with respect to q is restricted to the first Brillouin zone. Implementing these modifications, the potential $U(z)$ displayed in (3.12) becomes

$$U(z_i) = \frac{\dot{u}}{6} \int_{\mathbf{p}}^{(d-1)} \left[\sum_{\nu=1}^L \frac{\varphi_\nu(z_i) \varphi_\nu^*(z_i)}{\epsilon_\nu + \mathbf{p}^2 + \delta\tilde{\tau}} - \int_0^{2\pi} \frac{dq}{2\pi} \frac{1}{\mathbf{p}^2 + 4 \sin^2(q/2)} \right], \quad (3.16)$$

where the corresponding eigenvalue equation (3.13) now reads

$$[-\partial_z^2 + \mathbf{U}] \varphi_\nu = \epsilon_\nu \varphi_\nu. \quad (3.17)$$

Here the ∂_z^2 and \mathbf{U} are finite $L \times L$ matrices and the φ_ν are the corresponding finite L -component vectors. We specify these objects now: The ∂_z^2 stands for the symmetric differentiation operator for the second derivative of a discrete function. Usually this operator is defined by

$$\partial_z^2 \varphi_\nu(z_i) = \varphi_\nu(z_{i+1}) - 2\varphi_\nu(z_i) + \varphi_\nu(z_{i-1}) \quad (3.18)$$

and can be represented by the matrix

$$\partial_z^2 = \begin{pmatrix} -x & 1 & 0 & \dots & 0 & y \\ 1 & -2 & 1 & & & 0 \\ 0 & 1 & -2 & \ddots & & \vdots \\ \vdots & & \ddots & \ddots & & \vdots \\ 0 & & & & -2 & 1 \\ y & 0 & \dots & \dots & 1 & -x \end{pmatrix}. \quad (3.19)$$

At this stage the boundary conditions of the system come into play. We can control them by choosing adequate values for x and y . The reader can convince himself that if one chooses $x = 1$ [$x = 2$] and $y = 0$ this corresponds to open [Dirichlet] boundary conditions. If one sets $y = 1$ [$y = -1$] and $x = 2$ one gets periodic [antiperiodic] boundary conditions.

The matrix \mathbf{U} is the diagonal matrix of the $U(z_i)$

$$\mathbf{U} = \text{diag}[U(z_i)] \quad (3.20)$$

and the eigenfunctions of the discrete model are represented as vectors where the components are given by

$$\varphi_\nu(z_i) = \varphi_{\nu,i}. \quad (3.21)$$

In this discrete form the self-consistent eigenvalue problem can be implemented into an iterative routine to determine the eigensystem and the matrix \mathbf{U} . The calculations were carried out with build-in functions of the program MATHEMATICA [29].

The iteration starts from an initial guess for the potential. From this guess the associated eigensystem is computed. With the eigensystem one computes again the potential for the next iteration step. This procedure is repeated until the difference between the steps is small enough to fulfill a certain termination condition.

Figure 1 shows the numerical results for the potential $U(z_i)$ plotted over the scaling variable z_i/L . We show system sizes L in powers 2^n from $L = 256$ to $L = 4096$, and we set $\dot{u} = 1$ in to following. Figure 1(left) shows the results for the systems with Dirichlet boundary conditions on both surfaces. The potential as anticipated diverges at the

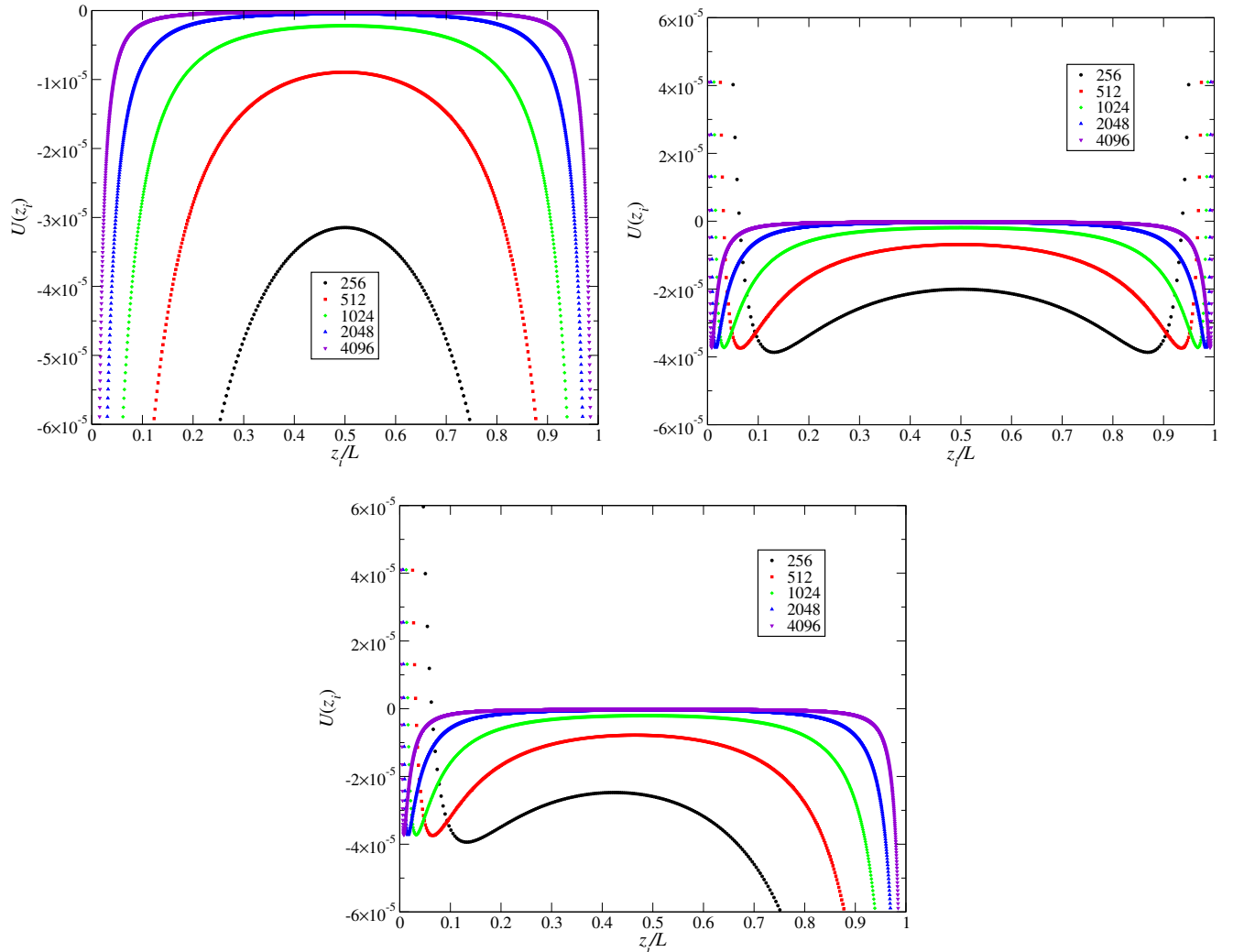


FIG. 1: Numerical data of the potential $U(z_i)$ for systems with Dirichlet-Dirichlet (left), open-open (right), and open-Dirichlet (bottom) boundary conditions.

boundaries to ensure that the eigenfunctions fall to zero on the surface. In the middle of the slab the potential tends with a characteristic algebraic behavior to its bulk value which is zero at criticality (see [22]). This tendency is more and more distinct for bigger systems because the influence of the boundaries in the middle of the slab decays with increasing system size. Figure 1(right) shows the results for open boundary conditions. In the middle of the slab the potential approaches the behavior of systems with Dirichlet boundary conditions. This approach becomes stronger for larger systems. But next to the surfaces the evolution differs very strongly from the Dirichlet case. The most remarkable difference is that the potential has now a finite, positive value at the surface. When there are both boundary conditions mixed in one system as it is shown in Figure 1(bottom) we find the diverging behavior on the Dirichlet side and the finite values on the open side. The values of the potential in the middle of the slab are still converging to the bulk value with increasing system size.

The Dirichlet and the open system are that similar because they are in the same surface universality class [13]. This means that their asymptotical behavior for large L and large values of z far away from the surface is identical.

To test the quality of our method we have also computed the potential $U(z)$ for the known cases of periodic and antiperiodic boundary conditions with our numerical method. We found that our results are in excellent agreement with the analytical results. A comparison between our results for the Casimir amplitude calculated from this potentials and the analytic results is shown in the next section.

IV. EXCESS FREE ENERGY AND CASIMIR AMPLITUDES

Now that the $U(z)$ is determined we can calculate the Casimir amplitudes. But first we have to modify the expression of the free energy by using the definitions $\hat{\tau} = \hat{\tau}_c + \delta\hat{\tau}$ and $\Sigma(z) = \hat{\tau}_c - U(z)$ to have only well defined quantities in it.

As we are not interested in the free energy itself but in the difference of the free energy of the slab and the bulk, called excess free energy we need an expression for the free energy of the bulk. We obtain this expression from a calculation analogous to that in the last chapter. The translational invariance of the bulk allows one to obtain its free energy analytically [22].

Now the exact expression for the excess free energy defined in Sec. I can be written in the form

$$f_{\text{ex}} = \frac{1}{2} \int_{\mathbf{p}}^{(d-1)} \sum_{\nu} \log(\epsilon_{\nu} + \mathbf{p}^2 + \delta\hat{\tau}) - \frac{3}{2\hat{u}} \int_0^L dz (\hat{\tau}_c - U(z))^2 - \frac{L}{2} \int_{\mathbf{p}}^{(d-1)} \int_{-\infty}^{\infty} \frac{dq}{2\pi} \log(\mathbf{p}^2 + q^2 + \delta\hat{\tau} + U_{\text{bulk}}) + \frac{3L}{2\hat{u}} (\hat{\tau}_c - U_{\text{bulk}})^2. \quad (4.1)$$

Because of the discrete numerical evaluation of the potential $U(z)$ all z dependencies in the last expression have to be discrete. This is what will be done the next section.

A. Discrete form of f_{ex}

We now obtain the form of the excess free energy with a discretized z dependence. This means substituting $z \rightarrow z_i$ like in Sec. III. With this change we have to replace the dispersion relation of the continuum by that of the lattice and restrict the q momentum integrations to the first Brillouin zone (see also Sec. III). Finally the real space integration along the z -axis has to be turned into a sum. This is achieved using $\int_0^L dz \rightarrow \sum_{i=1}^L$ as we have set $a = 1$. From this changes we obtain the excess free energy in the discrete form given by

$$f_{\text{ex}} = \frac{1}{2} \int_{\mathbf{p}}^{(d-1)} \sum_{\nu=1}^L \log(\epsilon_{\nu} + \mathbf{p}^2 + \delta\hat{\tau}) - \frac{3}{2\hat{u}} \sum_{i=1}^L (\hat{\tau}_c - U(z_i))^2 - \frac{L}{2} \int_{\mathbf{p}}^{(d-1)} \int_0^{2\pi} \log\left[\mathbf{p}^2 + 4 \sin^2\left(\frac{q}{2}\right) + \delta\hat{\tau} + U_{\text{bulk}}\right] + \frac{3L}{2\hat{u}} (\hat{\tau}_c - U_{\text{bulk}})^2. \quad (4.2)$$

Since we are interested in the Casimir amplitude we limit the following discussion to the case $T = T_{c,\infty}$ and set the temperature variable $\delta\hat{\tau} = 0$. In the following we use the result that the U_{bulk} equals zero at $T_{c,\infty}$ (see [22]).

After evaluating the momentum integrals we get the expression

$$f_{\text{ex}} = \frac{\pi^{1-\frac{d}{2}}}{\cos\left(\frac{\pi d}{2}\right)} \left[-\frac{2^{-d}\sqrt{\pi}}{\Gamma\left(\frac{d+1}{2}\right)} \sum_{\nu=1}^L \epsilon_{\nu}^{\frac{d-1}{2}} + \frac{L\Gamma\left(\frac{d}{2}\right)}{2\Gamma\left(\frac{d+1}{2}\right)^2} + \frac{\Gamma\left(\frac{d}{2}-1\right)}{8\Gamma\left(\frac{d-1}{2}\right)^2} \sum_{i=1}^L U(z_i) \right] - \frac{3}{2\hat{u}} \sum_{i=1}^L U(z_i)^2. \quad (4.3)$$

Examining this expression one recognizes that it has a remaining pole term in $d = 3$ space dimensions. This pole term can be understood by realizing that the q -integration is carried out but the corresponding summation over the eigenvalues is left unevaluated. The pole term needs to be removed to set $d = 3$ because the evaluation of the remaining sum in arbitrary dimensions is not feasible.

BC	a_0	a_2	a_3	a_4
OO	0.0297	-0.0122	0.0106	-6.06
DO	-0.0466	-0.0119	-2.97	441.
DD	0.0309	-0.0115	-4.53	427.
PBC	-	-0.1530	-1.23	51.0
APBC	-	0.2742	-27.4	3390.

TABLE I: Fit parameters for the excess free energy, Eq. (4.6), for $\hat{u} = 1$. OO means open boundary conditions on both sides, DD means the same with Dirichlet boundary conditions, and DO means the mix of both.

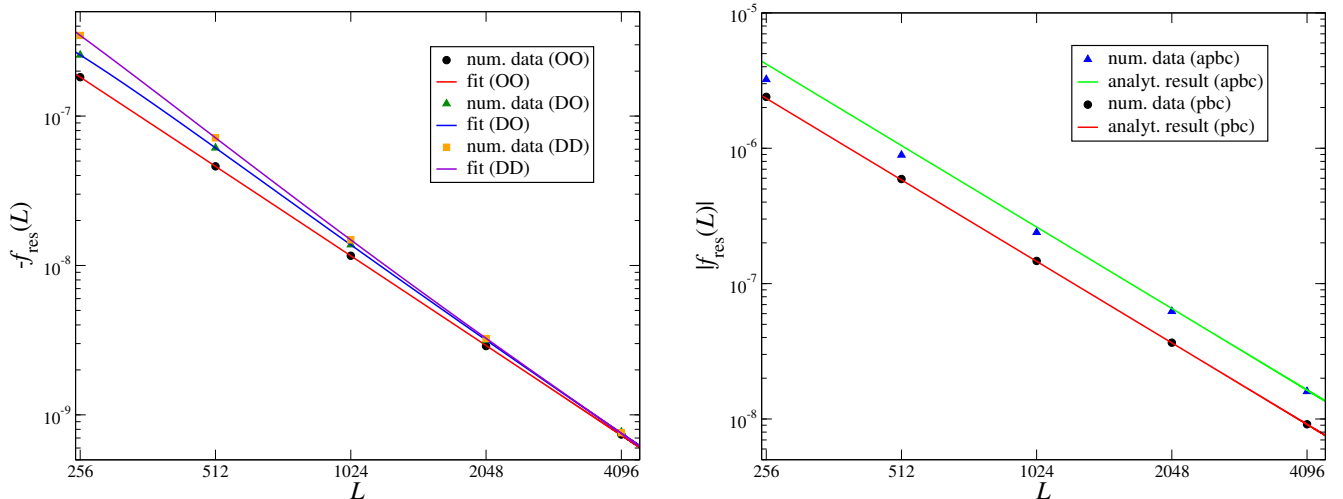


FIG. 2: Left: Numerical data with the corresponding fits for open-open (OO), Dirichlet-open (DO) and Dirichlet-Dirichlet (DD) boundary conditions. Right: Comparison between analytic and numeric results for periodic (PBC) and antiperiodic (APBC) boundary conditions.

To make the pole-term visible and isolate it we expand f_{ex} around space dimension $d = 3$. In this expansion we find a term of order $\mathcal{O}(1/(d-3))$ and a term of order $\mathcal{O}(1)$,

$$\frac{1}{8\pi} \left(\frac{2}{d-3} + \gamma - \log(4\pi) \right) \left\{ - \sum_{\nu=1}^L \epsilon_{\nu} + \sum_{i=1}^L [2 + U(z_i)] \right\}, \quad (4.4)$$

which vanish as both sums in the curly braces are equal to the trace of the matrix $-\partial_z^2 + U$. The zeroth order of the expansion contains the whole information of the excess free energy at $d = 3$ so we restrict us to the discussion of this term. The final result at $d = 3$ becomes

$$f_{\text{ex}} = \frac{1}{8\pi} \sum_{\nu=1}^L \epsilon_{\nu} (1 - \log \epsilon_{\nu}) - \frac{3}{2\hat{u}} \sum_{i=1}^L U(z_i)^2. \quad (4.5)$$

In this expression the remaining sums can be evaluated to obtain the excess free energies for the given system sizes.

To compute the Casimir amplitude from the evolution of the numerical evaluated excess free energy with increasing system size we fit the data using the *ansatz*

$$f_{\text{ex}} = a_0 + a_2 L^{-2} + a_3 L^{-3} + a_4 L^{-4} + \dots \quad (4.6)$$

where the factor a_2 will later be interpreted as the Casimir amplitude. This fitting *ansatz* is justified by the following: From fundamental arguments one knows that the order $O(L^{-1})$ is absent and the leading order is the order $O(L^{-2})$ [5, 8]. Higher orders are caused by corrections to the leading scaling behavior (for details see [30]). Here we restrict ourselves to orders up to $O(L^{-4})$. The constant term a_0 is caused by surface contributions introduced by the considered boundary conditions and is absent in the case of periodic and antiperiodic boundary conditions. The numerical data and the associated fits for $\hat{u} = 1$ are shown in Figure 2(left) and the results for the fitting parameters are assembled in Table I.

Interpreting the fit parameter a_2 as the Casimir amplitude we estimate the values

$$\begin{aligned} \Delta_{\text{C,OO}} &= -0.012(1) \\ \Delta_{\text{C,DO}} &= -0.012(3) \\ \Delta_{\text{C,DD}} &= -0.012(3), \end{aligned} \quad (4.7)$$

where the numbers in brackets give the error bars.

As anticipated the numerical values of the Casimir amplitudes lie all together in a small range. They are equal up to the third decimal place when we take the adjusted error bar into account. We see that due to the fact that the boundary conditions are all in the same surface universality class the evolutions of the excess free energies of the three

systems are asymptotically equivalent for large L . Looking at the non-universal corrections to the leading scaling behavior namely the terms of order $O(L^{-3})$ and $O(L^{-4})$ we see that their weights are much higher in the DD and DO case compared to the OO case.

We checked the accuracy of our method by computing results for the periodic and the antiperiodic case and comparing them to the analytical results. Our fit parameters are also shown in Tab. I and the numerical result are compared to the analytic results in Fig. 2(right). The analytical results for the Casimir amplitudes [12, 17] are given by

$$\Delta_{C,\text{PBC}} = -\frac{2\zeta(3)}{5\pi} = -0.153050\dots, \quad (4.8a)$$

$$\Delta_{C,\text{APBC}} = \frac{\text{Cl}_2(\pi/3)}{3} - \frac{\zeta(3)}{6\pi} = +0.274542\dots. \quad (4.8b)$$

where Cl_n denotes the Clausen function. For the case of periodic boundary conditions we find a perfect agreement with the analytic results. For the case of antiperiodic boundary conditions we find an asymptotic agreement for large L because there are more corrections due to the inhomogeneity introduced by this boundary condition.

V. SUMMARY AND CONCLUDING REMARKS

We showed a new method for the computation of Casimir amplitudes in the large- n limit. This method can be applied to the case of slabs with non translationally invariant boundary conditions as well as for those with periodic and antiperiodic boundary conditions. We evaluated the Casimir amplitudes for the cases of Dirichlet-Dirichlet, open-open and Dirichlet-open boundary conditions and reproduced their asymptotical equivalence in the limit of large systems. We find that the non-universal corrections to the leading scaling behavior in the open-open case are much smaller than in the other cases. From this we conclude that evaluations of Casimir amplitudes following our method in this universality class are simpler in this open-open case. We also confirmed the known analytic result for the Casimir amplitudes in the case of periodic and antiperiodic boundary conditions.

Acknowledgments

We would like to thank H. W. Diehl for the inspiration and initial ideas to work on this issue and for many constructive discussions. We also want to thank Felix M. Schmidt and Hassan Chamati for discussions and additional ideas.

-
- [1] H. B. G. Casimir, Proc. K. Ned. Akad. Wet., Ser. B, **51**, 793 (1948).
 - [2] U. Mohideen and A. Roy, Phys. Rev. Lett. **81**, 4549 (1998).
 - [3] G. Bressi, G. Carugno, R. Onofrio and G. Ruoso, Phys. Rev. Lett. **88**, 041804 (2002).
 - [4] T. Ederth, Phys. Rev. A **62**, 062104 (2000).
 - [5] M. E. Fisher and P.-G. de Gennes, C. R. Acad. Sci. Paris Série B **287**, 207 (1978).
 - [6] R. Garcia and M. H. W. Chan, Phys. Rev. Lett. **83**, 1187 (1999).
 - [7] A. Hucht, Phys. Rev. Lett. **99**, 185301 (2007).
 - [8] M. Krech and S. Dietrich, Phys. Rev. A **46**, 1886 (1992).
 - [9] M. N. Barber, in *Phase Transitions and Critical Phenomena*, edited by C. Domb and J. L. Lebowitz (Academic, London, 1983), vol. 8, pp. 145–266.
 - [10] M. Krech, *Casimir Effect in Critical Systems* (World Scientific, Singapore, 1994).
 - [11] M. Krech, J. Phys.: Condens. Matter **11**, R391 (1999).
 - [12] J. G. Brankov, D. M. Dantchev, and N. S. Tonchev, *Theory of Critical Phenomena in Finite-Size Systems — Scaling and Quantum Effects* (World Scientific, Singapore, 2000).
 - [13] H. W. Diehl, in *Phase Transitions and Critical Phenomena*, edited by C. Domb and J. L. Lebowitz (Academic, London, 1986), vol. 10, pp. 75–267.
 - [14] H. W. Diehl, D. Grüneberg, and M. A. Shpot, Europhys. Lett. **75**, 241 (2006).
 - [15] D. Grüneberg and H. W. Diehl, Phys. Rev. B **77**, 115409 (2008).
 - [16] F. M. Schmidt and H. W. Diehl, Phys. Rev. Lett. **101**, 100601 (2008).
 - [17] D. Dantchev and D. Grüneberg, Phys. Rev. E **79**, 041103 (2009).
 - [18] E. Brézin, J. Physique **43**, 15 (1982).

- [19] T. H. Berlin and M. Kac, Phys. Rev. **86**, 821 (1952).
- [20] H. E. Stanley, Phys. Rev. **176**, 718 (1968).
- [21] H. J. F. Knops, J. Phys. A **14**, 1918 (1973).
- [22] S.-K. Ma, in *Phase Transitions and Critical Phenomena*, edited by C. Domb and M. S. Green (Academic, London, 1976), vol. 6, chap. 4, pp. 249–292.
- [23] P. M. Chaikin and T. C. Lubensky, *Principles of condensed matter theory* (Cambridge University Press, Cambridge (GB), 1995).
- [24] D. J. Amit, *Field theory, the renormalization group, and critical phenomena* (World Scientific, Singapore, 2005), 3rd ed.
- [25] M. Moshe and J. Zinn-Justin, Physics Reports **385**, 69 (2003).
- [26] J. Hubbard, Phys. Lett. **3**, 77 (1959).
- [27] N. Goldenfeld, *Lectures on phase transitions and the renormalization group* (Addison-Wesley Publishing Company, Reading, 1992), 1st ed.
- [28] A. J. Bray and M. A. Moore, J. Phys. A **10**, 1927 (1977).
- [29] I. Wolfram Research, *Mathematica Edition: Version 6.0* (Wolfram Research, Inc., Champaign, 2007).
- [30] F. Wegner, Phys. Rev. B **5**, 4529 (1972).
- [31] \sim means "asymptotically equal", i.e., $f(x) \sim g(x) \Leftrightarrow \lim_{x \rightarrow \infty} f(x)/g(x) = 1$

Nonequilibrium phase transition in an exactly solvable driven Ising model with friction

Alfred Hucht

Fakultät für Physik und CeNIDE, Universität Duisburg–Essen, D-47048 Duisburg, Germany

(Received 3 September 2009; published 30 December 2009)

A driven Ising model with friction due to magnetic correlations was proposed by Kadau *et al.* [Phys. Rev. Lett. **101**, 137205 (2008)]. The nonequilibrium phase transition present in this system is investigated in detail using analytical methods as well as Monte Carlo simulations. In the limit of high driving velocities v the model shows mean-field behavior due to dimensional reduction and can be solved exactly for various geometries. The simulations are performed with three different single spin-flip rates: the common Metropolis and Glauber rates as well as a *multiplicative* rate. Due to the nonequilibrium nature of the model all rates lead to different critical temperatures at $v > 0$, while the exact solution matches the multiplicative rate. Finally, the crossover from Ising to mean-field behavior as function of velocity and system size is analyzed in one and two dimensions.

DOI: [10.1103/PhysRevE.80.061138](https://doi.org/10.1103/PhysRevE.80.061138)

PACS number(s): 05.50.+q, 68.35.Rh, 04.20.Jb

I. INTRODUCTION

Magnetic contributions to friction due to spin correlations have attracted increasing interest in recent years. One interesting aspect is the energy dissipation due to spin waves in magnetic force microscopy, where magnetic structures are investigated by moving a magnetic tip over a surface [1–3]. On the other hand, magnetic friction is also present in bulk magnetic systems which are in close proximity. In this context, Kadau *et al.* [4] proposed a simple model for magnetic friction mediated solely by spin degrees of freedom. In this model an Ising spin system is moved over a second spin system with constant velocity v along a boundary. This permanent perturbation drives the system to a steady state far away from equilibrium, leading to a permanent energy flow from the boundary to the heat bath.

This problem can be analyzed for several different geometries in one, two, and three dimensions, as shown in Fig. 1: besides the original problem of two half-infinite two-dimensional systems moving along the one-dimensional boundary, denoted by $2d_b$ in the following, we will consider the homogeneous cases $1d$ and $2d$ where all spins are at the boundary, as well as the experimentally relevant three-dimensional case ($3d_b$). Additionally, we will extend the analysis to sheared systems in two [5–7] and three [8] dimensions, denoted by $1+1d$ and $2+1d$. These systems are experimentally accessible within the framework of shear flow in binary liquid mixtures (for a review, see [9]), though with conserved order parameter, while we deal with a non-conserved order parameter.

This model has some similarities to the *driven lattice gas* (DLG) proposed by Katz *et al.* [10] (see [11] for a review), where a system is driven out of equilibrium by an applied field which favors the motion of particles in one direction. We will discuss these similarities throughout this work.

The paper is organized as follows: in the first part we will introduce the model and geometries and present, in the second part, an exact solution of the model in the limit of high driving velocities $v \rightarrow \infty$, which will be checked numerically in the last part using Monte Carlo (MC) simulations. There we will also investigate the case of finite velocities v .

II. MODEL

Let us start with the simplest case denoted $1d$ in Fig. 1 and consider two Ising chains with spin variables $\sigma = \pm 1$, nearest-neighbor coupling $K = \beta J$ ($\beta = 1/k_B T$ and we set $k_B = 1$) and L_{\parallel} sites each, interacting with boundary coupling $K_b = \beta J_b$ and moving along each other with relative velocity v . In the Monte Carlo simulation the upper system is moved v times by one lattice constant a_0 with respect to the lower system during each random sequential Monte Carlo sweep (MCS). As one MCS corresponds to a typical spin-relaxation time $t_0 = O(10^{-8} \text{ s})$ [12] and $a_0 = O(10^{-10} \text{ m})$, the velocity v is given in natural units $a_0/t_0 = O(1 \text{ cm/s})$ (we will set $a_0 = t_0 = 1$ in the following).

To simplify the implementation, instead of moving the upper part of the lattice with respect to the lower part we reorder the couplings at the boundary with time. This procedure is analogous to the Lees-Edwards or *moving boundary condition* in molecular-dynamics simulations of fluids [13] and leads to a system as shown in Fig. 2. Assuming periodic boundary conditions (PBCs) $\sigma_{k,l} \equiv \sigma_{k,l \bmod L_{\parallel}}$ in the parallel direction, the time-dependent Hamiltonian reads

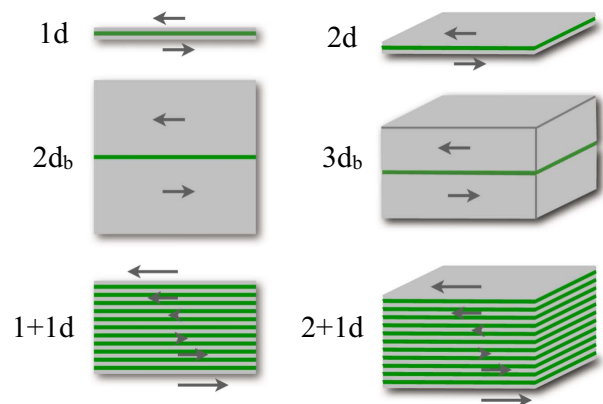


FIG. 1. (Color online) Overview of the geometries considered in this work. The gray regions are the magnetic systems, while the green (dark) regions are the moving boundaries. The arrows indicate the motion of the subsystems.

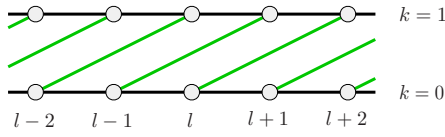


FIG. 2. (Color online) Sketch of geometry 1d after $\Delta=2$ moves. Spin $\sigma_{0,l}$ interacts with spin $\sigma_{1,l+2}$ with coupling J_b [green (gray) lines], while all other couplings are J (black lines).

$$\beta\mathcal{H}(t) = -K \sum_{k=0}^1 \sum_{l=1}^{L_{\parallel}} \sigma_{k,l} \sigma_{k,l+1} - K_b \sum_{l=1}^{L_{\parallel}} \sigma_{0,l} \sigma_{1,l+\Delta(t)}, \quad (1)$$

with the time-dependent displacement

$$\Delta(t) = vt. \quad (2)$$

The second geometry considered in this work is the 2d_b case shown in Fig. 3, which already was investigated by Kadau *et al.* [4]. Here we have a square lattice with $L_{\parallel} \times L_{\perp}$ sites and periodic boundary conditions in both directions, i.e., $\sigma_{k,l} \equiv \sigma_{k \bmod L_{\perp}, l \bmod L_{\parallel}}$. Note that especially $\sigma_{L_{\perp},l} \equiv \sigma_{0,l}$. The Hamiltonian of this system becomes

$$\beta\mathcal{H}(t) = - \sum_{k=1}^{L_{\perp}} \sum_{l=1}^{L_{\parallel}} K \sigma_{k,l} \sigma_{k,l+1} + K_{\perp,k} \sigma_{k,l} \sigma_{k+1,l+\Delta_k(t)}, \quad (3)$$

with $\Delta_k(t) \equiv 0$ and $K_{\perp,k} = K$ for all rows except row $k=0$, where the couplings to row $k=1$ are shifted with constant velocity $\Delta_0(t) \equiv \Delta(t) = vt$. The coupling $K_{\perp,0} \equiv K_b$ across the boundary is allowed to be different from K . For $v=0$ and $J_b = J = 1$ this system simplifies to the two-dimensional (2D) Ising model in equilibrium, which was solved exactly by [14] and shows a continuous phase transition at

$$T_{c,\text{eq}} = \frac{2}{\ln(1 + \sqrt{2})} = 2.269\,185\,3\dots \quad (4)$$

Note that both systems are translationally invariant in \parallel direction under the transformation $l \rightarrow l+1$ and obey reflection symmetry at the boundary under $k \rightarrow 1-k$.

III. EXACT SOLUTION AT HIGH VELOCITIES

In Ref. [4] it was shown that for high velocities $v \gg 1$ the properties of the 2d_b system become independent of v . This

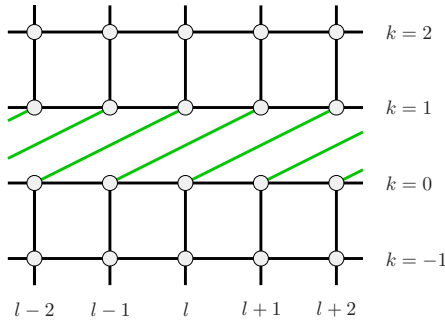


FIG. 3. (Color online) Sketch of geometry 2d_b after $\Delta=2$ moves.

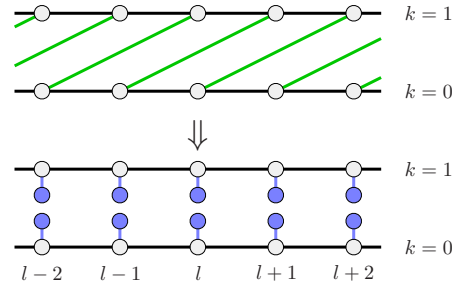


FIG. 4. (Color online) Mapping of the 1d driven system, shown for $\Delta=2$, on two disconnected 1D systems with fluctuating fields.

can be understood as follows: in the limit $v \rightarrow \infty$ the interaction $K_b \sigma_{0,l} \sigma_{1,l+\Delta(t)}$ across the driven boundary becomes uncorrelated, as, in the Monte Carlo simulations, at large v the spin $\sigma_{1,l+\Delta(t)}$ is different in every trial step and can, for simplicity, be a randomly chosen spin $\sigma_{1,\text{rnd}}$ from row 1. Note that this simplification was checked within the simulations and indeed gave the same results, enabling us to perform simulations *at* $v = \infty$. Thus the boundary coupling can be replaced by the action of a fluctuating boundary field μ , e.g.,

$$\sigma_{0,l} \sigma_{1,l+\Delta(t)} \rightarrow \sigma_{0,l} \sigma_{1,\text{rnd}} \rightarrow \sigma_{0,l} \mu_{0,l}, \quad (5)$$

with stochastic variables $\mu_{kl} = \pm 1$ ($k=0,1$) under the constraint $\langle \mu_{kl} \rangle = \langle \sigma_{kl} \rangle = m_b$, where m_b denotes the magnetization at the driven boundary. Here we used the translation symmetry $\langle \sigma_{kl} \rangle = m_k$ and the reflection symmetry at the boundary, $m_k = m_{1-k}$. In Fig. 4 this mapping of the driven system onto a system with fluctuating boundary fields is illustrated for the 1d case. The next step will be to map the fluctuating fields onto static fields by integrating out the degrees of freedom μ_{kl} .

A. Ising model in a fluctuating field

Consider a general Ising model with arbitrary couplings K_{ij} in a static external field h_i^{ext} and additional fluctuating fields of strength k_i (note the factor β in all field quantities)

$$\beta\mathcal{H}_{\mu} = - \sum_{i<j} K_{ij} \sigma_i \sigma_j - \sum_i (h_i^{\text{ext}} + k_i \mu_i) \sigma_i, \quad (6)$$

where the $\mu_i = \pm 1$ are stochastic variables at site i with given average

$$\langle \mu_i \rangle = m_i. \quad (7)$$

As this condition is given *a priori*, averages containing μ_i can be calculated using the trace formula

$$\text{Tr}_{\mu} f(\mu_i) = \sum_{\mu_i = \pm 1} f(\mu_i) p_i(\mu_i) \quad (8)$$

with the probability distribution $p_i(\mu_i) = (1 + \mu_i m_i) / 2$, as then

$$\langle \mu_i \rangle = \text{Tr}_{\mu} \mu_i = \sum_{\mu_i = \pm 1} \mu_i p_i(\mu_i) = m_i$$

as assumed. With the decomposition

$$\beta\mathcal{H}_\mu = \beta\mathcal{H}_0 - \sum_i k_i \mu_i \sigma_i, \quad (9)$$

the degrees of freedom μ in the partition function \mathcal{Z} can be traced out,

$$\begin{aligned} \mathcal{Z} &= \text{Tr}_{\sigma\mu} e^{-\beta\mathcal{H}_\mu} = \text{Tr}_\sigma e^{-\beta\mathcal{H}_0} \text{Tr}_\mu \prod_i e^{k_i \mu_i \sigma_i} \\ &= \text{Tr}_\sigma e^{-\beta\mathcal{H}_0} \prod_i \sum_{\mu_i=\pm 1} e^{k_i \mu_i \sigma_i} p_i(\mu_i) \\ &= \prod_i \cosh k_i \text{Tr}_\sigma e^{-\beta\mathcal{H}_0} \prod_i [1 + \sigma_i m_i \tanh k_i], \quad (10) \end{aligned}$$

where we used the fact that $\sigma_i = \pm 1$.

On the other hand, the Hamiltonian of the equilibrium Ising model without fluctuating fields in a static field h_i can be written as

$$\beta\mathcal{H}_{\text{eq}} = - \sum_{i<j} K_{ij} \sigma_i \sigma_j - \sum_i h_i \sigma_i = \beta\mathcal{H}_0 - \sum_i b_i \sigma_i, \quad (11)$$

with \mathcal{H}_0 from Eq. (9) if we let $b_i = h_i - h_i^{\text{ext}}$. The partition function of this model clearly fulfills

$$\begin{aligned} \mathcal{Z}_{\text{eq}} &= \text{Tr}_\sigma e^{-\beta\mathcal{H}_{\text{eq}}} \\ &= \text{Tr}_\sigma e^{-\beta\mathcal{H}_0} \prod_i e^{b_i \sigma_i} \\ &= \prod_i \cosh b_i \text{Tr}_\sigma e^{-\beta\mathcal{H}_0} \prod_i [1 + \sigma_i \tanh b_i]. \quad (12) \end{aligned}$$

Comparing Eqs. (10) and (12), we conclude that under the condition

$$\tanh b_i = m_i \tanh k_i, \quad (13)$$

the partition function \mathcal{Z} can be expressed in terms of \mathcal{Z}_{eq} ,

$$\mathcal{Z} = \prod_i \left. \frac{\cosh k_i}{\cosh b_i} \mathcal{Z}_{\text{eq}} \right|_{\text{Eq.(13)}}. \quad (14)$$

To summarize, the coupling with strength k_i to fluctuating fields $\mu_i = \pm 1$ with given average $\langle \mu_i \rangle = m_i$ can be written as coupling to static effective fields b_i with strength given by Eq. (13). In the next section we will use this mapping to exactly solve the driven Ising model for high velocities $v \rightarrow \infty$.

B. Application to the driven Ising model

The general condition [Eq. (13)] for the effective static fields b_i simplifies for the systems considered in this work: as all boundary spins are equivalent, $m_i = m_b$, with coupling $k_i = K_b$, leading to a uniform effective field $h_b = \text{artanh}(m_b \tanh K_b)$ at the boundary, as we assume no additional external fields, $h_i^{\text{ext}} = 0$. Inserting this into the equilibrium expression for the boundary magnetization $m_{b,\text{eq}}(K, h_b) = \partial \ln \mathcal{Z}_{\text{eq}} / \partial h_b$, we end with the self-consistence condition

$$m_{b,\text{eq}}[K, \text{artanh}(m_b \tanh K_b)] = m_b \quad (15)$$

for the nonequilibrium order parameter m_b .

As $1 = \partial m_{b,\text{eq}} / \partial m_b |_{m_b=0}$ at criticality, we obtain a very useful connection between the reduced zero-field boundary susceptibility of the equilibrium model $\chi_{b,\text{eq}}^{(0)}(K) = \partial m_{b,\text{eq}} / \partial h_b |_{h_b=0}$ and the critical temperature T_c of the driven system by expanding Eq. (15) to first order around $m_b = 0$, namely,

$$\chi_{b,\text{eq}}^{(0)}(K_c) \tanh K_{b,c} = 1. \quad (16)$$

In the following we will apply these results to the one- and two-dimensional models introduced in Sec. II.

C. 1d case

The effective Hamiltonian of the system 1d in a fluctuating field reads

$$\beta\mathcal{H} = - \sum_{l=1}^{L_\parallel} K \sigma_l \sigma_{l+1} + (h^{\text{ext}} + K_b \mu_l) \sigma_l. \quad (17)$$

Applying the self-consistence condition Eq. (15) to the well-known expression for the equilibrium magnetization of the one-dimensional (1D) Ising model (cf. [15])

$$m_{\text{eq}}(K, h) = \frac{\sinh h}{\sqrt{e^{-4K} + \sinh^2 h}}, \quad (18)$$

we obtain the zero-field magnetization of the 1d driven system in the ordered phase for velocity $v \rightarrow \infty$,

$$m(K, K_b) = \sqrt{\frac{\cosh 2K_b - \coth 2K}{\cosh 2K_b - 1}}, \quad (19)$$

with critical temperature fulfilling

$$e^{2K_c} \tanh K_{b,c} = 1, \quad (20)$$

as $\chi_{\text{eq}}^{(0)}(K) = e^{2K}$ in this case. Interestingly, Eq. (19) is equal to the spontaneous surface magnetization of the 2D equilibrium Ising model [[16], Chap. VI, Eq. 5.20] if we identify K and K_b with the couplings \parallel and \perp to the surface and consequently has the identical critical temperature T_c . For the special case $K = K_b$ this gives the well-known value from Eq. (4). However, we regard this equality as coincidence without deeper meaning, as Eq. (19) is solution of a simple quadratic equation with small integer coefficients when written in the natural variables. Nevertheless, we checked this identity in the 2d case and found that we do *not* get the surface magnetization of the 3D system by the same procedure, as the critical temperature is $T_c \approx 4.058$ [Eq. (60)] instead of the correct value $T_c = 4.511\,424(53)$ [17,18].

To calculate other quantities we use the transfer-matrix (TM) formulation: the TM of the 1D equilibrium Ising model reads (cf. [52])

$$\mathbf{T}_{\text{eq}} = \begin{pmatrix} e^{K+h} & e^{-K} \\ e^{-K} & e^{K-h} \end{pmatrix} \quad (21)$$

and the partition function of a periodic system with L_\parallel spins can be expressed as

$$\mathcal{Z}_{\text{eq}} = \text{Tr} \mathbf{T}_{\text{eq}}^{L_\parallel}. \quad (22)$$

Using Eq. (14) and the conditions Eq. (13) we can write

$$\mathcal{Z} = \text{Tr } \mathbf{T}^{L_{\parallel}} \quad (23)$$

with the TM (we set $h^{\text{ext}}=0$ from now on)

$$\mathbf{T} = \frac{\cosh K_b}{\cosh h} \mathbf{T}_{\text{eq}} \Big|_{\tanh h = m \tanh K_b}, \quad (24)$$

which can be written as

$$\mathbf{T} = \cosh K_b \begin{pmatrix} e^K(1 + \sin \psi) & e^{-K} \cos \psi \\ e^{-K} \cos \psi & e^K(1 - \sin \psi) \end{pmatrix} \quad (25)$$

using

$$\sin \psi = m \tanh K_b. \quad (26)$$

The angle ψ decreases from $\psi = \pi/2$ at $T=0$ to $\psi=0$ at $T \geq T_c$. The eigenvalues λ_{μ} of \mathbf{T} fulfill

$$\mathbf{T}|t_{\mu}\rangle = \lambda_{\mu}|t_{\mu}\rangle \quad (27)$$

and are given by

$$\lambda_{0,1} = \begin{cases} e^{K \pm K_b} & T \leq T_c \\ \cosh K_b (e^K \pm e^{-K}) & T \geq T_c, \end{cases} \quad (28)$$

where λ_0 denotes the larger eigenvalue dominant in the thermodynamic limit. Note that in this limit the analog to the free-energy density

$$f = -\frac{1}{\beta} \ln \lambda_0 = -(J + J_b) \quad (29)$$

of the driven system is simply a constant in the ordered phase $T \leq T_c$ [35]. Nevertheless, we can calculate physical quantities within this TM notation using expectation values as the whole information of the half-infinite system is contained in the normalized eigenvectors

$$|t_0\rangle = \begin{pmatrix} \cos \phi \\ \sin \phi \end{pmatrix}, \quad |t_1\rangle = \begin{pmatrix} -\sin \phi \\ \cos \phi \end{pmatrix}, \quad (30)$$

with $\cos 2\phi = m$. Using the normalized TM $\hat{\mathbf{T}} = \mathbf{T}/\lambda_0$ and the Pauli matrix $\mathbf{M} = \text{diag}(1, -1)$, the magnetization [Eq. (19)] can be expressed as

$$m = \langle t_0 | \mathbf{M} | t_0 \rangle, \quad (31)$$

while the correlation function in \parallel direction becomes

$$\begin{aligned} g_{\parallel}(n) &= \langle \sigma_l \sigma_{l+n} \rangle - \langle \sigma_l \rangle \langle \sigma_{l+n} \rangle \\ &= \langle t_0 | \mathbf{M} \hat{\mathbf{T}}^n \mathbf{M} | t_0 \rangle - \langle t_0 | \mathbf{M} | t_0 \rangle^2 \\ &= \lambda_1^n \lambda_0^{-n} \langle t_0 | \mathbf{M} | t_1 \rangle^2, \end{aligned} \quad (32)$$

as $\mathbf{T}^n = \sum_{\mu} \lambda_{\mu}^n |t_{\mu}\rangle \langle t_{\mu}|$. We get the result

$$g_{\parallel}(n) = \begin{cases} (1 - m^2) e^{-2nK_b} & T \leq T_c \\ \tanh^n K & T \geq T_c, \end{cases} \quad (33)$$

leading to the inverse correlation length

$$\xi_{\parallel}^{-1} = \ln \frac{\lambda_0}{\lambda_1} = \begin{cases} 2K_b & T \leq T_c \\ \ln \coth K & T \geq T_c. \end{cases} \quad (34)$$

Note that ξ_{\parallel} does not diverge at the critical point, a feature which would lead to a correlation length exponent $\nu=0$. In

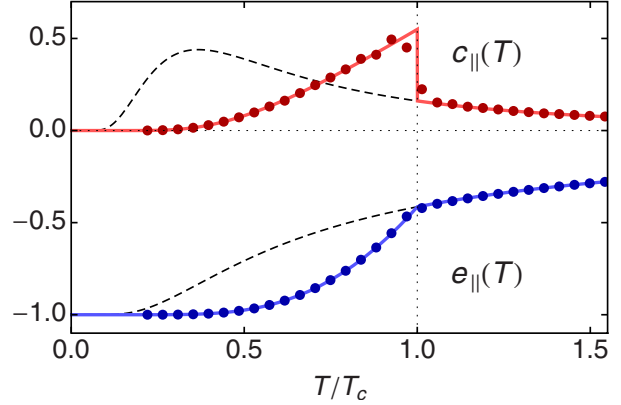


FIG. 5. (Color online) Internal energy $e_{\parallel}(T)$ [Eq. (35)] and specific heat $c_{\parallel}(T)$ [Eq. (36)] of the 1d driven system at $v \rightarrow \infty$. The points are MC results for $L_{\parallel} = 2^{11}$, and the dashed lines are results for the one-dimensional Ising model in equilibrium.

Sec. IV we will argue that in finite systems the spin fluctuations are not only mediated by the spins σ_i but also by the self-consistent field m which fluctuates at finite L_{\parallel} , an effect which vanishes in the exact solution, as $L_{\parallel} \rightarrow \infty$.

From the nearest-neighbor correlation function we can calculate the internal energy $e_{\parallel} = -J \langle \sigma_l \sigma_{l+1} \rangle$ in \parallel direction

$$e_{\parallel} = \begin{cases} \frac{J e^{-2K - K_b}}{\sinh 2K \sinh K_b} - 1 & T \leq T_c \\ -J \tanh K & T \geq T_c \end{cases} \quad (35)$$

as well as the specific heat $c_{\parallel} = \partial e_{\parallel} / \partial T$ in \parallel direction (Fig. 5)

$$c_{\parallel} = \begin{cases} \frac{2K^2}{\sinh^2 K} (\coth K_b - 1) & T < T_c \\ \frac{K^2}{\cosh^2 K} & T > T_c. \end{cases} \quad (36)$$

On the other hand, the internal energy in \perp direction is simply given by

$$e_{\perp} = -J_b m^2 \quad (37)$$

as the related spins are uncorrelated.

Now we turn to dynamical properties of this system under a concrete MC Glauber dynamics (see Sec. IV B for details) and calculate the spin-flip acceptance rate $A = \langle p_{\text{flip}} \rangle$ and the energy dissipation rate $P = \partial E / \partial t$: let $\langle \zeta_{\ell} \zeta_{\ell'} \rangle$ denote the probability of picking a spin σ with direction $\zeta = \uparrow, \downarrow$ and left and right neighbors $\sigma_{\ell, r}$ with direction $\zeta_{\ell, r}$. These probabilities can be calculated using the matrices $\mathbf{P}_{\uparrow} = \text{diag}(1, 0)$ and $\mathbf{P}_{\downarrow} = \text{diag}(0, 1)$, e.g., $\langle \uparrow \uparrow \downarrow \rangle = \langle t_0 | \mathbf{P}_{\zeta_{\ell}} \hat{\mathbf{T}} \mathbf{P}_{\zeta_{\ell'}} \hat{\mathbf{T}} \mathbf{P}_{\zeta_r} | t_0 \rangle$. As the third coupling partner μ of spin σ , with direction ζ_{μ} , is uncorrelated at infinite velocity, the probability of a particular spin configuration becomes

$$\langle \zeta_{\ell} \zeta_{\ell'} \zeta_r \rangle \langle \zeta_{\mu} \rangle = \langle t_0 | \mathbf{P}_{\zeta_{\ell}} \hat{\mathbf{T}} \mathbf{P}_{\zeta_{\ell'}} \hat{\mathbf{T}} \mathbf{P}_{\zeta_r} | t_0 \rangle \langle t_0 | \mathbf{P}_{\zeta_{\mu}} | t_0 \rangle. \quad (38)$$

The spin-flip probability of a given configuration is $p_{\text{flip}}(\Delta E)$, with $\Delta E = \Delta E_1 + \Delta E_2 = 2J\sigma(\sigma_{\ell} + \sigma_r) + 2J_b\sigma\mu$, and A becomes the sum over all 2^4 possible cases

$$A = \sum_{\zeta_\ell, \zeta_r, \zeta_\mu=\uparrow, \downarrow} p_{\text{flip}}(\Delta E) \langle \zeta_\ell \zeta_r \rangle \langle \zeta_\mu \rangle, \quad (39)$$

which can be written as

$$\begin{aligned} A &= \sum_{\zeta_\ell, \zeta_r, \zeta_\mu=\uparrow, \downarrow} p_{\text{flip}}^*(\Delta E_1) \langle \zeta_\ell \zeta_r \rangle \sum_{\zeta_\mu=\uparrow, \downarrow} p_{\text{flip}}^*(\Delta E_2) \langle \zeta_\mu \rangle \\ &= \sum_{\zeta=\uparrow, \downarrow} X_\zeta (e^{-2K_b} \langle \zeta \rangle + \langle \bar{\zeta} \rangle) \end{aligned} \quad (40)$$

for the multiplicative rate $p_{\text{flip}}^*(\Delta E) = p_{\text{flip}}^*(\Delta E_1) p_{\text{flip}}^*(\Delta E_2)$ introduced in Sec. IV B [Eq. (69)] using the abbreviation

$$\begin{aligned} X_\zeta &= \sum_{\zeta_\ell, \zeta_r=\uparrow, \downarrow} p_{\text{flip}}^*(\Delta E_1) \langle \zeta_\ell \zeta_r \rangle \\ &= e^{-4K} \langle \zeta \zeta \rangle + 2e^{-2K} \langle \zeta \zeta \bar{\zeta} \rangle + \langle \bar{\zeta} \zeta \bar{\zeta} \rangle. \end{aligned} \quad (41)$$

Note that the two terms in Eq. (40) are equal and the acceptance rate is independent of spin ζ because m is stationary. The resulting acceptance rate becomes

$$A = \begin{cases} \frac{\cosh(K + K_b) - \sinh(K - K_b)}{4e^{2(K+K_b)} \sinh K \cosh^2 K \sinh K_b} & T \leq T_c \\ e^{-K_b} \cosh K_b (1 - \tanh K)^2 & T \geq T_c, \end{cases} \quad (42)$$

which simplifies for $J=J_b$ to

$$A = \begin{cases} \frac{e^{-4K} \coth 2K}{\sinh 2K} & T \leq T_c \\ \frac{e^{-3K}}{\cosh K} & T \geq T_c. \end{cases} \quad (43)$$

The calculation of the energy dissipation rate P per spin is very similar to the acceptance rate A [Eq. (40)] and gives

$$P = -2J_b \sum_{\zeta=\uparrow, \downarrow} X_\zeta (e^{-2K_b} \langle \zeta \rangle - \langle \bar{\zeta} \rangle). \quad (44)$$

Furthermore, P/A can be calculated for arbitrary dimensions and geometries, as it is solely a property of the fluctuating field. We find

$$\begin{aligned} \frac{P}{A} &= -2J_b \frac{\sum_{\zeta=\uparrow, \downarrow} X_\zeta (e^{-2K_b} \langle \zeta \rangle - \langle \bar{\zeta} \rangle)}{\sum_{\zeta=\uparrow, \downarrow} X_\zeta (e^{-2K_b} \langle \zeta \rangle + \langle \bar{\zeta} \rangle)} \\ &= -J_b \sum_{\zeta=\uparrow, \downarrow} \frac{e^{-2K_b} \langle \zeta \rangle - \langle \bar{\zeta} \rangle}{e^{-2K_b} \langle \zeta \rangle + \langle \bar{\zeta} \rangle} \\ &= \frac{2J_b(m^2 + 1) \tanh K_b}{1 - m^2 \tanh^2 K_b}. \end{aligned} \quad (45)$$

For the magnetization [Eq. (19)] of the 1d system this gives

$$\frac{P}{A} = \begin{cases} \frac{2J_b e^{-4K}}{\tanh K_b} & T \leq T_c \\ 2J_b \tanh K_b & T \geq T_c, \end{cases} \quad (46)$$

which, multiplied with A from Eq. (71) and for $J=J_b$, becomes

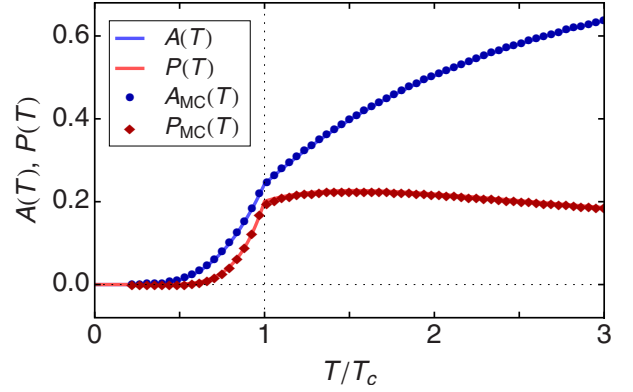


FIG. 6. (Color online) Spin-flip probability A [Eq. (43)] and energy dissipation rate P [Eq. (47)] versus reduced temperature T/T_c for the 1d system at $v \rightarrow \infty$, together with MC data for $L_{\parallel}=2^{11}$.

$$P = \begin{cases} \frac{2e^{-8K} \coth 2K}{\tanh K \sinh 2K} & T \leq T_c \\ \frac{2e^{-3K} \tanh K}{\cosh K} & T \geq T_c. \end{cases} \quad (47)$$

These results are shown in Fig. 6, together with data from MC simulations. Note that these results are only valid for the multiplicative rate p_{flip}^* from Eq. (69).

Finally we list the critical exponents for the 1d driven system at $v \rightarrow \infty$ to be

$$\beta = \frac{1}{2}, \quad \gamma = 1, \quad \alpha = 0. \quad (48)$$

The behavior of this system at finite velocities v will be discussed in Sec. IV.

D. 2d_b case

The 2d_b case can be solved exactly using the expression for the equilibrium surface magnetization $m_{b,\text{eq}}(z, y_b)$ of the 2D Ising model in a static surface field h_b obtained by McCoy and Wu [[16], Chap. VI, Eq. 5.1], with $z = \tanh K$ and $y_b = \tanh h_b$. The integral representation given in their work can be further evaluated and written in closed form, the results are given in Appendix A [Eq. (A2)]. If we again use Eq. (15) and set $y_b = m_b z_b$, with $z_b = \tanh K_b$, we can calculate the nonequilibrium boundary magnetization $m_b(z, z_b)$ numerically as solution of the self-consistence condition

$$m_{b,\text{eq}}(z, m_b z_b) = m_b, \quad (49)$$

which is shown for $J=1$ and several values of J_b in Fig. 7. The critical temperature T_c of the system can be evaluated from the reduced zero-field boundary susceptibility $\chi_{b,\text{eq}}(z)$ [Eq. (A3)] to give

$$T_c = 2.661\ 472\ 565\ 575\ 2\dots \quad (50)$$

for the case $J_b=J=1$ using $\chi_{b,\text{eq}}^{(0)}(z_c) z_{b,c} = 1$ [Eq. (16)].

As the critical temperature T_c [Eq. (50)] is larger than the equilibrium critical temperature $T_{c,\text{eq}} = 2.269\ 18\dots$, the driven

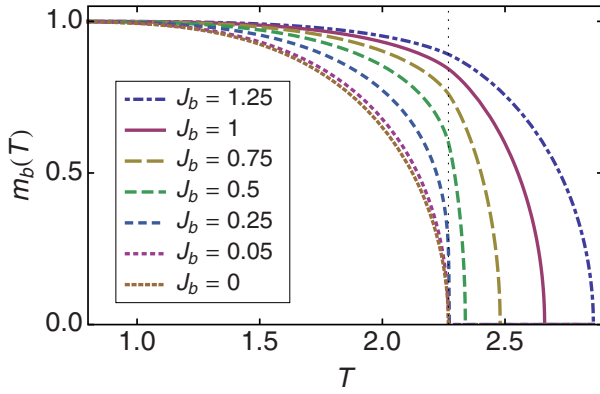


FIG. 7. (Color online) Boundary magnetization $m_b(T)$ [Eq. (49)] of the $2d_b$ system for $J=1$ and several values of J_b . For $J_b=0$ the m_b reduces to the surface magnetization of the 2D equilibrium Ising model [Eq. (A5)].

boundary induces a surface phase transition where only the driven surface has long range order above $T_{c,eq}$. The velocity dependence of this transition and the resulting phase diagram is discussed in more detail in Sec. IV.

E. 1+1d sheared case

If the motion of the lattice described by Eq. (3) is not restricted to one row but applied to the whole system, we get a system with uniform shear. Then all $\Delta_k(t) \equiv \Delta(t) = vt$ are equal, and we assume $K_{\perp,k} \equiv K_{\perp}$ to get

$$\beta\mathcal{H}(t) = - \sum_{k=1}^{L_{\perp}} \sum_{l=1}^{L_{\parallel}} K_{\parallel} \sigma_{k,l} \sigma_{k,l+1} + K_{\perp} \sigma_{k,l} \sigma_{k+1,l+\Delta(t)}. \quad (51)$$

Note that this system is translationally invariant in both directions, a fact that drastically simplifies the analysis of the critical behavior.

Now we will investigate this system in the limit $v \rightarrow \infty$. Then each spin σ_{kl} interacts, as depicted in Fig. 8, with its neighbors $\sigma_{k\pm 1, l \pm \Delta(t)}$ via fluctuating fields, while the interaction to the parallel neighbors $\sigma_{k, l \pm 1}$ remains unchanged. Thus the system decomposes into L_{\perp} identical 1D Ising models which again can be solved exactly: the coupling to two fluctuating fields $\mu_{i,1}$ and $\mu_{i,2}$ with equal strength k_i on each site can be traced similar to Eq. (10) to give

$$\begin{aligned} \mathcal{Z} &= \text{Tr}_{\sigma} e^{-\beta\mathcal{H}_0} \text{Tr}_{\mu} \prod_i \prod_{j=1}^2 e^{k_i \mu_{ij} \sigma_i} \\ &= \text{Tr}_{\sigma} e^{-\beta\mathcal{H}_0} \prod_i \prod_{j=1}^2 \sum_{\mu_{ij}=\pm 1} e^{k_i \mu_{ij} \sigma_i} p_i(\mu_{ij}) \\ &= \text{Tr}_{\sigma} e^{-\beta\mathcal{H}_0} \prod_i [\cosh k_i + m_i \sigma_i \sinh k_i]^2 \\ &= \prod_i C_i \text{Tr}_{\sigma} e^{-\beta\mathcal{H}_0} \prod_i \left[1 + \sigma_i \frac{m_i}{C_i} \sinh 2k_i \right], \quad (52) \end{aligned}$$

with

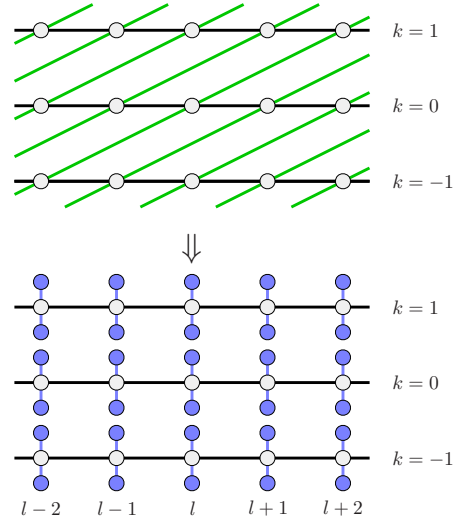


FIG. 8. (Color online) Mapping of the 1+1d sheared system, shown for $\Delta=2$, on L_{\perp} disconnected 1D systems with fluctuating fields.

$$C_i = \frac{1}{2} (1 - m_i^2 + (1 + m_i^2) \cosh 2k_i). \quad (53)$$

Equating Eq. (52) with Eq. (12) we conclude that static fields b_i can replace the fluctuating fields μ_{ij} , with average m_i , if

$$\tanh b_i = \frac{2m_i \sinh 2k_i}{1 - m_i^2 + (1 + m_i^2) \cosh 2k_i}. \quad (54)$$

The sheared system is translationally invariant in both directions, leading to homogeneous values $m_i = m$, $k_i = K_{\perp}$, and $b_i = h$. Inserting Eq. (54) into Eq. (19) we get the order parameter of the sheared 1+1d system

$$m(K_{\parallel}, K_{\perp}) = \frac{\sqrt{1 - 2e^{4K_{\parallel}} + 2e^{2K_{\parallel}} \sqrt{e^{4K_{\parallel}} - 1} + \tanh^2 K_{\perp}}}{\tanh K_{\perp}}, \quad (55)$$

with critical temperature fulfilling

$$2e^{2K_{\parallel,c}} \tanh K_{\perp,c} = 1, \quad (56)$$

which gives $T_c = 1 / \ln(\frac{1}{2} \sqrt{3 + \sqrt{17}}) = 3.46591\dots$ for $J_{\parallel} = J_{\perp} = 1$. A generalization of Eq. (52) from two to f fluctuating fields per spin is straightforward and leads to the general criticality condition

$$\chi_{eq}^{(0)}(K_c) f \tanh K_{b,c} = 1. \quad (57)$$

Although this geometry can be solved exactly at $v = \infty$ we expect the phase transition to be *strongly anisotropic* (see, e.g., [19]) with two different correlation length exponents $\nu_{\parallel} > \nu_{\perp}$. In fact we found such behavior, with strong evidence for the exponents $\nu_{\parallel} = 3/2$ and $\nu_{\perp} = 1/2$, details on this will be published elsewhere [20].

F. Other geometries

For two more cases we can derive highly accurate estimates for the critical temperature T_c of the driven system

when $v \rightarrow \infty$, namely, the 2d Ising double layer [20] with Hamiltonian

$$\beta\mathcal{H}(t) = - \sum_{k=0}^1 \sum_{l=1}^{L_{\parallel}} \sum_{m=1}^{L_{\parallel}} [K\sigma_{klm}(\sigma_{k,l,m+1} + \sigma_{k,l+1,m}) + K_{\text{b}}\sigma_{0lm}\sigma_{1,l+\Delta(t),m}] \quad (58)$$

and the experimentally relevant 2+1d sheared case

$$\beta\mathcal{H}(t) = - \sum_{k=1}^{L_{\perp}} \sum_{l=1}^{L_{\parallel}} \sum_{m=1}^{L_{\parallel}} [K_{\parallel}\sigma_{klm}(\sigma_{k,l,m+1} + \sigma_{k,l+1,m}) + K_{\perp}\sigma_{klm}\sigma_{k+1,l+\Delta(t),m}], \quad (59)$$

both on simple cubic lattices: with Eq. (57) we can express T_c using the high-temperature series expansion for the reduced zero-field susceptibility $\chi_{\text{eq}}^{(0)}(K)$ of the 2D Ising model, which was calculated to higher than 2000th order recently using a highly efficient polynomial time algorithm [21]. Using this extremely accurate result we find, for $J=J_{\text{b}}=1$, the critical temperatures

$$T_c = 4.058\ 782\ 423\ 137\ 980\ 000\ 987\ 775\ 040\ 680\dots \quad (60)$$

for the two 2d layers and

$$T_c = 5.264\ 750\ 414\ 514\ 743\ 550\ 598\ 017\ 203\ 424\dots \quad (61)$$

for the 2+1d sheared system with $f=2$ analogous to the 1+1d sheared system. Note that due to the high accuracy of the series these values can be calculated to approximately 500 and 700 digits, respectively.

Just for reference we also give the critical temperatures for two more cases: the experimentally relevant $3d_{\text{b}}$ case shown in Fig. 1 as well as the quite theoretical 3d case of two three-dimensional systems in direct contact along the fourth dimension. In the $3d_{\text{b}}$ case we find $T_c=4.8(1)$ using the eighth-order high-temperature series from Ref. [22] (Table IV), while in the 3d case we obtain $T_c=5.983\ 835(1)$ using the 32th order series from [23].

All these higher-dimensional geometries are expected to show strongly anisotropic behavior with two different correlation length exponents, the reader is referred to Ref. [20].

IV. MONTE CARLO SIMULATIONS

A. Method

We now describe the algorithms used to investigate the driven system: for finite velocities v we shift the boundary couplings by increasing $\Delta(t)$ from Eq. (2) after every N/v random sequential single spin-flip attempts, where N denotes the total number of spins. Using $10^5 - 10^6$ MCS per temperature, we measured the following boundary properties: the boundary magnetization per spin and the energy per bond parallel to and across the boundary of a given configuration

$$M_{\text{b}} = \frac{1}{2L_{\parallel}} \sum_{k=0}^1 \sum_{l=1}^{L_{\parallel}} \sigma_{k,l}, \quad (62a)$$

$$E_{\text{b},\parallel} = - \frac{J}{2L_{\parallel}} \sum_{k=0}^1 \sum_{l=1}^{L_{\parallel}} \sigma_{k,l}\sigma_{k,l+1}, \quad (62b)$$

$$E_{\text{b}} = - \frac{J_{\text{b}}}{L_{\parallel}} \sum_{l=1}^{L_{\parallel}} \sigma_{0,l}\sigma_{1,l+\Delta(t)}, \quad (62c)$$

as well as the corresponding bulk quantities. From these time-dependent quantities we calculate the averages of the magnetization, reduced susceptibility, Binder cumulant, internal energy, and specific heat at the boundary,

$$m_{\text{b,abs}} = \langle |M_{\text{b}}| \rangle, \quad (63a)$$

$$\chi_{\text{b,abs}} = 2L_{\parallel}(\langle M_{\text{b}}^2 \rangle - \langle |M_{\text{b}}| \rangle^2), \quad (63b)$$

$$U_{\text{b}} = 1 - \frac{\langle M_{\text{b}}^4 \rangle}{3\langle M_{\text{b}}^2 \rangle^2}, \quad (63c)$$

$$e_{\text{b}} = \langle E_{\text{b}} \rangle, \quad (63d)$$

$$c_{\text{b}} = L_{\parallel}\beta^2(\langle E_{\text{b}}^2 \rangle - \langle E_{\text{b}} \rangle^2). \quad (63e)$$

Note that we have absorbed the factor β^{-1} into χ . Near criticality these quantities show power-law behavior and fulfill

$$m_{\text{b,abs}}(\tau) \propto (-\tau)^{\beta}, \quad (64a)$$

$$\chi_{\text{b,abs}}(\tau) \propto |\tau|^{-\gamma}, \quad (64b)$$

$$c_{\text{b}}(\tau) \propto |\tau|^{-\alpha}, \quad (64c)$$

with reduced temperature $\tau = T/T_c - 1$ and critical exponents β , γ , and α . But before we present the results, we have to take a closer look at the used spin-flip rates.

B. Integrable algorithm

While equilibrium properties are most efficiently investigated in Monte Carlo simulations using cluster algorithms, nonequilibrium systems have to be treated with random sequential single spin-flip dynamics such as the nonconserved Glauber dynamics [24] or the conserved Kawasaki dynamics [25]. The driven system is permanently under an external perturbation which drives it out of equilibrium, while the internal degrees of freedom are coupled to a heat bath in thermal equilibrium. From this coupling the spin-flip probability $p_{\text{flip}}(\Delta E)$ of a given energy change ΔE fulfills the detailed balance condition

$$\frac{p_{\text{flip}}(\Delta E)}{p_{\text{flip}}(-\Delta E)} = e^{-\beta\Delta E}, \quad (65)$$

just like in the equilibrium case (for details, see [20]).

The most common rates fulfilling Eq. (65) are the Metropolis rate [26] and the Glauber rate [24],

$$p_{\text{flip}}^{\text{M}}(\Delta E) = \min(1, e^{-\beta\Delta E}), \quad (66a)$$

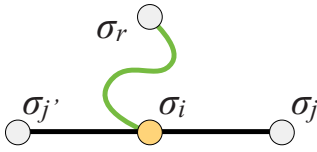


FIG. 9. (Color online) Interactions of surface spin σ_i in the 1d case.

$$p_{\text{flip}}^G(\Delta E) = \frac{1}{1 + e^{\beta \Delta E}}. \quad (66b)$$

Using these rates in simulations of, e.g., the 1d driven system [Eq. (1)], it turns out that for all $v > 0$ the critical temperature $T_c(v)$ depends on the used rate (see also Fig. 15): we find, for $v \rightarrow \infty$ and $J_b = J = 1$, the values $T_c^M = 1.910(2)$ and $T_c^G = 2.031(2)$ for the Metropolis and Glauber rate, respectively, while the exact solution [Eq. (20)] of the model presented in Sec. III gives $T_c = 2.269\dots$ Note that a similar dependency was recently found in the DLG by Kwak *et al.* [27].

How can these discrepancies be understood? And can we construct a rate that matches the analytical treatment, i.e., has the same T_c ? This is indeed possible: consider a microscopic change, i.e., a spin flip, of spin σ_i at the boundary (see Fig. 9) with energy difference

$$\Delta E = \underbrace{2J\sigma_i \sum_{\langle j \rangle}^z \sigma_j}_{\Delta E_1} + \underbrace{2J_b \sigma_i \sigma_r}_{\Delta E_2}, \quad (67)$$

where the sum runs over the z neighbors of σ_i in the same subsystem ($z=2$ in the 1d case), while σ_r is from the other side of the moving boundary. The idea of the exact solution presented in the last section was to treat spin σ_r as a fluctuating variable μ_i at site i with appropriate statistics. By contrast, correlations of different strength are introduced between the two subsystems by the rates [Eq. (65)] because the influence of spin σ_r depends on the actual state of the z spins σ_j . This can be seen most easily in the case of the Metropolis rate ($J_b = J$): if, e.g., $\sigma_i = -\sigma_j$ then $\Delta E_1 = -2zJ$ and $p_{\text{flip}}^M = 1$ independent of σ_r (note that $\Delta E_2 = \pm 2J$), while in the parallel case ($\sigma_i = \sigma_j$) $\Delta E_1 = 2zJ$ and p_{flip}^M strongly depends on σ_r (see Fig. 10).

Fortunately, these rate-induced correlations can be completely eliminated by requiring that *the flipping probability is multiplicative*,

$$p_{\text{flip}}(\Delta E_1 + \Delta E_2) = p_{\text{flip}}(\Delta E_1)p_{\text{flip}}(\Delta E_2). \quad (68)$$

Clearly this condition is not satisfied for the rates in Eq. (65), e.g., $p_{\text{flip}}^M(-2zJ + 2J) = 1$, while $p_{\text{flip}}^M(-2zJ)p_{\text{flip}}^M(2J) = e^{-2K}$ (again we assume $J_b = J$).

Instead, for simulations of driven systems we propose the rate

$$p_{\text{flip}}^*(\Delta E) = e^{-\beta/2(\Delta E - \Delta E_{\min})}, \quad (69)$$

which is uniquely defined by the detailed balance condition [Eq. (65)] and the multiplicity condition [Eq. (68)] [36]. The constant ΔE_{\min} is the minimum possible value of ΔE at given geometry; this assures that $p_{\text{flip}}^*(\Delta E)$ is maximal but never

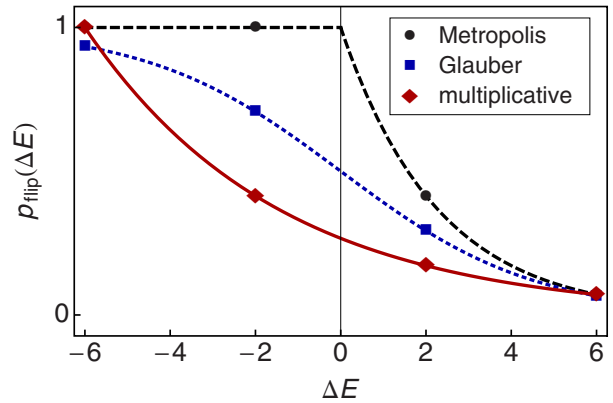


FIG. 10. (Color online) Spin-flip probabilities of the Metropolis rate [Eq. (66a)] (dashed black line, circles), the Glauber rate [Eq. (66b)] (dotted blue line, squares), and the multiplicative rate [Eq. (69)] (red line, diamonds) for the 1d system at criticality ($J = J_b = 1$).

larger than one. For our example [Eq. (67)] we find $\Delta E_{1,\min} = -2zJ$ and $\Delta E_{2,\min} = -2J_b$ to fulfill Eq. (68). This rate reproduces the calculated critical temperatures in all considered geometries, e.g., $T_c^* = 2.269(1)$ for the 1d case at $v \rightarrow \infty$.

The resulting spin-flip rates for the 1d case at criticality are shown in Fig. 10. Clearly, the multiplicative algorithm [Eq. (69)] has a smaller overall acceptance rate than Eqs. (66) and is thus slightly less efficient: a finite-size scaling analysis of the acceptance rate $A = \langle p_{\text{flip}} \rangle$ at criticality in the 1d case yields $A_c^M = 0.476(2)$, $A_c^G = 0.366(2)$ and $A_c^* = 0.242(2)$ for the three algorithms, rendering this method roughly two times slower than the Metropolis algorithm. In fact, $A_c = 3\sqrt{2} - 4 = 0.24264\dots$ can be calculated exactly from Eq. (43).

Note that the Metropolis and Glauber rates can be considered as many particle rates, as p_{flip} depends on the many particle state of all coupling partners, while the multiplicative rate corresponds to a product of two particle contributions. We believe that the dynamics generated by the multiplicative rate is generally simpler than the one generated by Metropolis or Glauber rates, making an exact solution more feasible. Whether this differentiation only holds for the non-conserved Glauber dynamics or also for the conserved Kawasaki dynamics is subject of future work.

In the next two sections we will investigate finite-size effects in the 1d case as well as the crossover behavior at finite velocities v in the 1d as well as in the 2d_b case. We first turn to the 1d case.

C. 1d case

The exact solution presented in Sec. III was derived in the thermodynamic limit $L_{\parallel} \rightarrow \infty$ as we assumed a constant and nonfluctuating order parameter m in the self-consistence condition [Eq. (15)]. This led to the result that the correlation length ξ_{\parallel} [Eq. (34)] remains finite at criticality. However, in a finite system the assumption $m = \text{const}$ is not fulfilled and finite-size effects occur, leading to a nontrivial dependency

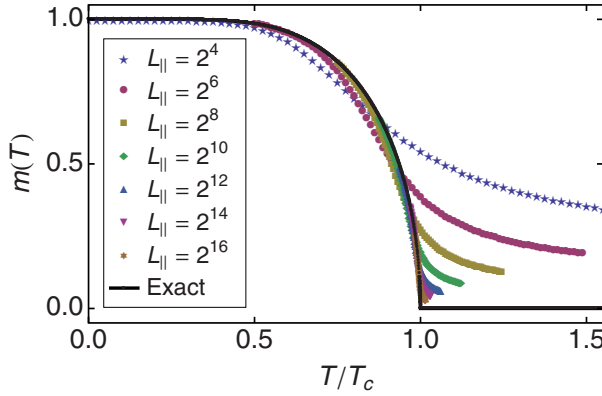


FIG. 11. (Color online) Magnetization $m_{\text{abs}}(T)$ [Eq. (64a)] of the 1d system at $v=\infty$ for several system sizes L_{\parallel} from Monte Carlo simulations, together with the exact solution Eq. (19).

of the physical quantities on system size. The fluctuating order parameter gives rise to additional correlations between spins at large distances not included in the exact solution. As the driven system shows mean-field behavior, we can use the standard finite-size scaling theory for mean-field systems: near criticality the correlation length parallel to the boundary fulfills $\xi_{\parallel}(\tau) \propto |\tau|^{-\nu_{\parallel}}$ with critical exponent $\nu_{\parallel}=2/d_b$, where d_b denotes the boundary dimension. We have $d_b=1$ in both the 1d and the $2d_b$ case, leading to $\nu_{\parallel}=2$ in these cases.

To illustrate these finite-size effects in the 1d case, in Fig. 11 we show the magnetization $m_{\text{abs}}(T)$ [Eq. (64a)] as function of temperature for $v=\infty$ and several system sizes L_{\parallel} . The exact solution [Eq. (19)] is only approached in the limit $L_{\parallel} \rightarrow \infty$.

The finite-size scaling behavior is demonstrated exemplarily for the susceptibility $\chi_{\text{abs}}(T)$ [Eq. (64b)], which is shown in a finite-size scaling plot in Fig. 12: after rescaling of the MC data in the usual way we indeed find the expected mean-field exponents $\gamma=1$ and $\nu_{\parallel}=2$, furthermore the data falls onto the universal finite-size scaling function calculated in Ref. [28]. The same analysis was performed for

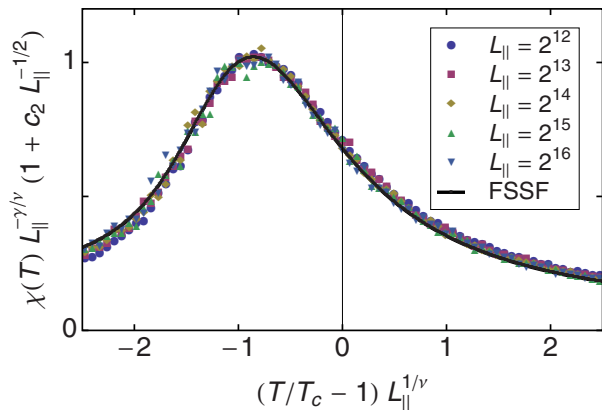


FIG. 12. (Color online) Finite-size scaling plot of the reduced susceptibility $\chi_{\text{abs}}(T)$ [Eq. (64b)] of the 1d system for $v=\infty$ and system sizes $L_{\parallel}=2^{12}, \dots, 2^{16}$, together with the exact mean-field finite-size scaling function (black line) from Ref. [28]. The correction factor $c_2=2.7$.

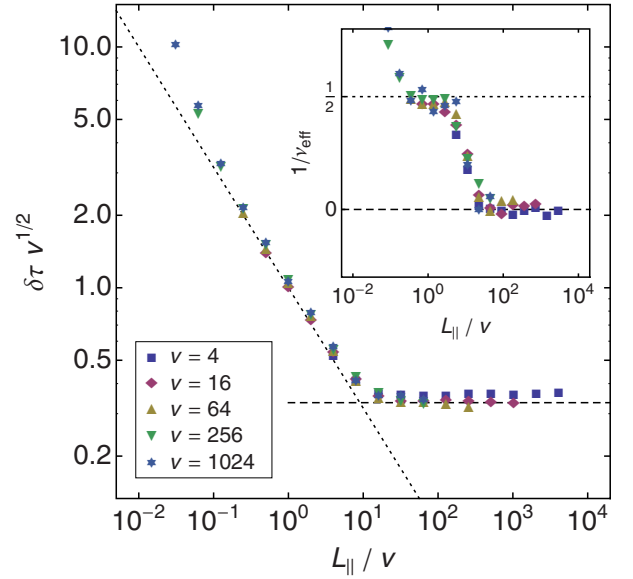


FIG. 13. (Color online) Velocity dependent crossover behavior in the 1d case. Shown is the rescaled width of the critical region $\delta\tau v^{1/2}$ as function of the crossover scaling variable L_{\parallel}/v for several velocities v and several system sizes $L_{\parallel}=2^4, \dots, 2^{16}$ (see text). The inset shows the corresponding crossover of the effective correlation length exponent ν_{eff}^{-1} from $\nu_{\text{eff}}^{-1}=1/2$ (MF, dotted line) to $\nu_{\text{eff}}^{-1}=0$ (Ising noncritical, dashed line).

the magnetization $m_{\text{abs}}(T)$ and specific heat $c(T)$ [Eq. (64c)], verifying the other two exponents $\beta=1/2$ and $\alpha=0$.

In summary, the 1d and the $2d_b$ systems with boundary dimension $d_b=1$ have the standard mean-field exponents and fulfill the exponent relations

$$2 - \alpha = 2\beta + \gamma = d_b \nu_{\parallel}. \quad (70)$$

We now turn to finite velocities v : then the 1d system always shows a crossover from mean field to Ising behavior with increasing system size L_{\parallel} . Only in the limit $v \rightarrow \infty$ the system undergoes a phase transition at finite temperatures. To investigate this velocity-dependent crossover, we measured the width $\delta\tau$ of the critical region by analyzing the Binder cumulant [Eq. (63c)]. Using least-squares fits of the simulation data to the simple approximation,

$$U_b(T) \approx \begin{cases} \frac{1}{3} [1 + \tanh(\tilde{\tau} \delta\tau)] & \tilde{\tau} \leq 0 \\ \frac{1}{3} \frac{1}{1 + \tilde{\tau} \delta\tau} & \tilde{\tau} > 0, \end{cases} \quad (71)$$

with $\tilde{\tau}=T/\tilde{T}_c-1$ and fit parameters \tilde{T}_c and $\delta\tau$, for several velocities v and system sizes L_{\parallel} we determined $\delta\tau$ and plotted them in Fig. 13. We find that the crossover scaling variable is L_{\parallel}/v in this case, while the y axis has to be rescaled as $\delta\tau v^{1/2}$ to get the correct limit $L_{\parallel}^{1/\nu_{\parallel}} \delta\tau = \text{const}$ with $\nu_{\parallel}=2$ in the limit $v \rightarrow \infty$. At finite v the width $\delta\tau$ stops shrinking at $L_{\parallel}^{\times} \approx 9v$, where L_{\parallel}^{\times} denotes the crossover system size, and only goes to zero for $v \rightarrow \infty$, indicating a sharp phase transition in this limit. The inset shows the effective exponent ν_{eff} obtained from the logarithmic derivative,

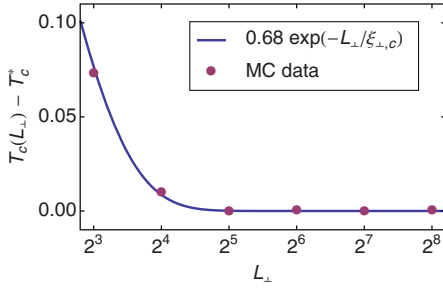


FIG. 14. (Color online) Influence of the system size L_{\perp} on the critical point in the $2d_b$ case at $v=\infty$ and $L_{\parallel}=256$. The effective critical temperature $T_c(L_{\perp})$ shifts to higher values if $L_{\perp} \lesssim 10\xi_{\perp,c}$ (see text).

$$\nu_{\text{eff}}^{-1} = - \frac{\partial \ln \delta\tau}{\partial \ln L_{\parallel}}, \quad (72)$$

whose value changes from $\nu_{\text{eff}}^{-1}=1/2$ (MF) to $\nu_{\text{eff}}^{-1}=0$ (Ising) with growing system size. In the next section we will see that this behavior changes substantially in the $2d_b$ case.

D. $2d_b$ case

In the $2d_b$ case the moving boundary is coupled to a two-dimensional Ising model, which undergoes a phase transition at $T_{c,\text{eq}}$ [Eq. (4)], independent of the velocity v . In addition, the moving boundary shows a boundary phase transition at temperature $T_c(v)$, which grows with increasing v and eventually approaches the value given in Eq. (50) for $v \rightarrow \infty$. As $T_c(v) > T_{c,\text{eq}}$ for all $v > 0$ we expect a boundary phase transition with paramagnetic bulk. Then the correlation length ξ_{\perp} perpendicular to the boundary is finite at criticality and has the Ising value

$$\xi_{\perp,c}(v) = \xi_{\text{eq}}[T_c(v)], \quad (73)$$

with [16]

$$\xi_{\text{eq}}^{-1}(T) = \begin{cases} 4K - 2 \ln \coth K & T < T_{c,\text{eq}} \\ \ln \coth K - 2K & T > T_{c,\text{eq}}. \end{cases} \quad (74)$$

For that reason, in the finite-size scaling analysis it is sufficient for given v to simulate systems with varying length L_{\parallel} while holding the height L_{\perp} fixed at a value $L_{\perp} \gg \xi_{\perp,c}(v)$. To illustrate this behavior, in Fig. 14 we show the effect of different values of L_{\perp} for $v=\infty$ and $L_{\parallel}=256$. Only below $L_{\perp} \approx 32$ the system feels the finite width L_{\perp} , resulting in a shift of the effective critical temperature $T_c(L_{\perp})$ to higher values. The strength of the shift is proportional to the correlation function in \perp direction, $\langle \sigma_{0,l} \sigma_{L_{\perp},l} \rangle \propto \exp(-L_{\perp} / \xi_{\perp,c})$. The curves collapse for $L_{\perp} > 32$ showing that a ratio $L_{\perp} / \xi_{\perp,c} \approx 10$ is sufficient as $\xi_{\perp,c}(\infty) = 3.663\ 23\dots$ in this case.

We performed MC simulations and determined the critical temperatures for different velocities v by performing a finite-size scaling analysis of the boundary susceptibility $\chi_{\text{abs},b}(T)$ and the boundary cumulant $U_b(T)$. For the multiplicative algorithm, Eq. (69), we used 400.000 MC steps per temperature, while for the Metropolis algorithm 50.000 MC steps per

TABLE I. Velocity dependent critical temperatures $T_c(v)$ for the $2d_b$ case, estimated using the multiplicative rate, [Eq. (69)] with 400.000 MC sweeps per temperature as well as using the Metropolis rate [Eq. (66a)] with 50.000 MC sweeps per temperature.

v	$T_c^*(v)$	$T_c^M(v)$
1/16	2.301(2)	
1/4	2.33(1)	
1	2.41(1)	2.30(2)
4	2.52(1)	2.37(2)
16	2.61(1)	2.42(2)
64	2.644(3)	2.44(2)
256	2.654(2)	2.44(2)
1024	2.659(2)	2.45(2)
∞	2.661(1)	2.45(2)

temperature were used. The results are given in Table I and are compiled into a phase diagram of the $2d_b$ case shown in Fig. 15. An important aspect of this phase diagram is the possibility of a velocity driven nonequilibrium phase transition at fixed temperature (double arrow): while the system is paramagnetic at $v=0$ and up to $v_c(T)$ (thick blue line), the boundary shows long range order above that velocity. It would be interesting to see this transition in experiments, which could be performed in the corresponding geometry $3d_b$ (see Fig. 1), e.g., using two close rotating magnets slightly above the Curie temperature. The magnets should be isolating to avoid eddy currents [4].

In the $2d_b$ case the crossover scaling variable can be determined from the $T_c(v)$ dependency discussed above. The correlation length ξ_{eq} at the critical point of the driven sys-

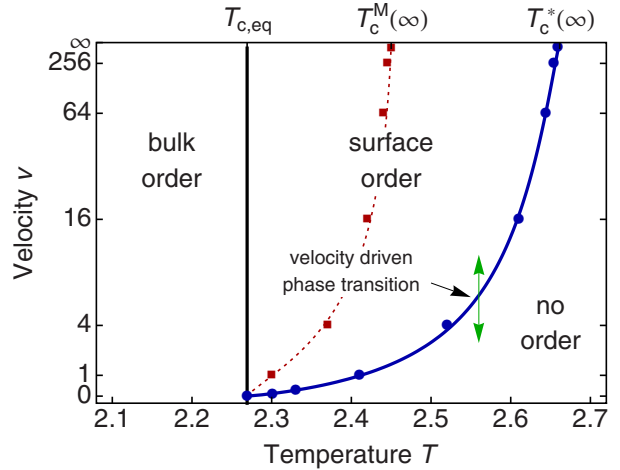


FIG. 15. (Color online) Phase diagram of the $2d_b$ case. Below $T_{c,\text{eq}}$ the two-dimensional bulk is ordered, while surface order is observed even above $T_{c,\text{eq}}$ up to the velocity dependent phase boundary $T_c(v)$. The position of this boundary depends on the algorithm, the blue line holds for the multiplicative rate [Eq. (69)], while the thin red dotted line holds for the Metropolis rate [Eq. (66a)]. At fixed temperatures between $T_{c,\text{eq}}$ and $T_c(v)$ a velocity driven phase transition is possible. The points are results from MC simulations.

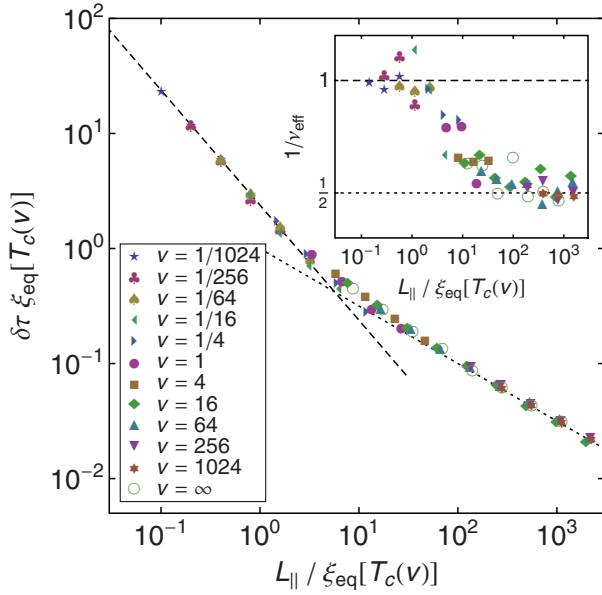


FIG. 16. (Color online) Velocity dependent crossover behavior in the $2d_b$ case. Shown is the rescaled width of the critical region $\delta\tau\xi_{\text{eq}}[T_c(v)]$ as function of the crossover scaling variable $L_{\parallel}/\xi_{\text{eq}}[T_c(v)]$ for several velocities v and different system sizes $L_{\parallel}=2^4, \dots, 2^{10}$ (see text). The inset shows the corresponding crossover of the effective correlation length exponent ν_{eff} from $\nu_{\text{eff}}=1$ (Ising, dashed line) to $\nu_{\text{eff}}=2$ (MF, dotted line).

tem, $T_c(v)$, plays a key role: The system is Ising-like as long as correlations span the whole system in both directions \parallel and \perp , i.e., as long as the system size L_{\parallel} is of the order of the bulk correlation length ξ_{eq} at the critical point $T_c(v)$ of the driven system, leading to the crossover scaling variable $L_{\parallel}/\xi_{\text{eq}}[T_c(v)]$. Again, the rescaling of the y axis can be determined by requiring that a data collapse is obtained in the limit $v \rightarrow 0$, leading to the expression $\delta\tau\xi_{\text{eq}}[T_c(v)]$, as ξ_{eq} cancels in this case and we get the required condition $L_{\parallel}\delta\tau=\text{const}$, as $\xi_{\text{eq}} \propto \tau^{-\nu_{\text{eq}}}$ in this limit and $\nu_{\text{eq}}=1$.

The resulting crossover scaling plot is shown in Fig. 16. For all finite $v > 0$ the critical behavior changes from Ising to mean field at the crossover system size $L_{\parallel}^{\times} \approx 6\xi_{\text{eq}}[T_c(v)]$: below this value $\delta\tau$ shrinks according to $\delta\tau \propto L_{\parallel}^{-1}$ (Ising, dashed line), while above this value $\delta\tau \propto L_{\parallel}^{-1/2}$ holds (MF, dotted line). As the shift exponent θ at small velocities defined by

$$T_c(v) - T_c(0) \propto v^{\theta} \quad (75)$$

is close to $1/2$ we have, for small v , $L_{\parallel}^{\times} \propto v^{-\theta} \approx v^{-1/2}$. The shift exponent $\theta=1/2$ has also been found in a field theoretical calculation of the $2+1d$ system [29].

V. SUMMARY

In this work we investigated a recently proposed driven Ising model with friction due to magnetic correlations. The nonequilibrium phase transition present in this system was investigated in detail using analytical methods and Monte Carlo simulations. In the far from equilibrium limit of high

driving velocities $v \rightarrow \infty$ the model was solved exactly by integrating out the nonequilibrium degrees of freedom. The resulting exact self-consistence equation was analyzed for various geometries, leading in many cases to precise values of the critical temperature T_c of the nonequilibrium phase transition. In the limit $v \rightarrow \infty$ the system always shows mean-field behavior due to dimensional reduction independent of geometry. In the simplest one-dimensional case denoted 1d a complete analysis of both equilibrium as well as nonequilibrium quantities has been presented. These exact results are another example of mean-field critical behavior in an exactly solvable driven system, just as in the case of the DLG in a certain limit [30].

The analytic results were reproduced using a multiplicative Monte Carlo rate originally introduced in [30], which eliminates correlations due to many particle dynamics introduced by the common Metropolis and Glauber rates. We claim that this algorithm is generally favorable to the Metropolis and Glauber rates if an analytical treatment is considered.

The finite-size effects naturally emerging in the simulations were analyzed using finite-size scaling techniques, a perfect agreement with exactly known universal finite-size scaling functions [28] were found.

We analyzed the critical behavior at finite velocities and studied the crossover behavior from low to high velocities: we found that the 1d system only has a phase transition in the thermodynamic limit for $v=\infty$, while systems with finite v always become noncritical at the crossover system size $L_{\parallel}^{\times} \approx 9v$. On the contrary, the two-dimensional case $2d_b$ already has an Ising type phase transition at $v=0$, which changes to mean-field behavior for *all* finite $v > 0$ in the thermodynamic limit, at a crossover length $L_{\parallel}^{\times} \approx 6\xi_{\text{eq}}[T_c(v)]$. In this sense, the velocity v is a relevant perturbation, always driving the system to a nonequilibrium state.

The 1d system changes from mean field to noncritical Ising universality, while the $2d_b$ case changes from Ising to mean-field type with growing system size L_{\parallel} . This somewhat puzzling fact can be understood in terms of the critical width $\delta\tau$ of the transition as follows: as in general $\delta\tau \propto L_{\parallel}^{-1/\nu}$ at criticality, in the two-dimensional Ising case $\delta\tau \propto L_{\parallel}^{-1}$, while in the mean-field case with one-dimensional boundary $\delta\tau \propto L_{\parallel}^{-1/2}$. Third, $\delta\tau \propto L_{\parallel}^0 = \text{const}$ in the 1d case at finite v . In the crossover the actual critical width $\delta\tau$ is always governed by the largest contribution and so at sufficiently large system size L_{\parallel} the contribution with smallest ν^{-1} dominates and determines the critical behavior. As consequence in both cases the effective inverse correlation length exponent ν_{eff}^{-1} changes from a larger value at small L_{\parallel} to a smaller value at large L_{\parallel} ($1/2 \rightarrow 0$ in the 1d case, $1 \rightarrow 1/2$ in the $2d_b$ case).

Comparing the results to the driven lattice gas (DLG) [10], we note that the DLG also shows a continuous nonequilibrium phase transition from an ordered to a disordered state at a critical temperature which grows with growing driving field. However, in the DLG the particle number is conserved, while we deal with a nonconserved magnetization.

Finally some remarks on strongly anisotropic critical behavior: the sheared system denoted $1+1d$ shows strongly anisotropic behavior at criticality and $v \rightarrow \infty$, with strong evidence for the correlation length exponents $\nu_{\parallel}=3/2$ and ν_{\perp}

$=1/2$, details on this will be published elsewhere [20]. Remarkably, this is a rare case of an exactly solvable nonequilibrium system with strongly anisotropic critical behavior.

ACKNOWLEDGMENTS

Special thanks go to Dietrich E. Wolf for very valuable discussions, criticism, and comments within the framework of the Sonderforschungsbereich 616, "Energy Dissipation at Surfaces." Thanks also to Sebastian Angst, Lothar Brendel, and Felix Schmidt for helpful discussions and to Sven Lübeck for critical reading of the paper.

APPENDIX A: SURFACE MAGNETIZATION OF THE 2D ISING MODEL

The equilibrium surface magnetization $m_{b,\text{eq}}$ of the 2D Ising model in a static surface field h_b obtained by McCoy and Wu ([16], Chapter VI, Eq. 5.1) as well as the reduced zero-field boundary susceptibility

$$\chi_{b,\text{eq}}^{(0)} = \left. \frac{\partial m_{b,\text{eq}}}{\partial h_b} \right|_{h_b \rightarrow 0} \quad (\text{A1})$$

can be written in closed form not present in the literature yet [31]. $\chi_{b,\text{eq}}^{(0)}$ is sometimes denoted χ_{11} , and a high-temperature series expansion was derived up to tenth order in Ref. [32] and up to 23th order in Ref. [33]. As the expressions for anisotropic couplings K_{\parallel} and K_{\perp} become way too complicated, we only give the results for the isotropic Ising model with $K_{\parallel}=K_{\perp}=K$ here: using the definitions $z=\tanh K$, $y=\tanh h_b$ we find

$$m_{b,\text{eq}}(z,y) = \frac{z^{-1}-z}{\frac{z}{y}-\frac{y}{z}} \left[\frac{b^2}{2\pi} K(16w^2) + \frac{b^2}{4\pi w} \frac{\left(a + \frac{y^2}{z}\right)^2}{1 - \frac{by^2}{c^2z}} \right. \\ \left. \times \Pi \left(\frac{\left(1 - \frac{by^2}{z}\right)^2}{1 - \frac{by^2}{c^2z}}, 16w^2 \right) + \frac{Y^{1/2} - Y^{-1/2}}{2(z^{-1} - z)} - \frac{1}{4} \right], \quad (\text{A2})$$

$$\chi_{b,\text{eq}}^{(0)}(z) = \left(\frac{1}{z^2} - 1 \right) \\ \times \left[(1 + 2w - 8w^2) \frac{K(16w^2)}{4\pi w} - \frac{E(16w^2)}{4\pi w} - \frac{1}{4} \right], \quad (\text{A3})$$

with the abbreviations

$$w = \frac{z(1-z^2)}{(1+z^2)^2}, \quad (\text{A4a})$$

$$a = \frac{1-2z-z^2}{1+z^2}, \quad (\text{A4b})$$

$$b = \frac{1+2z-z^2}{1+z^2}, \quad (\text{A4c})$$

$$c = \frac{2z}{1+z^2}, \quad (\text{A4d})$$

$$Y = \left(\frac{az}{c^2y^2} + 1 \right) \left(\frac{by^2}{c^2z} - 1 \right)^{-1}, \quad (\text{A4e})$$

and the complete elliptic integrals [37] of the first, second, and third kind, $K(m)$, $E(m)$, and $\Pi(n,m)$. Note that the variable w is also used in high-temperature series analysis of the bulk zero-field susceptibility [21]. For $h_b=0$ the surface magnetization Eq. (A2) reduces to the well-known expression

$$m_{b,\text{eq}}(K) = \sqrt{\frac{\cosh 2K - \coth 2K}{\cosh 2K - 1}}. \quad (\text{A5})$$

-
- [1] C. Fusco, D. E. Wolf, and U. Nowak, Phys. Rev. B **77**, 174426 (2008).
[2] M. P. Magiera, L. Brendel, D. E. Wolf, and U. Nowak, EPL **87**, 26002 (2009).
[3] M. P. Magiera, D. E. Wolf, L. Brendel, and U. Nowak, IEEE Trans. Magn. **45**, 3938 (2009).
[4] D. Kadau, A. Hucht, and D. E. Wolf, Phys. Rev. Lett. **101**, 137205 (2008).
[5] C. K. Chan and L. Lin, Europhys. Lett. **11**, 13 (1990).
[6] F. Corberi, G. Gonnella, and A. Lamura, Phys. Rev. Lett. **81**, 3852 (1998).
[7] E. N. M. Cirillo, G. Gonnella, and G. P. Saracco, Phys. Rev. E **72**, 026139 (2005).
[8] T. Imaeda and K. Kawasaki, Prog. Theor. Phys. **73**, 559 (1985).
[9] A. Onuki, J. Phys.: Condens. Matter **9**, 6119 (1997).
[10] S. Katz, J. L. Lebowitz, and H. Spohn, Phys. Rev. B **28**, 1655 (1983).
[11] B. Schmittmann and R. K. P. Zia, in *Phase Transitions and Critical Phenomena*, edited by C. Domb and J. L. Lebowitz (Academic Press, London, 1995), Vol. 17.
[12] M. B. Stearns, in *Magnetic Properties of Metals*, Landolt-Börnstein, New Series, Vol. III/19a, edited by H. P. J. Wijn (Springer, Berlin, 1986).
[13] M. P. Allen and D. J. Tildesley, *Computer Simulation of Liquids* (Clarendon Press, Oxford, 1987).
[14] L. Onsager, Phys. Rev. **65**, 117 (1944).
[15] R. J. Baxter, *Exactly Solved Models in Statistical Mechanics* (Academic Press, London, 1982).
[16] B. M. McCoy and T. T. Wu, *The Two-Dimensional Ising Model*

- (Harvard University Press, Cambridge, 1973).
- [17] A. M. Ferrenberg and D. P. Landau, *Phys. Rev. B* **44**, 5081 (1991).
- [18] N. Ito, K. Hukushima, K. Ogawa, and Y. Ozeki, *J. Phys. Soc. Jpn.* **69**, 1931 (2000).
- [19] A. Hucht, *J. Phys. A* **35**, L481 (2002).
- [20] S. Angst, A. Hucht, and D. E. Wolf (unpublished).
- [21] S. Boukraa, A. J. Guttmann, S. Hassani, I. Jensen, J.-M. Mailard, B. Nickel, and N. Zenine, *J. Phys. A: Math. Theor.* **41**, 455202 (2008), URL http://www.ms.unimelb.edu.au/~iwan/ising/Ising_ser.html
- [22] K. Binder and P. C. Hohenberg, *Phys. Rev. B* **9**, 2194 (1974).
- [23] H. Arisue and T. Fujiwara, *Nucl. Phys. B (Proc. Suppl.)* **119**, 855 (2003); <http://www.rccp.tsukuba.ac.jp/kenkyukai/asia-pacific/program/transparency/arisue/asia-pacific2003b@.ps>.
- [24] R. J. Glauber, *J. Math. Phys.* **4**, 294 (1963).
- [25] K. Kawasaki, *Phys. Rev.* **145**, 224 (1966).
- [26] N. Metropolis, A. W. Rosenbluth, M. N. Rosenbluth, A. H. Teller, and E. Teller, *J. Chem. Phys.* **21**, 1087 (1953).
- [27] W. Kwak, D. P. Landau, and B. Schmittmann, *Phys. Rev. E* **69**, 066134 (2004).
- [28] D. Grüneberg and A. Hucht, *Phys. Rev. E* **69**, 036104 (2004).
- [29] G. Gonnella and M. Pellicoro, *J. Phys. A* **33**, 7043 (2000).
- [30] H. van Beijeren and L. S. Schulman, *Phys. Rev. Lett.* **53**, 806 (1984).
- [31] B. M. McCoy (private communication).
- [32] K. Binder and P. C. Hohenberg, *Phys. Rev. B* **6**, 3461 (1972).
- [33] I. G. Enting and A. J. Guttmann, *J. Phys. A* **13**, 1043 (1980).
- [34] M. E. J. Newman and G. T. Barkema, *Monte Carlo Methods in Statistical Mechanics* (Clarendon Press, Oxford, 1999).
- [35] TM calculations for stripes of width $L_{\perp} > 1$ show that this is only the case for $L_{\perp} = 1$.
- [36] Note that Eq. (69) is mentioned in the literature [30,34] without stressing the multiplicative property [Eq. (68)].
- [37] We use the definition of elliptic functions without square, e.g., $K(m) = \int_0^{\pi/2} (1 - m \sin^2 \theta)^{-1/2} d\theta$.

Aspect-ratio dependence of thermodynamic Casimir forces

Alfred Hucht, Daniel Grüneberg, and Felix M. Schmidt

Fakultät für Physik, Universität Duisburg–Essen, D-47048 Duisburg, Germany

(Received 21 December 2010; published 2 May 2011)

We consider the three-dimensional Ising model in a $L_{\perp} \times L_{\parallel} \times L_{\parallel}$ cuboid geometry with a finite aspect ratio $\rho = L_{\perp}/L_{\parallel}$ and periodic boundary conditions along all directions. For this model the finite-size scaling functions of the excess free energy and thermodynamic Casimir force are evaluated numerically by means of Monte Carlo simulations. The Monte Carlo results compare well with recent field theoretical results for the Ising universality class at temperatures above and slightly below the bulk critical temperature T_c . Furthermore, the excess free energy and Casimir force scaling functions of the two-dimensional Ising model are calculated exactly for arbitrary ρ and compared to the three-dimensional case. We give a general argument that the Casimir force vanishes at the critical point for $\rho = 1$ and becomes repulsive in periodic systems for $\rho > 1$.

DOI: [10.1103/PhysRevE.83.051101](https://doi.org/10.1103/PhysRevE.83.051101)

PACS number(s): 05.50.+q, 05.70.Jk, 05.10.Ln

I. INTRODUCTION

The spatial confinement of a fluctuating and highly correlated medium may cause long-range forces. The Casimir effect, which was theoretically predicted in 1948 by the Dutch physicist H. B. G. Casimir [1], is a prominent example. This quantum effect is caused by the vacuum fluctuations of the electromagnetic field and has been proven experimentally in the late 1990's [2,3]. It becomes manifest in an attractive long-range *Casimir force* acting between two parallel, perfectly conducting plates in an electromagnetic vacuum.

Another example for a fluctuation-induced force being of a similar nature to the Casimir force in quantum electrodynamics can be found in the physics of critical phenomena [4,5]. This *thermodynamic Casimir effect* is caused by the spatial confinement of thermal fluctuations near the critical point of a second-order phase transition. Experimentally, it has been proven by measuring the film thickness of superfluid ^4He films as a function of the temperature in the vicinity of the λ transition [6,7]. Since then, the thermodynamic Casimir effect was measured in several different systems, including binary liquid mixtures [8–10] and tricritical ^3He - ^4He [11].

For several years the shape of the finite-size scaling function determined by Garcia and Chan [6] from the experimental data has not been understood theoretically, in particular, its deep minimum right below T_c . While the value of the Casimir force at criticality as well as the decay above T_c could be calculated using field theory [12–15], no quantitative results were available for the scaling region $T \lesssim T_c$ except for mean-field-theoretical approaches [16,17]. Analytical results exist only for the noncritical region below T_c , where contributions to the thermodynamic Casimir force from Goldstone modes [18–20] and from the excitation of capillary waves of the liquid-vapor ^4He interface [21] become dominant.

This unsatisfactory situation was resolved in Ref. [22], where a method was proposed to calculate the thermodynamic Casimir force for $O(n)$ -symmetrical lattice models using Monte Carlo simulations without any approximations, in contrast to, e.g., the stress tensor method used by Dantchev and Krech [23], which, furthermore, was restricted to periodic systems. The Monte Carlo simulations were done for the three-dimensional (3D) XY model on a simple cubic lattice with film

geometry $L_{\perp} \times L_{\parallel} \times L_{\parallel}$ and open boundary conditions along the \perp direction, as this system is known to be in the same universality class as the superfluid transition in ^4He and thus displays the same asymptotic critical behavior. The results were found to be in excellent agreement with the experimental results by Garcia, Chan, and co-workers [6,7] and provided a theoretical explanation for the characteristic shape of the finite-size scaling function and, in particular, its deep minimum below T_c . In the following, this method was used to determine Casimir forces in various systems and geometries [24,25], while other methods for the evaluation of thermodynamic Casimir forces using Monte Carlo simulations have also been presented [26–28].

In the present work, this method is used to derive the universal finite-size scaling function of the excess free energy and thermodynamic Casimir force as functions of the aspect ratio $\rho = L_{\perp}/L_{\parallel}$ for the 3D Ising model with cuboid geometry and periodic boundary conditions. Here ρ is allowed to take arbitrary values from $\rho \rightarrow 0$ (film geometry) to $\rho \rightarrow \infty$ (rod geometry), while former investigations were either at $\rho = 0$ [12–17] or limited to the case $\rho \ll 1$ [22–30]. The paper is structured as follows: In the remainder of Sec. I the basic principles and definitions concerning the thermodynamic Casimir effect are discussed and the Monte Carlo method will be revisited. In Sec. II, our Monte Carlo results are discussed and compared to recently published results by Dohm [31], who calculated the Casimir force within a minimal renormalization scheme of the $O(n)$ model at finite ρ , covering temperatures below and above T_c , as well as to field-theoretical results obtained for $T \geq T_c$ in the framework of the renormalization group-improved perturbation theory (RG) to two-loop order [14,15]. In Sec. III, we present an exact calculation of the excess free energy and Casimir force scaling functions for the two-dimensional (2D) Ising model with arbitrary aspect ratios ρ . We conclude with a discussion and a summary.

A. Basic principles

When a thermodynamical system in d dimensions such as a simple classical fluid or a classical n -vector magnet is confined to a region with thickness L_{\perp} and cross-sectional area L_{\parallel}^{d-1} ,

its total free energy F becomes explicitly size dependent. Then the reduced free energy per unit volume,

$$\begin{aligned} f(T, L_{\perp}, L_{\parallel}) &\equiv \frac{F(T, L_{\perp}, L_{\parallel})}{L_{\perp} L_{\parallel}^{d-1} k_B T} \\ &= f_{\infty}(T) + \delta f(T, L_{\perp}, L_{\parallel}), \end{aligned} \quad (1)$$

can be decomposed [32] into a sum of the bulk free-energy density f_{∞} and a finite-size contribution δf . As we assume periodic boundary conditions in all directions, the surface terms in \perp and \parallel directions as well as edge and corner contributions are omitted in (1). In this case the residual free energy δf equals the excess free energy f_{ex} , and we will use f_{ex} instead of δf in the following.

In terms of f_{ex} , the reduced thermodynamic Casimir force per surface area in the \perp direction is defined as [13]

$$\beta \mathcal{F}_{\text{C}}(T, L_{\perp}, L_{\parallel}) \equiv - \frac{\partial [L_{\perp} f_{\text{ex}}(T, L_{\perp}, L_{\parallel})]}{\partial L_{\perp}}, \quad (2)$$

where $\beta = 1/k_B T$, and the derivative is taken at fixed L_{\parallel} . We omit the index \perp for the Casimir force, as we will not consider Casimir forces in parallel directions in this work.

When in the absence of symmetry-breaking external fields the critical point is approached from higher temperatures, which corresponds to the liquid-vapor critical point in the case of a simple classical fluid or to the Curie point in a classical n -vector magnet, the bulk correlation length $\xi_{\infty}(t)$ grows and diverges as [33]

$$\xi_{\infty}(t) \underset{t>0}{\sim} \xi_+ t^{-\nu}, \quad (3)$$

with correlation length exponent ν , reduced temperature $t = T/T_{\text{c},\infty} - 1$, and nonuniversal amplitude ξ_+ . In this work we use $\xi_+ = Q_{\xi}^+ f^+ = 1.000\,183(2) \times 0.506(1)$ valid for the 3D Ising model on a simple cubic lattice [34,35].

According to the theory of finite-size scaling [36] and under the assumption that long-range interactions and other contributions irrelevant in the RG sense are negligible, as for instance subleading long-range interactions [37], the thermodynamic Casimir force in the regime $L_{\perp}, L_{\parallel}, \xi_{\infty} \gg a$, where a is a characteristic microscopic length scale such as the lattice constant in the case of a lattice model, obeys a finite-size scaling form

$$\beta \mathcal{F}_{\text{C}}(T, L_{\perp}, L_{\parallel}) \sim L_{\perp}^{-d} \vartheta_{\perp}(x_{\perp}, \rho), \quad (4)$$

where the scaling variable x_{\perp} can be defined as

$$x_{\perp} \equiv t \left(\frac{L_{\perp}}{\xi_+} \right)^{\frac{1}{\nu}} \underset{t>0}{\sim} \left(\frac{L_{\perp}}{\xi_{\infty}(t)} \right)^{\frac{1}{\nu}}, \quad (5)$$

$\rho = L_{\perp}/L_{\parallel}$ denotes the aspect ratio, and ϑ_{\perp} is a finite-size scaling function. Note that in this work ϑ always denotes the scaling function of the Casimir force in the \perp direction, while the index describes the reference direction \perp or \parallel of length L .

An analogous finite-size scaling relation holds for the excess free energy,

$$f_{\text{ex}}(T, L_{\perp}, L_{\parallel}) \sim L_{\perp}^{-d} \Theta_{\perp}(x_{\perp}, \rho), \quad (6)$$

and ϑ_{\perp} is related to Θ_{\perp} according to [31]

$$\vartheta_{\perp}(x_{\perp}, \rho) = \left[d - 1 - \frac{1}{\nu} \frac{x_{\perp} \partial}{\partial x_{\perp}} - \frac{\rho \partial}{\partial \rho} \right] \Theta_{\perp}(x_{\perp}, \rho). \quad (7)$$

The dimensionless finite-size scaling functions Θ_{\perp} and ϑ_{\perp} are universal, that is, they only depend on gross properties of the system such as the bulk and surface universality classes of the phase transition, the system shape, and boundary conditions, but not on its microscopic details [37,38].

At the critical point T_{c} the thermodynamic Casimir force becomes long ranged and for sufficiently large values of the length L_{\perp} asymptotically decays as

$$\begin{aligned} \beta \mathcal{F}_{\text{C}}(T_{\text{c}}, L_{\perp}, L_{\parallel}) &\sim L_{\perp}^{-d} \vartheta_{\perp}(0, \rho) \\ &\sim L_{\perp}^{-d} [(d-1)\Delta_{\perp}(\rho) - \rho \Delta'_{\perp}(\rho)], \end{aligned} \quad (8)$$

where $\Delta_{\perp}(\rho) \equiv \Theta_{\perp}(0, \rho)$ is the so-called Casimir amplitude [4], being—as the finite-size scaling function ϑ_{\perp} —an universal quantity. Note that for finite aspect ratios $\rho > 0$ the Casimir amplitude becomes ρ dependent. The film geometry is recovered by letting $\rho \rightarrow 0$, and Eq. (8) simplifies to

$$\beta \mathcal{F}_{\text{C}}(T_{\text{c}}, L_{\perp}, \infty) \sim L_{\perp}^{-d} (d-1)\Delta_{\perp}(0). \quad (9)$$

Since the 1990's, such universal quantities have been subject to extensive theoretical research. They were studied by means of exactly solvable models [13,23,37,39–42], Monte Carlo simulations [9,16,22–29,43], as well as within field-theoretical approaches [12–15,31,44–46].

B. Reformulation for arbitrary ρ

The formulation of the Casimir force finite-size scaling laws in the previous section was done by assuming film geometry $\rho \ll 1$, i.e., having in mind the limit $\rho \rightarrow 0$. However, if $\rho \gtrsim 1$, this picture is not appropriate and should be replaced by a more general treatment. In the following, we rewrite the basic scaling laws in terms of the system volume $V = L_{\perp} L_{\parallel}^{d-1}$ instead of the film thickness L_{\perp} . The resulting scaling functions can be used in the whole regime $0 < \rho < \infty$.

Using the substitution $L_{\perp}^d \rightarrow V \rho^{d-1}$ in Eq. (6) we get

$$f_{\text{ex}}(T, L_{\perp}, L_{\parallel}) \sim V^{-1} \Theta(x, \rho), \quad (10)$$

with an universal scaling function Θ and the generalized scaling variable

$$x \equiv t \left(\frac{V}{\xi_+^d} \right)^{\frac{1}{d\nu}}, \quad (11)$$

while the scaling function Θ_{\perp} from Eq. (6) is recovered as

$$\Theta_{\perp}(x_{\perp}, \rho) = \rho^{d-1} \Theta(x, \rho), \quad (12)$$

with

$$x_{\perp} = \rho^{\frac{1}{\nu} - \frac{1}{d\nu}} x. \quad (13)$$

Similarly, the Casimir force obeys

$$\beta \mathcal{F}_{\text{C}}(T, L_{\perp}, L_{\parallel}) \sim V^{-1} \vartheta(x, \rho), \quad (14)$$

from which we derive the scaling identity

$$\vartheta(x, \rho) = - \left[\frac{1}{d\nu} \frac{x \partial}{\partial x} + \frac{\rho \partial}{\partial \rho} \right] \Theta(x, \rho). \quad (15)$$

Note that this identity is equivalent to but simpler than Eq. (7). At criticality we now define the generalized Casimir amplitude as

$$\Delta(\rho) = \Theta(0, \rho) \quad (16)$$

and find

$$f_{\text{ex}}(T_c, L_{\perp}, L_{\parallel}) \sim V^{-1} \Delta(\rho), \quad (17)$$

$$\beta \mathcal{F}_C(T_c, L_{\perp}, L_{\parallel}) \sim -V^{-1} \rho \Delta'(\rho). \quad (18)$$

The case $\rho = 1$ deserves special attention: As

$$\left. \frac{\partial}{\partial \rho} \Theta(x, \rho) \right|_{\rho=1} = 0 \quad (19)$$

in cubic geometry (see Appendix A), Eq. (15) simplifies to

$$\vartheta(x, 1) = -\frac{1}{d} \frac{x \partial}{\partial x} \Theta(x, 1) \quad (20)$$

at $\rho = 1$, and gives a remarkably simple connection between the Casimir force and the excess internal energy, Eq. (30), in the cube-shaped system, namely,

$$\beta \mathcal{F}_C(T, L, L) \sim \frac{t}{d} u_{\text{ex}}(T, L, L). \quad (21)$$

Obviously, the Casimir force vanishes at the critical point if $\rho = 1$, i.e.,

$$\vartheta(0, 1) = 0. \quad (22)$$

For completeness we also give the definitions of the scaling functions in terms of L_{\parallel} . As

$$f_{\text{ex}}(T, L_{\perp}, L_{\parallel}) \sim L_{\parallel}^{-d} \Theta_{\parallel}(x_{\parallel}, \rho), \quad (23)$$

we find

$$\Theta_{\parallel}(x_{\parallel}, \rho) = \rho^{-1} \Theta(x, \rho), \quad (24)$$

with $x_{\parallel} \equiv t(L_{\parallel}/\xi_+)^{1/\nu}$. Note that in this representation the scaling identity, Eq. (7) reads

$$\vartheta_{\parallel}(x_{\parallel}, \rho) = -\left[1 + \frac{\rho \partial}{\partial \rho}\right] \Theta_{\parallel}(x_{\parallel}, \rho), \quad (25)$$

and in the limit $\rho \rightarrow \infty$ simplifies to

$$\vartheta_{\parallel}(x_{\parallel}, \infty) = -\Theta_{\parallel}(x_{\parallel}, \infty), \quad (26)$$

leading to the simple relation

$$\beta \mathcal{F}_C(T, \infty, L_{\parallel}) \sim -f_{\text{ex}}(T, \infty, L_{\parallel}). \quad (27)$$

C. Monte Carlo method

In this work we focus on the 3D isotropic nearest-neighbor Ising model on a $L_{\perp} \times L_{\parallel} \times L_{\parallel}$ simple cubic lattice with periodic boundary conditions and Hamiltonian

$$\beta \mathcal{H} = -\frac{K}{2} \sum_{\langle ij \rangle} \sigma_i \sigma_j, \quad (28)$$

where $K = \beta J > 0$ is the ferromagnetic reduced exchange interaction and $\sigma_i = \pm 1$ are one-component spin variables at lattice sites i . The Monte Carlo simulations were done using

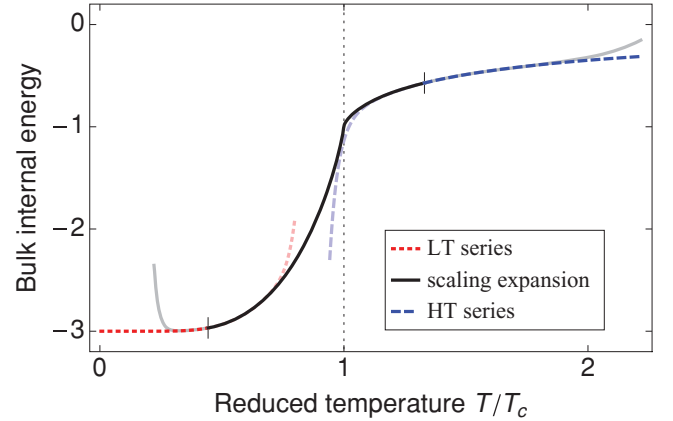


FIG. 1. (Color online) Bulk internal energy density $e_{\infty}(T)$ obtained from three different methods: low-temperature series [47] (red dotted line), scaling expansion [48] (black line), and high-temperature series [49] (blue dashed line).

the Wolff single-cluster algorithm [50]. Measuring the reduced internal energy density

$$u(T, L_{\perp}, L_{\parallel}) = \frac{\langle \beta \mathcal{H} \rangle}{L_{\parallel}^{d-1} L_{\perp}}, \quad (29)$$

the excess free energy and Casimir force is calculated as follows [22]: First we determined the excess internal energy,

$$u_{\text{ex}}(T, L_{\perp}, L_{\parallel}) \equiv u(T, L_{\perp}, L_{\parallel}) - u_{\infty}(T), \quad (30)$$

by subtracting the reduced bulk internal energy density $u_{\infty}(T)$. We used three different results to get precise estimates for $u_{\infty}(T)$ of the 3D Ising model in the different temperature regimes: For low temperatures $K > 1/2$ we used the low-temperature series expansion (54th order) by Bhanot *et al.* [47], while for $K < 1/6$ the high-temperature series expansion (46th order) by Arisue and Fujiwara [49] was utilized. Finally, in the vicinity of the critical point we used the expansion recently obtained by Feng and Blöte [48], where we also took the bulk critical indices [51] $K_c = 0.221\,654\,55(3)$, $\nu^{-1} = 1.5868(3)$, and $\omega = 0.821(5)$. These three estimates of $u_{\infty}(T)$ show a broad overlap (see also the discussion by Feng and Blöte [48]), the resulting nonreduced bulk internal energy density $e_{\infty}(T) = u_{\infty}(T)/\beta$ is depicted in Fig. 1. With the identity

$$f_{\text{ex}}(T, L_{\perp}, L_{\parallel}) = -\int_T^{\infty} \frac{d\tau}{\tau} u_{\text{ex}}(\tau, L_{\perp}, L_{\parallel}), \quad (31)$$

we determined f_{ex} by numerical integration, using the fact that u_{ex} goes exponentially fast to zero above T_c [22].

To obtain the Casimir force, we first calculated the *internal Casimir force*

$$\beta \mathcal{F}_I(T, L_{\perp}, L_{\parallel}) = -\frac{\partial [L_{\perp} u_{\text{ex}}(T, L_{\perp}, L_{\parallel})]}{\partial L_{\perp}}, \quad (32)$$

which is defined similar to Eq. (2), by numerical differentiation, using thicknesses $L'_{\perp} = L_{\perp} \pm 1$ in order to get an integral effective thickness L_{\perp} . With Eqs. (4) and (35) and the hyperscaling relation $d\nu = 2 - \alpha$ with specific-heat exponent

α , it is straightforward to show that this quantity fulfills the finite-size scaling form

$$-\beta\mathcal{F}_I(T, L_\perp, L_\parallel) \sim \xi_+^{-1/\nu} L_\perp^{(\alpha-1)/\nu} \vartheta'_\perp(x_\perp, \rho), \quad (33)$$

with an universal finite-size scaling function

$$\vartheta'_\perp(x_\perp, \rho) = \frac{\partial \vartheta_\perp(x_\perp, \rho)}{\partial x_\perp}. \quad (34)$$

This quantity turns out to be very useful in understanding the Casimir force scaling function $\vartheta_\perp(x_\perp, \rho)$ for $\rho \rightarrow 0$, as will be shown in the next section. Finally, the thermodynamic Casimir force is obtained from Eq. (32) by integration,

$$\beta\mathcal{F}_C(T, L_\perp, L_\parallel) = - \int_T^\infty \frac{d\tau}{\tau} \beta\mathcal{F}_I(\tau, L_\perp, L_\parallel), \quad (35)$$

where again the exponential decay above T_c simplifies the numerical integration.

II. RESULTS

A. Casimir force in film geometry $\rho \rightarrow 0$

In Fig. 2 we plot the internal Casimir force $\beta\mathcal{F}_I$, Eq. (32), for small aspect ratios $\rho = 1/8$ and $1/16$. In the limit of film geometry $\rho \rightarrow 0$ we observe strong finite-size effects below the critical point [22], which are caused by the influence of the phase transition in the $(d-1)$ -dimensional system. In this section we will analyze this influence in detail and show that $\beta\mathcal{F}_I$ is directly connected to the specific heat of the $(d-1)$ -dimensional system. We will give the derivation for periodic systems where no surface terms occur, as these terms will complicate the analysis [24].

From the scaling identity Eq. (7) for $\rho \rightarrow 0$,

$$\vartheta_\perp(x_\perp, 0) = \left[d - 1 - \frac{1}{\nu} \frac{x_\perp \partial}{\partial x_\perp} \right] \Theta_\perp(x_\perp, 0), \quad (36)$$

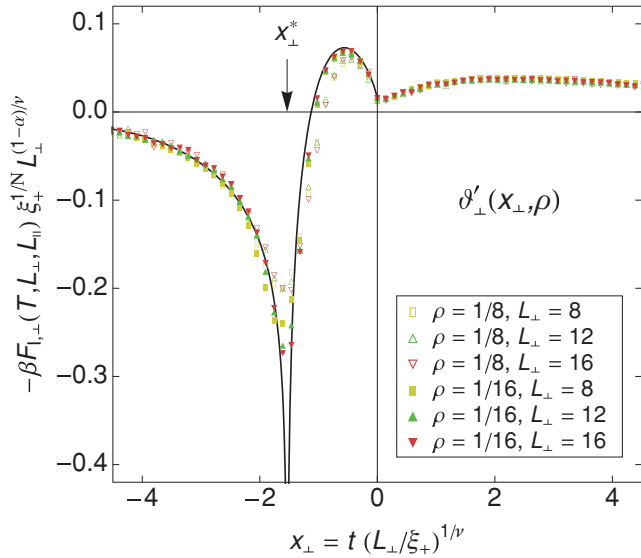


FIG. 2. (Color online) Internal Casimir force scaling function $\vartheta'_\perp(x_\perp, \rho)$ for small aspect ratios $\rho = 1/16$ and $1/8$. The black thin line is the extrapolation $\rho \rightarrow 0$, showing a logarithmic singularity at $x_\perp^* = 1.535(10)$ (see text).

we get

$$\beta\mathcal{F}_C \underset{\rho \rightarrow 0}{\sim} (d-1)f_{\text{ex}} + t\nu^{-1}u_{\text{ex}}, \quad (37)$$

i.e., within the scaling region and for $\rho \rightarrow 0$ the Casimir force can alternatively be calculated without L_\perp -derivative [24]. For the internal Casimir force scaling function

$$\vartheta'_\perp(x_\perp, 0) = \left[d - 1 - \frac{1}{\nu} - \frac{1}{\nu} \frac{x_\perp \partial}{\partial x_\perp} \right] \frac{\partial \Theta_\perp(x_\perp, 0)}{\partial x_\perp}, \quad (38)$$

we find the asymptotic identity

$$-\beta\mathcal{F}_I \underset{\rho \rightarrow 0}{\sim} - \left[d - 1 - \frac{1-t}{\nu} \right] u_{\text{ex}} + \frac{t}{\nu} c_{\text{ex}} \quad (39)$$

with the excess specific heat

$$c_{\text{ex}}(T, L_\perp, L_\parallel) \equiv c(T, L_\perp, L_\parallel) - c_\infty(T) \quad (40)$$

and $c = \partial T u / \partial T$ as usual. For $\rho \rightarrow 0$, this quantity contains both the bulk singularity

$$c_\infty(T) \sim A_\pm |t|^{-\alpha}, \quad (41)$$

with amplitudes A_\pm , as well as the singularity of the laterally infinite film with finite thickness L_\perp at $t_c(L_\perp) = T_c(L_\perp)/T_c - 1$, which scales as

$$c(T, L_\perp, \infty) \sim A_\pm^* \left(\frac{L_\perp}{\xi_+} \right)^{\frac{\alpha-\alpha^*}{\nu}} |t - t_c(L_\perp)|^{-\alpha^*}. \quad (42)$$

Here, α^* denotes the specific heat exponent of the $(d-1)$ -dimensional system, A_\pm^* are amplitudes, and the factor $(L_\perp/\xi_+)^{(\alpha-\alpha^*)/\nu}$ guarantees the correct scaling behavior for $L_\perp \rightarrow \infty$ by cancelation of terms containing α^* .

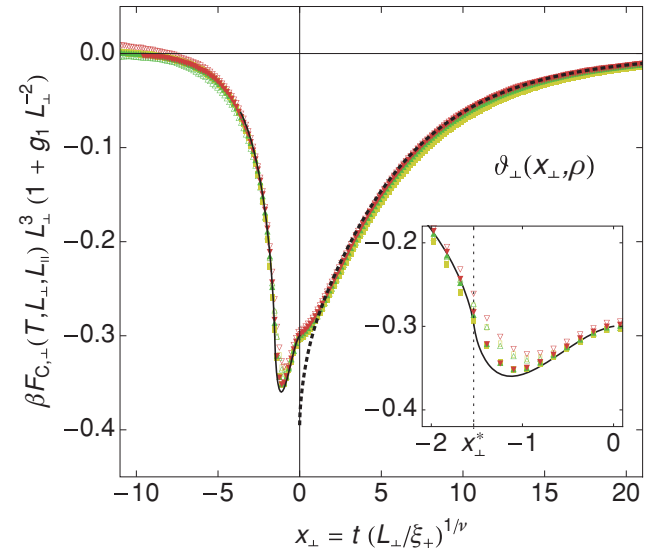


FIG. 3. (Color online) Casimir force scaling function $\vartheta_\perp(x_\perp, \rho)$ for small aspect ratios $\rho = 1/16$ and $1/8$. The solid line is the extrapolation $\rho \rightarrow 0$ calculated from the integrated logarithmic singularity in $\vartheta'_\perp(x_\perp, 0)$. The dotted line is the RG calculation of Grüneberg and Diehl [15].

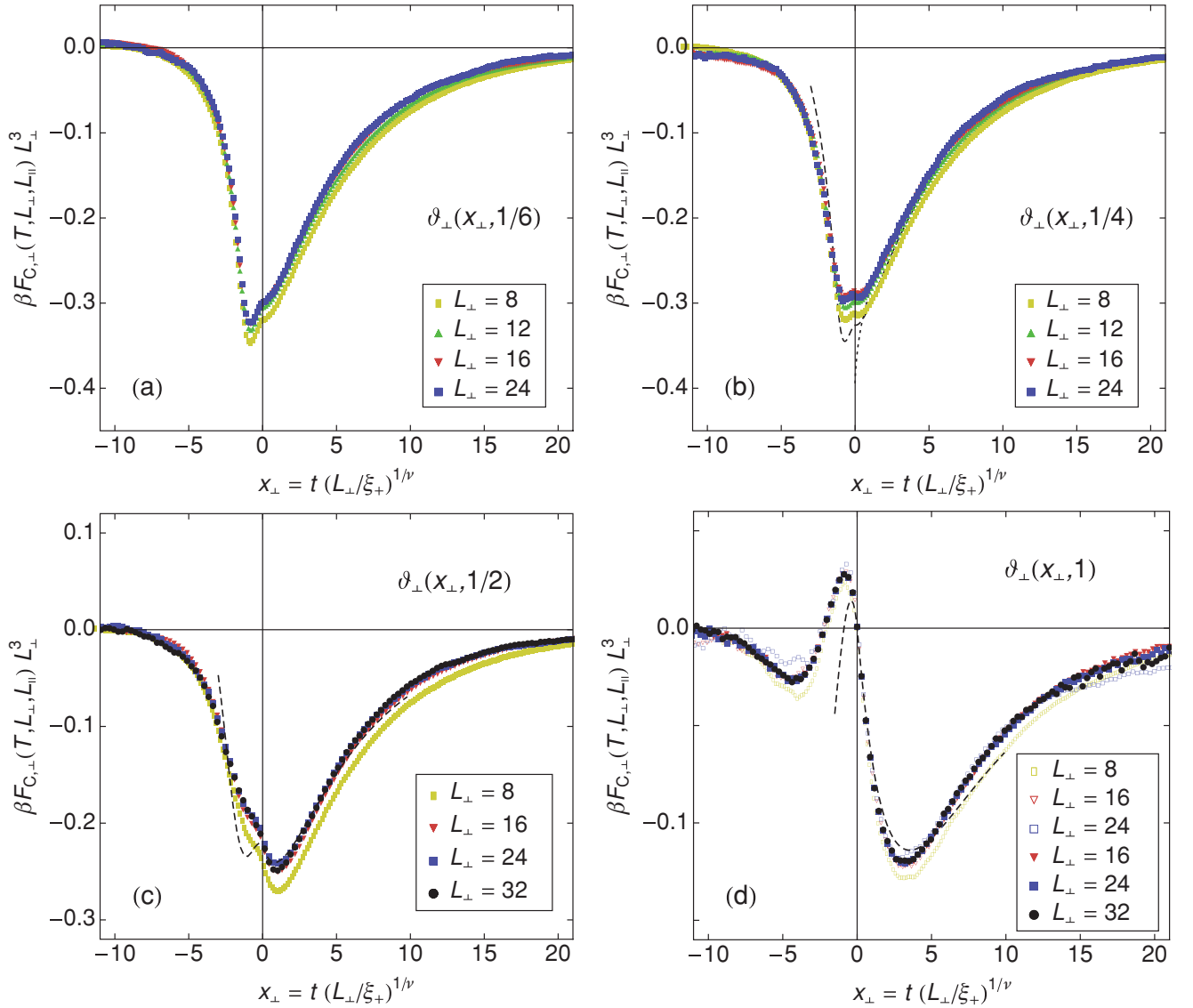


FIG. 4. (Color online) Casimir force scaling function $\vartheta_{\perp}(x_{\perp}, \rho)$ for several aspect ratios $\rho = \{1/6, 1/4, 1/2, 1\}$. The dotted line is the result of Grüneberg and Diehl [15] for $\rho = 0$, while the dashed lines are the predictions of Dohm [31]. For $\rho = 1$ we also show results from scaling relation Eq. (20) (filled symbols), which have much better statistics, as they are directly calculated from the internal energy.

However, as c_{ex} enters Eq. (39) with prefactor t only, the bulk singularity at $t = 0$ is suppressed (as $\alpha < 1$) and c_{ex} is dominated by the singularity from Eq. (42), at

$$x_{\perp}^* \sim t_c(L_{\perp}) \left(\frac{L_{\perp}}{\xi_{+}} \right)^{\frac{1}{\nu}}. \quad (43)$$

The location of the critical point was reanalyzed from the data of Kitatani *et al.* [52] including corrections to scaling, as well as from the data of Caselle and Hasenbusch [53], giving the value $x_{\perp}^* = -1.535(10)$. This improves the value $x_{\perp}^* = -1.60(2)$ found by Vasilyev *et al.* [29]. Furthermore, the other terms in (39) are $O(1)$ near x_{\perp}^* , which leads us to the conclusion that the specific-heat singularity of the $(d-1)$ -dimensional film is directly visible in the scaling function $\vartheta'_{\perp}(x_{\perp}, 0)$

around $x_{\perp} = x_{\perp}^*$,

$$\vartheta'_{\perp}(x_{\perp} \approx x_{\perp}^*, 0) \sim \frac{A_{\pm}^* \xi_{+}^d}{\nu} x_{\perp} |x_{\perp} - x_{\perp}^*|^{-\alpha^*} + O(1). \quad (44)$$

From this argument we conclude that the scaling function $\vartheta'_{\perp}(x_{\perp}, 0)$ has a singularity at x_{\perp}^* dominated by the specific-heat singularity of the $(d-1)$ -dimensional system, with critical exponent α^* . In our case, $\alpha^* = 0$ and the singularity is logarithmic. This asymptotic behavior is included in Fig. 2 as a solid line.

In Fig. 3 we show the scaling function of the Casimir force for $\rho = 1/8, 1/16$, together with the RG results of Grüneberg and Diehl [15]. The solid line is the integrated extrapolation discussed above. We used a correction factor $(1 + g_1 L_{\perp}^{-2})$, with $g_1 = -4(1)$, to account for leading systematic errors from the discrete derivative, which are expected to be $\propto L_{\perp}^{-2}$

TABLE I. Monte Carlo results for the Casimir amplitudes $\Delta(\rho)$, $\Delta_\mu(\rho)$ and $\vartheta_\mu(0, \rho)$, with $\mu = \perp$ for $\rho \leq 1$ and $\mu = \parallel$ for $\rho \geq 1$. Note that the critical Casimir force changes sign at $\rho = 1$.

ρ	$\Delta(\rho)$	$\Delta_\mu(\rho)$	$\vartheta_\mu(0, \rho)$
0	$-\infty$	-0.155(3)	-0.310(6)
1/16	-39.8(8)	-0.155(3)	-0.310(6)
1/8	-9.9(2)	-0.155(3)	-0.310(6)
1/6	-5.7(1)	-0.157(3)	-0.30(1)
1/4	-2.60(5)	-0.161(3)	-0.290(5)
1/2	-0.89(2)	-0.223(4)	-0.22(1)
1	-0.63(1)	-0.63(1)	0.000(5)
3/2	-0.68(3)	-0.45(2)	0.17(1)
2	-0.78(3)	-0.39(2)	0.25(1)
8	-2.86(5)	-0.357(8)	0.36(1)
∞	$-\infty$	-0.36(1)	0.36(1)

in periodic systems. The inset is a magnification of the minimum, from the divergence of $\vartheta'_\perp(x_\perp = x_\perp^*, 0)$ the slope of $\vartheta_\perp(x_\perp, 0)$ at x_\perp^* diverges logarithmically. We find a critical amplitude $\vartheta_\perp(0, 0) = -0.310(6)$ (see Table I), which agrees within error bars with the values $\vartheta_\perp(0, 0) = -0.3040(4)$ [29] as well as $\vartheta_\perp(0, 0) = -0.3052(20)$ [54]. The zero at $\vartheta'_\perp(x_\perp^{\min}, 0)$ (solid line in Fig. 2) gives the minimum position $x_\perp^{\min} = -1.13(5)$, with $\vartheta_\perp(x_\perp^{\min}, 0) = -0.360(5)$, while the finite ρ results are $\vartheta_\perp(x_\perp^{\min} = -1.10(5), 1/16) = -0.352(5)$ and $\vartheta_\perp(x_\perp^{\min} = -0.95(5), 1/8) = -0.340(5)$.

B. Casimir force for finite ρ

If we increase ρ to finite values, the Casimir force scaling function $\vartheta_\perp(x_\perp, \rho)$ first changes its shape around the minimum. The results for $\rho = 1/6$ [Fig. 4(a)] already deviate distinctly from the thinner systems, the minimum below T_c is not so deep anymore, with $\vartheta_\perp(x_\perp^{\min} = -0.77(5), 1/6) = -0.323(5)$. These values deviate only slightly from the results of Vasilyev *et al.* [29], $x_\perp^{\min} = -0.681(1)$ and $\vartheta_\perp(x_\perp^{\min}, 1/6) = -0.329(1)$, which we attribute to the larger statistical error in Ref. [29].

When the aspect ratio is further increased to $\rho = 1/4$ [Fig. 4(b)], the curve has two minima below and above T_c which are nearly equal in depth. Note that the results for $\rho \geq 1/4$ are compared to the predictions of Dohm [31] and show similar behavior. For $\rho \gtrsim 1/4$ the minimum below T_c vanishes, while the one above T_c remains. This is shown in Fig. 4(c), where we plot the Casimir scaling function for $\rho = 1/2$.

The results for the cube-shaped system with $\rho = 1$ are shown in Fig. 4(d) [55]. The case $\rho = 1$ is quite interesting, as here the Casimir force at $x = 0$ vanishes [Eq. (22)] and even becomes positive for $\rho > 1$, although the system has symmetric, i.e., periodic boundary conditions. However, this sign change of the Casimir force at $\rho = 1$ does not contradict the predictions of Bachas [56], as he assumed an infinite system in the parallel direction, i.e., $\rho = 0$. The scaling function $\vartheta(x, 1)$ has a negative slope $\vartheta'(0, 1) = -\Theta'(0, 1)/d\nu$ at $x = 0$. This behavior is in perfect agreement with Eq. (21), as the excess internal energy $u_{\text{ex}}(T_c, L, L)$ is negative for our model. Furthermore, $\vartheta(x, 1)$ has a second zero at $x = -2.25(5)$, where $u(T, L, L) = u_\infty(T)$ holds. Figure 4(d) shows results from both

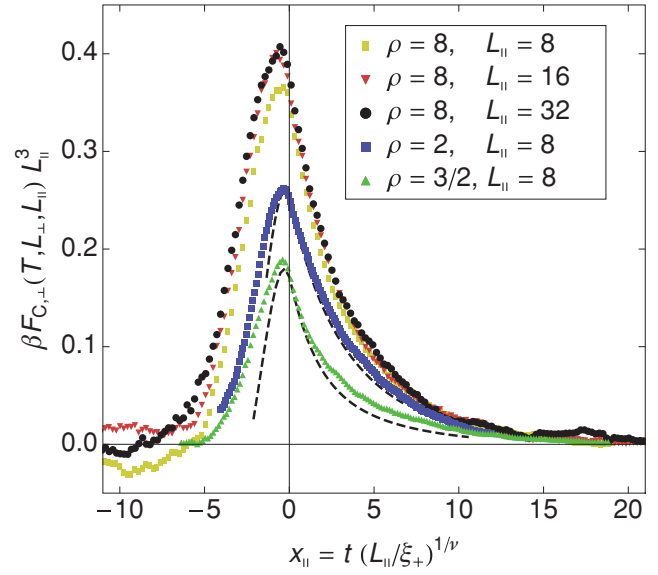


FIG. 5. (Color online) Casimir force scaling function $\vartheta_{\parallel}(x_{\parallel}, \rho)$ for aspect ratios $\rho > 1$, now as function of the proper scaling variable x_{\parallel} . The dashed lines are the predictions of Dohm [31].

the calculation using Eqs. (29)–(35) (open symbols) as well as Eq. (21) (filled symbols), where the latter have a much better statistics, as no numerical differentiation and integration is necessary.

Finally, in Fig. 5 we depict the Casimir scaling function for values of ρ larger than one. Now we are in rod geometry and use the appropriate scaling variable L_{\parallel} instead of L_{\perp} . Due to this rescaling, the scaling function $\vartheta_{\parallel}(x_{\parallel}, \rho)$ converges to a finite limit $\vartheta_{\parallel}(x_{\parallel}, \infty)$ which should only slightly deviate from curves for $\rho = 8$, just as in the inverse case $\rho = 1/8$ (see Fig. 3). In this regime the Casimir force is always positive, leading to a repulsion of the opposite surfaces. Note that for $\rho = 8$ we increased the thickness difference for the calculation of the derivative in Eq. (32) to $L'_{\perp} = L_{\perp} \pm 4$, as, e.g., $L_{\perp} = 256$ for $L_{\parallel} = 32$.

C. Excess free energy

The excess free energy is shown in Fig. 6 for $\rho \leq 1$. An interesting feature of these curves is the nonvanishing limit for $x_{\perp} \rightarrow -\infty$, which means that for fixed temperatures $T < T_c$ and $L_{\perp}, L_{\parallel} \rightarrow \infty$ the total excess free energy Vf_{ex} approaches a finite value. This behavior is a direct consequence of the broken symmetry in the ordered phase [57]: In this phase, which only exists in the thermodynamic limit below T_c , the Ising partition function is reduced by a factor of 2, as the system cannot reach the whole phase space anymore. This leads to the term $-\ln 2$ in the total excess free energy of a periodic Ising system below T_c ,

$$\Theta(-\infty, \rho) = -\ln 2, \quad (45)$$

independent of shape and dimensionality. Note that, e.g., for the q -state Potts model this argument directly generalizes to $\Theta(-\infty, \rho) = -\ln q$. Using Eq. (12), we find

$$\Theta_{\perp}(-\infty, \rho) = -\rho^{d-1} \ln 2, \quad (46)$$

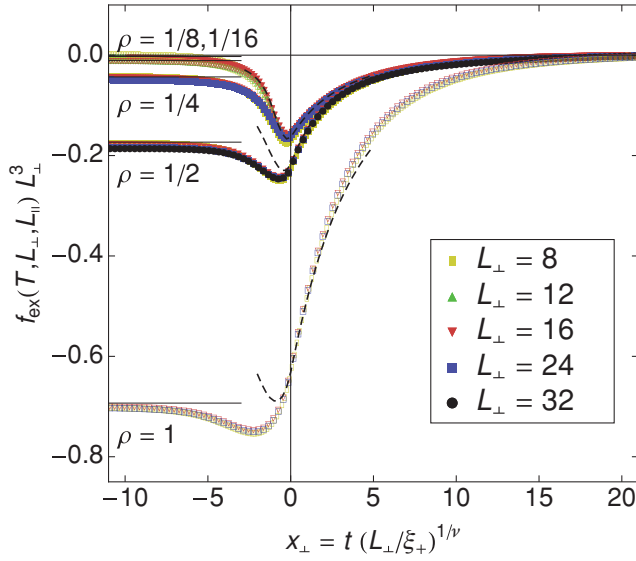


FIG. 6. (Color online) Excess free-energy scaling function $\Theta_{\perp}(x_{\perp}, \rho)$ for several aspect ratios ρ . The dashed lines are the predictions of Dohm [31] for $\rho = 1/4, 1/2, 1$, while the solid lines are the limits for $x_{\perp} \rightarrow -\infty$, Eq. (46).

and this limit is shown as thin solid lines in Fig. 6. The results are compared to the field theoretical predictions of Dohm [31], we find a satisfactory agreement for positive and also for slightly negative values of x_{\perp} . Furthermore, our value $\Delta(1) = -0.63(1)$ for the cube is compatible with the value $-0.657(30)$ obtained by Mon [58].

The generalized Casimir amplitude at criticality, $\Delta(\rho) = \Theta(0, \rho)$ [Eq. (16)], is listed in Table I for several values of ρ and is depicted in Fig. 7, together with the predictions of Dohm [31] (dashed line) as well as the asymptotes (dotted lines). The inset shows $\Delta_{\perp}(\rho)$ (circles) and $\Delta_{\parallel}(1/\rho)$ (squares), showing good agreement with these predictions for $1/4 \lesssim \rho \lesssim 3$.

III. EXACT RESULTS IN TWO DIMENSIONS

The scaling function Θ_{\perp} of the excess free energy in $d = 2$ is calculated exactly based on the work of Ferdinand and Fisher [59] [Note that the term $\xi S_1(n)\tau^2/2$ is missing in Eq. (3.36) of this work]. Our scaling variables differ from theirs, we use $x_{\perp} = t(L_{\perp}/\xi_{\perp})$ and $\rho = L_{\perp}/L_{\parallel}$, while they used $\tau = x_{\perp}/2$ and $\xi = 1/\rho$ as temperature and aspect-ratio variables.

We start from the partition function of the $L_{\perp} \times L_{\parallel}$ isotropic Ising model on a torus [60],

$$Z(T, L_{\perp}, L_{\parallel}) = \frac{1}{2} (2 \sinh 2K)^{\frac{1}{2} L_{\perp} L_{\parallel}} \times (Z_1^+ + Z_1^- + Z_0^+ \pm Z_0^-), \quad (47a)$$

with + above and - below T_c , the four partial sums,

$$Z_{\delta}^{\pm} = \prod_{n=0}^{L_{\perp}-1} \left(e^{\frac{1}{2} L_{\parallel} \gamma_{2n+\delta}} \pm e^{\frac{1}{2} L_{\parallel} \gamma_{2n}} \right), \quad (47b)$$

and $\cosh \gamma_l = \cosh 2K \coth 2K - \cos(l\pi/L_{\perp})$.

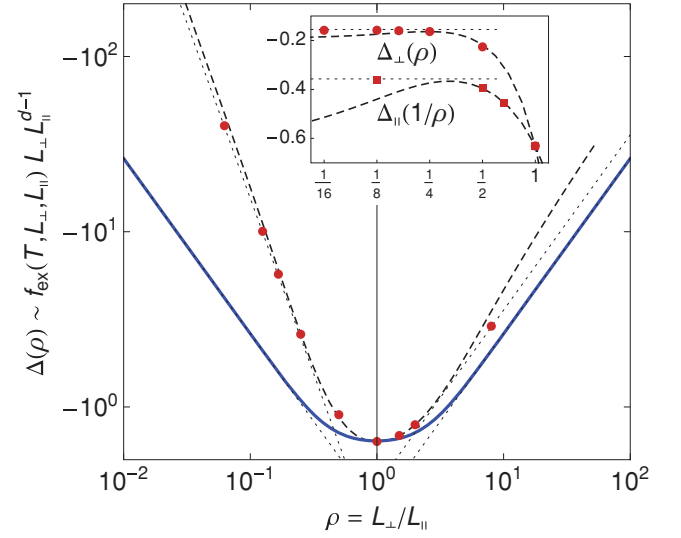


FIG. 7. (Color online) Generalized Casimir amplitude $\Delta(\rho) = \Theta(0, \rho)$, Eq. (16), of the Ising universality class in $d = 3$ (red circles; see also Table I) and in $d = 2$ [Eq. (56), blue solid line]. The dashed line is the prediction of Dohm [31], while the dotted lines show the asymptotes. The inset depicts $\Delta_{\perp}(\rho)$ (circles) and $\Delta_{\parallel}(1/\rho)$ (squares).

For the bulk free-energy density of the 2D Ising model, using *Mathematica* [61], we derived a nice closed-form expression, namely,

$$f_{\infty} = -\ln(2 \cosh 2K) + \frac{k^2}{16} {}_4F_3 \left(\begin{matrix} 1, 1, \frac{3}{2}, \frac{3}{2} \\ 2, 2, 2 \end{matrix} \middle| k^2 \right), \quad (48)$$

with $k = 2 \tanh 2K / \cosh 2K$ and the generalized hypergeometric function ${}_4F_3(\cdot)$ [61].

After some algebra, the scaling function Θ_{\perp} for arbitrary x_{\perp} and ρ can be written as

$$\Theta_{\perp}(x_{\perp}, \rho) = -\rho \ln \left(\frac{P_{1/2}^+ + P_{1/2}^-}{2e^{-I_{\perp}/\rho}} + \frac{P_0^+ \pm P_0^-}{2e^{-I_{\perp}/\rho}} \right), \quad (49a)$$

with

$$P_{\delta}^{\pm}(x_{\perp}, \rho) = \prod_{n=-\infty}^{\infty} (1 \pm e^{-\sqrt{x_{\perp}^2 + 4\pi^2(n-\delta)^2/\rho}}) \quad (49b)$$

and

$$I_{\pm}(x_{\perp}) = \int_{-\infty}^{\infty} d\omega \ln(1 \pm e^{-\sqrt{x_{\perp}^2 + 4\pi^2\omega^2}}). \quad (49c)$$

Note that

$$I_{\pm}(x_{\perp}) = \lim_{r \rightarrow \infty} \frac{1}{r} \ln P_{\delta}^{\pm}(rx_{\perp}, r), \quad (50)$$

independent of δ . As the 2D system is invariant under exchange of the directions \perp and \parallel ,

$$\Theta(x, \rho) = \Theta(x, 1/\rho), \quad (51)$$

which, using Eq. (12), gives

$$\Theta_{\perp}(x_{\perp}, \rho)/\rho = \rho \Theta_{\perp}(x_{\perp}/\rho, 1/\rho), \quad (52)$$

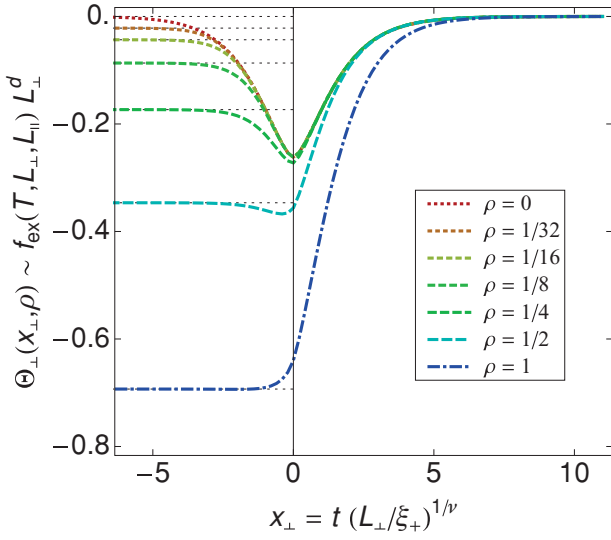


FIG. 8. (Color online) Excess free-energy scaling function of the 2D Ising model for several aspect ratios $\rho \leq 1$. The scaling functions for $\rho \geq 1$ can be calculated using Eq. (52).

we can derive the identities

$$\frac{P_{1/2}^+(x_\perp, \rho)}{P_{1/2}^+(x_\perp/\rho, 1/\rho)} = \frac{e^{\rho I_+(x_\perp/\rho)}}{e^{I_+(x_\perp)/\rho}}, \quad (53a)$$

$$\frac{P_{1/2}^-(x_\perp, \rho)}{P_0^+(x_\perp/\rho, 1/\rho)} = \frac{e^{\rho I_-(x_\perp/\rho)}}{e^{I_+(x_\perp)/\rho}}, \quad (53b)$$

$$\frac{P_0^-(x_\perp, \rho)}{P_0^-(x_\perp/\rho, 1/\rho)} = \frac{e^{\rho I_-(x_\perp/\rho)}}{e^{I_-(x_\perp)/\rho}}, \quad (53c)$$

which are a generalization of Jacobi's imaginary transformations for elliptic ϑ functions [62].

The resulting excess free-energy scaling function $\Theta_\perp(x_\perp, \rho)$ is depicted in Fig. 8, showing a similar behavior as in the 3D case. For $x_\perp \rightarrow -\infty$ Eq. (49) simplifies to

$$\Theta_\perp(-\infty, \rho) = -\rho \ln 2, \quad (54)$$

as explained in Sec. II C.

From Eq. (49) we directly obtain values of the scaling function at the critical point $x_\perp = 0$, as

$$I_+(0) = \frac{\pi}{12}, \quad I_-(0) = -\frac{\pi}{6}, \quad (55a)$$

and

$$P_{1/2}^\pm(0, \rho) = (\mp q; q^2)_\infty^2, \quad P_0^\pm(0, \rho) = \frac{1}{2}(\mp 1; q^2)_\infty^2, \quad (55b)$$

with $q = e^{-\pi/\rho}$ and the q -Pochhammer symbol [61] $(a; q)_\infty$, leading to

$$\begin{aligned} \Theta_\perp(0, \rho) &= -\rho \ln \left(\frac{(-q; q^2)_\infty^2 + (q; q^2)_\infty^2}{2q^{1/12}} + \frac{(-1; q^2)_\infty^2}{4q^{-1/6}} \right) \\ &= -\rho \ln \frac{\vartheta_2(0, q) + \vartheta_3(0, q) + \vartheta_4(0, q)}{(4\vartheta_2(0, q)\vartheta_3(0, q)\vartheta_4(0, q))^{1/3}}, \end{aligned} \quad (56)$$

after expressing the q -Pochhammer symbols in terms of elliptic ϑ functions. This result was already given by Ferdinand and Fisher [59] [Eq. (3.37)]. The resulting Casimir amplitude $\Delta(\rho)$ is shown as a blue solid line in Fig. 7.

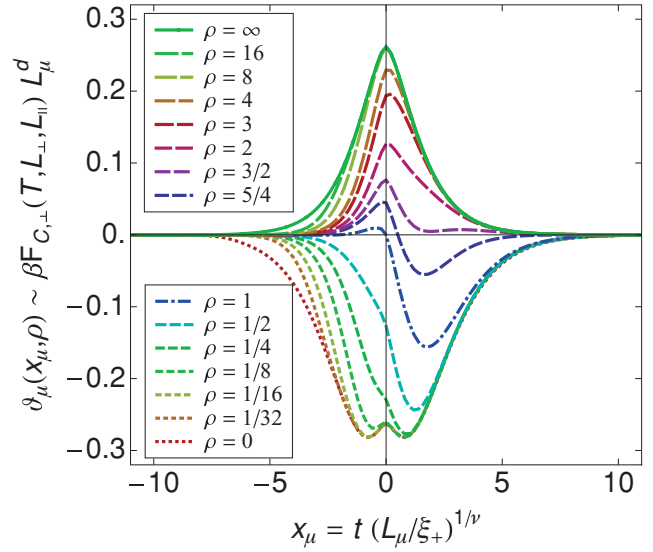


FIG. 9. (Color online) Casimir force scaling function $\vartheta_\mu(x_\mu, \rho)$ of the 2D Ising model for several aspect ratios ρ . Shown is $\vartheta_\perp(x_\perp, \rho)$ for $\rho \leq 1$ and $\vartheta_\parallel(x_\parallel, \rho)$ for $\rho \geq 1$. Note that $\vartheta_\perp(x_\perp, \rho) = \rho^2 \vartheta_\parallel(x_\parallel, \rho)$.

From the exact solution Eq. (49) we calculated the Casimir force scaling function by numerical differentiation using the scaling relation Eq. (7), as an analytic derivation would be too lengthy for arbitrary ρ . The results are shown in Fig. 9, for $\rho \leq 1$ we show $\vartheta_\perp(x_\perp, \rho)$, while for $\rho \geq 1$ we show $\vartheta_\parallel(x_\parallel, \rho)$. Clearly the Casimir force changes sign from negative to positive values with increasing aspect ratio ρ , as in the three-dimensional case.

Finally we give expressions for the limits $\rho \rightarrow 0$ and $\rho \rightarrow \infty$. In film geometry, $\rho \rightarrow 0$, Eq. (49) reduces to the simple result

$$\begin{aligned} \Theta_\perp(x_\perp, 0) &= -I_+(x_\perp) \\ &= -\frac{1}{\pi} \int_0^\infty d\omega \ln(1 + e^{-\sqrt{x_\perp^2 + \omega^2}}), \end{aligned} \quad (57)$$

yielding the already exactly known Casimir force scaling function [63]

$$\vartheta_\perp(x_\perp, 0) = -\frac{1}{\pi} \int_0^\infty d\omega \frac{\sqrt{x_\perp^2 + \omega^2}}{1 + e^{\sqrt{x_\perp^2 + \omega^2}}}. \quad (58)$$

In the opposite limit $\rho \rightarrow \infty$ we have

$$\Theta_\parallel(x_\parallel, \infty) = -\vartheta_\parallel(x_\parallel, \infty) = -I_+(x_\parallel) \quad (59)$$

using Eq. (26). For both $\rho \rightarrow 0$ and $\rho \rightarrow \infty$ we have the symmetries $\Theta_\perp(x_\perp, \rho) = \Theta_\perp(-x_\perp, \rho)$ and $\vartheta_\perp(x_\perp, \rho) = \vartheta_\perp(-x_\perp, \rho)$. Note that all scaling predictions from the previous sections have been verified in the 2D Ising case. Finally, we remark that these calculations can be easily extended to mixed periodic-antiperiodic boundary conditions by modifying the prefactors of the four terms $P_\delta^\pm(x_\perp, \rho)$ in Eq. (49a) according to Table II.

TABLE II. Signs of the terms $P_\delta^\pm(x_\perp, \rho)$ in Eq. (49a) for different boundary conditions.

BC $_\perp$	BC $_\parallel$	$P_{1/2}^+$	$P_{1/2}^-$	P_0^+	P_0^-
Periodic	Periodic	+	+	+	-
Periodic	Antiperiodic	+	+	-	+
Antiperiodic	Periodic	+	-	+	+
Antiperiodic	Antiperiodic	-	+	+	+

IV. SUMMARY

In this work we calculated the universal excess free energy and Casimir force scaling functions, $\Theta(x, \rho)$ and $\vartheta(x, \rho)$, of the three- and two-dimensional Ising model with arbitrary aspect ratio ρ and periodic boundary conditions in all directions. In $d = 3$ we used Monte Carlo simulations based on the method by Hucht [22], while in $d = 2$ we derived an analytic expression, Eq. (49), for the excess free-energy scaling function $\Theta(x, \rho)$. Furthermore, we derived several scaling identities for the scaling functions: We showed that the Casimir force scaling function $\vartheta_\perp(x_\perp, 0)$ in the film limit has a singularity of order $(x_\perp - x_\perp^*)^{1-\alpha^*}$ at the point $x_\perp^* < 0$, where the $(d-1)$ -dimensional system has a phase transition [Eq. (44)], where α^* denotes the specific-heat exponent of the $(d-1)$ -dimensional system. In our case $\alpha^* = 0$ and the singularity is logarithmic as shown in Figs. 2 and 3. At finite values of $\rho \gtrsim 1/4$ our results are compared to field-theoretical results of Dohm, and we find good agreement in the regime $x \gtrsim -2$ where his theory is expected to be valid [31]. For the cube with $\rho = 1$ we observed another interesting result: Here the Casimir force vanishes exactly at the critical point, $\vartheta(0, 1) = 0$. In Appendix A this property is shown to hold for all systems that are invariant under permutation of the directions, and is not restricted to periodic systems. The vanishing Casimir force could serve as a stability and/or instability criterion with respect to ρ : If we assume that the system can change the lengths L_μ at constant volume, we see that the cube with $\rho = 1$ and periodic boundary conditions is unstable under variation of ρ at $x = 0$, as $\rho < 1$ tends to $\rho \rightarrow 0$ and $\rho > 1$ tends to $\rho \rightarrow \infty$. Note that this behavior would reverse for antiperiodic boundary conditions, then the cube would be stable at $x = 0$ and the equilibrium shape would even be temperature dependent, as the zero of $\vartheta(x, \rho)$ varies with x ; see Fig. 9. For $\rho > 1$ the Casimir force is positive and converges against the negative excess free energy, $\vartheta_\parallel(x_\parallel, \infty) = -\Theta_\parallel(x_\parallel, \infty)$, Eq. (26).

The excess free energy below T_c is $f_{\text{ex}} \sim -V^{-1} \ln 2$ in periodic Ising systems [57] independent of system shape [Eq. (45)], leading to a finite ρ -dependent limit of $\Theta_\perp(-\infty, \rho)$, Eq. (46).

Finally, the universal scaling function $\Theta_\perp(x_\perp, \rho)$ is calculated exactly in $d = 2$, and the results are found to be in qualitative agreement with the results for $d = 3$. The most important difference between these two cases is the fact that the 2D system has several symmetries not present in the 3D system, i.e., $(x_\perp, \rho) \leftrightarrow (x_\parallel, 1/\rho)$, $(x, 0) \leftrightarrow (-x, 0)$, and $(x, \infty) \leftrightarrow (-x, \infty)$.

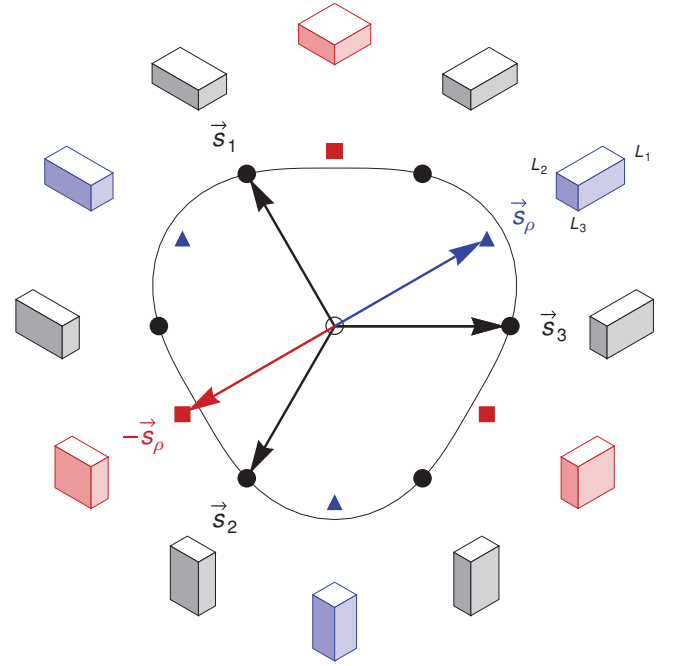


FIG. 10. (Color online) The $(d-1)$ -dimensional plane \mathcal{B} of constant volume L^d for $d = 3$, viewed from the normal direction $(1, 1, 1)$. The origin at the center (o) is the cube with $\vec{b} = \vec{0}$, while the filled symbols are deformed systems as indicated by the pictures: The black points mark the directions $\pm \vec{s}_\mu$ with constant L_μ symmetric under permutation \mathcal{P} , Eq. (A3). The blue arrow \vec{s}_ρ ($\rho > 1$) and the red arrow $-\vec{s}_\rho$ ($\rho < 1$) mark the direction of the shape variation in terms of ρ used in this work. The black curve sketches a line of constant $\Theta(x, \vec{b})$. Note that $\Theta(x, \vec{s}_\rho) \neq \Theta(x, -\vec{s}_\rho)$, as the shape and thus Θ is not symmetric under the transformation $\rho \rightarrow 1/\rho$; see also Fig. 7.

ACKNOWLEDGMENT

One of the authors (A.H.) would like to thank Martin Hasenbusch for very useful discussions.

APPENDIX A: STATIONARITY OF $\Theta(x, \rho)$ AT $\rho = 1$

The stationarity of the excess free-energy scaling function $\Theta(x, \rho)$ at $\rho = 1$ can be derived for isotropic systems with arbitrary symmetric boundary conditions and in arbitrary dimensions d : We allow arbitrary shape changes of $f_{\text{ex}}(T, L_1, \dots, L_d)$ and write $L_\mu = e^{b_\mu} L$, so that Eq. (10) now reads

$$f_{\text{ex}}(T, e^{b_1} L, \dots, e^{b_d} L) \sim L^{-d} \Theta(x, \vec{b}), \quad (\text{A1})$$

under the condition

$$\sum_{\mu=1}^d b_\mu = 0 \quad (\text{A2})$$

defining the plane \mathcal{B} with constant volume L^d . The symmetry under permutation of the d lattice axes implies

$$\Theta(x, \vec{b}) = \Theta(x, \mathcal{P}(\vec{b})) \quad (\text{A3})$$

with permutation operator \mathcal{P} . This symmetry holds if the boundary conditions in all directions are equal. Without loss of generality we now assume $d = 3$, $b_1 = 0$ and vary the shape of the system along directions 2 and 3, i.e., $b_2 = -b_3$, so that $\Theta(x, \epsilon \vec{s}_1) = \Theta(x, -\epsilon \vec{s}_1)$ with $\vec{s}_1 = (0, 1, -1)$ and real ϵ . Hence $\Theta(x, \epsilon \vec{s}_1)$ is an even function of ϵ and thus the directional derivative along \vec{s}_1 at the origin vanishes,

$$\left. \frac{\partial}{\partial \epsilon} \Theta(x, \epsilon \vec{s}_1) \right|_{\epsilon=0} = 0. \quad (\text{A4})$$

The same argument holds for the symmetric directions $\vec{s}_2 = (-1, 0, 1)$ and $\vec{s}_3 = (1, -1, 0)$ (see Fig. 10). As the $d(d-1)/2$ vectors \vec{s}_μ form an (over)complete base in the $(d-1)$ -dimensional plane \mathcal{B} , and all directional derivatives vanish at the origin $\vec{b} = \vec{0}$, we conclude that Eq. (A4) holds for all directions $\vec{s} \in \mathcal{B}$. Hence Eq. (A4) also holds for the special case $\vec{s}_\rho = (2/3, -1/3, -1/3)$, which is the direction of the shape variation used in this work (with $\rho = e^\epsilon$), if we set $L_1 = L_\perp$ and $L_2 = L_3 = L_\parallel$. From this we conclude that Eq. (10) satisfies

$$\left. \frac{\partial}{\partial \rho} \Theta(x, \rho) \right|_{\rho=1} = 0. \quad (\text{A5})$$

Note that these arguments can be extended to weakly anisotropic systems, while less is known in the strongly anisotropic case [46,64].

APPENDIX B: PROOF OF $\vartheta(\mathbf{0}, \mathbf{1}) = \mathbf{0}$ IN THE LARGE- n LIMIT

In this Appendix we show for the large- n limit [31] that the finite-size scaling function of the thermodynamic Casimir

force vanishes at bulk criticality in the case of a cubic system geometry $\rho = 1$. To this end we start from the scaling function of the singular free energy per volume given by Dohm [Eq. (3) in Ref. [31]], together with the self-consistency equation for the parameter $P(x_\perp, \rho)$ at $x_\perp = 0$,

$$P(0, \rho) = -4\pi \mathcal{G}_1(P(0, \rho)^2, \rho), \quad (\text{B1})$$

and the functions $\mathcal{G}_j(P^2, \rho)$ [Eq. (4) in Ref. [31]]. Introducing the parameter $\hat{P}(\rho) \equiv \rho^\mu P(0, \rho)$ and furthermore the integration variable $\hat{z} = \rho^\delta z$ in the integral $\mathcal{G}_0(P^2, \rho)$, the value of the excess free-energy scaling function Θ_\perp [see Eq. (6)] at bulk criticality can be cast in the form

$$\Theta_\perp(0, \rho) = \Delta_\perp(\rho) = \rho^2 \Delta(\rho) \quad (\text{B2})$$

upon setting $\mu = -2/3$ and $\delta = 4/3$, where $\Delta(\rho)$ is given by

$$\begin{aligned} \Delta(\rho) = & -\frac{\hat{P}(\rho)^3}{12\pi} + \frac{1}{2} \int_0^\infty \frac{d\hat{z}}{\hat{z}} \exp\left(-\frac{\hat{z} \hat{P}(\rho)^2}{4\pi^2}\right) \\ & \times \left[\left(\frac{\pi}{\hat{z}}\right)^{3/2} - K(\rho^{-4/3} \hat{z}) K(\rho^{2/3} \hat{z})^2 \right]. \end{aligned} \quad (\text{B3})$$

According to Eq. (18) one has

$$\vartheta_\perp(x_\perp = 0, \rho = 1) = -\Delta'(1), \quad (\text{B4})$$

where the derivative of $\Delta(\rho)$ with respect to ρ at $\rho = 1$ becomes

$$\Delta'(1) = -\frac{\hat{P}(1) \hat{P}'(1)}{4\pi} [\hat{P}(1) + 4\pi \mathcal{G}_1(\hat{P}(1)^2, 1)]. \quad (\text{B5})$$

Since $\hat{P}(1) = P(0, 1)$ is the solution to Eq. (B1) at $\rho = 1$, the expression in square brackets vanishes and thus $\Delta'(1) = 0$.

-
- [1] H. B. G. Casimir, Proc. K. Ned. Akad. Wet. **51**, 793 (1948).
 - [2] S. K. Lamoreaux, Phys. Rev. Lett. **78**, 5 (1997); **81**, 5475 (1998).
 - [3] U. Mohideen and A. Roy, Phys. Rev. Lett. **81**, 4549 (1998).
 - [4] M. E. Fisher and P.-G. de Gennes, C. R. Acad. Sci. Paris, Ser. B, **287**, 207 (1978).
 - [5] A. Gambassi, J. Phys. Conf. Ser. **161**, 012037 (2009).
 - [6] R. Garcia and M. H. W. Chan, Phys. Rev. Lett. **83**, 1187 (1999).
 - [7] A. Ganshin, S. Scheidemantel, R. Garcia, and M. H. W. Chan, Phys. Rev. Lett. **97**, 075301 (2006).
 - [8] M. Fukuto, Y. F. Yano, and P. S. Pershan, Phys. Rev. Lett. **94**, 135702 (2005).
 - [9] C. Hertlein, L. Helden, A. Gambassi, S. Dietrich, and C. Bechinger, Nature (London) **451**, 172 (2008).
 - [10] A. Gambassi, A. Maciołek, C. Hertlein, U. Nellen, L. Helden, C. Bechinger, and S. Dietrich, Phys. Rev. E **80**, 061143 (2009).
 - [11] R. Garcia and M. H. W. Chan, Phys. Rev. Lett. **88**, 086101 (2002).
 - [12] M. Krech and S. Dietrich, Phys. Rev. A **46**, 1886 (1992).
 - [13] M. Krech, Casimir Effect in Critical Systems (World Scientific, Singapore, 1994).
 - [14] H. W. Diehl, D. Grüneberg, and M. A. Shpot, Europhys. Lett. **75**, 241 (2006).
 - [15] D. Grüneberg and H. W. Diehl, Phys. Rev. B **77**, 115409 (2008).
 - [16] A. Maciołek, A. Gambassi, and S. Dietrich, Phys. Rev. E **76**, 031124 (2007).
 - [17] R. Zandi, A. Shackell, J. Rudnick, M. Kardar, and L. P. Chayes, Phys. Rev. E **76**, 030601 (2007).
 - [18] H. Li and M. Kardar, Phys. Rev. Lett. **67**, 3275 (1991).
 - [19] H. Li and M. Kardar, Phys. Rev. A **46**, 6490 (1992).
 - [20] M. Kardar and R. Golestanian, Rev. Mod. Phys. **71**, 1233 (1999).
 - [21] R. Zandi, J. Rudnick, and M. Kardar, Phys. Rev. Lett. **93**, 155302 (2004).
 - [22] A. Hucht, Phys. Rev. Lett. **99**, 185301 (2007).
 - [23] D. Dantchev and M. Krech, Phys. Rev. E **69**, 046119 (2004).
 - [24] M. Hasenbusch, Phys. Rev. B **81**, 165412 (2010).
 - [25] M. Hasenbusch, Phys. Rev. B **82**, 104425 (2010).
 - [26] O. Vasilyev, A. Gambassi, A. Maciołek, and S. Dietrich, Europhys. Lett. **80**, 60009 (2007).
 - [27] M. Hasenbusch, J. Stat. Mech.: Theory Exp. (2009) P07031.
 - [28] M. Hasenbusch, Phys. Rev. E **80**, 061120 (2009).
 - [29] O. Vasilyev, A. Gambassi, A. Maciołek, and S. Dietrich, Phys. Rev. E **79**, 041142 (2009).
 - [30] F. P. Toldin and S. Dietrich, J. Stat. Mech. (2010) P11003.
 - [31] V. Dohm, Europhys. Lett. **86**, 20001 (2009).

- [32] V. Privman, in *Finite Size Scaling and Numerical Simulation of Statistical Systems*, edited by V. Privman (World Scientific, Singapore, 1990), Chap. 1.
- [33] Throughout this work, the symbol \sim means “asymptotically equal” in the respective limit, $L_{\parallel}, L_{\perp} \rightarrow \infty$, $T \rightarrow T_c$, keeping the scaling variables x and ρ fixed, i.e., $f(L) \sim g(L) \Leftrightarrow \lim_{L \rightarrow \infty} f(L)/g(L) = 1$.
- [34] M. Campostrini, A. Pelissetto, P. Rossi, and E. Vicari, *Phys. Rev. E* **60**, 3526 (1999).
- [35] P. Butera and M. Comi, *Phys. Rev. B* **65**, 144431 (2002).
- [36] M. E. Fisher, in *Critical Phenomena, Proceedings of the 51st Enrico Fermi Summer School, Varenna, Italy*, edited by M. S. Green (Academic, New York, 1971), pp. 73–98.
- [37] D. Dantchev, H. W. Diehl, and D. Grüneberg, *Phys. Rev. E* **73**, 016131 (2006).
- [38] D. Grüneberg and A. Hucht, *Phys. Rev. E* **69**, 036104 (2004).
- [39] D. M. Danchev, *Phys. Rev. E* **58**, 1455 (1998).
- [40] J. G. Brankov, D. M. Dantchev, and N. S. Tonchev, *Theory of Critical Phenomena in Finite-Size Systems—Scaling and Quantum Effects* (World Scientific, Singapore, 2000).
- [41] D. Dantchev, M. Krech, and S. Dietrich, *Phys. Rev. E* **67**, 066120 (2003).
- [42] D. Dantchev and D. Grüneberg, *Phys. Rev. E* **79**, 041103 (2009).
- [43] M. Krech and D. P. Landau, *Phys. Rev. E* **53**, 4414 (1996).
- [44] F. M. Schmidt and H. W. Diehl, *Phys. Rev. Lett.* **101**, 100601 (2008).
- [45] H. W. Diehl and D. Grüneberg, *Nucl. Phys. B* **822**, 517 (2009).
- [46] M. Burgsmüller, H. W. Diehl, and M. A. Shtot, *J. Stat. Mech.: Theory Exp.* (2010) P11020.
- [47] G. Bhanot, M. Creutz, I. Horvath, J. Lacki, and J. Weckel, *Phys. Rev. E* **49**, 2445 (1994).
- [48] X. Feng and H. W. J. Blöte, *Phys. Rev. E* **81**, 031103 (2010).
- [49] H. Arisue and T. Fujiwara, *Phys. Rev. E* **67**, 066109 (2003). There is a typo in the 42th-order term. The correct value appears in arXiv:hep-lat/0209002.
- [50] U. Wolff, *Phys. Rev. Lett.* **62**, 361 (1989).
- [51] Y. Deng and H. W. J. Blöte, *Phys. Rev. E* **68**, 036125 (2003).
- [52] H. Kitatani, M. Ohta, and N. Ito, *J. Phys. Soc. Jpn.* **65**, 4050 (1996).
- [53] M. Caselle and M. Hasenbusch, *Nucl. Phys. B* **470**, 435 (1996).
- [54] M. Krech, *Phys. Rev. E* **56**, 1642 (1997).
- [55] At $\rho = 1$ all quantities q obey $q = q_{\perp} = q_{\parallel}$.
- [56] C. P. Bachas, *J. Phys. A* **40**, 9089 (2007).
- [57] V. Privman and M. E. Fisher, *J. Stat. Phys.* **33**, 385 (1983).
- [58] K. K. Mon, *Phys. Rev. Lett.* **54**, 2671 (1985).
- [59] A. E. Ferdinand and M. E. Fisher, *Phys. Rev.* **185**, 832 (1969). There is a typo in Eq. (3.36). The term $\xi S_1(n)\tau^2/2$ is missing.
- [60] B. Kaufman, *Phys. Rev.* **76**, 1232 (1949).
- [61] Wolfram Research, Inc., *Mathematica V7.0*, Champaign, Illinois (2008).
- [62] E. T. Whittaker and G. N. Watson, *A Course in Modern Analysis*, 4th ed. (Cambridge University Press, Cambridge, UK, 1990).
- [63] J. Rudnick, R. Zandi, A. Shackell, and D. Abraham, *Phys. Rev. E* **82**, 041118 (2010).
- [64] A. Hucht, *J. Phys. A* **35**, L481 (2002).

Magnetic friction: From Stokes to Coulomb behavior

Martin P. Magiera,^{*} Sebastian Angst, Alfred Hucht, and Dietrich E. Wolf

Faculty of Physics and CeNIDE, University of Duisburg-Essen, D-47048 Duisburg, Germany

(Received 22 October 2011; published 19 December 2011)

We demonstrate that in a ferromagnetic substrate which is continuously driven out of equilibrium by a field moving with constant velocity v , at least two types of friction may occur when v goes to zero. The substrate may feel a friction force proportional to v (Stokes friction) if the field changes on a time scale which is larger than the intrinsic relaxation time. On the other hand, the friction force may become independent of v in the opposite case (Coulomb friction). These observations are analogous to, e.g., solid friction. The effect is demonstrated in both the Ising (one spin dimension) and the Heisenberg (three spin dimensions) models, irrespective of which kind of dynamics (Metropolis spin-flip dynamics or Landau-Lifshitz-Gilbert precessional dynamics) is used. For both models the limiting case of Coulomb friction can be treated analytically. Furthermore we present an empiric expression reflecting the correct Stokes behavior and therefore yielding the correct crossover velocity and dissipation.

DOI: [10.1103/PhysRevB.84.212301](https://doi.org/10.1103/PhysRevB.84.212301)

PACS number(s): 75.10.Pq, 68.35.Af, 75.10.Hk, 75.70.-i

Friction phenomena, despite their huge importance in everyday life, are still not fully understood. Different friction mechanisms are possible, leading to different dependencies of the friction forces on the driving velocity. Microscopically, one often assumes Stokes-like friction, i.e., a linear velocity dependence. However, this atomistic view is in conflict with Coulomb friction at the interface between solids, because it approaches a nonzero absolute value in the limit of small velocities, independent of the materials and their surface conditions.¹⁻⁶ A possible solution was offered by the simple model developed by Prandtl and Tomlinson, in which a stick-slip instability was responsible for Coulomb friction.^{7,8} They suggested a surface atom to be coupled by a spring of stiffness k to a slider which moves with constant velocity v . The atom interacts with the surface via a periodic potential and experiences a viscous friction force proportional to its velocity \dot{x} . If k is sufficiently small with respect to the potential height, the atom first gets stuck in the potential minima and slips when the tension gets large enough. The slip motion \dot{x} does not depend on the slider's velocity v , and one observes Coulomb friction. However, when k is large with respect to the potential height, the atom moves with the slider's velocity and the friction force is Stokesian. The crossover from one regime to the other has been studied recently.⁹

What remains a puzzle, however, is that Coulomb friction is a far more general phenomenon than one might expect from the Prandtl-Tomlinson model, which is formulated in terms of elastic forces in a periodic potential. For example, Stokes as well as Coulomb behavior has also been observed for magnetic friction, where elastic forces are absent. Being guided by a detailed investigation of the crossover between both types of magnetic friction, a unifying principle can be formulated that applies to the magnetic as well as to the elastic case.

So far, magnetic friction has been studied in two different types of models. Ising models with single-spin-flip dynamics, where two half spaces move with respect to each other, yield Coulomb friction.¹⁰⁻¹² Analogous results have been obtained in the Potts model.¹³ On the other hand, a magnetic dipole scanning a Heisenberg surface showed Stokesian friction¹⁴⁻¹⁷ (always provided the velocity is not too large).

Recently a work has been published in which a point-like magnetic perturbation moves through an Ising model.^{18,19} The authors claim to have observed Stokes friction, which is in conflict with our results for similar models.^{10,11} Here we present an explanation of this discrepancy and clarify under what conditions either Stokes or Coulomb friction occurs.

The systems studied in Refs. 10–13 have in common that the motion occurs in a discretized way: The system is at rest for a certain number a/v of Monte Carlo sweeps (MCS), after which one half space is moved by one lattice constant a . Accordingly we have a periodic excitation and relaxation procedure, where excitation is fast (happens in between two subsequent spin-flip attempts), whereas relaxation extends over a/v MCS. By contrast, in Refs. 14–17 excitation is slow, because due to the dipole-dipole interaction, a substrate spin feels the approaching tip a long time in advance.

Now we present a simple one-dimensional model that interpolates between both cases. We consider a position-dependent field $h_z(r')$, which is moved continuously with constant velocity v . r is given in units of a , and $v = \dot{r}$. Then the discrete motion can be modeled as a step function, as shown in Fig. 1 as solid line. For a certain time $1/v$, exactly one spin is exposed to the field with constant amplitude until the field reaches the next spin. Additionally the amplitude of the dipole field used in Refs. 14–17 is plotted. From Ref. 15 we know that for this case the adjustment of the spins with respect to the moved field happens in an adiabatic way, or in other words, the time scale of relaxation is below that of the excitation. To generalize these setups, we consider a field with steepness $\delta r \ll 1$,

$$h_z(r') = \frac{h}{(e^{-\frac{r'}{\delta r}} + 1)(e^{-\frac{1-r'}{\delta r}} + 1)}, \quad (1)$$

which may be tuned from the step-like field [$\delta r = 0$, now called limiting case (i)] to a slowly varying field [$\delta r \approx 0.1$, case (ii)]. By shifting this field according to $r' = r - vt$,²⁰ we can directly influence the time scale at which the excitation at a fixed position r occurs, $\tau_{\text{switch}} \propto \delta r/v$.

We first consider a chain of classical, normalized Heisenberg spins ($|\mathbf{S}_r| = 1$) of length L with lattice spacing a ,

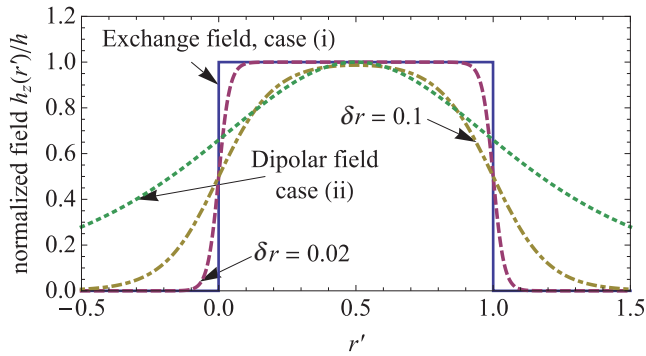


FIG. 1. (Color online) The dynamics in the different studies can be mapped on a time-dependent field with amplitude $h_z(r')$ (here normalized by its maximal value h) interacting with the spins positioned at integer sites. The discrete motion in the Ising and Potts model then corresponds to a step function, which may be treated as a fixed spin interacting via exchange with one partner on the chain. The amplitude of a dipole field is sketched for comparison. The field used in this work may be tuned by adjusting the parameter δr from one limiting case to the other.

which interact with the field defined above. The corresponding time-dependent Hamiltonian is

$$\mathcal{H}(t) = - \sum_{r=1}^L J \mathbf{S}_r \cdot \mathbf{S}_{r+1} + d_x S_{r,x}^2 + h_z(r - vt) S_{r,z}, \quad (2)$$

with the exchange constant J . To get a well-defined ground state, we use an easy axis anisotropy ($d_x > 0$) and antiperiodic boundary conditions $\mathbf{S}_{r+L} = -\mathbf{S}_r$. The spins perform Landau-Lifshitz-Gilbert dynamics,^{21,22}

$$\frac{\mu_s(1 + \alpha^2)}{\gamma} \frac{\partial \mathbf{S}_r}{\partial t} = \mathbf{S}_r \times \frac{\partial \mathcal{H}}{\partial \mathbf{S}_r} + \alpha \mathbf{S}_r \times \left(\mathbf{S}_r \times \frac{\partial \mathcal{H}}{\partial \mathbf{S}_r} \right), \quad (3)$$

consisting of a precessional motion with a frequency proportional to γ/μ_s , and a damping with the damping constant α . For simplicity, we neglect temperature here, and the dynamic parameters yield a spin relaxation time τ_{rel} . The friction force F can be either calculated from the dissipated power P_{diss} or the pumping power P_{pump} , which are equal in the stationary state due to energy conservation and therefore we subsequently use $F = \langle P \rangle / v$ after time averaging. The two cases can be described by

$$P(v) \propto v^\phi, \quad (4)$$

with the dissipation exponent $\phi = 1$ ($\phi = 2$) for the Coulomb (Stokes) case. P can be extracted from the energy terms by

$$P(t) = \frac{\partial \mathcal{H}}{\partial t} = \sum_{r=1}^L \frac{\partial h_z(r - vt)}{\partial t} S_{r,z}, \quad (5)$$

which represents the power pumped into the system by the motion. In our simulations [see Fig. 3(a)], we found $\phi = 2$ for large τ_{switch} , which corresponds to the results in Refs. 14–17. For sufficiently small τ_{switch} we get $\phi = 1$, which was known from simulations in the Ising model and was now reproduced in the Heisenberg model.

In the following we calculate the velocity v_x at which a crossover from one regime to the other occurs. For case (i)

only two spins contribute to the sum in Eq. (5) at the discrete times $vt \in \mathbb{Z}$ (at all other times and positions the field remains constant), and we can calculate the averaged pumping power by discretizing $\partial_t h_z$,

$$P_C = -h v (\langle S_{1',z} \rangle - \langle S_{0',z} \rangle). \quad (6)$$

For the time τ_{ca} , corresponding to the time at which the amplitude of the field stays nearly constant, no pumping or excitation occurs. We consider $\tau_{\text{ca}} > \tau_{\text{rel}}$, i.e., the system always relaxes to equilibrium after a pumping event. Since the equilibrium configuration does not depend on the dynamics, Eq. (6) tells us that here $\phi = 1$. The equilibrium configuration for our choice of boundary conditions is a domain wall (DW) state, where the out-of-axis component is determined by the field and thus points in the z direction. As the field interacts mainly with only one spin, the shape of the DW is not influenced by h and we may use the continuum limit profile ($a \rightarrow 0$),²³

$$\mathbf{m}^H(r') = (\tanh(r'/\ell), 0, \text{sech}(r'/\ell)), \quad (7)$$

with the DW width $\ell = \sqrt{J/(2d_x)}$, which can be calculated from minimizing the free energy.²⁴ By inserting $\langle \mathbf{S}_0 \rangle = \mathbf{m}^H(0)$ and $\langle \mathbf{S}_1 \rangle = \mathbf{m}^H(1)$ into Eq. (6) we now can calculate the power which is pumped into the system during each switching event. This quantity can be visualized in a potential plot. We again assume that h does not influence the shape of the DW but rather its center r_{dw} . Because in limiting case (ii) the system is always near equilibrium and in limiting case (i) it always reaches the ground state before being excited out of equilibrium, this assumption is justified and we can describe the whole configuration with r_{dw} . We look at one cycle at which the field's peak moves from 0 to 1, corresponding to the times $-1/2 \leq vt \leq 1/2$. For given t we can calculate the system's total energy as a function of r_{dw} (see the potential lines in Fig. 2). If the system evolved quasistatically, it would always be in the current potential minimum. In this picture P_C/v corresponds to the energy difference between the energy at $r_{\text{dw}} = 0$, $vt = -1/2$ (the equilibrium state) and $vt = 1/2$ (the state which is present when the peak of the field has moved to the next spin while the DW is still at the same site). Results from simulations (plotted as squares in Fig. 2) confirm this: At $vt = 0$ the system is excited to the upper state in a short time, and relaxes to the new ground state by adjusting r_{dw} slowly afterward, until it reaches the new ground-state configuration with $r_{\text{dw}} = 1$. Simulations of the second limiting case (circles in Fig. 2) confirm that the system is always near equilibrium, thus the DW slightly lags behind the ground state.

From our simulations, we found the pumping power

$$P_S^H = \frac{d_x \mu_s}{J \gamma \delta r} \alpha v^2. \quad (8)$$

The factor $d_x v / (\delta r J)$ originates in the synchronization with the field, which changes at the time scale τ_{switch} . The factor $\alpha v \mu_s / \gamma$ emerges from spin dynamics, yielding a retardation of the DW as derived in Ref. 15. Setting

$$P_C^H(v) \stackrel{!}{=} P_S^H(v) := P_{\times}^H(v_{\times}^H) \quad (9)$$

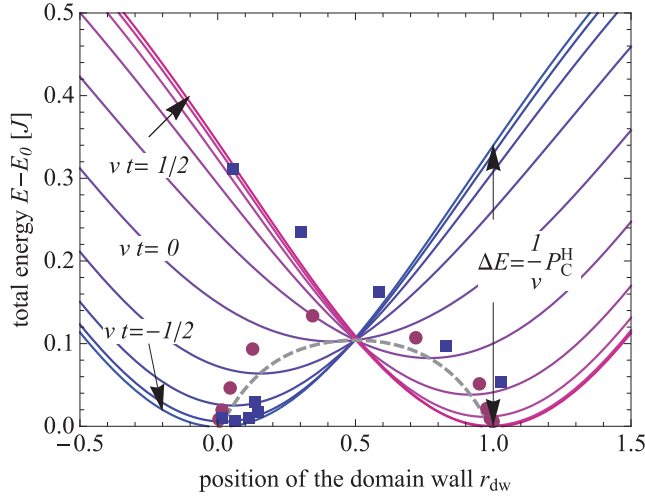


FIG. 2. (Color online) The system can be parametrized by the center of the DW r_{dw} , thus for different times the total energy of the system can be calculated. This is done for field parameter $\delta r = 0.1$ for 10 equidistant times (blue to purple curves). If the system evolved quasistatically, it would follow the configuration of minimal energy, marked by the curve. Simulation results show both cases, the points indicate energy vs r_{dw} for 10 time steps: (i) ■ The energy P_C^H/v is periodically pumped into the system, which relaxes independent from τ_{switch} afterward. As the switching occurs at $vt = 0$, we first see the relaxation from the preceding excitation in the left minimum, and at $vt = 1/2$ the relaxation in the right minimum is not finished. (ii) ● The system follows with a lag, but stays near equilibrium, slightly above the minimal energy configuration.

yields the crossover velocity²⁵

$$v_{\times}^H = \frac{h\delta r}{\alpha d_x} \frac{\gamma J}{\mu_s} [1 - \text{sech}(1/\ell)], \quad (10)$$

where the system performs a crossover from the Stokes-friction state to the Coulomb-friction state. In Fig. 3(c) these crossover quantities have been calculated and the simulation results have been rescaled appropriately. The simulation data fit excellently over several magnitudes with the derived crossover quantities; the remaining deviations are discussed below. We performed also simulations of the isotropic Ising model with the same field and periodic boundary conditions ($S_{r+N} = S_r$). The Ising spins undergo spin-flip dynamics with Metropolis probability.²⁶ Randomly chosen spins are flipped with the probability $p_f = \min[1, \exp(-\beta \Delta E)]$, where β is the inverse temperature and ΔE the energy difference between the flipped and the not flipped state.

For (i) we again find a behavior $\phi = 1$. We assume that for (i) the spins relax after each switching event to the ground-state profile which can be calculated via transfer matrix methods:¹¹

$$m^I(r') = \tanh(\beta h) [\tanh(\beta J)]^{|r'|}. \quad (11)$$

With $\langle S_{0,z} \rangle = m^I(0)$ and $\langle S_{1,z} \rangle = m^I(1)$ in Eq. (6), we get P_C^I . $\phi = 2$ is observed for (ii), and we fitted

$$P_S^I \propto v^2/\delta r. \quad (12)$$

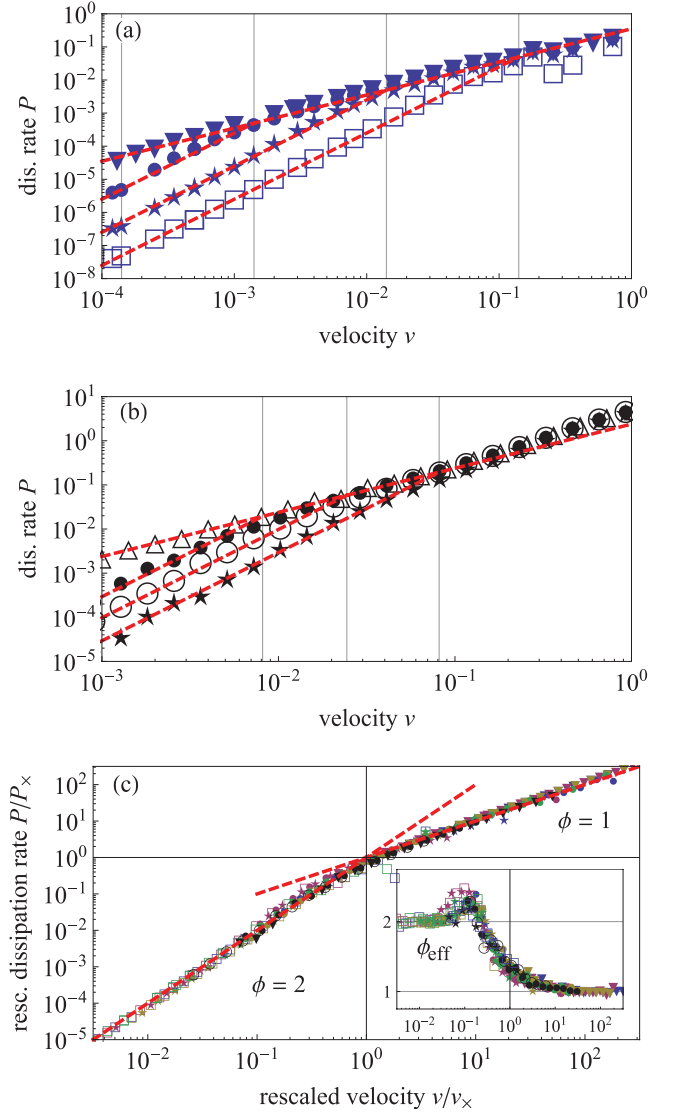


FIG. 3. (Color online) Dissipated power vs velocity (in natural units) for the (a) Heisenberg ($d_x = 0.5J, \alpha = 0.5, h = J$, blue or gray) and the (b) Ising ($\beta = 1/J, h = 10J$, black) models. The simulated δr are $\delta r = \infty$ (Δ), 10^{-4} (\blacktriangledown), 10^{-3} (\bullet), 3×10^{-3} (\circ), 10^{-2} (\star), and 10^{-1} (\square). The grid lines mark the corresponding v_{\times} , the dashed lines display the calculated $P_C(v)$ from Eq. (6) and fitted $P_S(v)$. For (c) we calculated explicitly the crossover quantities P_{\times} and v_{\times} for both models from Eqs. (9) and (10), and plot the data again rescaled. Additionally we varied $\alpha = 0.3$ (purple), $h = 2J$ (green), and $d_x = 0.25J$ (yellow) for the same δr set. In the inset we plot an effective exponent $\phi_{\text{eff}} = \partial \log P / \partial \log v$, and get a universal crossover from 2 to 1.

We calculated again the crossover velocity v_{\times}^I , which is additionally plotted in Fig. 3(b), and rescaled all data points for the crossover plot, Fig. 3(c).

Comparing Figs. 3(a) and 3(b), we come to the main result of our investigation, namely, the coincidence concerning the crossover between both models, despite the substantial remaining differences such as the dynamics of the models. The present deviations from the crossover curve are discussed below. The slight increase of P , observed in the regime $v > 0.1$

for all δr in the Ising model, is due to the fact that the system has not enough time to relax back to equilibrium before the next shift takes place and $m^1(1)$ becomes significantly smaller than its equilibrium value. As the Heisenberg model contains spin wave excitations, we observed the generation of spin waves above a threshold velocity.¹⁶ In the crossover plot these spin waves cause a kink above $v/v_x = 0.1$ for $\alpha = 0.3$ (and a higher peak in the effective exponent plot). For very high velocities we observe a lowering of the power, which is due to a segregation of the peak of the field and the DW, leading to a reduced $m_z^H(0) < 1$. This state with lowered dissipation has already been observed and reported.¹⁷

In conclusion, we presented a new model which shows for the case of magnetic friction a transition from Stokes to Coulomb behavior, analogous to the Prandtl-Tomlinson model for solid friction. Whereas there the elastic stiffness of the slider is the crucial parameter, it is the switching time of the magnetic field in our case. The comparison of both models

sheds new light on the universal origin of Coulomb behavior, which is based on a separation of the relaxation time from the much larger time scale on which the system gets excited. Our findings are in accordance to field theoretical results by Demery *et al.*,^{18,19} who also found Stokes-like friction because their model does not contain discrete sites and thus $\tau_{ca} = 0$, i.e., the field is continuously driving the system. However, their simulation results are not correct, because they simulated an Ising model with a discontinuous motion of a field, which is known to show Coulomb friction. This discrepancy stems from an incorrect definition of the friction force [Eq. (50) in Ref. 19]; a correct definition has been presented in Ref. 10.

This work was supported by the German Research Foundation (DFG) via SFB 616 and the German Academic Exchange Service (DAAD) through the PROBRAL program.

*martin.magiera@uni-due.de

¹C. M. Mate, G. M. McClelland, R. Erlandsson, and S. Chiang, *Phys. Rev. Lett.* **59**, 1942 (1987).

²Y. Liu, T. Wu, and D. F. Evans, *Langmuir* **10**, 2241 (1994).

³O. Zwörner, H. Hölscher, U. Schwarz, and R. Wiesendanger, *Appl. Phys. A* **66**, S263 (1998).

⁴R. Bennowitz, T. Gyalog, M. Guggisberg, M. Bammerlin, E. Meyer, and H.-J. Güntherodt, *Phys. Rev. B* **60**, R11301 (1999).

⁵E. Gnecco, R. Bennowitz, T. Gyalog, C. Loppacher, M. Bammerlin, E. Meyer, and H.-J. Güntherodt, *Phys. Rev. Lett.* **84**, 1172 (2000).

⁶M. H. Müser, *Phys. Rev. Lett.* **89**, 224301 (2002).

⁷L. Prandtl, *Z. Angew. Math. Mech.* **8**, 85 (1928).

⁸G. A. Tomlinson, *Philos. Mag.* **7**, 905 (1929).

⁹M. H. Müser, *Phys. Rev. B* **84**, 125419 (2011).

¹⁰D. Kadau, A. Hucht, and D. E. Wolf, *Phys. Rev. Lett.* **101**, 137205 (2008).

¹¹A. Hucht, *Phys. Rev. E* **80**, 061138 (2009).

¹²H. J. Hilhorst, *J. Stat. Mech.* (2011) P04009.

¹³F. Iglói, M. Pleimling, and L. Turban, *Phys. Rev. E* **83**, 041110 (2011).

¹⁴C. Fusco, D. E. Wolf, and U. Nowak, *Phys. Rev. B* **77**, 174426 (2008).

¹⁵M. P. Magiera, L. Brendel, D. E. Wolf, and U. Nowak, *Europhys. Lett.* **87**, 26002 (2009).

¹⁶M. P. Magiera, L. Brendel, D. E. Wolf, and U. Nowak, *Europhys. Lett.* **95**, 17010 (2011).

¹⁷M. P. Magiera and D. E. Wolf, in *Proceedings of the NIC Symposium, 2010*, edited by G. Münster, D. E. Wolf, and M. Kremer (Jülich, Germany, 2010), p. 243.

¹⁸V. Démery and D. S. Dean, *Phys. Rev. Lett.* **104**, 080601 (2010).

¹⁹V. Démery and D. S. Dean, *Eur. Phys. J. E* **32**, 377 (2010).

²⁰A prime denotes a quantity in the field's frame of reference, otherwise in the laboratory frame; i.e., at l' (l) is the front (rear) inflection point of h .

²¹L. D. Landau and E. M. Lifshitz, *Phys. Z. Sowjetunion* **8**, 153 (1935).

²²T. L. Gilbert, *IEEE Trans. Magn.* **40**, 3443 (2004).

²³Quantities with the superscript H are dedicated to the Heisenberg model, those with the superscript I to the Ising model.

²⁴L. N. Bulaevskii and V. L. Ginzburg, *Sov. Phys. JETP* **18**, 530 (1964).

²⁵The unit of time is $\mu_s/(\gamma J)$. d_x and h are energies and given in units of J , thus the velocity's unit is $a\gamma J/\mu_s$.

²⁶N. Metropolis, A. W. Rosenbluth, M. N. Rosenbluth, A. H. Teller, and E. Teller, *J. Chem. Phys.* **21**, 1087 (1953).

Strongly anisotropic nonequilibrium phase transition in Ising models with friction

Sebastian Angst, Alfred Hucht, and Dietrich E. Wolf

Fakultät für Physik und CeNIDE, Universität Duisburg-Essen, D-47048 Duisburg, Germany

(Received 9 January 2012; published 16 May 2012)

The nonequilibrium phase transition in driven two-dimensional Ising models with two different geometries is investigated using Monte Carlo methods as well as analytical calculations. The models show dissipation through fluctuation induced friction near the critical point. We first consider high driving velocities and demonstrate that both systems are in the same universality class and undergo a strongly anisotropic nonequilibrium phase transition, with anisotropy exponent $\theta = 3$. Within a field theoretical ansatz the simulation results are confirmed. The crossover from Ising to mean field behavior in dependency of system size and driving velocity is analyzed using crossover scaling. It turns out that for all finite velocities the phase transition becomes strongly anisotropic in the thermodynamic limit.

DOI: [10.1103/PhysRevE.85.051120](https://doi.org/10.1103/PhysRevE.85.051120)

PACS number(s): 05.70.Ln, 68.35.Af, 05.50.+q, 05.70.Fh

I. INTRODUCTION

The interest in magnetic contributions to friction due to spin correlations has strongly increased in recent years. One interesting aspect is the energy dissipation due to the formation of spin waves in a two-dimensional Heisenberg model induced by a moving magnetic tip [1–3], which can be of Stokes or Coulomb type depending on the intrinsic relaxation time scales [4]. On the other hand, magnetic friction occurs also in bulk systems moving relative to each other. Kadau *et al.* [5] used a two-dimensional Ising model, cut into two halves parallel to one axis and moved along this cut with the velocity v , to explore surface friction. The motion drives the system out of equilibrium into a steady state, leading to a permanent energy flux from the surface to the heat bath. This model exhibits a nonequilibrium phase transition, which has been investigated in several different geometries [6] by means of analytical treatment as well as Monte Carlo (MC) simulations. The critical temperature T_c of the considered models depends on the velocity v and has been calculated exactly for various geometries in the limit $v \rightarrow \infty$. In this limit the class of models show mean-field-like critical behavior. Subsequent investigations have been done in a variety of context, in particular for driven Potts models [7] and for rotating Ising chains of finite length [8].

The nature of nonequilibrium phase transitions is still a field of large interest, and simple models helping to explore this field are seldom. A very famous example is the driven lattice gas (DLG) [9–11], exhibiting a strongly anisotropic phase transition. Despite many similarities between the driven lattice gas and the Ising model with friction, there is an important difference: The order parameter is conserved in the former, while it is nonconserved in the latter model. A further class of models characterized by nonequilibrium phase transitions are sheared systems [12–14], experimentally accessible within the framework of binary liquid mixtures.

Like the driven lattice gas, the systems investigated in the following exhibit a strongly anisotropic phase transition, which is investigated by means of Monte Carlo (MC) simulations as well as a field theoretical ansatz. In addition, the case of finite velocities v is analyzed by means of crossover scaling, where a broad range of velocities and system sizes are analyzed. We show that for all $v > 0$ the considered models end up in

the mean field class with strongly anisotropic correlations as soon as the system size exceeds a velocity-dependent crossover length $L_\times(v)$.

While a crossover behavior from Ising to mean-field class occurs in various thermodynamic systems such as ionic fluid [15,16] and spin systems with long-range interactions [17], to our knowledge such a crossover including a change from isotropic to strongly anisotropic behavior has not been investigated in detail. The paper is organized as follows: After introducing the model and geometries, we determine the anisotropy exponent for $v = \infty$ using MC simulations as well as a field theoretical model. Then we turn to finite velocities and present the crossover scaling analysis. Finally we discuss our results.

II. MODELS

The systems considered in this work are denoted 2d and 1+1d and are shown in Fig. 1 (for a classification see Ref. [6]). The 2d system is a two-dimensional two-layer Ising model with $L_\parallel \times L_\perp \times 2$ lattice sites, where the two layers are moved relative to each other along the parallel direction. Each lattice site carries one spin variable $\sigma_{i,j,k} = \pm 1$, and only nearest-neighbor interactions are taken into account. Periodic boundary conditions are applied in both planar directions (i.e., $\sigma_{i,j,k} = \sigma_{i+L_\parallel,j,k} = \sigma_{i,j+L_\perp,k}$). In order to simulate a finite velocity v using Monte Carlo simulations the upper subsystem is moved v times by one lattice constant during each random sequential Monte Carlo sweep (MCS). Since one MCS corresponds to the typical time $t_0 \approx 10^{-8}$ s a spin needs to relax into the direction of its local Weiss field, and as the lattice constant is of the order $a_0 \approx 10^{-10}$ m, the velocity v is given in natural units $a_0/t_0 \approx 1$ cm/s.

Instead of moving the two layers against each other, we reorder the couplings between the subsystems with time to simplify the implementation [6]. Introducing a time-dependent displacement

$$\Delta(t) = vt, \quad (1)$$

which is increased by one after each $2L_\parallel L_\perp/v$ random sequential spin flip attempts, the Hamiltonian can be expressed

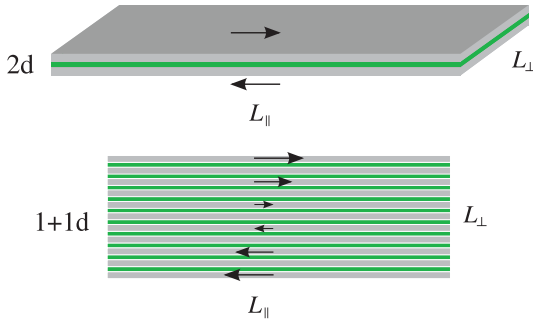


FIG. 1. (Color online) The systems considered in this work. The gray regions represent the magnetic systems, while the green (dark) regions are the moving boundaries. The arrows indicate the motion of the subsystems.

as

$$\beta\mathcal{H}(t) = -K \sum_{i=1}^{L_{\parallel}} \sum_{j=1}^{L_{\perp}} \sum_{k=0}^1 \sigma_{i,j,k} (\sigma_{i+1,j,k} + \sigma_{i,j+1,k}) - K_b \sum_{i=1}^{L_{\parallel}} \sum_{j=1}^{L_{\perp}} \sigma_{i,j,0} \sigma_{i+\Delta(t),j,1}, \quad (2)$$

with the reduced nearest neighbor coupling $K = \beta J$, the reduced boundary coupling $K_b = \beta J_b$, and $\beta = 1/k_B T$. In the following we assume $J = J_b = 1$.

The critical temperature $T_c(v)$ of the regarded systems increases with v and saturates for high velocities. In the limit $v \rightarrow \infty$ an analytical calculation of the critical temperature for the 2d geometry yield

$$T_c^{2d}(\infty) = 4.058782423 \dots \quad (3)$$

for $J = J_b = 1$ [6]. The basic idea of the analytic solution provides the approach for the implementation of infinite velocity, which works as follows: The interaction partner for a spin in the lower layer is chosen randomly from the same row in the upper layer. Thus we can use Eq. (2) with a random value $1 \leq \Delta(t) \leq L_{\parallel}$.

The 1+1d system consists of a two-dimensional Ising model, where all rows are moved relative to each other. The displacement $\Delta(t) = vt$ as well as the coupling K_{\perp} is equal for all adjacent rows, leading to the Hamiltonian

$$\beta\mathcal{H}(t) = - \sum_{i=1}^{L_{\parallel}} \sum_{j=1}^{L_{\perp}} K_{\parallel} \sigma_{i,j} \sigma_{i+1,j} + K_{\perp} \sigma_{i,j} \sigma_{i+\Delta(t),j+1}. \quad (4)$$

Again, periodic boundary conditions are applied in both directions, where discontinuities in \perp direction are avoided through the homogeneous displacement $\Delta(t)$ [6]. The analytical treatment at $v \rightarrow \infty$ gave the critical temperature

$$T_c^{1+1d}(\infty) = 1/\ln\left(\frac{1}{2}\sqrt{3+\sqrt{17}}\right) = 3.46591 \dots \quad (5)$$

for $J_{\parallel} = J_{\perp} = 1$ in this case [6]. Within the scope of the 1+1d model the velocity v corresponds to a shear rate, which is often denoted as $\dot{\gamma}$ [18,19]. However, we will use the term velocity for both driving mechanisms throughout this work.

In the following we argue that both systems show the same underlying critical behavior. In order to emphasize the

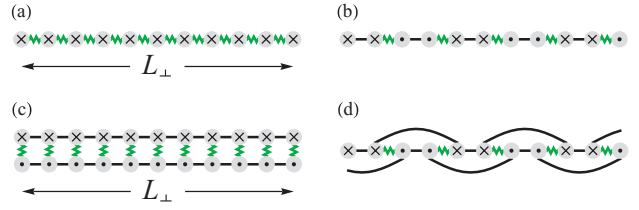


FIG. 2. (Color online) Cross sections of the 1+1d (a) and the 2d model (c), and slight modifications of both models [(b) and (d)]. The gray circles represent spin chains and the connecting lines substitute for the coupling, where green wiggled lines stand for moving and black lines for stationary couplings. Black crosses and dots indicate a motion into and out of the plane, respectively.

similarity, Fig. 2 illustrates slight variations of both models. First of all we start with the 1+1d model [Fig. 2(a)] and change every second bond perpendicular to the motion into a stationary bond. Additionally, we perform a transformation that changes the homogeneous shear $\Delta(t)$ into an alternating shift $\pm\Delta(t)$ of the double chains and reverses ($i \rightarrow -i$) every second double chain, leading to the configuration in Fig. 2(b). These modifications do not change the critical behavior of the 1+1d system, since still one-dimensional chains (now consisting of two rows) are moved relative to each other. On the other hand, the cross section of the 2d model can be visualized in a slightly different way [see Fig. 2(d)] without altering the corresponding Hamiltonian, Eq. (2). Since the next nearest double chains in Fig. 2(b) are not moving relative to each other, the only difference between Figs. 2(b) and 2(d) are the third nearest neighbor bonds in Fig. 2(d), which are irrelevant at the critical point where long-range correlations dominate. Hence we conclude that both systems belong to the same universality class.

Finally we mention that we must use the multiplicative rate

$$p_{\text{flip}}(\Delta E) = e^{-\frac{\beta}{2}(\Delta E - \Delta E_{\min})}, \quad (6)$$

with $\Delta E_{\min} = \min(\{\Delta E\})$ to reproduce the critical temperatures, Eqs. (3) and (5), in simulations (for a discussion see Ref. [6]).

III. RESULTS

In order to illustrate symptomatic features of both systems, Fig. 3 shows a sequence of spin configurations of one layer of the 2d system (note that the same characteristics are observed in the 1+1d system). On the left-hand side an equilibrated system at $T = 3.5$ well above the critical temperature of the nonmoving system, $T_c^{2d}(0) = 3.20755(5)$ [20], is presented. Shortly after starting the motion stripelike domains arise, spanning the whole system parallel to the motion. The stripes are rather stable, but are nonetheless transient, since they grow in time until the system ends up in a homogeneously magnetized state. The evolution in Fig. 3 is an example for a velocity-driven phase transition already described in Refs. [5,6], which is triggered by the onset of the motion and the associated increase of the critical temperature. The circumstances are comparable to a quench, which is characterized by a temperature decrease below T_c . After a quench a coarsening of domains is observed, whereas the growth of the domains can be described by a

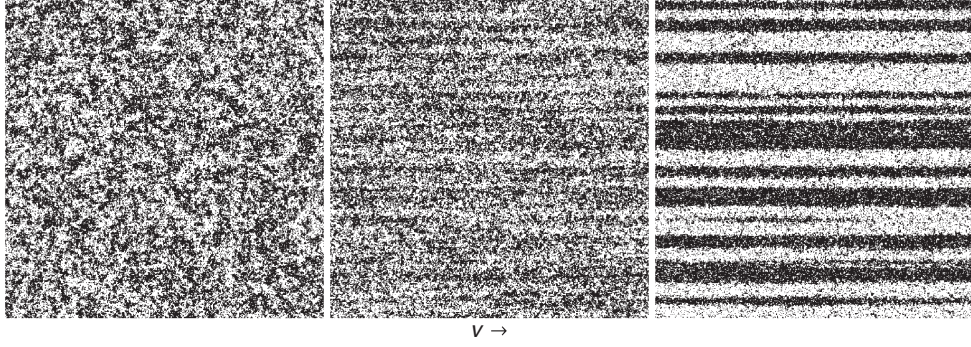


FIG. 3. Snapshots of one layer of the 2d model with $L_{\parallel} = L_{\perp} = 512$ and $J_{\parallel} = J_{\perp} = 1$ at temperature $T = 3.5$, which fulfills $T_c^{2d}(0) < T < T_c^{2d}(\infty)$. We start with an equilibrium system at $v = 0$ (left), set $v = \infty$, and show the evolution at $t = 42$ MCS (center) and $t = 360$ MCS (right).

power law (e.g., Refs. [21,22]). Domain growth in systems exhibiting a strongly anisotropic phase transition, e.g., the DLG model, is also a well-investigated subject [10,23,24]. The corresponding time evolution of spin configurations are similar to those shown in Fig. 3, leading to the assumption that the 2d and the 1 + 1d geometries are also characterized by strongly anisotropic correlations, which is shown in the following section.

A. Determination of θ in the limit $v \rightarrow \infty$

A strongly anisotropic phase transition is characterized by a correlation length ξ_{μ} which diverges with direction dependent critical exponents ν_{μ} at the critical point [25],

$$\xi_{\mu}(t) \stackrel{t \gg 0}{\sim} \hat{\xi}_{\mu} t^{-\nu_{\mu}}, \quad (7)$$

with direction $\mu = \{\perp, \parallel\}$ and reduced critical temperature $t = T/T_c - 1$. Defining the anisotropy exponent [26–28]

$$\theta = \frac{\nu_{\parallel}}{\nu_{\perp}}, \quad (8)$$

we find

$$\xi_{\parallel}(t)/\xi_{\perp}^{\theta}(t) \sim \hat{\xi}_{\parallel}/\hat{\xi}_{\perp}^{\theta} \quad (9)$$

independent of t . Isotropic scaling takes place for $\theta = 1$ and strongly anisotropic scaling is implied by $\theta \neq 1$. Several models with strongly anisotropic behavior were studied in the past. Examples are Lifshitz points as present in the anisotropic next nearest neighbor Ising (ANNNI) model [29,30], the nonequilibrium phase transition in the DLG [10], the two-dimensional dipolar in-plane Ising-model [28]. Furthermore, strongly anisotropic behavior usually occurs in dynamical systems, where the parallel direction can be identified with time and the perpendicular direction(s) with space [27,31]. In the latter case the anisotropy exponent θ corresponds to the dynamical exponent z .

The knowledge of the anisotropy exponent is essential and necessary for appropriate simulations of strongly anisotropic systems. To avoid complicated shape effects it is required to keep the generalized aspect ratio [26–28]

$$\rho = \frac{L_{\parallel}/\hat{\xi}_{\parallel}}{(L_{\perp}/\hat{\xi}_{\perp})^{\theta}} \quad (10)$$

fixed, which requires the knowledge of θ . We will show in the following that the limit $\rho \rightarrow 0$ simplifies the analysis for infinite velocity v and turns out to be essential at finite v .

We first discuss the case $v \rightarrow \infty$ and always assume criticality, $t = 0$. In order to determine the anisotropy exponent θ we calculate the perpendicular correlation function $G_{\perp}(L_{\parallel}, L_{\perp}; r_{\perp}) = \langle \sigma_{i,j} \sigma_{i,j+r_{\perp}} \rangle$ between spins at distance r_{\perp} in cylinder geometry $L_{\perp} \rightarrow \infty$ (leading to $\rho \rightarrow 0$), and thereby gain the correlation length $\xi_{\perp}(L_{\parallel})$ through

$$G_{\perp}(L_{\parallel}, \infty; r_{\perp}) \sim \hat{G}_{\perp}(L_{\parallel}) e^{-r_{\perp}/\xi_{\perp}(L_{\parallel})}, \quad (11)$$

where the prefactor $\hat{G}_{\perp}(L_{\parallel})$ is shown to be proportional to $L_{\parallel}^{-2/3}$ in the Appendix. Approaching the critical point within the given geometry, the correlation length $\xi_{\parallel}(t)$ is limited by L_{\parallel} , and using Eq. (9) this leads to the relation

$$\xi_{\perp}(L_{\parallel}) \sim A_{\perp} L_{\parallel}^{1/\theta} \quad (12)$$

with nonuniversal amplitude A_{\perp} [28,32]. Measuring the correlation length ξ_{\perp} in dependency of the parallel extension L_{\parallel} allows us to determine the anisotropy exponent θ .

In the simulations, the limit $L_{\perp} \rightarrow \infty$ is implemented by the condition $L_{\perp}/\xi_{\perp} \gtrsim 10$. This is sufficient to keep the systematic errors in G_{\perp} smaller than the statistical error $\epsilon = 10^{-3}$ adequate to calculate ξ_{\perp} . From ϵ we can determine the required system sizes via $L_{\perp}/\xi_{\perp} = -2 \ln[\epsilon/\hat{G}_{\perp}(L_{\parallel})]$, where the factor 2 accounts for the periodic boundary conditions. As $\hat{G}_{\perp} \approx 0.1$ for $L_{\parallel} = 40$ and $\hat{G}_{\perp} \approx 0.02$ for $L_{\parallel} = 10^4$ for the 1 + 1d model [see Fig. 4 (left)] we yield $L_{\perp}/\xi_{\perp} \approx 10$ for $L_{\parallel} = 40$ and $L_{\perp}/\xi_{\perp} \approx 0.7$ for $L_{\parallel} = 10^4$, meaning that for large systems a much smaller value of L_{\perp}/ξ_{\perp} would be sufficient.

Figure 4 displays the correlation functions for both models. For the 1 + 1d case these correlations are purely exponential also at short distances, since the coupling in \perp direction is mediated through fluctuating fields [6], leading to dimensional reduction to an effectively one-dimensional system. The resulting correlation length ξ_{\perp} is shown in the inset of Fig. 4 (left). The growth of $\xi_{\perp}(L_{\parallel})$ follows a power law with exponent $\theta^{-1} = 1/3$ and with prefactor

$$A_{\perp}^{1+1d} = \lim_{L_{\parallel} \rightarrow \infty} L_{\parallel}^{-1/3} \xi_{\perp}^{1+1d}(L_{\parallel}) = 0.68(2), \quad (13)$$

indicated as a black line.

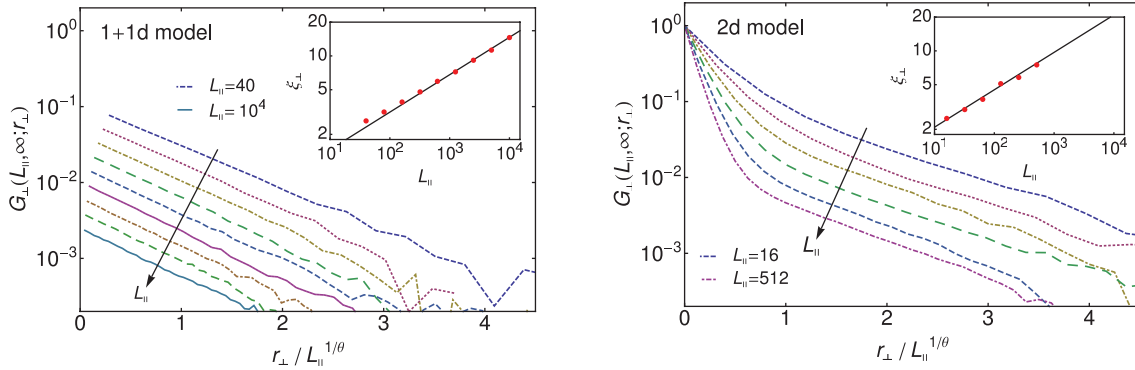


FIG. 4. (Color online) Rescaled correlation function $G_{\perp}(L_{\parallel}, \infty; r_{\perp})$ at criticality for both models for varying system extensions, $L_{\parallel} = \{40, 80, 160, 320, 625, 1250, 2500, 5000, 10000\}$ (1 + 1d) and $L_{\parallel} = \{16, 32, 64, 128, 256, 512\}$ (2d), respectively. The insets show $\xi_{\perp}(L_{\parallel})$ whereby we yield ξ_{\perp} by fitting an exponential function to the long-range part of $G_{\perp}(L_{\parallel}, \infty; r_{\perp})$. The solid line is a power law with exponent $\theta^{-1} = 1/3$ as predicted by the field theoretical analysis (see text).

In the case of the 2d model (right figure in Fig. 4) we find two regions with different characteristics. The short-distance correlations are affected by the \perp nearest-neighbor interactions within the planes, which are not present in the 1 + 1d model. These correlations decay with a correlation length of the order $\xi_{\perp}^{\text{eq}}[T_c^{2d}(\infty)] \approx 1$. For large distances the correlations crossover to an exponential behavior. The exponential correlations are propagated by the fluctuations of stripelike domains. The analysis yields

$$A_{\perp}^{2d} = \lim_{L_{\parallel} \rightarrow \infty} L_{\parallel}^{-1/3} \xi_{\perp}^{2d}(L_{\parallel}) = 0.94(3) \quad (14)$$

in this case.

From the anisotropy exponent $\theta = 3$ we can derive the correlation length exponents $\nu_{\parallel} = 3/2$ and $\nu_{\perp} = 1/2$ using the generalized hyperscaling relation

$$2 - \alpha = 2\beta + \gamma = \nu_{\parallel} + (d - 1)\nu_{\perp}, \quad (15)$$

with $d = 2$ and mean field exponents $\alpha = 0$, $\beta = 1/2$, and $\gamma = 1$, whose validity has been demonstrated in Ref. [6] by a mapping onto a mean field equilibrium model.

The calculation of θ in the limit $v \rightarrow \infty$ is done within a one-dimensional Ginzburg-Landau-Wilson (GLW) field theory [33]. For $v \rightarrow \infty$ it was shown in Ref. [6] that the 1 + 1d model can be mapped onto an equilibrium system consisting of one-dimensional chains that only couple via fluctuating magnetic fields. Due to the stripe geometry with short length L_{\parallel} and the periodic boundary conditions in \parallel direction the magnetization is homogeneous in \parallel direction, and parallel correlations are irrelevant. Hence we can use the zero mode approximation in this direction. However, it is necessary to include a term representing the interaction between adjacent spin chains. This can be expressed by the square of the spatial derivative of the magnetization in the direction \perp to the motion. Hence the minimal GLW model to describe this strongly anisotropic mean field system is given by

$$\beta\mathcal{H} = L_{\parallel} \int_0^{L_{\perp}} dx \left(\frac{t}{2} m(x)^2 + \frac{1}{2} m'(x)^2 + \frac{u}{4!} m(x)^4 \right) \quad (16)$$

with phenomenological parameters t and u , where $m(x)$ represents the magnetization of the spin chain at \perp coordinate x . Equation (16) corresponds to the Hamiltonian used for

the description of a cylinderlike spin system, which is infinite along one dimension, and finite and periodic in $d - 1$ dimensions [33]. The partition function of Eq. (16) can be mapped onto a one-dimensional Schrödinger equation in a quartic anharmonic oscillator potential using a rescaling, which yields the critical exponents $\nu_{\parallel} = 3/2$ and $\theta = 3$. The detailed derivation is given in the Appendix.

B. Crossover scaling at finite velocities

We now turn to finite velocities. The following analysis is exemplarily done for the 1 + 1d model, but as stated above, both models belong to the same universality class and similar results are expected for the 2d model. As we expect a crossover from an isotropic Ising model with $\theta = 1$ to a strongly anisotropic system with $\theta = 3$, we must be careful with the system geometry: We cannot use a fixed finite generalized aspect ratio ρ , Eq. (10), in the simulations, as θ is not constant. The only possible choice is $\rho \rightarrow 0$ (or $\rho \rightarrow \infty$), where the θ dependency drops out.

We consider the correlation length $\xi_{\perp}(t_c(v), v, L_{\parallel})$ at reduced critical temperature

$$t_c(v) = \frac{T_c(v)}{T_c(0)} - 1, \quad (17)$$

where $T_c(0) = 2/\ln(\sqrt{2} + 1)$. $t_c(v)$ is calculated via a finite-size scaling analysis of the perpendicular correlation length (not shown). As this procedure becomes inaccurate for small velocities $v < 2^{-8}$, we calculate the critical temperature according to

$$t_c(v) \stackrel{v \rightarrow 0}{\sim} \hat{c} v^{\phi} \quad (18)$$

with $\hat{c} = 0.29(1)$ in these cases, where we assume $\phi = 1/2$ in agreement with the literature [10, 18, 19]. The results are shown in the inset of Fig. 5(a).

Figure 5(a) shows the unscaled data, which gives evidence that the correlation length of systems moved at high velocities v are well described by the exponent $\theta = 3$ (dotted line), whereas for low velocities $v \lesssim 2^{-12}$ effectively the Ising exponent $\theta = 1$ (dashed line) holds for the simulated system sizes L_{\parallel} . The curvature of the data of intermediate velocities suggest the crossover. As a data collapse on the analytical known [34]

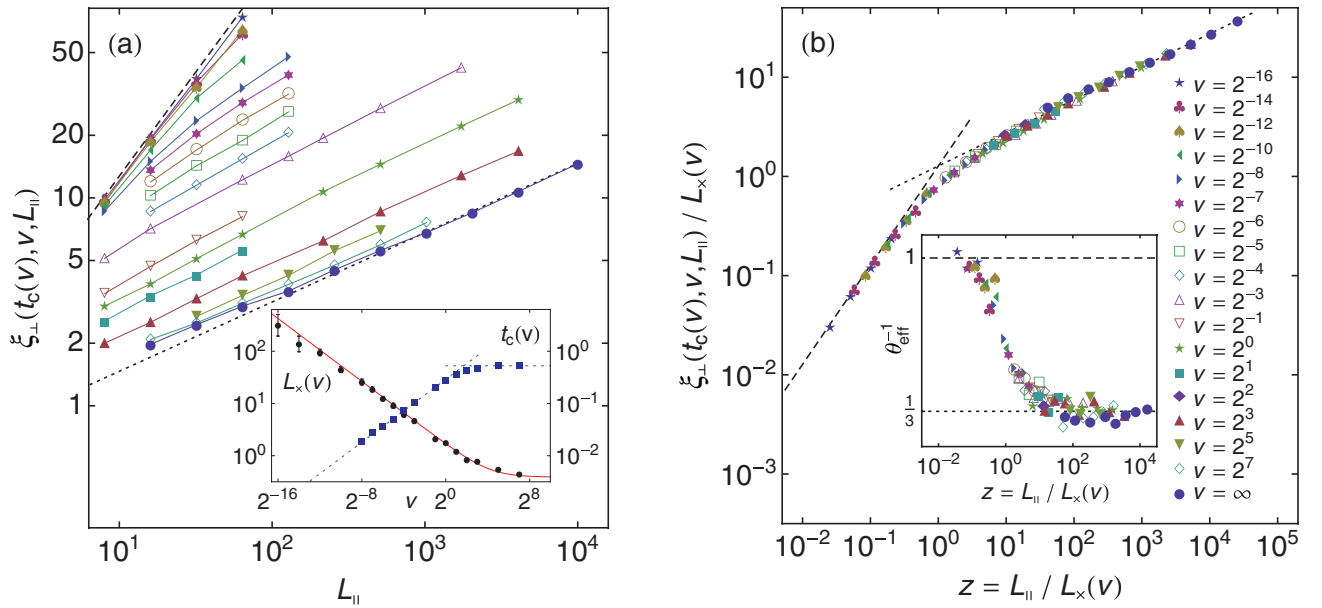


FIG. 5. (Color online) Velocity-dependent crossover behavior in the 1 + 1d case. Both pictures show log-log plots of the correlation length $\xi_{\perp}(t_c(v), v, L_{\parallel})$ as function of the system size L_{\parallel} at reduced critical temperature $t_c(v)$ for a broad range of different velocities v . The dashed line is the analytically known Ising limit $\xi_{\perp}(0,0,L_{\parallel})/L_{\parallel} \sim 4/\pi$ valid for $v \rightarrow 0$ [34], while the dotted line has slope $\theta^{-1} = 1/3$. The left figure shows the unscaled data and the inset displays the rescaling factor $L_{\times}(v)$ for different velocities v (black dots, see text) and a function approximating the data given in Eq. (19), (red solid line) as well as the reduced critical temperature $t_c(v)$ (blue squares) together with its asymptotes, Eqs. (5) and (18). The right figure displays the same data rescaled with the crossover length $L_{\times}(v)$, leading to an excellent data collapse. The inset shows the crossover of the effective anisotropy exponent θ_{eff} from $\theta_{\text{eff}} = 1$ (Ising, dashed line) to $\theta_{\text{eff}} = 3$ (MF, dotted line).

relation $\xi_{\perp}(0,0,L_{\parallel})/L_{\parallel} \sim A^{\text{eq}} = 4/\pi$ (dashed line in Fig. 5) has to be obtained in the limit $v \rightarrow 0$, both axes must be rescaled by the same factor $L_{\times}(v)$. This crossover length can be determined by applying the following method: We start with plotting the correlation length in the mean field limit $\xi_{\perp}[t_c(\infty), \infty, L_{\parallel}]$. Then we subsequently add the data for smaller v by rescaling ξ_{\perp} and L_{\parallel} with $L_{\times}^{-1}(v)$, which shifts the points parallel to the dashed line, until a data collapse is obtained [see Fig. 5(b)]. This procedure works quite accurate for velocities $v \gtrsim 2^{-3}$, only at very small $v \lesssim 2^{-12}$ the errors in $L_{\times}(v)$ grow due to the fact that we just shift the data along the dashed line. The resulting crossover length $L_{\times}(v)$ is pictured as black dots in the inset of Fig. 5(a). The behavior of $L_{\times}(v)$ is analogous to the velocity dependency of other quantities like the critical temperature or the energy dissipation, which are characterized by a power law for $v \ll 1$ and a saturation for $v \gg 1$.

We conclude that for all finite velocities $v > 0$ the critical behavior changes from Ising type to mean field type at a velocity dependent crossover length $L_{\times}(v)$ approximately given by

$$L_{\times}(v) \approx \left(\frac{A_{\perp}^{1+1d}}{A^{\text{eq}}} \right)^{3/2} \sqrt{1 + \frac{v_{\times}}{v}} \quad (19)$$

[solid red curve in the inset of Fig. 5(a)], where the velocity is measured in units 10^{-8} m/s and the size in 10^{-10} m. The velocity-independent prefactor was added to shift the crossover point (i.e., the intersection of the asymptotes) to $z = 1$. The saturation of L_{\times} at $v_{\times} = 18(2)$ results from the lattice cutoff, as $L_{\times}(v_{\times}) \approx 1$. The inset in Fig. 5(b) shows the effective

exponent θ_{eff} , obtained from the logarithmic derivative

$$\theta_{\text{eff}}^{-1} = \frac{\partial \ln \xi_{\perp}}{\partial \ln L_{\parallel}}, \quad (20)$$

whose value changes from $\theta_{\text{eff}} = 1$ (Ising, isotropic) to $\theta_{\text{eff}} = 3$ (MF, strongly anisotropic). Note that we verified the mean field exponents for $v \gtrsim 1/8$ with finite-size scaling methods and also found good agreement of the scaling function with the universal finite-size scaling function [35] (not shown). In order to illustrate the change of the critical behavior, Fig. 6 shows typical critical spin configurations for different values of the crossover scaling variable $z = L_{\parallel}/L_{\times}(v)$.

We are now able to compare our results with the literature. If the crossover scaling variable $z \ll 1$ Ising-like behavior occurs, whereas for $z \gg 1$ mean field exponents and strongly anisotropic correlations are expected. In experiments [13], even slow shear rates of the order of 10^{-4} (in natural units t_0^{-1} , where now t_0 is the time scale of the fluid dynamics), lead to a crossover length $L_{\times} \lesssim 100$ and, as the typical system size is large with respect to the atomic distances, give $z \gg 1$, indicating that experimental data are always obtained in the mean field limit.

In relation to the results of Winter *et al.* [19] we find that the correlation length exponent has been measured in the regime $29 \lesssim z \lesssim 239$, leading to the anisotropy exponent $\theta \approx 3$ in agreement with our results. In Ref. [18] the correlation length exponents have also been determined in the mean field limit. Looking at the lowest velocity $v = 1/32$ we find $53 \lesssim z \lesssim 1066$, where a surprisingly small anisotropy exponent $\theta \approx 0.73$ has been estimated. The highest velocity $v = 50$ leads to $\theta \approx 1.2$ and $1100 \lesssim z \lesssim 22000$. These discrepancies might

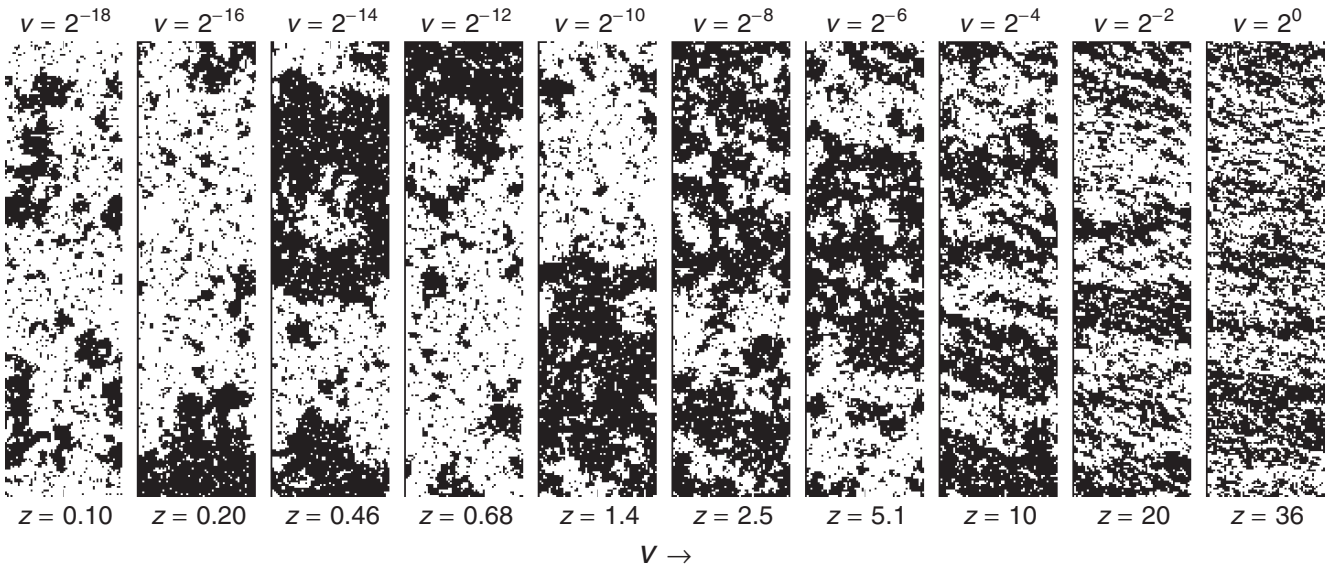


FIG. 6. Typical spin configurations of the critical 1 + 1d system for $L_{\parallel} = 64$ and different velocities $v = 2^{-18}, \dots, 1$. $z = L_{\parallel}/L_{\times}(v)$ denotes the crossover scaling variable (see text). The critical domains are isotropic and Ising-like for $z \ll 1$ and become anisotropic for $z \gtrsim 1$.

be attributed to the fact that an integral quantity, the order parameter, has been measured, as well as to strong surface effects induced by the open boundary conditions used in the \perp direction.

IV. CONCLUSION

In this work we investigated two recently proposed driven Ising models with friction due to magnetic interactions, namely the 1 + 1d and 2d model, using MC simulations as well as analytical methods. At first we focused on the strongly anisotropic critical behavior and calculated the anisotropy exponent θ in the limit of high driving velocity $v \rightarrow \infty$. Therefore the perpendicular correlation function of a cylinderlike geometry was calculated at criticality for different system sizes. Evaluating the connection between system size and correlation length, Eq. (12), we were able to find the critical exponents $\theta = 3$ as well as $\nu_{\parallel} = 3/2$ and $\nu_{\perp} = 1/2$. The analytic deviation of these exponents within the framework of a Ginzburg-Landau-Wilson Hamiltonian led to the same values. Comparing the results to the driven lattice gas [9, 10] we note that it also shows a strongly anisotropic phase transition at a critical temperature, which grows with the velocity. Remarkably this phase transition is characterized by the same critical exponents at large fields.

Finally we focused on the critical behavior for finite velocities v and performed extensive MC simulations in order to calculate the crossover scaling function describing the crossover from the Ising universality class at $v = 0$ to the nonequilibrium critical behavior at $v \rightarrow \infty$. The analysis has exemplarily been done for the 1 + 1d model, but as shown, both models belong to the same universality class and similar results are expected for the 2d model. In the analysis an additional complexity arose due to the strongly anisotropic characteristics of the correlations. Therefore we calculated the correlation length in a cylindrical system, circumventing intricate shape effects. We were able to identify a crossover

length $L_{\times}(v)$ using a simple method based on the rescaling of data for each velocity such that a data collapse occurs. This procedure leads to an excellent data collapse of all simulation results for different velocities v and system sizes L_{\parallel} .

It turns out that for all finite velocities $v > 0$ the models undergo a crossover, at crossover length $L_{\times}(v)$, from an quasi-equilibrium isotropic Ising-like phase transition to a nonequilibrium mean-field behavior with strongly anisotropic correlations.

ACKNOWLEDGMENTS

We thank Felix M. Schmidt and Matthias Burgsmüller for valuable discussions. This work was supported by Coordenação de Aperfeiçoamento de Pessoal de Nível Superior - Deutscher Akademischer Austauschdienst (CAPES-DAAD) through the Project Related Exchange Brazil-Germany (PROBRAL) program as well as by the German Research Society (DFG) through SFB 616 “Energy Dissipation at Surfaces”.

APPENDIX: SCALING EXPONENTS OF THE GINZBURG-LANDAU-WILSON MODEL

The following calculation is similar to Ref. [33]. Discretizing the integral

$$\beta\bar{\mathcal{H}} = L_{\parallel} \int_0^{L_{\perp}} dx \left(\frac{t}{2} m(x)^2 + \frac{1}{2} m'(x)^2 + \frac{u}{4!} m(x)^4 \right) \quad (\text{A1})$$

with step size δx , $N\delta x = L_{\perp}$, $m_i = m(i\delta x)$, and $\delta m_i = m_{i+1} - m_i$ gives

$$\beta\bar{\mathcal{H}} = L_{\parallel} \sum_{i=1}^N \delta x \left(\frac{t}{2} m_i^2 + \frac{1}{2} \frac{\delta m_i^2}{\delta x^2} + \frac{u}{4!} m_i^4 \right). \quad (\text{A2})$$

In order to evaluate the partition function

$$\mathcal{Z} = \int_{-\infty}^{\infty} \mathcal{D}[m(x)] e^{-\beta\bar{\mathcal{H}}}, \quad (\text{A3})$$

we use abbreviations in analogy to transfer matrices,

$$T(m, m^+) = \underbrace{e^{-L_{\parallel} \delta x \left(\frac{t}{2} m^2 + \frac{u}{4!} m^4 \right)}}_{V(m)} \underbrace{\sqrt{\frac{L_{\parallel}}{2\pi \delta x}} e^{-\frac{L_{\parallel} \delta m^2}{2\delta x}}}_{U(\delta m)}, \quad (\text{A4})$$

with $m^+ = m + \delta m$ to get

$$\begin{aligned} \mathcal{Z} &= \int_{-\infty}^{\infty} dm_1 \int_{-\infty}^{\infty} dm_2 T(m_1, m_2) \int_{-\infty}^{\infty} dm_3 T(m_2, m_3) \times \dots \\ &\times \int_{-\infty}^{\infty} dm_N T(m_{N-1}, m_N) T(m_N, m_1) \end{aligned} \quad (\text{A5})$$

for the assumed periodic boundary conditions.

Let $x^+ = x + \delta x$ and $\psi(m^+)$ be the result of the integrations for the interval $]x^+, L_{\perp}]$. Since $T(m, m^+)$ is near-diagonal for $L_{\parallel} \rightarrow \infty$, we can write $\psi(m^+)$ as

$$\lambda \psi(m^+) \approx \psi(m) + \psi'(m) \delta m + \frac{1}{2} \psi''(m) \delta m^2, \quad (\text{A6})$$

where λ denotes the growth factor of the integrations corresponding to the leading eigenvalue of the transfer matrix $T(m, m^+)$. The integral over m^+ in the partition function becomes

$$\begin{aligned} \psi(m) &= \int_{-\infty}^{\infty} dm^+ V(m) U(m^+ - m) \psi(m^+) \\ &= V(m) \sqrt{\frac{L_{\parallel}}{2\pi \delta x}} \int_{-\infty}^{\infty} dm^+ e^{-\frac{L_{\parallel} \delta m^2}{2\delta x}} \psi(m^+) \\ &= \frac{V(m)}{\lambda} \left(\psi(m) + \frac{\delta x}{2L_{\parallel}} \psi''(m) \right), \end{aligned} \quad (\text{A7})$$

and yields the solution of the integrations for the interval $]x^+, L_{\perp}]$. Hence we get a differential equation for $\psi(m)$,

$$V(m) \left(\psi(m) + \frac{\delta x}{2L_{\parallel}} \psi''(m) \right) = \lambda \psi(m). \quad (\text{A8})$$

We now substitute

$$\psi(m) \rightarrow \Psi(\tilde{m}) \quad (\text{A9a})$$

$$m \rightarrow \tilde{m} u^{-1/6} L_{\parallel}^{-1/3} \quad (\text{A9b})$$

$$\lambda \rightarrow 1 - \Lambda \delta x u^{1/3} L_{\parallel}^{-1/3} \quad (\text{A9c})$$

$$t \rightarrow x u^{2/3} L_{\parallel}^{-2/3} \quad (\text{A9d})$$

and expand to lowest order around $L_{\parallel} = \infty$ to yield the Schrödinger equation in a quartic potential,

$$\left(-\frac{1}{2} \partial_{\tilde{m}}^2 + \frac{x}{2} \tilde{m}^2 + \frac{1}{4!} \tilde{m}^4 - \Lambda \right) \Psi(\tilde{m}) = 0, \quad (\text{A10})$$

valid in the scaling limit $L_{\parallel} \rightarrow \infty$, $t \rightarrow 0$ with $x = t(L_{\parallel}/u)^{1/\nu_{\parallel}}$ kept fixed.

The correlation length $\xi_{\perp}(L_{\parallel})$ is determined from the lowest eigenvalues $\Lambda_{0,1}$ of this equation, as

$$\xi_{\perp} = \delta x \left(\ln \frac{\lambda_0}{\lambda_1} \right)^{-1} \sim \frac{1}{\Lambda_1 - \Lambda_0} \left(\frac{L_{\parallel}}{u} \right)^{1/3}. \quad (\text{A11})$$

From the substitution, Eqs. (A9), we directly read off the exponents $\nu_{\parallel} = 3/2$, and $\theta = 3$.

The correlation function amplitude $\hat{G}_{\perp}(L_{\parallel})$ from Eq. (11) is proportional to m^2 and thus scales as $L_{\parallel}^{-2/3}$ as can be seen from Eq. (A9b).

-
- [1] C. Fusco, D. E. Wolf, and U. Nowak, *Phys. Rev. B* **77**, 174426 (2008).
- [2] M. P. Magiera, L. Brendel, D. E. Wolf, and U. Nowak, *Europhys. Lett.* **87**, 26002 (2009).
- [3] M. P. Magiera, D. E. Wolf, L. Brendel, and U. Nowak, *IEEE Trans. Magn.* **45**, 3938 (2009).
- [4] M. P. Magiera, S. Angst, A. Hucht, and D. E. Wolf, *Phys. Rev. B* **84**, 212301 (2011).
- [5] D. Kadau, A. Hucht, and D. E. Wolf, *Phys. Rev. Lett.* **101**, 137205 (2008).
- [6] A. Hucht, *Phys. Rev. E* **80**, 061138 (2009).
- [7] F. Igloi, M. Pleimling, and L. Turban, *Phys. Rev. E* **83**, 041110 (2011).
- [8] H. J. Hilhorst, *J. Stat. Mech. Theor. Exp.* (2011) P04009.
- [9] S. Katz, J. L. Lebowitz, and H. Spohn, *Phys. Rev. B* **28**, 1655 (1983).
- [10] B. Schmittmann and R. K. P. Zia, in *Phase Transitions and Critical Phenomena*, Vol. 17, edited by C. Domb and J. L. Lebowitz (Academic Press, London, 1995).
- [11] R. K. P. Zia, *J. Stat. Phys.* **138**, 20 (2010).
- [12] C. K. Chan and L. Lin, *Europhys. Lett.* **11**, 13 (1990).
- [13] A. Onuki, *J. Phys.: Condens. Matter* **9**, 6119 (1997).
- [14] E. N. M. Cirillo, G. Gonnella, and G. P. Saracco, *Phys. Rev. E* **72**, 026139 (2005).
- [15] M. E. Fisher, *J. Stat. Phys.* **75**, 1 (1994).
- [16] K. Gutkowski, M. A. Anisimov, and J. V. Sengers, *J. Chem. Phys.* **114**, 3133 (2001).
- [17] E. Luijten, H. W. J. Blöte, and K. Binder, *Phys. Rev. E* **56**, 6540 (1997).
- [18] G. P. Saracco and G. Gonnella, *Phys. Rev. E* **80**, 051126 (2009).
- [19] D. Winter, P. Virnau, J. Horbach, and K. Binder, *Europhys. Lett.* **91**, 60002 (2010).
- [20] A. Lipowski and M. Suzuki, *Physica A* **198**, 227 (1993).
- [21] A. J. Bray, *Adv. Phys.* **43**, 357 (1994).
- [22] R. Paul, S. Puri, and H. Rieger, *Europhys. Lett.* **68**, 881 (2004).
- [23] C. Yeung, T. Rogers, A. Hernandez-Machado, and D. Jasnow, *J. Stat. Phys.* **66**, 1071 (1992).
- [24] P. I. Hurtado, J. Marro, and E. V. Albano, *Europhys. Lett.* **59**, 14 (2002).
- [25] Throughout this work, the symbol \sim means asymptotically equal in the respective limit [e. g., $f(L) \sim g(L) \Leftrightarrow \lim_{L \rightarrow \infty} f(L)/g(L) = 1$]. Note that the variable t is used for the reduced temperature throughout the rest of this work.

- [26] K. Binder, in *Finite Size Scaling and Numerical Simulations of Statistical Systems*, edited by V. Privman (World Scientific, Singapore, 1990), ch. 4.
- [27] M. Henkel, *Conformal Invariance and Critical Phenomena* (Springer-Verlag, Berlin, 1999).
- [28] A. Hucht, *J. Phys A: Math. Gen.* **35**, L481 (2002).
- [29] W. Selke, *Phys. Rep.* **170**, 213 (1988).
- [30] M. Pleimling and M. Henkel, *Phys. Rev. Lett.* **87**, 125702 (2001).
- [31] H. Hinrichsen, *Adv. Phys.* **49**, 815 (2000).
- [32] M. Henkel and U. Schollwöck, *J. Phys A: Math. Gen.* **34**, 3333 (2001).
- [33] E. Brézin and J. Zinn-Justin, *Nucl. Phys. B*, **257**, 867 (1985).
- [34] J. L. Cardy, *J. Phys A: Math. Gen.* **17**, L385 (1984).
- [35] D. Grüneberg and A. Hucht, *Phys. Rev. E* **69**, 036104 (2004).

LETTER

Explosive Ising

**Sebastian Angst¹, Silvio R Dahmen², Haye Hinrichsen³,
Alfred Hucht¹ and Martin P Magiera¹**

¹ Fakultät für Physik, Universität Duisburg-Essen, 47048 Duisburg, Germany

² Instituto de Física, Universidade Federal do Rio Grande do Sul, 91501-970
Porto Alegre RS, Brazil

³ Fakultät für Physik und Astronomie, Universität Würzburg, 97074 Würzburg,
Germany

E-mail: sebastian.angst@uni-due.de, silvio.dahmen@ufrgs.br,
hinrichsen@physik.uni-wuerzburg.de, fred@thp.uni-due.de and
martin.magiera@uni-due.de

Received 27 April 2012

Accepted 8 June 2012

Published 27 June 2012

Online at stacks.iop.org/JSTAT/2012/L06002

doi:10.1088/1742-5468/2012/06/L06002

Abstract. We study a two-dimensional kinetic Ising model with Swendsen–Wang dynamics, replacing the usual percolation on top of Ising clusters by explosive percolation. The model exhibits a reversible first-order phase transition with hysteresis. Surprisingly, at one of the transition flanks the global bond density seems to be equal to the percolation threshold.

Keywords: classical phase transitions (theory), percolation problems (theory)

ArXiv ePrint: [1204.5196](https://arxiv.org/abs/1204.5196)

Contents

1. Definition of the model	3
2. Order parameter hysteresis	4
3. Spontaneous flipping and order parameter distribution	6
4. Density of equally oriented neighbors at the transition flanks	6
5. Concluding remarks	7
Acknowledgments	8
References	8

Three years ago Achlioptas *et al* discovered that a slight modification of standard percolation on a complete graph turns the continuous transition into an abrupt one [1]. This surprising phenomenon, marketed as ‘explosive percolation’, attracted a lot of attention and was studied on scale-free networks [2, 3], regular two-dimensional lattices [4], and in various other situations [5]–[12]. Initially the explosive transition was believed to be discontinuous, but later studies revealed that the transition is extremely sudden but actually continuous [13]–[17].

While in ordinary bond percolation each bond is set independently with probability p , the Achlioptas process uses a dynamical procedure, where the bonds are placed in sequence. To this end one randomly selects two pairs of neighboring lattice sites which are not yet connected by a bond. Depending on the actual bond configuration, a weight is assigned to each of the pairs by multiplying the sizes of the clusters to which the two lattice sites belong (or squaring the size if both sites belong to the same cluster). If the weights of the two pairs are different, the pair with the *lower* weight is connected by a new bond. Otherwise, if the weights are equal, one of the pairs is randomly chosen and connected. This process is repeated until the density of bonds exceeds the value of the control parameter p .

As the dynamic rule is defined in such a way that new connections are preferentially added between *small* clusters, it is plausible that the transition point is shifted to higher values of the percolation probability. For example, on a two-dimensional square lattice, where the transition of ordinary bond percolation takes place at $p_c^{\text{perc}} = 1/2$, the Achlioptas-dynamics described above shifts the transition point to $p_c^{\text{expl}} = 0.526\,562(3)$ [14]. Surprisingly, the transition is not only shifted, but it changes also qualitatively, exhibiting a sudden transition, where a large percolation cluster is formed. This is why the transition is called ‘explosive’.

In this letter we demonstrate that the concept of explosive cluster growth can also be applied successfully to kinetic spin models with cluster dynamics. Here we will focus on a particularly simple case, namely, the two-dimensional Ising model with Swendsen–Wang dynamics [18]. As will be shown below, the use of an explosive cluster dynamics turns the continuous Ising transition into a discontinuous one, preserving the Z_2 -symmetry of the

model. As this modification of the dynamics is expected to break detailed balance, the stationary state of such an explosive Ising model will no longer be an equilibrium state.

1. Definition of the model

Before defining the explosive Ising model let us briefly recall the Swendsen–Wang (SW) algorithm applied to the Ising model [18]. The SW cluster algorithm is a dynamical update rule which works as follows. At first percolation clusters are grown *within* the actual spin clusters. For each of these clusters one chooses a random number ± 1 which is then assigned to all its spins. More specifically, in the case of the Ising model the SW update for a given configuration of spins consists of the following steps.

- (i) Remove all bonds.
- (ii) Set all bonds between equally oriented nearest-neighbor spins with probability p .
- (iii) Identify all clusters of sites which are connected by bonds.
- (iv) For each of these clusters generate a random number ± 1 with equal probability and assign it to all its spins.

It was proven that this dynamics evolves into the equilibrium state of the Ising model without critical-slowing-down and that the percolation probability is related to the temperature by $p = 1 - e^{-2J/k_B T}$.

Let us now modify the SW dynamics of the Ising model by replacing ordinary with explosive percolation. Since bonds can no longer be distributed independently, one first has to determine the number of potential bonds n . This results in the following ‘explosive’ Swendsen–Wang dynamics for the Ising model (see right panel of figure 1).

- (i) Clear all bonds.
- (ii) Count the number n of links between neighboring spins of the same orientation.
- (iii) Select two vacant bonds between equally oriented spins and determine their weight according to the product rule in the same way as in explosive percolation.
- (iv) Place a bond at the link with the lower weight (if the weights are equal select one of them randomly).
- (v) Repeat (iii) and (iv) until the number of bonds exceeds np , where $p \in [0, 1]$ is the control parameter of the model.
- (vi) Finally, as in ordinary SW dynamics, assign a random spin orientation to each of the clusters.

Figure 2 shows typical spin configurations of the ordinary Ising model compared with those of the explosive variant defined above, increasing the parameter p from 0.55 to 0.59. For small values of p both models are in the disordered phase, although the domains in the explosive variant seem to be somewhat smaller. As p is increased, the Ising model displays a continuous transition at $p_c^{\text{Ising}} = 2 - \sqrt{2} \approx 0.585786$ into a partially ordered state, while the explosive variant switches suddenly to an almost completely ordered state at some value between 0.57 and 0.58 (see below).

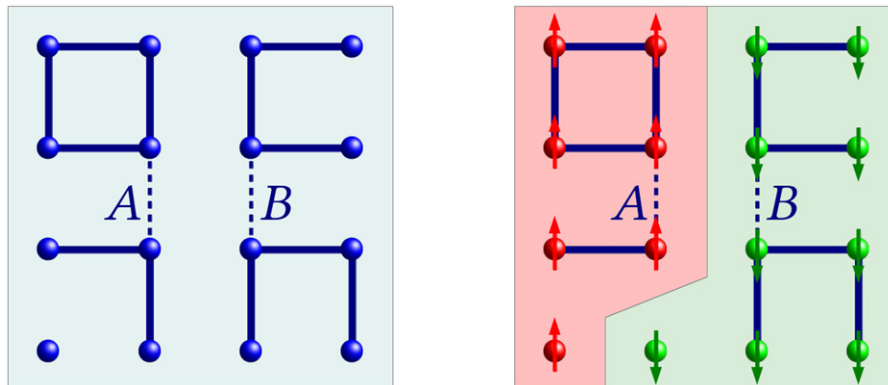


Figure 1. Left: dynamics of explosive bond percolation on a square lattice. Two vacant bonds A, B (shown as dashed lines) are randomly selected. As bond A would connect two clusters of sizes 2 and 4, its weight is $2 \times 4 = 8$, whereas bond B has weight $3 \times 3 = 9$. The bond with the *lower* weight is set and the procedure is repeated until the density of bonds exceeds the parameter p . Right: ‘explosive’ Ising model with two spin domains (red and green). Here a Swendsen–Wang update uses the same dynamical rule for placing bonds but only within domains of equally oriented spins.

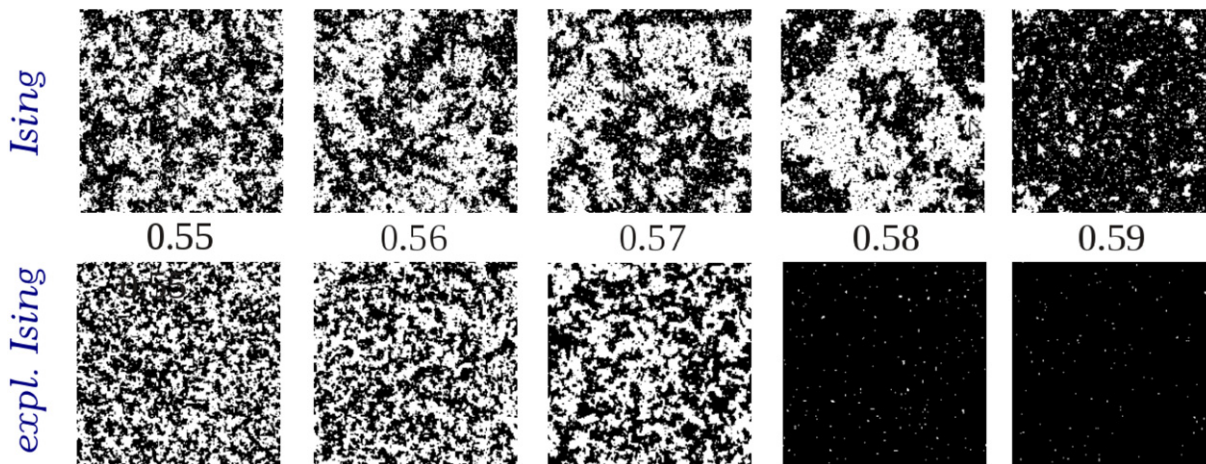


Figure 2. Typical snapshots of spin configurations for the ordinary and the explosive Ising model with p increasing from 0.55 to 0.59.

2. Order parameter hysteresis

In explosive percolation the process of adding new bonds is not reversible, i.e. in a single realization the density of bonds can only be increased. In the present model, however, the explosive cluster dynamics is part of a continually repeating update procedure, allowing one to increase and decrease the percolation probability while the model evolves in time.

Since a spin model with cluster dynamics switches frequently from positive to negative magnetization in the ordered phase, the appropriate order parameter is the absolute value of the magnetization M . The solid lines in figure 3 show how $|M|$ varies with the control

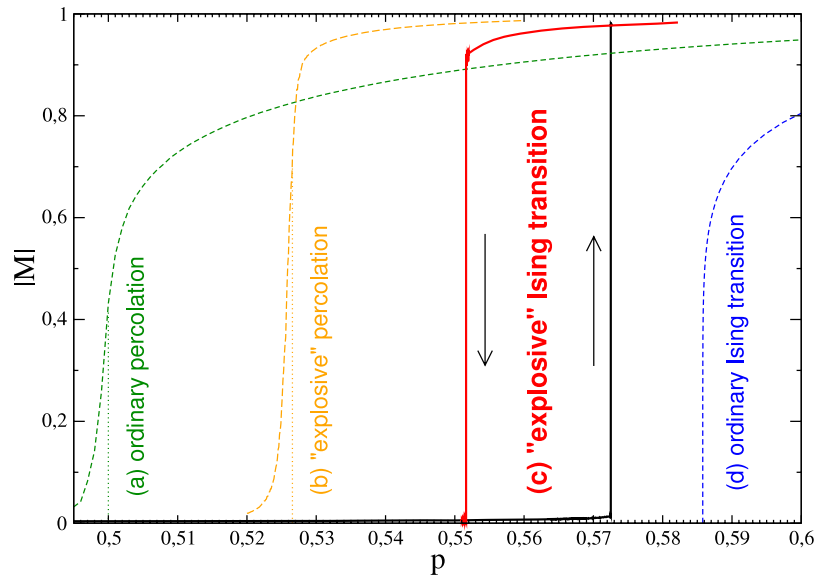


Figure 3. Order parameter as a function of the percolation probability p for various models discussed in the text. From left to right: (a) average density of the largest cluster in ordinary bond percolation on a 3000×3000 lattice and periodic boundary conditions. The dotted line indicates the transition point in the limit $L \rightarrow \infty$. (b) Largest cluster size in explosive percolation as defined above on a periodic 500×500 lattice. (c) Hysteresis of the order parameter $|M|$ in the explosive Ising model on a square lattice with 512×512 sites and periodic boundary conditions. (d) Same data for the ordinary two-dimensional Ising model (analytical result).

Table 1. Transition points for various models discussed in the text.

Ordinary percolation	Explosive percolation	Explosive Ising left flank	Explosive Ising right flank	Ordinary Ising
$p_c^{\text{perc}} = 1/2$	$p_c^{\text{expl}} = 0.526\,562(3)$	$p_{c,1} = 0.5516(3)$	$p_{c,2} = 0.5725(3)$	$p_c^{\text{Ising}} = 0.585\,786$

parameter p on a lattice with $N = 512 \times 512$ sites and periodic boundary conditions. As can be seen, the transition seems to be discontinuous, exhibiting a pronounced hysteresis with the flanks located at the values $p_{c,1}$ and $p_{c,2}$ (see table 1).

The hysteresis may be explained as follows. For $p \approx 0.5$ the Achlioptas selection rule generates smaller clusters than in the usual Ising model. Since the percolation clusters are confined to domains of the same spin orientation, their growth is suppressed like in a finite system with open boundary conditions, explaining why nothing happens at the usual threshold $p_c^{\text{expl}} \approx 0.527$ of explosive percolation. However, as the size of the Ising domains grows with p , one eventually reaches a point $p_{c,2}$ where this stabilization mechanism breaks down. Here one observes the immediate formation of a system-spanning cluster, self-sustained from inside by the as-from-now super-critical Achlioptas process. Lowering

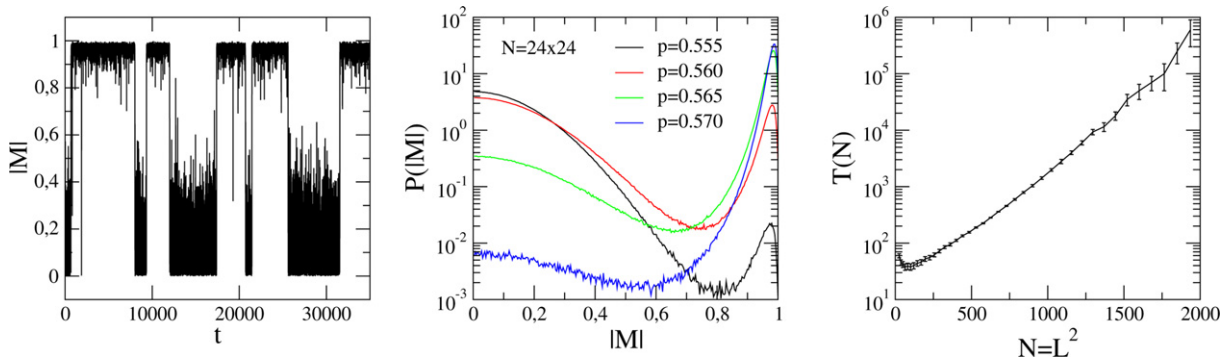


Figure 4. Left: spontaneous flipping of the order parameter $|M|$ in a system with 24×24 sites inside the hysteresis loop at $p = 0.563$. Middle: distribution of the order parameter averaged over a long time for various values of p in a 24×24 system. Right: the average time $T(N)$ between two flips at $p = 0.563$ grows exponentially with the system size.

p again, the system first remains in the ordered state until the explosive percolation transition is reached from above. As the percolation process takes place on a slightly porous support, the transition point is already reached at a value $p_{c,1}$ which is somewhat higher than the usual transition point of explosive percolation p_c^{expl} .

3. Spontaneous flipping and order parameter distribution

As usual in systems with a first-order phase transition, we find that the order parameter in finite systems flips occasionally between the disordered and the ordered phase (left panel of figure 4). As expected, the corresponding probability distributions of the order parameter (see central panel) show two maxima separated by a valley, whose relative sizes depend on p . We also verified that the flipping time $T(N)$ diverges exponentially with the number of sites $N = L^2$, meaning that the ordered and the disordered phase are both thermodynamically stable in the coexistence region $p_{c,1} < p < p_{c,2}$.

4. Density of equally oriented neighbors at the transition flanks

Let b be the total number of bonds generated in the update procedure. We finally present the surprising conjecture that the global bond density

$$q = \frac{b}{2N} \tag{1}$$

is exactly equal to p_c^{expl} at the left transition flank in the thermodynamic limit.

Remarkably, a similar relation holds at the transition point of the *ordinary* Ising model on a square lattice⁴. To see this let us consider the number n of equally oriented neighboring spins, which is related to the internal energy $E = -J \sum_{\langle i,j \rangle} s_i s_j$ by

$$n = -\frac{E + E_0}{2J}, \tag{2}$$

⁴ Although this result should be already known, we could not identify an explicit reference.

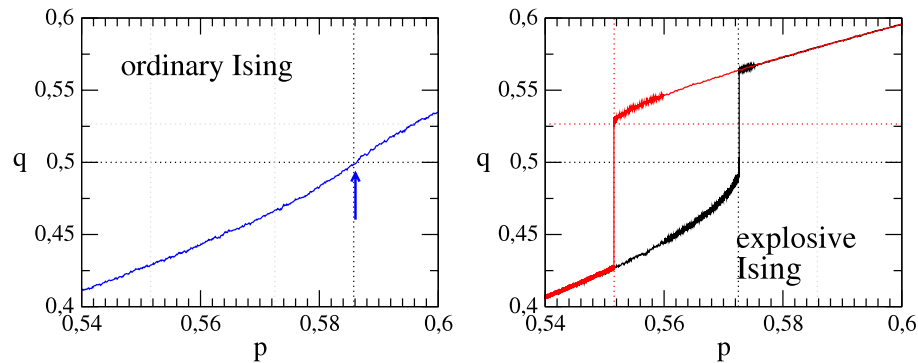


Figure 5. Left: global bond density q set during the SW update as a function of the percolation probability p in the ordinary Ising model (left) and the explosive variant (right). The horizontal dotted lines indicate where $q = p_c^{\text{perc}} = 1/2$ and $q = p_c^{\text{expl}} = 0.526\,562(3)$.

where $E_0 = -2NJ$ the lowest possible energy where all spins are parallel. As bonds are randomly set between equally oriented spins with probability p , we have $b \approx np$ so that the global bond density is given by

$$q = \lim_{N \rightarrow \infty} \frac{np}{2N}. \quad (3)$$

Since the internal energy of the Ising model on a square lattice at the critical point $p_c^{\text{Ising}} = 1 - e^{-2J/k_B T_c} = 2 - \sqrt{2}$ is known to be $E_c = -\sqrt{2}NJ$, we find that

$$q_c = \frac{n_c p_c^{\text{Ising}}}{2N} = \frac{\sqrt{2} + 2}{4} (2 - \sqrt{2}) = \frac{1}{2}. \quad (4)$$

This means that the transition in the ordinary Ising model with Swendsen–Wang dynamics takes place when the global bond density reaches the value $1/2$ —the same value as the critical threshold for percolation *without* Ising spins. The actual transition point $p_c^{\text{Ising}} \approx 0.5858$ is of course larger since bonds between different spin clusters cannot be set so that an enhanced probability is needed to reach a global bond density of $1/2$.

Surprisingly, we find numerically that the same relation holds at the left transition flank of the explosive Ising model, where the bond density $q_{c,1}$ reaches the value p_c^{expl} of explosive percolation without Ising spins (see figure 5). However, at the right flank the transition occurs at a lower value $q_{c,2} \approx 0.49$ which may tend to $1/2$ in the limit of very large lattices.

5. Concluding remarks

In this letter we introduced and studied an explosive variant of the Ising model, arriving at two conjectures.

- Even though the Achlioptas process was found to be continuous, we think that the transition in the explosive Ising model is genuinely discontinuous because it exhibits a very clear hysteresis.

- The global density of bonds in the SW update at the left transition flank of the hysteresis is conjectured to be equal to the threshold p_c^{expl} of explosive percolation without Ising spins. An analogous relation holds already for the usual Ising model. At the right transition flank the bond density is lower, probably close to $1/2$.

It would be interesting to explore these conjectures more deeply and to apply similar ideas to other spin systems with cluster dynamics.

Acknowledgments

This work was supported financially by the German Academic Exchange Service (DAAD) under the Joint Brazil–Germany Cooperation Program PROBRAL.

References

- [1] Achlioptas D, D'Souza R M and Spencer J, 2009 *Science* **323** 1453
- [2] Radicchi F and Fortunato S, 2009 *Phys. Rev. Lett.* **103** 168701
Radicchi F and Fortunato S, 2010 *Phys. Rev. E* **81** 036110
- [3] Cho Y S, Kim J S, Park J, Kahng B and Kim D, 2009 *Phys. Rev. Lett.* **103** 135702
- [4] Ziff R M, 2009 *Phys. Rev. Lett.* **103** 045701
Ziff R M, 2010 *Phys. Rev. E* **82** 051105
- [5] Moreira A A, Oliveira E A, Reis S D S, Herrmann H J and Andrade J S Jr, 2010 *Phys. Rev. E* **81** 040101(R)
- [6] Cho Y S, Kahng B and Kim D, 2010 *Phys. Rev. E* **81** 030103(R)
- [7] Cho Y S, Kim S-W, Noh J D, Kahng B and Kim D, 2010 *Phys. Rev. E* **82** 042102
- [8] Friedman E J and Landsberg A S, 2009 *Phys. Rev. Lett.* **103** 255701
- [9] Manna S S and Chatterjee A, 2011 *Physica A* **390** 177
- [10] D'Souza R M and Mitzenmacher M, 2010 *Phys. Rev. Lett.* **104** 195702
- [11] Rozenfeld H D, Gallos L K and Makse H A, 2010 *Eur. Phys. J. B* **75** 305
- [12] Araújo N A M and Herrmann H J, 2010 *Phys. Rev. Lett.* **105** 035701
- [13] da Costa R A, Dorogovtsev S N, Goltsev A V and Mendes J F F, 2010 *Phys. Rev. Lett.* **105** 255701
- [14] Grassberger P, Christensen C, Bizhani G, Son S-W and Paczuski M, 2011 *Phys. Rev. Lett.* **106** 225701
- [15] Riordan O and Warnke L, 2011 *Science* **333** 322
- [16] Lee H K, Kim B J and Park H, 2011 *Phys. Rev. E* **84** 020101(R)
- [17] Tian L and Shi D-N, 2012 *Phys. Lett. A* **376** 286
- [18] Swendsen R H and Wang J-S, 1987 *Phys. Rev. Lett.* **58** 86

Exact thermodynamic Casimir forces for an interacting three-dimensional model system in film geometry with free surfaces

H. W. DIEHL¹, DANIEL GRÜNEBERG¹, MARTIN HASENBUSCH², ALFRED HUCHT¹, SERGEI B. RUTKEVICH^{1,3} and FELIX M. SCHMIDT¹

¹ *Fakultät für Physik, Universität Duisburg-Essen - D-47058 Duisburg, Germany, EU*

² *Institut für Physik, Humboldt-Universität zu Berlin - Newtonstr. 15, D-12489 Berlin, Germany, EU*

³ *Institute of Solid State and Semiconductor Physics - Minsk, Belarus*

received 6 August 2012; accepted in final form 11 September 2012
published online 16 October 2012

PACS 05.70.Jk – Critical point phenomena
PACS 11.10.-z – Field theory
PACS 64.60.an – Finite-size systems

Abstract – The limit $n \rightarrow \infty$ of the classical $O(n)$ ϕ^4 model on a 3d film with free surfaces is studied. Its exact solution involves a self-consistent 1d Schrödinger equation, which is solved numerically for a partially discretized as well as for a fully discrete lattice model. Extremely precise results are obtained for the scaled Casimir force at all temperatures. Obtained via a single framework, they exhibit all relevant qualitative features of the thermodynamic Casimir force known from wetting experiments on ${}^4\text{He}$ and Monte Carlo simulations, including a pronounced minimum below the bulk critical point.

Copyright © EPLA, 2012

A celebrated example of fluctuation-induced forces is the Casimir force between two metallic, grounded plates in vacuum [1]¹. Such forces caused by the confinement of quantum electrodynamics (QED) vacuum fluctuations of the electromagnetic fields are expected to have considerable technological relevance. This has made them the focus of much ongoing research activity. During the past two decades, it has become increasingly clear that a wealth of similarly interesting classical analogs of such effective forces, induced by thermal rather than quantum fluctuations, exist [3]². Two important classes of such “thermodynamic Casimir forces”³ are forces induced by fluctuations in nearly (multi)critical media between immersed macroscopic bodies or boundaries, and forces due to confined

Goldstone modes [6]. Clear experimental evidence for the existence of such thermodynamic Casimir forces was provided first indirectly by measurements of the thinning of ${}^4\text{He}$ wetting films at the λ -point as the temperature T is lowered below the bulk critical temperature T_c [7]. Subsequently, direct measurements of the thermodynamic Casimir force on colloidal particles in binary liquids near the consolute point could be achieved [8].

Despite obvious analogies, crucial qualitative differences between thermodynamic and QED Casimir forces exist. First, the latter usually can be studied in terms of effective *free* field theories in confined geometries where the interaction of the electromagnetic field with the material boundaries is taken into account through boundary conditions. By contrast, investigations of thermodynamic Casimir forces at (multi)critical points necessarily involve *interacting* field theories. Second, whereas electromagnetic fields average to zero in the ground state, the thermal averages $\langle \phi(\mathbf{x}) \rangle$ of fluctuating densities $\phi(\mathbf{x})$ (order parameters) associated with thermodynamic Casimir forces do not necessarily vanish. Nonzero profiles $\langle \phi(\mathbf{x}) \rangle$ can occur at all temperatures T when the symmetry $\phi \rightarrow -\phi$ is explicitly broken (as it generically is for fluids and binary fluid mixtures in contact with walls), and at low temperatures if this symmetry is spontaneously broken.

¹For a review of the Casimir effect in QED and an extensive lists of references, see [2].

²For reviews of the thermodynamic Casimir effect and extensive lists of references, see [4].

³Following established conventions we use the term “thermodynamic Casimir forces” for forces induced by thermal fluctuations, in particular, also for near-critical Casimir forces, reserving the name critical Casimir forces to those where the medium is at a critical point. This topic must not be confused with those of thermal effects on QED Casimir forces and thermal Casimir-Polder forces, which are less universal since material properties of the media and confining objects matter; see, *e.g.*, [5].

When a nonzero profile exists, it will respond to a change of the separation between boundaries and hence cause an effective force even in the absence of fluctuations. The presence of such nonfluctuating background contributions to thermodynamic Casimir forces substantially spoils the analogy with the QED case. Obviously, thermodynamic Casimir forces in ${}^4\text{He}$ films provide much better analogs than those in binary mixed fluids because neither a spontaneous breakdown of the $U(1)$ symmetry is possible for finite thickness L of the film, nor an explicit breakdown of the symmetry through the boundary planes.

It is therefore very unfortunate that no viable theory other than sophisticated Monte Carlo simulations of lattice XY models [9–11] has emerged which is capable to yield, within a single framework, all experimentally observed [7] relevant qualitative features of the reduced Casimir force $\beta\mathcal{F}_C(T, L)$, where $\beta = 1/k_B T$. For a d -dimensional film, the latter takes the scaling form $\beta\mathcal{F}_C(T, L) \simeq L^{-d} \vartheta(x)$ with scaling variable $x = t(L/\xi_+)^{1/\nu}$ on large length scales⁴, where $t = T/T_c - 1$ while ν and ξ_+ are the critical exponent and $t > 0$ amplitude of the bulk correlation length, respectively. The observed features of the scaling function $\vartheta(x)$ are: (i) $\vartheta(x) < 0$ for all x , (ii) a relatively small critical value $\vartheta(0)$, (iii) a smooth minimum at $x_{\min} < 0$, and (iv) a non-vanishing $T \rightarrow 0$ limit $\vartheta(-\infty)$. A theory based on renormalization-group (RG) improved Landau theory [12,13], though giving some insight, suffers from severe deficiencies: it erroneously predicts (d1) an ordered low-temperature phase for $d=3$ and $L < \infty$, (d2) a much too deep minimum of ϑ whose derivative has a (d3) jump discontinuity there, and (d4) a vanishing $T \rightarrow 0$ limit $\vartheta(-\infty)$.

In this letter, we report exact results for the Casimir force of the $O(n)$ ϕ^4 model on a film $\mathbb{R}^2 \times [0, L]$ with free surfaces at $z=0$ and $z=L$ in the limit $n \rightarrow \infty$. Its $n=2$ analog describes ${}^4\text{He}$ fluid films near the λ -point. The model has, for general $n \geq 2$, an ordered low- T bulk ($L = \infty$) phase. For finite L , long-range order is restricted to $T=0$ since low-energy (spin wave) excitations destroy long-range order at any temperature $T > 0$. Further, the presence of confined Goldstone modes at $T=0$ implies a nonzero $T \rightarrow 0$ limit of the Casimir force. Owing to the breakdown of translation invariance along the z -direction perpendicular to the surfaces, the exact $n \rightarrow \infty$ solution does not correspond to a mean spherical model with global constraint [14], but involves a 1d Schrödinger equation with a self-consistent potential $V(z)$. The exact scaling function $\vartheta(x)$ for $n = \infty$ can be expressed in terms of the eigenvalues and eigenfunctions of this equation. Determining them by numerical means, we managed to get the extremely precise results displayed in fig. 1. Determined within a single theoretical framework, these exhibit all features (i)–(iv) mentioned above but none of the deficiencies (d1)–(d4).

⁴Throughout this work, the symbol \simeq means “asymptotically equal” in the respective limit, *e.g.*, $f(L) \simeq g(L) \Leftrightarrow \lim_{L \rightarrow \infty} f(L)/g(L) = 1$.

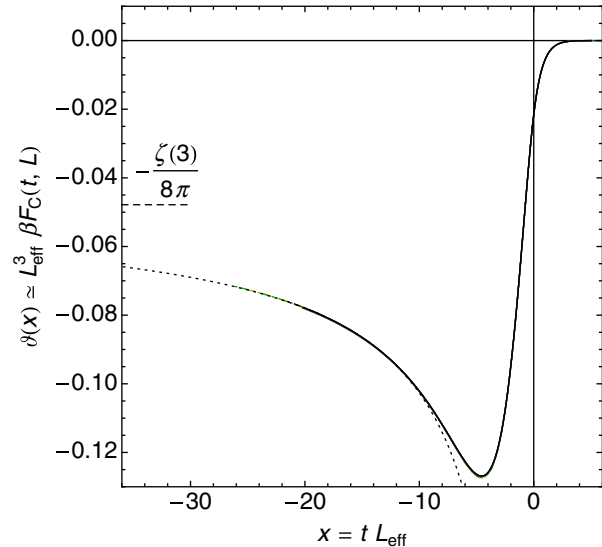


Fig. 1: (Color online) Scaling function $\vartheta(x)$ of the critical Casimir force for $L = \{65, 97, 129, 193, 257\}$ (model A, solid lines) and $L = \{97, 129, 193, 257\}$ (model B, dash-dotted lines, for model definition see text). The dashed horizontal line indicates the Goldstone value $\vartheta(-\infty) = -\zeta(3)/8\pi$, and the dotted curve represents the limiting behavior $\vartheta(x) \simeq \vartheta(-\infty) + (c \ln|x| + d)/x$, with $c = 0.07856(5)$ and $d = 0.3673(5)$. The effective thickness L_{eff} accounts for leading scaling corrections (see text). Note that deviations from the excellent data collapse are only visible under magnification.

Our best estimate for the Casimir amplitude is

$$\Delta_C = \vartheta(0)/2 = -0.01077340685024782(1). \quad (1)$$

The function $\vartheta(x)$ has a pronounced minimum $\vartheta_{\min} = -0.1268565841360(1)$ at $x_{\min} = -4.55702477008(1)$. In the low-temperature limit $x \rightarrow -\infty$, it approaches the value $-\zeta(3)/8\pi = -0.0478283245\dots$ [15] of a massless free theory with Neumann boundary conditions⁵. Using an appropriate low- T model — a nonlinear σ model on a film with Neumann boundary conditions [16] — we can show that the asymptotic behavior is of the form $\vartheta(x) - \vartheta(-\infty) \simeq c x^{-1} \ln|x|$ (see footnote ⁶).

Both the form of these logarithmic anomalies and the existence of a minimum at $x_{\min} < 0$ are intimately related to the breaking of translational invariance across the slab. To appreciate this, one should note the following. As may be gleaned from [17] and will be shown below, the exact $n \rightarrow \infty$ solution reduces to a constrained Gaussian model with an effective $\phi^2/2$ term whose interaction constant $\hat{\tau} - V(z)$ involves a self-consistent potential $V(z)$. According to [18], the $t=0$ analog of $V(z)$ for the semi-infinite case $L = \infty$ is given by $-1/4z^2$ [17]. This algebraic behavior carries over to the near-boundary behavior of $V(z)$ for $t < 0$ on scales small compared to both the

⁵Arguments similar to those used in [16] show that the low- T limit is described by a nonlinear σ model on a film with Neumann boundary conditions.

⁶Details will be published elsewhere.

Josephson coherence length $\propto |t|^{-\nu}$ and L (see footnote ⁶). By contrast, the counterpart of $V(z)$ for periodic boundary conditions is independent of z , an enormous simplification which enables one to determine the corresponding scaling function $\vartheta^{\text{pb}c}(x)$ in closed analytical form [18]. It decreases quickly and monotonically from zero to its Goldstone value $\vartheta^{\text{pb}c}(-\infty) = -\zeta(3)/\pi$, has no minimum at finite $x < 0$, and approaches the $x \rightarrow -\infty$ limit $\sim |x|e^{-|x|}$.

We next turn to an outline of the essentials of our calculations. The model is described by the Hamiltonian

$$\mathcal{H} = \int d^{d-1}y \left\{ \int_0^L dz \left[\frac{1}{2}(\nabla\phi)^2 + \frac{\hat{\tau}}{2}\phi^2 + \frac{g}{4!n}\phi^4 \right] + \frac{\hat{c}_1}{2}\phi^2(\mathbf{y}, 0) + \frac{\hat{c}_2}{2}\phi^2(\mathbf{y}, L) \right\} \quad (2)$$

with $d=3$, where $\phi = (\phi_\alpha)$ is an n -component field and $\mathbf{y} \in \mathbb{R}^{d-1}$ denotes the lateral coordinates. The boundary terms entail the boundary conditions $(\partial_z - \hat{c}_1)\phi|_{z=0}$ and $(\partial_z + \hat{c}_2)\phi|_{z=L}$.

The $n \rightarrow \infty$ limit can be derived by standard means. Upon making a Hubbard-Stratonovich transformation, the partition function $Z = \int \mathcal{D}[\phi] e^{-\mathcal{H}}$ can be written as

$$Z \propto \int \mathcal{D}[\phi] \mathcal{D}[\psi] e^{-\frac{1}{2} \int d^{d-1}y \int_0^L dz [\phi(\hat{\tau} + i\psi - \nabla^2)\phi - \frac{3n}{g}\psi^2]}, \quad (3)$$

where the Laplacian ∇^2 is subject to the above-mentioned boundary conditions. In the limit $n \rightarrow \infty$, the ψ -integral can be evaluated by saddle-point integration. Writing the saddle point as $i\psi_0(z) = V(z) - \hat{\tau}$, the reduced free energy per area $A = \int d^{d-1}y$, $f_L \equiv -(An)^{-1} \ln Z$, becomes

$$f_L = \frac{1}{2} \int_0^L dz \left\{ \int \frac{d^{d-1}p}{(2\pi)^{d-1}} \langle z | \ln(\mathbf{p}^2 - \partial_z^2 + V) | z \rangle - \frac{3}{g} [\hat{\tau} - V(z)]^2 \right\} + f_L^{(0)}, \quad (4)$$

where $f_L^{(0)}$ is a trivial background term which does not matter henceforth.

The stationarity condition $\delta f_L / \delta V(z) = 0$ yields

$$\hat{\tau} - V(z) = -\frac{g}{6} \int \frac{d^{d-1}p}{(2\pi)^{d-1}} \sum_\nu \frac{|\varphi_\nu(z)|^2}{\mathbf{p}^2 + \epsilon_\nu}, \quad (5)$$

where ϵ_ν and $\varphi_\nu(z) = \langle z | \nu \rangle$ are the eigensolutions of

$$[-\partial_z^2 + V(z)]\varphi_\nu(z) = \epsilon_\nu \varphi_\nu(z). \quad (6)$$

The \mathbf{p} -integrals on the right-hand sides of eqs. (4) and (5) are ultraviolet (UV) divergent at $d=3$. To make the model (2) well defined and suitable for numerical calculations, we must regularize these divergences. We study two distinct regularized versions of model (2). In the first (A), only the z -coordinate is discretized, and the \mathbf{p} -integrals are regularized dimensionally. In the second (B), a fully discrete lattice model is investigated.

Model A: The system consists of L layers located at $z = 1, \dots, L$, where we replace the operator ∂_z^2 in eq. (6)

by its discrete analog, the $L \times L$ matrix $\mathbf{D}^2 = (-2\delta_{z,z'} + \delta_{|z-z'|,1})$. Rather than including analogs of the boundary terms $\propto \hat{c}_j$, we impose the Dirichlet boundary conditions $\phi|_{z=0} = \phi|_{z=L+1} = \mathbf{0}$. The thickness change $L \rightarrow L+1$ is accounted for in the numerical analysis by introducing an effective thickness L_{eff} (see below). The Hamiltonian of eq. (6) becomes the matrix $\mathbf{H} = -\mathbf{D}^2 + \mathbf{V}$ with $\mathbf{V} = \text{diag}(V_z)$ (see footnote ⁷). The dimensionally regularized \mathbf{p} -integral in eq. (5) is straightforward. It produces a simple pole at $d=3$, which gets absorbed in the bulk critical value $\hat{\tau}_c$. To see this, we subtract from eq. (5) its bulk analog, making the appropriate replacements $\sum_\nu \dots |\varphi_\nu z|^2 \rightarrow \int_{-\pi}^{\pi} \frac{dk}{2\pi}$ and $\epsilon_\nu \rightarrow \epsilon(k) = r_b + 4 \sin^2(k/2)$, where r_b is the inverse bulk susceptibility. Writing $\hat{\tau} = \hat{\tau}_c + \tau$ and noting that $r_b = 0$ at $\hat{\tau}_c$, we can set $d=3$ to obtain

$$24\pi g^{-1}(\tau - V_c) = \langle z | \ln \mathbf{H} | z \rangle. \quad (7a)$$

To eliminate the UV singularities of the bulk free energy density $f_b = \lim_{L \rightarrow \infty} f_L / L$ we subtract from it its Taylor expansion to first order in τ . This gives an UV finite renormalized $f_b(\tau, g)$ which at $d=3$ becomes

$$f_b(\tau, g) = \frac{1}{8\pi} \sqrt{r_b(4+r_b)} - \frac{2+r_b}{4\pi} \text{arsinh} \sqrt{r_b/4} - \frac{3}{2g} (\tau - r_b)^2, \quad (7b)$$

where r_b is the solution to $r_b = \tau - \frac{g}{12\pi} \text{arsinh} \sqrt{r_b/4}$ or 0 depending on whether $\tau \geq 0$ or < 0 . The chosen bulk counterterms also absorb the UV singularities of f_L . Their contributions cancel in the excess free energy $f_{\text{ex}} = f_L - Lf_b$, yielding the UV finite $d=3$ result (see footnote ⁶)

$$f_{\text{ex}}(\tau, g, L) = \frac{1}{8\pi} \text{tr}[\mathbf{H}(1 - \ln \mathbf{H})] - \frac{3}{2g} \text{tr}[(\tau - \mathbf{V})^2] - Lf_b(\tau, g). \quad (7c)$$

Solving eq. (7a) numerically first for $\tau=0$, we compute $f_{\text{ex}}(0, g, L)$ to determine the surface free energy $f_s(0, g) = f_{\text{ex}}(0, g, \infty)/2$ and the Casimir amplitude $\Delta_C \equiv \lim_{L \rightarrow \infty} L^2 [f_{\text{ex}}(0, g, L) - 2f_s(0, g)]$. To extract precise values from the data, knowledge about corrections to scaling is important. Clearly, the usual Wegner corrections governed by the $n \rightarrow \infty$ exponent $\omega = 4 - d$ must be expected. Further, deviations from asymptotic Dirichlet boundary conditions are known to be described by irrelevant surface scaling fields $\lambda_j \propto 1/\hat{c}_j$ (“extrapolation lengths”) that scale naively [20,21], so that their correction-to-scaling exponent is $\omega_\lambda = 1$. Noting the degeneracy $\omega = \omega_\lambda = 1$ at $d=3$, standard RG considerations can be used to show that leading corrections to scaling $\propto L^{-1} \ln L$ along with those $\propto L^{-1}$ should occur for the effective amplitude $\tilde{\Delta}_C(g, L) \equiv L^2 [f_{\text{ex}}(0, g, L) - 2f_s(0, g)]$. As can be seen from the results for Δ_C depicted in fig. 2, convergence is very poor when g is small, *e.g.*,

⁷A preliminary analysis of the critical case was made in [19].

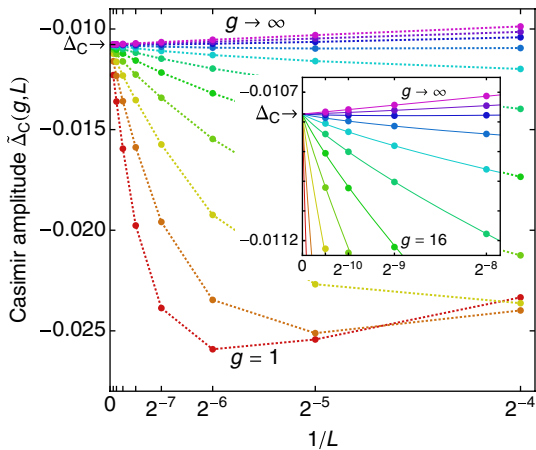


Fig. 2: (Color online) Effective Casimir amplitude $\tilde{\Delta}_C(g, L)$ for different values of $g = \{1, 2, 4, \dots, 512, \infty\}$. The solid lines are fits including corrections $\propto L^{-1} \ln L$, which vanish as $1/g$ for $g \rightarrow \infty$ (see text). The dotted lines are guides to the eyes.

for $g=1$. Relying on the results for $\tilde{\Delta}_C(1, L \lesssim 64)$, one could easily infer an incorrect value of $-0.026(1)$ for Δ_C , more than twice as large as the correct asymptotic one $\tilde{\Delta}_C(1, \infty) = -0.0108(1)$, see fig. 2. Convergence is far better for $g \gg 1$, as the minimum in $\tilde{\Delta}_C$ is at $L_{\min} \approx 80/g$. Fast convergence and high precision can be achieved by solving eqs. (7) with $\tau=0$ and g set to its fixed-point value⁸ $g^* = \infty$, where the corrections $\propto L^{-1} \ln L$ vanish.

To extend this $g \rightarrow \infty$ analysis to $\tau \neq 0$, we note that the critical exponent $\nu=1$ and absorb the amplitude $\xi_+(g) = g/24\pi$ of the bulk correlation length $\xi_b^{(+)} = r_b^{-1/2} \simeq \xi_+ \tau^{-\nu}$ for $T > T_c$ in the temperature variable, defining $t = \tau/\xi_+(g)$ so that the scaling variable becomes $x = tL$. In this limit, eqs. (1) reduce to

$$t = \langle z | \ln \mathbf{H} | z \rangle, \quad (8a)$$

$$f_b(t) = \frac{1}{4\pi} \begin{cases} \sinh t - t, & \text{for } t \geq 0, \\ 0, & \text{for } t < 0, \end{cases} \quad (8b)$$

$$f_{\text{ex}}(t, L) = \frac{1}{8\pi} \text{tr}[\mathbf{H}(1+t - \ln \mathbf{H})] - \frac{tL}{4\pi} - Lf_b(t). \quad (8c)$$

From eqs. (8) we calculate the Casimir force $\beta\mathcal{F}_C(t, L) = -\partial f_{\text{ex}}(t, L)/\partial L \approx -[f_{\text{ex}}(t, L+1) - f_{\text{ex}}(t, L-1)]/2$. To achieve the excellent data collapse shown in fig. 1, it turns out to be sufficient to write $\vartheta(x) \simeq L_{\text{eff}}^3 \beta\mathcal{F}_C(t, L)$, introducing an effective thickness $L_{\text{eff}} = L + \delta L$, as proposed in [23] and substantiated by field theory [20].

Inspection of eq. (8a) reveals that the scaled lowest eigenvalue $\epsilon_0 L^2$ is positive for all x and vanishes $\sim |x|e^{-|x|}$ as $x \rightarrow -\infty$. That is, for finite $L < \infty$, the system remains

⁸Recall that the bulk analog of the integral in eq. (5) contains a regularization-dependent term, which reads $-a(d)r_b$ in the notation of ref. [22]. Its coefficient $a(d)$ may be identified as $1/g^*$ if $a(d) > 0$. For our regularization method A, $a(d) = 0$ as $n \rightarrow \infty$, so that $g^* = \infty$. For method B, $a(d) < 0$. Hence no infrared-stable $g^* > 0$ exists and corrections to scaling cannot be suppressed in this manner; cf. ref. [22], sect. 2.4.

paramagnetic whenever $T > 0$, due to the nonperturbative generation of a mass. Furthermore, the remaining eigenvalues $\epsilon_{\nu > 0}$ approach the Neumann values.

The numerical calculations are performed with 33 digits precision. This yields about 30 significant digits in f_{ex} . For the effective thickness the form $L_{\text{eff}} = L + \delta L + \sum_{i=1}^m b_i L^{-i}$ is chosen. The estimates of Δ_C and δL are then determined by analyzing $f_{\text{ex}}(0, L)$ for $L = 1600, 1800, \dots, 3800$ and $L = 4096$ with the ansatz $f_{\text{ex}}(0, L) = 2f_s(0) + \Delta_C L_{\text{eff}}^{-2}$. Our final results, eq. (1) and $\delta L = 0.7255032704723(3)$, are obtained using $m = 5$. As benchmark for the errors, the variations of the estimates resulting from analogous analyses with $m = 4$ and different choices of thicknesses L are used.

Model B: A simple cubic lattice model of sites $\mathbf{x} \equiv (\mathbf{y}, z) \in \mathbb{Z}^d$ with $x_i = 1, \dots, N_i$ is considered whose Hamiltonian follows from eq. (2) through the replacements $\int d^{d-1}y \int_0^L dz \rightarrow \sum_{\mathbf{x}}$ and $(\nabla\phi)^2 \rightarrow \sum_{i=1}^d |\phi(\mathbf{x}) - \phi(\mathbf{x} + \mathbf{e}_i)|^2$, where \mathbf{e}_i are unit vectors along the principal axes. Along the z -direction, Dirichlet boundary conditions are again imposed; along all y_i -directions, periodic boundary conditions $\phi_{\mathbf{y}} \equiv \phi_{\mathbf{y} + N_i \mathbf{e}_i}$ are chosen and the limits $N_{i < d} \rightarrow \infty$ taken at fixed $L \equiv N_d$. Just as in model A, the operator ∂_z^2 in eqs. (4) and (6) is replaced by its discrete analog \mathbf{D}^2 . Owing to the discreteness of the lattice, the momentum integrations are restricted to $|p_i| \leq \pi$. Further, to account for the modified dispersion relation, $4 \sum_{i=1}^{d-1} \sin^2(p_i/2)$ must be substituted for \mathbf{p}^2 . Thus the \mathbf{p} -integral of each series coefficient of the spectral sum \sum_{ν} in eq. (5) becomes an analytically computable ϵ_{ν} -dependent two-dimensional Watson integral. Its three-dimensional bulk analog can also be determined analytically [24], along with their antiderivatives one encounters in the analogous momentum integrals of the right-hand side of eq. (4).

For model B no fixed-point value $g^* > 0$ exists to which g could be set to eliminate leading scaling corrections [22]. Thus, scaling corrections $\propto L^{-1} \ln L$ remain for any value of g . However, the amplitudes of these corrections become minimal in the limit $g \rightarrow \infty$. We use $L_{\text{eff}} = L + a_0 \ln L + \delta L + \sum_{i=1}^m (a_i \ln L + b_i) L^{-i}$ with $m = 3$ to analyse $f_{\text{ex}}(0, L)$, which we computed for various thicknesses up to $L = 4096$. We reproduce the value (1) for the Casimir amplitude to 13 significant digits—a striking confirmation of universality. Furthermore, we get $a_0 = -0.123903101(1)$ and $\delta L = 0.81422072(1)$. Analyzing our data also at the minimum of the thermodynamic Casimir force, we obtain results for x_{\min} and ϑ_{\min} that are fully consistent with those obtained from model A. The value of a_0 is consistent with the one obtained above from the analysis of $f_{\text{ex}}(0, L)$. However, we get $\delta L = 1.1979(1)$ and $\delta L = 0.8924(1)$ from the location and the value of the minimum of the thermodynamic Casimir force, respectively. The plot of ϑ in fig. 1 uses $L_{\text{eff}} = L - 0.1239031 \ln L + 1$, which results in a good data collapse. However, we should keep in mind that this way corrections $\propto L^{-1}$ cannot be eliminated completely for the whole range of the scaling argument x .

Finally, let us comment on the stability of our results with respect to a change of boundary conditions, as investigated recently in [25]. For both models A and B, the nearest-neighbor (NN) bonds βJ_j in the two boundary layers $j=1$ and $j=L$ were chosen to agree with the NN bonds βJ in all other layers. Allowing for boundary couplings⁹ J_1 and $J_L \neq J$, one can change the corresponding diagonal elements of \mathbf{D}^2 . However, this change is compensated by a corresponding change of the potential \mathbf{V} . As expected for $d=3$, the self-consistent solutions remain asymptotically the same.

In summary, considering the $O(n)$ vector model on a slab with free boundary conditions, we expressed its universal scaling function for the Casimir force in the limit $n \rightarrow \infty$ exactly in terms of the eigensystem of the resulting self-consistent 1d Schrödinger equation, which we then solved by numerical means using two qualitatively distinct regularization methods. We obtained consistent results that agree with many digits. They exhibit all qualitative features (i)–(iv) one expects to hold for general $n \geq 2$, in particular, nontrivial crossovers from three-dimensional critical to two-dimensional pseudo-critical behavior and to the low-temperature behavior dictated by confined Goldstone modes¹⁰: Besides being interesting in their own right, these results could pave the way to successful approximate analytical treatments of such challenging problems. We expect them to play a role as fruitful as large- n solutions have done in the theory of quantum-critical phenomena [28]. Furthermore, our analysis can be extended in a straightforward fashion to include bulk and surface magnetic fields and to study appropriate quantum versions of the model.

Some of us (DG, AH, FMS) would like to thank DENIS COMTESSE for fruitful discussions. We gratefully acknowledge partial support by DFG for two of us (HWD and FMS) via grant DI 378/5 and for one of us (MH) via grant HA 3150/2-2. SBR was partially supported by the Belarusian Foundation for Fundamental Research.

REFERENCES

- [1] CASIMIR H. B. G., *Proc. K. Ned. Akad. Wet. B*, **51** (1948) 793.
- [2] BORDAG M., MOHIDEEN U. and MOSTEPANENKO V. M., *Phys. Rep.*, **353** (2001) 1.
- [3] FISHER M. E. and DE GENNES P.-G., *C. R. Séances Acad. Sci. Sér. B*, **287** (1978) 207.
- [4] KRECH M., *Casimir Effect in Critical Systems* (World Scientific, Singapore) 1994; BRANKOV J. G., DANTCHEV D. M. and TONCHEV N. S., *Theory of Critical Phenomena in Finite-Size Systems – Scaling and Quantum Effects* (World Scientific, Singapore) 2000; GAMBASSI A., *J. Phys.: Conf. Ser.*, **161** (2009) 012037.
- [5] KLIMCHITSKAYA G. L., MOHIDEEN U. and MOSTEPANENKO V. M., *Rev. Mod. Phys.*, **81** (2009) 1827.
- [6] KARDAR M. and GOLESTANIAN R., *Rev. Mod. Phys.*, **71** (1999) 1233.
- [7] GARCIA R. and CHAN M. H. W., *Phys. Rev. Lett.*, **83** (1999) 1187; GANSHIN A., SCHEIDEMANTEL S., GARCIA R. and CHAN M. H. W., *Phys. Rev. Lett.*, **97** (2006) 075301.
- [8] HERTLEIN C., HELDEN L., GAMBASSI A., DIETRICH S. and BECHINGER C., *Nature*, **451** (2008) 172.
- [9] HUCHT A., *Phys. Rev. Lett.*, **99** (2007) 185301.
- [10] VASILYEV O., GAMBASSI A., MACIOLEK A. and DIETRICH S., *EPL*, **80** (2007) 60009.
- [11] HASENBUSCH M., *J. Stat. Mech.: Theory Exp.* (2009) P07031; HASENBUSCH M., *Phys. Rev. B*, **81** (2010) 165412.
- [12] ZANDI R., SHACKELL A., RUDNICK J., KARDAR M. and CHAYES L. P., *Phys. Rev. E*, **76** (2007) 030601.
- [13] MACIOLEK A., GAMBASSI A. and DIETRICH S., *Phys. Rev. E*, **76** (2007) 031124.
- [14] KNOPS H. J. F., *J. Math. Phys.*, **14** (1973) 1918.
- [15] LI H. and KARDAR M., *Phys. Rev. A*, **46** (1992) 6490.
- [16] DIEHL H. W. and NÜSSER A., *Phys. Rev. Lett.*, **56** (1986) 2834; DIEHL H. W., *Phys. Lett. A*, **75** (1980) 375.
- [17] BRAY A. J. and MOORE M. A., *J. Phys. A*, **10** (1977) 1927.
- [18] DANCHEV D. M., *Phys. Rev. E*, **58** (1998) 1455.
- [19] COMTESSE D., Diplomarbeit, Universität Duisburg-Essen (2008); COMTESSE D., HUCHT A. and GRÜNEBERG D., arXiv:0904.3661v2.
- [20] DIEHL H. W., DIETRICH S. and EISENRIEGLER E., *Phys. Rev. B*, **27** (1983) 2937.
- [21] DIEHL H. W., in *Phase Transitions and Critical Phenomena*, edited by DOMB C. and LEBOWITZ J. L., Vol. **10** (Academic Press, London) 1986, pp. 75–267; *Int. J. Mod. Phys. B*, **11** (1997) 3503.
- [22] MOSHE M. and ZINN-JUSTIN J., *Phys. Rep.*, **385** (2003) 69.
- [23] CAPEHART T. W. and FISHER M. E., *Phys. Rev. B*, **13** (1976) 5021.
- [24] JOYCE G. S. and ZUCKER I. J., *J. Phys. A*, **34** (2001) 7349.
- [25] SCHMIDT F. M. and DIEHL H. W., *Phys. Rev. Lett.*, **101** (2008) 100601; DIEHL H. W. and SCHMIDT F. M., *New J. Phys.*, **13** (2011) 123025.
- [26] HASENBUSCH M., *J. Stat. Mech.: Theory Exp.* (2009) P02005.
- [27] HUCHT A., GRÜNEBERG D. and SCHMIDT F. M., *Phys. Rev. E*, **83** (2011) 051101.
- [28] SACHDEV S., *Quantum Phase Transitions*, 2nd edition (Cambridge University Press, Cambridge, UK) 2011.

⁹A sc lattice model of type B with boundary bonds $J_1 \neq J$ and $J_L \neq J$ can be mapped approximately onto the continuum field theory (2) with $c_1 = 1 - 2(d-1)(J_1/J - 1)$ and $c_2 = 1 - 2(d-1)(J_L/J - 1)$ ([21], p. 92.)

¹⁰In the $O(2)$ case, a Kosterlitz-Thouless transition occurs at a temperature T_{KT} ([26] and references therein), which is the inflection point below the location of the minimum of the Casimir force, cf. [27]. This is absent when $n > 2$ and hence for $n \rightarrow \infty$. For $n = 2$, it is barely detectable in ϑ ; see refs. [9,11].

Sheared Ising models in three dimensions

ALFRED HUCHT and SEBASTIAN ANGST

Fakultät für Physik, Universität Duisburg-Essen - D-47048 Duisburg, Germany, EU

received 17 July 2012; accepted in final form 22 September 2012

published online 29 October 2012

PACS 05.70.Ln – Nonequilibrium and irreversible thermodynamics

PACS 68.35.Af – Atomic scale friction

PACS 05.50.+q – Lattice theory and statistics (Ising, Potts, etc.)

Abstract – The nonequilibrium phase transition in sheared three-dimensional Ising models is investigated using Monte Carlo simulations in two different geometries corresponding to different shear normals. We demonstrate that in the high shear limit both systems undergo a strongly anisotropic phase transition at exactly known critical temperatures T_c which depend on the direction of the shear normal. Using dimensional analysis, we determine the anisotropy exponent $\theta = 2$ as well as the correlation length exponents $\nu_{\parallel} = 1$ and $\nu_{\perp} = 1/2$. These results are verified by simulations, though considerable corrections to scaling are found. The correlation functions perpendicular to the shear direction can be calculated exactly and show Ornstein-Zernike behavior.

Copyright © EPLA, 2012

Introduction. – While the occurrence of nonequilibrium phase transitions is ubiquitous in nature, its investigation in the framework of nonequilibrium statistical mechanics is intricate and restricted to a few simple models, like the driven lattice gas (DLG) [1–3] or, recently, to the driven two-dimensional Ising model [4]. In this model the system is cut into two halves parallel to one axis and moved along this cut with velocity v . The model exhibits energy dissipation and subsequently friction due to spin correlations, which also occurs in a suitable Heisenberg model [5–8] and, of interest for the current context, undergoes a nonequilibrium phase transition from an ordered low-temperature phase to a disordered high-temperature phase. This transition has been investigated analytically as well as with Monte Carlo (MC) simulations for various geometries [9]. Since then, this model has been generalized to the driven Potts models [10], and finite-size effects were calculated analytically in the driven Ising chain [11].

A lot of similarities and comparable critical behavior between the Ising model with friction and the very famous and well-investigated DLG have been found [12]. Both models are characterized by a critical temperature T_c , which increases with the external drive, which is the field or the shift/shear velocity v , respectively, and saturates in the high driving limit. The critical temperature has been calculated analytically in the limit $v \rightarrow \infty$ for various geometries of the Ising model with friction [9].

Moreover, it was discovered that the DLG and two-dimensional sheared Ising systems with non-conserved

order parameter [12–14] show strongly anisotropic critical behavior, with direction-dependent correlation length exponents ν_{\parallel} and ν_{\perp} . For the 2d and 1+1d geometry of the Ising model with shear the same exponents $\nu_{\parallel} = 3/2$ and $\nu_{\perp} = 1/2$ [12] as in the two-dimensional DLG have been determined. Additionally, finite velocities v have been studied and it was found that for all finite v the 2d model and 1+1d model cross over from isotropic Ising-like behavior to strongly anisotropic mean-field behavior in the thermodynamic limit, demonstrating that the external drive is a relevant perturbation.

In the following we shall extend the investigations to a three-dimensional model with two different shear geometries and focus on the high shear velocity limit $v \rightarrow \infty$. This three-dimensional model is experimentally accessible in the framework of sheared binary liquids [15–18], albeit the order parameter is not conserved here. Using dimensional analysis, we predict the correlation length exponents for arbitrary dimension d . These predictions are verified by simulations; however we find strong corrections to scaling at small system sizes.

Model. – The systems considered in this work are denoted 2+1d and 1+2d and are shown in fig. 1, for a classification see ref. [9]. In the 2+1d geometry shear is applied such that two-dimensional Ising models are moved relative to their upper (lower) neighboring layer with velocity v ($-v$) along one axis. In the following we denote the direction parallel to the shear with \parallel , the direction perpendicular to the planes with \perp_1 and the

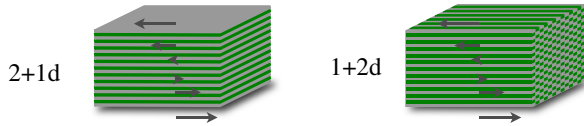


Fig. 1: (Colour on-line) Sketches of the systems considered in this work. On the left-hand side the 2+1d system and on the right-hand side the 1+2d system are shown. The gray regions represent the magnetic systems and the green (dark) regions are the moving boundaries, while the arrows indicate the motion of the subsystems.

inplane direction perpendicular to the shear direction with \perp_2 . The model contains $L_{\perp_1} \times L_{\perp_2} \times L_{\parallel}$ spins (lattice sites), where we choose $L_{\perp_1} = L_{\perp_2} =: L_{\perp}$ throughout this work, and periodic boundary conditions are applied in all directions. The shear velocity v corresponds to a shear rate, which is often denoted as $\dot{\gamma}$ [13,14]. Using the notation $(\perp_1 \perp_2 \parallel)$ for directions, the shear is in (001)-direction and the shear normal is in (100)-direction.

A finite shear velocity v is implemented by shifting neighboring layers v times by one lattice constant during one MC step (for details see [4,9]). A simplification of the implementation is yielded by reordering the couplings between moved layers instead, and by introducing a time-dependent displacement $\Delta(t) = vt$. Hence we get the Hamiltonian

$$\beta\mathcal{H}(t) = - \sum_{k=1}^{L_{\perp_1}} \sum_{l=1}^{L_{\perp_2}} \sum_{m=1}^{L_{\parallel}} \sigma_{klm} \left(K_{\parallel} \sigma_{k,l,m+1} + K_{\perp_2} \sigma_{k,l+1,m} + K_{\perp_1} \sigma_{k+1,l,m+\Delta(t)} \right), \quad (1)$$

where $K_{\mu} = \beta J_{\mu}$ is the reduced nearest-neighbor coupling with $\mu = \{\perp_1, \perp_2, \parallel\}$, and $\beta = 1/k_{\text{B}}T$. In the following we shall concentrate on the infinite shear velocity limit $v \rightarrow \infty$, which can easily be implemented by choosing $1 \leq \Delta(t) \leq L_{\parallel}$ randomly. In this limit an analytical calculation [9] yield the equation

$$\chi_{\text{eq}}^{(0)}(K_{c,\parallel}) f \tanh K_{c,\perp} = 1, \quad (2)$$

from which we can determine the critical temperature, where $\chi_{\text{eq}}^{(0)}$ is the zero-field equilibrium susceptibility of the subsystems moved relative to each other and f the number of fluctuating adjacent fields. Here $\chi_{\text{eq}}^{(0)}$ of the two-dimensional Ising model is required, which has been calculated to higher than 2000th order by a polynomial algorithm [19]. Using $f = 2$ and $J_{\parallel} = J_{\perp_1} = J_{\perp_2} = 1$ we get

$$T_c^{2+1d}(\infty) = 5.2647504145147435505980 \dots \quad (3)$$

The second considered geometry 1+2d is similar to the previous case, but now the shear normal is in the (110)-direction. As a consequence, all four perpendicular

coupling partners of a spin σ are in neighboring shear planes. The corresponding Hamiltonian reads

$$\beta\mathcal{H}(t) = - \sum_{k=1}^{L_{\perp_1}} \sum_{l=1}^{L_{\perp_2}} \sum_{m=1}^{L_{\parallel}} \sigma_{klm} \left(K_{\parallel} \sigma_{k,l,m+1} + K_{\perp} [\sigma_{k,l+1,m+\Delta(t)} + \sigma_{k+1,l,m+\Delta(t)}] \right), \quad (4)$$

where $K_{\perp_1} = K_{\perp_2} =: K_{\perp}$. For $v \rightarrow \infty$ we set $f = 4$ and use $\chi_{\text{eq}}^{(0)}(K_{c,\parallel}) = e^{2K_{c,\parallel}}$ from the one-dimensional Ising model in eq. (2) to get, for $J_{\parallel} = J_{\perp} = 1$, the critical temperature

$$T_c^{1+2d}(\infty) = \frac{2}{\ln[\frac{1}{8}(5 + \sqrt{41})]} = 5.642611138 \dots, \quad (5)$$

which notably is different from eq. (2). Hence the critical temperature depends on the direction of the shear normal.

Finally we comment on the simulation method: in MC simulations of nonequilibrium models the critical temperature often depends on the used acceptance rates [20]. It has been shown that the multiplicative rate [9]

$$p_{\text{flip}}(\Delta E) = e^{-\frac{\beta}{2}(\Delta E - E_{\text{min}})} \quad (6)$$

with the energy change ΔE and the minimal energy change $\Delta E_{\text{min}} = \min\{\Delta E\}$ must be used in order to reproduce the critical temperatures, eqs. (3) and (5).

Anisotropic scaling. – Our aim is to prove that both models exhibit a strongly anisotropic phase transition and calculate the corresponding exponents. Such a phase transition is characterized by bulk correlation lengths ξ_{μ} diverging with direction-dependent critical exponents ν_{μ} at criticality¹,

$$\xi_{\mu}(t) \stackrel{t \rightarrow 0}{\simeq} \hat{\xi}_{\mu} t^{-\nu_{\mu}}, \quad (7)$$

with direction $\mu = \{\perp_1, \perp_2, \parallel\}$, amplitude $\hat{\xi}_{\mu}$, and reduced critical temperature $t = T/T_c - 1$. Usually one defines the anisotropy exponent $\theta = \nu_{\parallel}/\nu_{\perp}$, which is $\theta = 1$ for isotropic scaling and $\theta \neq 1$ for strongly anisotropic scaling [2,21–24]. As mentioned above, the phase transitions of the Ising model with shear in the 2d geometry and the 1+1d geometry become strongly anisotropic for $v > 0$ in the thermodynamic limit, with $\theta = 3$ [12].

In ref. [12] it was shown that the application of a stripe geometry $L_{\perp} \rightarrow \infty$ with finite L_{\parallel} is an appropriate way to determine the anisotropy exponent and subsequently the correlation length exponents. Hence we measure the perpendicular correlation function

$$G_{\perp}(L_{\parallel}; \mathbf{r}_{\perp}) = \langle \sigma_{000} \sigma_{r_{\perp_1}, r_{\perp_2}, 0} \rangle \quad (8)$$

at the critical point T_c , from which we can determine the correlation lengths ξ_{μ} with $\mu = \{\perp_1, \perp_2\}$ as shown below (in the following the index μ only represents

¹Throughout this work the symbol \simeq means “asymptotically equal” in the respective limit, e.g., $f(L) \simeq g(L) \Leftrightarrow \lim_{L \rightarrow \infty} f(L)/g(L) = 1$.

the perpendicular directions \perp_1 and \perp_2). Note that by symmetry $G_{\perp}(L_{\parallel}, r_{\perp_1}) = G_{\perp}(L_{\parallel}, r_{\perp_2})$ for the 1+2d system. From ξ_{μ} we can then determine θ using the relation [23,25]

$$\xi_{\mu}(L_{\parallel}) \simeq A_{\mu} L_{\parallel}^{1/\theta}. \quad (9)$$

The above-mentioned stripe geometry is a film geometry in three dimensions, and we choose $L_{\perp}/\xi_{\perp}(L_{\parallel}) \gtrsim 10$ sufficient for our purpose [12].

Dimensional analysis. – For $v \rightarrow \infty$ it was shown in ref. [9] that the 1+1d model can be mapped onto an *equilibrium* system consisting of one-dimensional chains that only couple via fluctuating magnetic fields. Now we generalize these ideas to a d -dimensional driven system. Due to the film geometry with confining length L_{\parallel} and the periodic boundary conditions in parallel direction the magnetization $m(\mathbf{x})$ with $\mathbf{x} = (\mathbf{x}_{\perp}, x_{\parallel})$ is homogeneous in this direction, and parallel correlations are irrelevant. Hence we can use the zero-mode approximation in this direction, leading to an order parameter $m = m(\mathbf{x}_{\perp})$ only.

The resulting Ginzburg-Landau-Wilson (GLW) Hamiltonian

$$\beta\mathcal{H} = L_{\parallel} \int dx_{\perp}^{d-1} \left(\frac{t}{2} m^2 + \frac{1}{2} (\nabla m)^2 + \frac{u}{4!} m^4 \right) \quad (10)$$

cannot, however, be mapped onto a Schrödinger equation for systems with $d > 2$ as done in ref. [12], as the $(d-1)$ -dimensional integral cannot be interpreted as a time integral. Instead we use dimensional analysis in order to predict the critical exponents: starting from the GLW Hamiltonian (10) in d dimensions we eliminate L_{\parallel} with the substitution

$$m \rightarrow \tilde{m} L_{\parallel}^{-1/(5-d)}, \quad (11a)$$

$$\mathbf{x}_{\perp} \rightarrow \tilde{\mathbf{x}} L_{\parallel}^{1/(5-d)}, \quad (11b)$$

$$t \rightarrow \tilde{t} L_{\parallel}^{-2/(5-d)} \quad (11c)$$

to get the $(d-1)$ -dimensional Hamiltonian

$$\beta\mathcal{H} = \int d\tilde{x}^{d-1} \left(\frac{\tilde{t}}{2} \tilde{m}^2 + \frac{1}{2} (\nabla \tilde{m})^2 + \frac{u}{4!} \tilde{m}^4 \right), \quad (12)$$

with $\tilde{m} = \tilde{m}(\tilde{\mathbf{x}})$, where quantities in the $(d-1)$ -dimensional system are denoted by a tilde. From eqs. (11b) and (11c) we directly read off² the exponents

$$\theta = 5 - d, \quad \nu_{\parallel} = \frac{5-d}{2} \Rightarrow \nu_{\perp} = \frac{1}{2}, \quad (13)$$

reproducing the results for $d=1$ [9] and $d=2$ [12] and fulfilling the generalized hyperscaling relation [26]

$$\nu_{\parallel} + (d-1)\nu_{\perp} = 2 - \alpha \quad (14)$$

²Note that $\tilde{\mathbf{x}} = \mathbf{x}_{\perp}/L_{\parallel}^{1/\theta}$, $\tilde{t} = tL_{\parallel}^{1/\nu_{\parallel}}$, and $\theta = \nu_{\parallel}/\nu_{\perp}$.

with $\alpha = 0$ [9,12]. For our case $d=3$ we find

$$\theta = 2, \quad \nu_{\parallel} = 1, \quad \nu_{\perp} = \frac{1}{2}, \quad (15)$$

while for $d \geq 4$ we predict isotropic or weakly anisotropic behavior with $\theta = 1$ and $\nu_{\parallel} = \nu_{\perp} = 1/2$, as then the upper critical dimension $d_c = 4$ is reached and the shear becomes an irrelevant perturbation.

Correlation functions. – The perpendicular correlation function can be calculated from eq. (12) using a Gaussian approximation, which is valid, since we investigate the system at the critical temperature of the bulk, which is higher than the critical temperature of the studied film geometry. Setting $u=0$ in eq. (12) and using $\tilde{\xi} \propto \tilde{t}^{-1/2}$ we get the Ornstein-Zernike structure factor

$$\tilde{S}(\tilde{\mathbf{k}}) \propto \frac{1}{\tilde{k}^2 + \tilde{\xi}^{-2}}. \quad (16)$$

In our case the dimension is $d-1=2$, and a Fourier transformation yields the correlation function

$$\tilde{G}(\tilde{\mathbf{r}}) \propto K_0(\tilde{r}/\tilde{\xi}), \quad (17)$$

with modified Bessel function of the second kind K_0 . Using $\tilde{G} \propto \tilde{m}^2$ and back-substituting with eqs. (11) gives the result

$$G(L_{\parallel}; \mathbf{r}_{\perp}) \propto L_{\parallel}^{-1/\nu_{\parallel}} K_0[r_{\perp}/\xi_{\perp}(L_{\parallel})] \quad (18)$$

for the perpendicular correlation function of the GLW Hamiltonian (10).

The 2+1d geometry is weakly anisotropic in perpendicular direction at least for different couplings $J_{\perp_1} \neq J_{\perp_2}$, *i.e.*, the correlation lengths ξ_{\perp_1} and ξ_{\perp_2} have the same exponent ν_{\perp} but different amplitudes $\hat{\xi}_{\mu}$ [23]. This anisotropy can be removed by the rescaling

$$l_{\mu} \rightarrow \bar{l}_{\mu} = \frac{l_{\mu}}{A_{\mu}}, \quad (19)$$

with amplitude A_{μ} from eq. (9). Now the perpendicular directions are isotropic and we can use eq. (18) to get the final result

$$G_{\perp}(L_{\parallel}; r_{\mu}) \simeq \hat{G} L_{\parallel}^{-1/\nu_{\parallel}} K_0[r_{\mu}/\xi_{\mu}(L_{\parallel})]. \quad (20)$$

Here we already have back-substituted with eq. (19). Note that especially in the 2+1d case the amplitude \hat{G} should not depend on the direction μ .

Results. – We measured $G_{\perp}(L_{\parallel}; r_{\mu})$ at criticality for both models using extensive Monte Carlo simulations and fitted the results against eq. (20) to get $\xi_{\mu}(L_{\parallel})$ shown in fig. 2. Similar to the 1+1d case we find corrections to scaling for $L_{\parallel} \lesssim 300$ which are problematic in these three-dimensional cases, as we cannot³ simulate systems

³Remember that L_{\parallel} is the confining length and that $L_{\perp} \gtrsim 10\xi_{\perp}(L_{\parallel})$ (see above), leading to system sizes up to $128 \times 128 \times 1024$ which took ≈ 1 CPU year on an Opteron cluster for the required 3×10^6 MC sweeps.

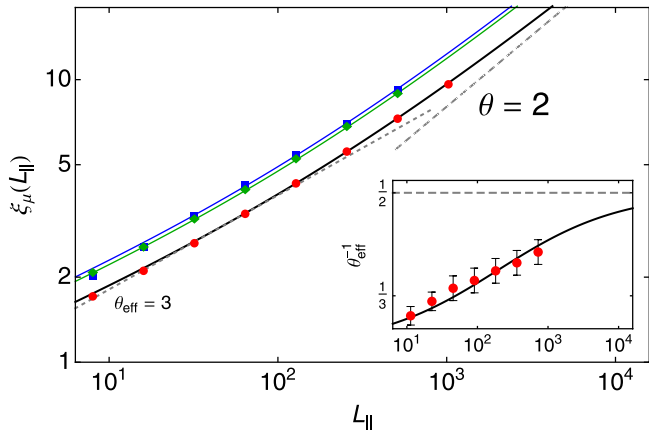


Fig. 2: (Colour on-line) Perpendicular correlation lengths $\xi_\mu(L_\parallel)$ for the 1 + 2d geometry (red circles), the 2 + 1d geometry in the \perp_1 -direction (green diamonds) and in the \perp_2 -direction (blue squares) at criticality. The statistical error is smaller than the symbol size. Due to corrections to scaling, small systems have effective anisotropy exponent $\theta_{\text{eff}} \approx 3$ (dotted line), which is obtained from the logarithmic derivative and shown exemplary for system 1 + 2d in the inset.

Table 1: Amplitudes and corrections to scaling parameter c_0 for both models.

Model	μ	A_μ	\hat{G}	c_0
1 + 2d	\perp	0.254(5)	0.93(1)	14(1)
	\perp_1	0.320(5)	0.85(1)	12(1)
2 + 1d	\perp_2	0.331(5)	0.85(1)	12(1)

larger than $L_\parallel = 1024$. Hence we have to introduce a lattice correction term in the perpendicular correlation length and improve relation (9) using the *ansatz*

$$\xi_\mu(L_\parallel) = A_\mu (L_\parallel + c_0 L_\parallel^{1/2} + \dots)^{1/\theta} \quad (21)$$

with $\theta = 2$, which gives the best fit to the data. From the numerical data we find the amplitudes A_μ and \hat{G} as well as the correction parameter c_0 listed in table 1, and the resulting fit is shown as a solid line in fig. 2. For large systems the curve approaches the theoretical limit, eq. (9), with slope $\theta^{-1} = 1/2$. Note that for $L_\parallel \lesssim 64$ we could also find a reasonable data collapse with exponent $\theta_{\text{eff}} = 3$ (dotted line).

The resulting rescaled correlation functions for both models are presented in fig. 3. In all cases the data can be rescaled with L_\parallel as predicted, without notable corrections, to obtain a convincing data collapse onto the mean-field correlation function $K_0(r/\xi)$ from eq. (20). For small distances $r_{\perp_2} = \mathcal{O}(1)$ the correlation function $G_\perp(L_\parallel; r_{\perp_2})$ differs from eq. (20) due to the inplane nearest-neighbor interactions.

Now we comment on the four-dimensional geometry 1+3d, which decouples to a three-dimensional array of

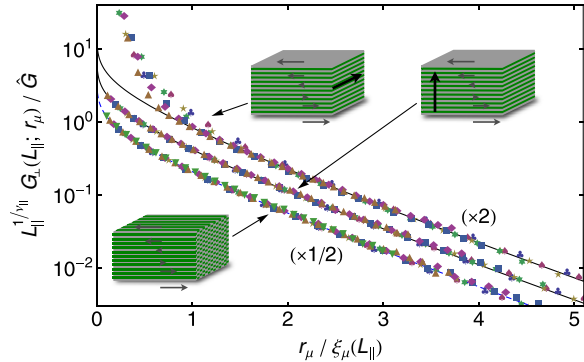


Fig. 3: (Colour on-line) Rescaled correlation function $G_\perp(L_\parallel; r_\mu)$ with $\mu = \{\perp, \perp_1, \perp_2\}$ for both models at criticality. We show varying system extensions $L_\parallel = \{8, 16, 32, 64, 128, 256, 512, 1024\}$ for both cases. A rescaling of the abscissa with $\xi_\mu(L_\parallel)$ and of the ordinate with L_\parallel results in an excellent data collapse, verifying $\theta = 2$ and $\nu_\parallel = 1$. The solid lines represent the calculated Ornstein-Zernike correlation function, eq. (20). Note that we multiplied the collapsed data by different factors as indicated in order to show them in one plot.

interacting chains, with $f = 6$ in eq. (2). We performed test simulations for system sizes up to $32^3 \times 32$ and found very strong, possibly logarithmic corrections to scaling. From the scaling behavior of the available data we estimate that system sizes $L_\parallel, L_\perp \gtrsim 1000$ would be required to find the correct scaling behavior.

Finally, we extend the dimensional analysis to the general case of a d -dimensional hyper-cubic sheared lattice with d_\parallel driven dimensions and d_\perp perpendicular dimensions. We again must distinguish between the d_{\perp_1} dimensions normal to the shear and d_{\perp_2} “inplane” dimensions without shear motion, with $d_\perp = d_{\perp_1} + d_{\perp_2}$. The critical temperature T_c at infinite shear velocity v is given by eq. (2), with the equilibrium zero-field susceptibility $\chi_{\text{eq}}^{(0)}$ of the d_{eq} -dimensional system having f fluctuating fields at each lattice point, where $d_{\text{eq}} = d_\parallel + d_{\perp_2}$, and $f = 2d_{\perp_1}$. From a simple generalization of eq. (13) we find the exponents

$$\theta = \frac{4 - d_\perp}{d_\parallel}, \quad \nu_\parallel = \frac{4 - d_\perp}{2d_\parallel}, \quad \nu_\perp = \frac{1}{2}, \quad (22)$$

fulfilling the hyperscaling relation $d_\parallel \nu_\parallel + d_\perp \nu_\perp = 2$.

We conclude with a tabular summary of the found exponents and critical temperatures T_c at infinite driving velocity v given in table 2, including two cases denoted “mix” where we assumed a suitable two-dimensional motion of the interacting planes. These systems have $d_\parallel = 2$, but notwithstanding the same T_c as the corresponding systems with unidirectional motion at infinite v . For the layered case 2 + 1d_m we predict the exponents $\theta = 3/2$ and $\nu_\parallel = 3/4$. A test of these predictions is left for future work.

Table 2: Relevant dimensions, exponents and parameters of the considered models as defined in the text, together with geometries from the literature [9]. 1d, 2d and 3d denote two d -dimensional Ising models (with $d = 1, 2, 3$) moved against each other such that every spin in one system has a coupling partner in the other system, while $2d_b$ and $3d_b$ denote two d -dimensional Ising models (with $d = 2, 3$) moved along a $(d - 1)$ -dimensional boundary. For details and a classification see ref. [9].

	Model	d	d_{\parallel}	d_{\perp}	d_{\perp_1}	d_{\perp_2}	θ	ν_{\parallel}	f	d_{eq}	$T_c(\infty)/J$
moved	1d	1	1	–	–	–	–	2	1	1	2.2691853...
	2d	2	1	1	0	1	3	$3/2$	1	2	4.0587824...
	3d	3	1	2	0	2	2	1	1	3	5.983835(1)
	$2d_b$	1	1	–	–	–	–	2	1	2	2.6614725...
	$3d_b$	2	1	1	0	1	3	$3/2$	1	3	4.8(1)
sheared	1 + 1d	2	1	1	1	0	3	$3/2$	2	1	3.4659074...
	2 + 1d	3	1	2	1	1	2	1	2	2	5.2647504...
	1 + 2d	3	1	2	2	0	2	1	4	1	5.6426111...
	1 + 3d	4	1	3	3	0	1	$1/2$	6	1	7.728921...
mix	$2d_m$	2	2	–	–	–	–	1	1	1	4.0587824...
	$2 + 1d_m$	3	2	1	1	0	$3/2$	$3/4$	2	2	5.2647504...

Conclusion. – We investigated the nonequilibrium phase transition in three-dimensional Ising models with shear and two different shear normals by means of Monte Carlo simulations. In the limit of infinitely high shear velocity v we found a critical temperature $T_c(\infty)$ that depends on the direction of the shear normal. At criticality, strongly anisotropic diverging correlation lengths with exponents $\nu_{\parallel} = 1$ and $\nu_{\perp} = 1/2$ occur, leading to an anisotropy exponent $\theta = 2$, which confirms the results of a dimensional analysis of the corresponding Ginzburg-Landau-Wilson Hamiltonian. Furthermore, the dimensional analysis reproduces the anisotropy exponents as well as the correlation length exponents of the previously studied two-dimensional cases [12] and the parallel correlation length exponent of the one-dimensional cases [9]. The dimensional analysis also gives predictions for two-dimensional shear directions, leading to, *e.g.*, the exponents $\theta = 3/2$ and $\nu_{\parallel} = 3/4$ in a three-dimensional model. This strongly anisotropic behavior provides a natural explanation for the string domains found in real three-dimensional sheared binary liquids [15–18].

Fluctuations perpendicular to the shear were shown to be Gaussian, resulting in a correlation function with Ornstein-Zernike behavior. Additionally, in the case of the $2 + 1d$ geometry we found weakly anisotropic perpendicular correlations. As for $v = 0$ both the $2 + 1d$ geometry and the $1 + 2d$ geometry reduce to the three-dimensional equilibrium Ising model, we expect a crossover from this case to strongly anisotropic mean-field behavior, similar to the $1 + 1d$ geometry. In ref. [12] an expensive analysis for finite velocities has been done leading to a crossover scaling, pointing out that all $v \neq 0$ provoke strongly anisotropic mean-field behavior, which is expected to occur in the current systems as well. However, we did not prove this in detail, due to the additional complexity in three-dimensional systems.

We thank FELIX M. SCHMIDT and D. E. WOLF for very valuable discussions, as well as S. R. DAHMEN for the warm hospitality during our stay at the Universidade Federal do Rio Grande do Sul (UFRGS) in Porto Alegre, Brazil, where parts of this work have been done. This work was supported by CAPES-DAAD through the PROBRAL program as well as by the German Research Society (DFG) through SFB 616 “Energy Dissipation at Surfaces”.

REFERENCES

- [1] KATZ S., LEBOWITZ J. L. and SPOHN H., *Phys. Rev. B*, **28** (1983) 1655.
- [2] SCHMITTMANN B. and ZIA R. K. P., *Statistical mechanics of driven diffusive systems, in Phase Transitions and Critical Phenomena*, edited by DOMB C. and LEBOWITZ J. L., Vol. **17** (Academic Press, London) 1995.
- [3] ZIA R. K. P., *J. Stat. Phys.*, **138** (2010) 20.
- [4] KADAU D., HUCHT A. and WOLF D. E., *Phys. Rev. Lett.*, **101** (2008) 137205.
- [5] MAGIERA M. P., BRENDEL L., WOLF D. E. and NOWAK U., *EPL*, **87** (2009) 26002.
- [6] MAGIERA M. P., WOLF D. E., BRENDEL L. and NOWAK U., *IEEE Trans. Magn.*, **45** (2009) 3938.
- [7] MAGIERA M. P., BRENDEL L., WOLF D. E. and NOWAK U., *EPL*, **95** (2011) 17010.
- [8] MAGIERA M. P., ANGST S., HUCHT A. and WOLF D. E., *Phys. Rev. B*, **84** (2011) 212301.
- [9] HUCHT A., *Phys. Rev. E*, **80** (2009) 061138.
- [10] IGLOI F., PLEIMLING M. and TURBAN L., *Phys. Rev. E*, **83** (2011) 041110.
- [11] HILHORST H. J., *J. Stat. Mech.* (2011) P04009.
- [12] ANGST S., HUCHT A. and WOLF D. E., *Phys. Rev. E*, **85** (2012) 051120, arXiv:1201.1998.
- [13] SARACCO G. P. and GONNELLA G., *Phys. Rev. E*, **80** (2009) 051126.

- [14] WINTER D., VIRNAU P., HORBACH J. and BINDER K., *EPL*, **91** (2010) 60002.
- [15] CROSS M. C. and HOHENBERG P. C., *Rev. Mod. Phys.*, **65** (1993) 851.
- [16] HASHIMOTO T., MATSUZAKA K., MOSES E. and ONUKI A., *Phys. Rev. Lett.*, **74** (1995) 126.
- [17] ONUKI A., *J. Phys.: Condens. Matter*, **9** (1997) 6119.
- [18] MIGLER K. B., *Phys. Rev. Lett.*, **86** (2001) 1023.
- [19] BOUKRAA S., GUTTMANN A. J., HASSANI S., JENSEN I., MAILLARD J.-M., NICKEL B. and ZENINE N., *J. Phys A: Math. Theor.*, **41** (2008) 455202.
- [20] KWAK W., LANDAU D. P. and SCHMITTMANN B., *Phys. Rev. E*, **69** (2004) 066134.
- [21] SELKE W., *Phys. Rep.*, **170** (1988) 213.
- [22] BINDER K. and WANG J.-S., *J. Stat. Phys.*, **55** (1989) 87.
- [23] HUCHT A., *J. Phys A: Math. Gen.*, **35** (2002) L481.
- [24] ALBANO E. V. and BINDER K., *Phys. Rev. E*, **85** (2012) 061601.
- [25] HENKEL M. and SCHOLLWÖCK U., *J. Phys A: Math. Gen.*, **34** (2001) 3333.
- [26] BINDER K., *Some recent progress in the phenomenological theory of finite size scaling and applications to Monte Carlo studies of critical phenomena*, in *Finite Size Scaling and Numerical Simulation of Statistical Systems*, edited by PRIVMAN V. (World Scientific, Singapore) 1990, Chapt. 4.

Magnetic vortices induced by a moving tip

MARTIN P. MAGIERA^{1(a)}, ALFRED HUCHT¹, HAYE HINRICHSSEN², SILVIO R. DAHMEN³ and DIETRICH E. WOLF¹

¹ Faculty of Physics and CeNIDE, University of Duisburg-Essen - D-47048 Duisburg, Germany, EU

² Universität Würzburg, Fakultät für Physik und Astronomie - D-97074 Würzburg, Germany, EU

³ Instituto de Física, Universidade Federal do Rio Grande do Sul - 91501-970 Porto Alegre, RS, Brazil

received 13 July 2012; accepted in final form 4 October 2012

published online 31 October 2012

PACS 75.70.Kw – Domain structure (including magnetic bubbles and vortices)

PACS 75.78.Fg – Dynamics of domain structures

PACS 75.10.Hk – Classical spin models

Abstract – A two-dimensional easy-plane ferromagnetic substrate, interacting with a dipolar tip which is magnetised perpendicular with respect to the easy plane is studied numerically by solving the Landau-Lifshitz Gilbert equation. Due to the symmetry of the dipolar field of the tip, in addition to the collinear structure a magnetic vortex structure becomes stable. It is robust against excitations caused by the motion of the tip. We show that for high excitations the system may perform a transition between the two states. The influence of domain walls, which may also induce this transition, is examined.

Copyright © EPLA, 2012

Introduction. – Vortices in magnetic layers have been intensely studied [1–7]. They are topological defects, and can be characterised by a chirality (an integer winding number, which is a conserved quantity for topological reasons) and a polarity (the out-of-plane magnetisation). They can annihilate by antivortices having a winding number of opposite sign. Vortex-antivortex pairs are important excitations in two-dimensional magnetic systems. In open systems one can also excite isolated vortices, when the corresponding antivortex leaves the system at the boundary.

The polarity of a vortex may be treated as a bit, as it possesses two very stable states which can be easily probed, *e.g.*, with GMR sensors, as those used in reading heads of magnetic disks. Thus magnetic vortex structures are promising candidates for novel non-volatile storage concepts. An important question in this context is, how to “write” a vortex. To switch the polarization, magnetic-field pulses [8,9], alternating magnetic fields [10] or spin-polarised currents [11] have been proposed.

In this letter we present and analyse a new method, by which vortices can be generated or removed. The excitation energy is provided by a moving magnetic tip as used in magnetic force microscopy (MFM). It is known that MFM tips do influence the substrate, which they are supposed to probe—an undesired effect for the microscopy purpose. It has been observed in experiments that domain walls are

deformed by the passing tip [12, 13]. Tip controlled domain wall manipulation has been achieved [14,15]. The manipulation of vortices by an MFM tip has been realized in a type-II superconductor [16,17]. Thus, it is of great interest from the microscopy and the manipulatory point of view to study how an MFM tip interacts with the scanned surface.

We first show that vortex states are stable configurations in easy-plane ferromagnetic structures in the presence of a magnetic tip, positioned above the ferromagnetic structure. Such a system has been studied recently in order to explore the friction force decelerating the magnetic tip [18–20]. Then we show that the vortex remains stable when the tip is moved along the substrate, dragging the vortex through the substrate. Moreover, the moving tip may also create or destroy a vortex structure, depending on the tip magnetisation and velocity, offering an alternative way to switch between three states: A collinear state, as well as a vortex state with up or down polarity. Finally we study the stability of the dragged vortex structure when it passes through a domain wall.

The system. – Our system consists of $N = L_x \times L_y$ classical Heisenberg spins $\mathbf{S}_i = \boldsymbol{\mu}_i / \mu_s$ on a square grid, where μ_s is a material specific saturation magnetisation. The Hamiltonian contains two terms, corresponding to a substrate and a tip part

$$\mathcal{H} = \mathcal{H}_{\text{sub}} + \mathcal{H}_{\text{tip}}, \quad (1)$$

^(a)E-mail: martin.magiera@uni-due.de

For the spin-spin interaction in the substrate we assume an isotropic exchange with interaction constant J and equivalent easy axes in x - and y -direction,

$$\mathcal{H}_{\text{sub}} = -J \sum_{\langle i,j \rangle} \mathbf{S}_i \cdot \mathbf{S}_j - d_z \sum_i S_{i,z}^2 - e_{xy} \sum_i (S_{i,x}^4 + S_{i,y}^4). \quad (2)$$

The easy-plane anisotropy $d_z < 0$ alone would lead to an infinite domain wall width, as all in-plane magnetisation configurations would be degenerated. Correspondingly, the Mermin-Wagner theorem would rule out long-range magnetic order at finite temperatures [21]. The fourth-order anisotropy term $e_{xy} > 0$, however, breaks the continuous symmetry, so that the Hamiltonian (2) has a ferromagnetic low-temperature phase with domain walls of finite width. We use the anisotropy parameters $d_z = -0.1J$ and $e_{xy} = 0.1J$ in this letter.

The substrate-tip interaction is introduced via a dipolar term,

$$\mathcal{H}_{\text{tip}} = -w \sum_i \frac{3(\mathbf{S}_i \cdot \mathbf{e}_i)(\mathbf{S}_{\text{tip}} \cdot \mathbf{e}_i) - \mathbf{S}_i \cdot \mathbf{S}_{\text{tip}}}{R_i^3}, \quad (3)$$

where $R_i = |\mathbf{R}_i|$ denotes the norm of the position of spin i relative to the tip $\mathbf{R}_i = \mathbf{r}_i - \mathbf{r}_{\text{tip}}$, and \mathbf{e}_i its unit vector $\mathbf{e}_i = \mathbf{R}_i/R_i$. \mathbf{r}_i and \mathbf{r}_{tip} are the position vectors of the substrate spins and the tip respectively. w is a free parameter that quantifies the dipole-dipole coupling between the substrate spins and the tip, thus controlling the strength of the tip. We use $\mathbf{S}_{\text{tip}} = (0, 0, -1)$, w is a free parameter representing the tip strength. The tip is moved with constant velocity $(v, 0, 0)$ two lattice constants above the substrate, along the middle line between two spin rows.

For a real system the tip is of course not a point dipole as represented by (3). It rather resembles a magnetic cone of micrometer length. Depending on the scanned length scales the distance between surface and probe, as well as on the length and shape of the probe, different approximations of the tip field are used, see ref. [22] and references therein. While the dipole approximation yields the correct far-field behavior, it has been shown in refs. [23–25] that the stray field of a hollow cone-type tip may be approximated by a magnetic point charge, if the tip extension is large compared to the distance between tip and surface. As the tip magnetization is assumed perpendicular to the surface in this work, both the dipole and the monopole approximation favor a vortex directly underneath the tip. The effects described in the following are therefore expected to be qualitatively similar in both cases, however they may be more pronounced for the monopole field due to its longer range.

Two different kinds of boundary conditions will be used. First we consider the case that all inhomogeneities in the system are due to the tip. Then it is natural to describe the system in the comoving frame of the tip [18]: In the y -direction, the boundaries are open, in the x -direction dynamical. When the tip advances by exactly one lattice

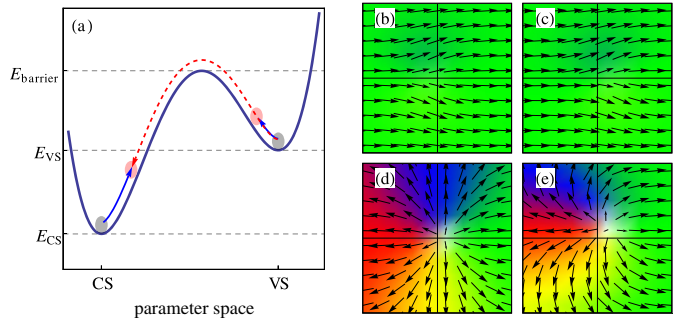


Fig. 1: (Colour on-line) (a) Sketch of the energy landscape. At least two local minima, corresponding to the CS (collinear state) and the VS (vortex state), exist. The absolute minimum depends on the tip strength w . There is a potential barrier between the two states and thus the CS and the VS may be very stable against external driving (blue arrows). A strong perturbation may lead to the transition from the VS to the CS (red dashed arrow) and vice versa. (b)–(e) A part of a system near equilibrium, initialised in the CS ((b), (c)) or the VS ((d), (e)). The scanning velocities are $v = 0.01$ ((b), (d)) and $v = 0.3$ ((c), (e)). The colour coding as well as the arrows represent the magnetisation in the xy -plane, cf. fig. 4.

constant, the foremost row is duplicated, and the last one is deleted. That way, arbitrarily long times can be simulated. In the second part we investigate, how vortex generation is influenced by a domain wall that is pinned far away from the tip. In this case, a combination of open (x -direction) and fixed (y -direction) boundary conditions is more appropriate. The system sizes used are 64×48 for the case of simulations in the absence of domain walls, and 200×48 for the case where domain walls are of interest.

The equation of motion is the Landau-Lifshitz-Gilbert (LLG) equation [26,27]

$$\frac{\partial}{\partial t} \mathbf{S}_i = -\frac{\gamma}{(1 + \alpha^2)\mu_s} [\mathbf{S}_i \times \mathbf{h}_i + \alpha \mathbf{S}_i \times (\mathbf{S}_i \times \mathbf{h}_i)], \quad (4)$$

with saturation magnetisation μ_s , gyromagnetic ratio γ , the phenomenological damping constant α (we use the high damping value $\alpha = 0.5$ in this letter to reach a steady state in a short simulation time) and the local field $\mathbf{h}_i = -\partial\mathcal{H}/\partial\mathbf{S}_i$. It produces Larmor precession with frequency $|\mathbf{h}_i|\gamma/\mu_s$, and a damping in the direction of the local field. In equilibrium, each spin points in the direction of its local field. To solve the LLG we use the Heun integration scheme [28].

Non-equilibrium steady states. – Before studying the driven system, let us discuss the equilibrium case ($v = 0$). If the tip is absent ($w = 0$), the equilibrium configuration corresponds to all spins pointing in the same direction, the collinear state (CS).

As we increase the tip strength, a second minimum appears in the potential landscape, the cylindrically symmetric vortex state (VS, cf. fig. 1(d)). At the same time, the CS minimum is continuously moved to the

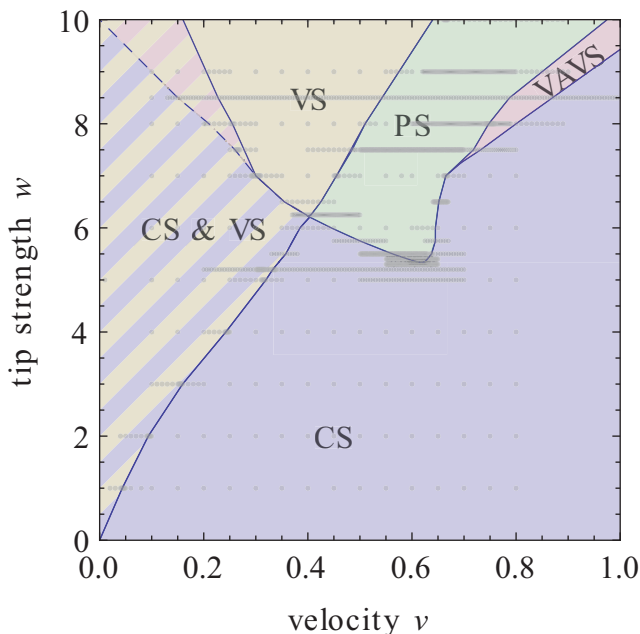


Fig. 2: (Colour on-line) Non-equilibrium steady-state diagram with the pure states (collinear state, CS, and vortex state, VS), the co-existence state (CS & VS), the periodic state (PS) and the vortex-antivortex state (VAVS). The grey points represent the underlying simulations.

configuration of a slightly disturbed collinear configuration (cf. fig. 1(b)). For any reasonably small tip strength, both equilibrium states, the CS and the VS, are stable. If we initialise a VS, and switch off the tip, the VS is still stable: Being a topological defect, its winding number is a conserved quantity which cannot spontaneously change.

Let us now move the tip with constant velocity ($v > 0$): The system is driven into a non-equilibrium steady state (NESS), which is near the equilibrium for small excitations. Accordingly, in the NESS diagram (cf. fig. 2) we see at $v > 0$ a region where the CS and the VS coexist. Here the initial configuration determines the finally stabilised NESS. As the excitation overcomes a threshold by increasing the tip strength w or scanning velocity v (see footnote ¹), the system may perform a transition from the VS to the CS (when the CS represents the total minimum) or vice versa, as sketched in fig. 1(a) by the red dashed arrow. In the NESS, we then observe either the pure CS or the pure VS.

Another mixed state is the periodic state: Here the system is excited so strongly that neither the VS nor the CS is stable. The system then flips between the states back and forth continuously. We explain this state in more detail, because it sheds also more light onto the transitions to the pure states mentioned above. Let us start in the VS. Here the vortex is bound by the tip,

¹A value $w = 1$ in our model corresponds to a magnetic field of about 0.1 T in the substrate under the tip.

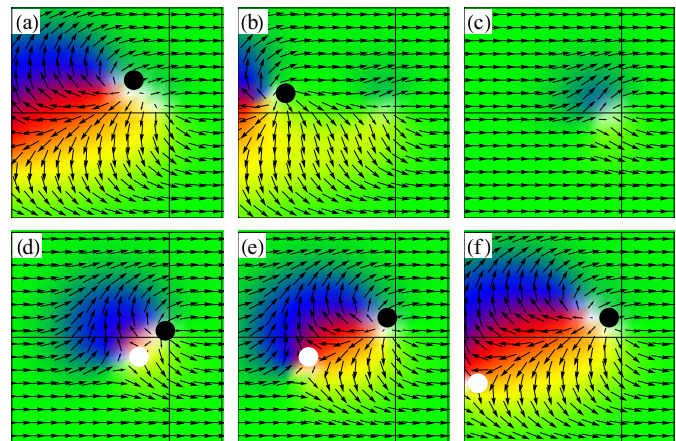


Fig. 3: (Colour on-line) Some snapshots of a system in the PS in a co-moving frame of reference, the tip positioned at the origin (the two lines correspond to the x - and y -axis). Vortex cores are marked as black dots, antivortex cores as white dots. Here we observe the periodical transition from the VS to the CS ((a)–(c)) via the release of the vortex from the tip, as well as the transition from the CS to the VS ((c)–(f)) via a VAVP creation. See the complete cycle as a supplementary on-line movie ([figure_3.avi](#)).

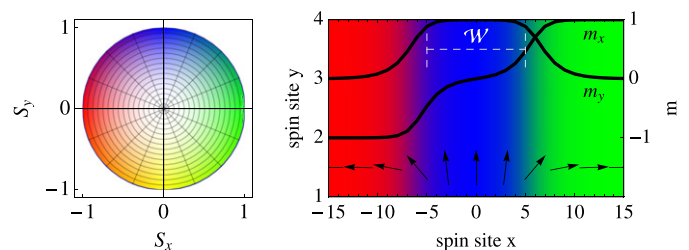


Fig. 4: (Colour on-line) The legend for the colour coded plots, and the equilibrium configuration of a system with two domain walls, as is used for the simulations as an initial state. The width of the middle domain \mathcal{W} is a free parameter.

because the cylindrically symmetric structure minimises the tip energy. However, in the PS (or when the CS is the corresponding NESS) the tip pumps so much energy into the substrate that the vortex may decouple from the tip, and moves away towards the system boundary (fig. 3(b)), leaving a CS behind (fig. 3(c)). Accordingly the potential barrier in fig. 1(a) corresponds to the energy of a free moving vortex and a CS. If the system's NESS is the CS, the system has now reached its steady state. If the initial state was the CS, but the corresponding NESS is the VS or the PS, the system is again excited further by the tip, and a vortex-antivortex pair (VAVP) may nucleate under the tip (fig. 3(d)). The energy of a VAVP represents the potential barrier which the system has to overcome at this transition. After the nucleation, the antivortex moves away from the tip. It may stay at a constant distance (e.g., fig. 3(e)), and we end up in a NESS called

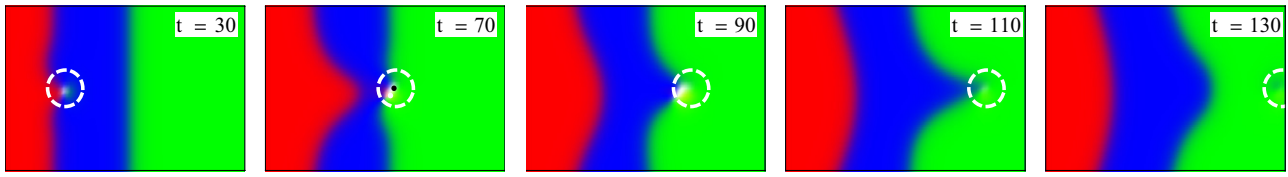


Fig. 5: (Colour on-line) Fast magnetic tip (marked by the dashed circle, $w = 3, v = 0.5$), interacting with two domain walls, with the domain wall distance $\mathcal{W} = 20$. The snapshots show a part of the whole system containing 50^2 spins. The high excitation may lead to the creation of a VAVP, see the middle panel. As the NESS of the system is a CS, the VAVP is annihilated again, leaving the initial domain wall configuration. (See the supplementary on-line movie [figure_5.avi](#).)

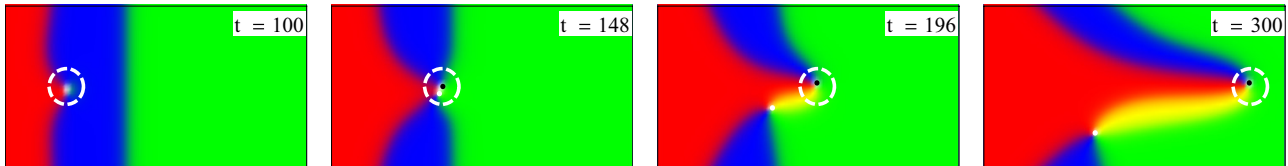


Fig. 6: (Colour on-line) Slow, but strong magnetic tip ($w = 5, v = 0.3$), interacting with two domain walls. Again only a part of the system (70×50 spins) is plotted. A VAVP is created. As the NESS for the present v - w combination is the VS, the vortex stays bound by the tip, and the antivortex travels out of the system, leaving a VS instead of the domain wall state. (See the supplementary on-line movie [figure_6.avi](#).)

vortex-antivortex state (VAVS). If the antivortex moves out of the system, we again get a VS (fig. 3(f)).

The two transitions lead to very different paths in configuration space. The reason why two different barriers have to be passed, as well as why one barrier is higher than the other, can be found in the topology of the system: For the transition $CS \rightarrow VS$, a vortex must be created. However, an isolated vortex cannot be created, as it represents a topological defect, which violates vorticity conservation (the total number of vortex and antivortex cores). Only VAVPs can be created, and thus the energy barrier here is higher than that of the $VS \rightarrow CS$ transition. The reason why the latter transition (which violates vorticity conservation) can occur at all, is that here the antivortex core interacts with the open system boundary. The different transition paths of the PS lead to a hysteresis.

Influence of domain walls. – In the section above we studied a perfect system in order to get an insight into the occurring NESSs. However, a real magnetic specimen contains domain walls, which the tip has to pass through. The open question is, how stable the above-characterised NESSs are against, *e.g.*, domain walls. In order to answer this question we now initialise a system which contains two $\pi/2$ domain walls in equilibrium, where the distance between the two domain walls (or the length of the middle domain) is a free parameter \mathcal{W} (cf. fig. 4). Additionally we fix the boundaries in y -direction by the equilibrium magnetisation, as it is sketched in fig. 4, to emulate infinitely long domain walls. The initial condition corresponds to the simulations initialised in the CS above, as we always start in the left domain. Let us start with a weak excitation ($w \rightarrow 0$). Then the domain wall configuration is not disturbed by the scanning tip. We may observe a slight bending when the tip just passes by (like

in the very left panel of fig. 5), which soon relaxes again, like a rubber band. After the tip has passed the domain walls the configuration is again in its initial state.

When the perturbation by the tip is stronger, a VAVP may nucleate at the domain walls, even if the energy of the moving tip alone is not sufficient, as the domain walls provide additional energy (cf. fig. 5). Which state is finally adopted depends on the NESS, cf. fig. 7. If the corresponding state is the CS, the VAVP get annihilated, and the initial domain wall state appears again. If the corresponding state is the VS, the distance between the vortex and the antivortex increases. Finally, the antivortex stays at the system boundary (as we have fixed boundary conditions in this part the antivortex cannot leave the system), leaving a VS that trails along with the tip. We observed that in the coexistence regime (CS & VS) the system ends up in the VS. The PS is not influenced by the domain wall. It may occur that at the domain walls additional VAVPs nucleate, which after a short lifetime annihilate again.

The influence of the domain wall distance \mathcal{W} is the following: The smaller \mathcal{W} , the larger is the energy density, the domain wall may provide to a VAVP creation process. Accordingly, the lowest tip strength w , at which a VAVP is created, is larger for larger \mathcal{W} .

Finally, we discuss the influence of the boundary conditions. For instance from the right panel of fig. 6 one may claim that the fixed boundaries have a strong impact on the stability of the VS, and enforce the annihilation of the antivortex, as the separation of the VAVP generates continuously growing domain walls. These may become arbitrarily large and thus energetically much more unfavorable than the domain wall state. To get an annihilation process, vortex and antivortex must first move toward each other. This is only possible when the vortex is released

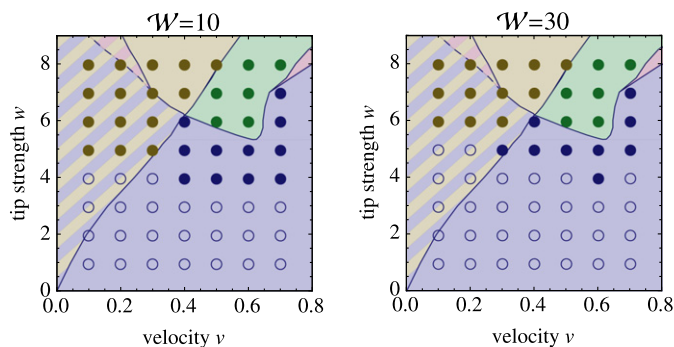


Fig. 7: (Colour on-line) Influence of domain walls on the NESS. Empty circles represent simulations, where the system does not create any VAVP, filled circles represent these simulations where at least one VAVP is created. The colour coding denotes which final state has been observed: blue circles represent the CS, yellow ones the VS, and green ones the PS.

from the tip first, as a free moving vortex or antivortex cannot move at velocities comparable to that of the tip. If the vortex is released or not from the tip depends solely on the current NESS, and not, *e.g.*, on the tailing domain walls, as they cannot provide additional energy density under the tip for a vortex release event. All observed VAVP annihilation processes occur directly after the tip-domain wall interaction, where the events under the tip may be seen as completely decoupled from the boundaries.

Conclusion. – A tip, which is aligned above a ferromagnet with an easy-plane anisotropy, and magnetised perpendicular to the easy plane, energetically stabilises a vortex state in the substrate. The vortex state is stable against slight perturbations, occurring, *e.g.*, when the tip is moved with constant velocity v parallel to the substrate. At a threshold velocity, which depends on the tip magnetisation, the substrate may perform a transition from the vortex phase to the collinear phase and vice versa, but it may also exhibit a periodic switching for strong excitations. In a real system, w is replaced by an effective value, which varies with the characteristics of the tip and the distance between the tip and the substrate, because both parameters determine the field acting at the surface and thus the energy injected into the system. In summary we have three possible states the system may adopt (the CS state and the VS state with up or down polarity), and which may be switched by a moving tip. The presence of a domain wall effectively shifts the state separation line between the coexistence state and the pure vortex state to lower tip magnetisation values.

We thank SEBASTIAN ANGST for valuable discussions. This work was supported by the German Research Foundation (DFG) through SFB 616 “Energy Dissipation

at Surfaces”. A part of the work has been performed during a stay in Porto Alegre, Brazil, granted by the German Exchange Association (DAAD) through the Project Related Exchange Brazil-Germany (PROBRAL). Computing time by the Neumann Institute for Computing (NIC) is gratefully acknowledged.

REFERENCES

- [1] BELAVIN A. A. and POLYAKOV A. M., *JETP Lett.*, **22** (1975) 245.
- [2] NIKIFOROV A. V. and SONIN E. B., *Sov. Phys. JETP*, **58** (1983) 373.
- [3] HUBER D. L., *Phys. Rev. B*, **26** (1982) 3758.
- [4] GOUVÉA M., WYSIN G., BISHOP A. and MERTENS F., *Phys. Rev. B*, **39** (1989) 11840.
- [5] SHINJO T., *Science*, **289** (2000) 930.
- [6] WACHOWIAK A., WIEBE J., BODE M., PIETZSCH O., MORGENSTERN M. and WIESENDANGER R., *Science*, **298** (2002) 577.
- [7] COSTA B. V., *Braz. J. Phys.*, **41** (2011) 94.
- [8] XIAO Q. F., RUDGE J., CHOI B. C., HONG Y. K. and DONOHOE G., *Appl. Phys. Lett.*, **89** (2006) 262507.
- [9] HERTEL R., GLIGA S., FÄHNLE M. and SCHNEIDER C., *Phys. Rev. Lett.* **98** (2007).
- [10] VAN WAEYENBERGE B., PUZIC A., STOLL H., CHOU K. W., TYLISZCZAK T., HERTEL R., FÄHNLE M., BRÜCKL H., ROTT K., REISS G., NEUDECKER I., WEISS D., BACK C. H. and SCHÜTZ G., *Nature*, **444** (2006) 461.
- [11] YAMADA K., KASAI S., NAKATANI Y., KOBAYASHI K., KOHNO H., THIAVILLE A. and ONO T., *Nat. Mater.*, **6** (2007) 269.
- [12] MAMIN H. J., RUGAR D., STERN J. E., FONTANA R. E. and KASIRAJ P., *Appl. Phys. Lett.*, **55** (1989) 318.
- [13] LEE I., KIM J., OBUKHOV Y., BANERJEE P., XIANG G., PELEKHOV D. V., HAUSER A., YANG F. and CHRIS HAMMEL P., *Appl. Phys. Lett.*, **99** (2011) 162514.
- [14] IMRE A., CSABA G., METLUSHKO V., BERNSTEIN G. and POROD W., *Physica E*, **19** (2003) 240.
- [15] YAMAOKA T., WATANABE K., SHIRAKAWABE Y., CHINONE K., SAITOH E. and MIYAJIMA H., *Jpn. J. Appl. Phys.*, **45** (2006) 2230.
- [16] AUSLAENDER O. M., LUAN L., STRAVER E. W. J., HOFFMAN J. E., KOSHNIK N. C., ZELDOV E., BONN D. A., LIANG R., HARDY W. N. and MOLER K. A., *Nat. Phys.*, **5** (2008) 35.
- [17] BRANDT E., MIKITIK G. and ZELDOV E., *Physica C*, **470** (2010) 782.
- [18] MAGIERA M. P., BRENDEL L., WOLF D. E. and NOWAK U., *EPL*, **87** (2009) 26002.
- [19] MAGIERA M. P., BRENDEL L., WOLF D. E. and NOWAK U., *EPL*, **95** (2011) 17010.
- [20] MAGIERA M. P., ANGST S., HUCHT A. and WOLF D. E., *Phys. Rev. B*, **84** (2011) 212301.
- [21] MERMIN N. D. and WAGNER H., *Phys. Rev. Lett.*, **17** (1966) 1133.
- [22] HÄBERLE T., HAERING F., PFEIFER H., HAN L., KUERBANJIANG B., WIEDWALD U., HERR U. and KOSLOWSKI B., *New J. Phys.*, **14** (2012) 043044.

- [23] THIAVILLE A., BELLIARD L., MAJER D., ZELDOV E. and MILTAT J., *J. Appl. Phys.*, **82** (1997) 3182.
- [24] HUG H. J., STIEFEL B., VAN SCHENDEL P. J. A., MOSER A., HOFER R., MARTIN S., GUNTHERODT H.-J., PORTHUN S., ABELMANN L., LODDER J. C., BOCHI G. and OHANDLEY R. C., *J. Appl. Phys.*, **83** (1998) 5609.
- [25] GARCÍA J. M., THIAVILLE A., MILTAT J., KIRK K. J., CHAPMAN J. N. and ALOUGES F., *Appl. Phys. Lett.*, **79** (2001) 656.
- [26] LANDAU L. D. and LIFSHITZ E. M., *Phys. Z. Sowj.*, **8** (1935) 153.
- [27] GILBERT T. L., *IEEE Trans. Magn.*, **40** (2004) 3443.
- [28] GARCÍA-PALACIOS J. and LÁZARO F., *Phys. Rev. B*, **58** (1998) 14937.